Diss. ETH No. 13579

Topological Defects in Unconventional Superconductors

A dissertation submitted to the

SWISS FEDERAL INSTITUTE OF TECHNOLOGY ZURICH
(ETH Zürich)

for the degree of

Doctor of Natural Sciences

presented by

ROLF HEEB

Dipl. Phys. ETH

born March 14, 1970

Swiss citizen

accepted on the recommendation of

Prof. Dr. G. Blatter, examiner

Prof. Dr. T. M. Rice, co-examiner

2000

Abstract

The subject of this thesis is the study of individual vortices and vortex lattices in unconventional superconductors. In a first part, we use mainly phenomenological Ginzburg-Landau theories to determine the detailed shape of individual vortex lines and the symmetry of the vortex lattice. The second part of the thesis is dedicated to the problem of elementary excitations in the vortex cores of unconventional superconductors. We use the mean-field Bogoliubov-de Gennes theory to determine the energy spectra and local density of states self-consistently.

Unconventional superconductors are materials, in which the electron pairing does not occur in the interaction channel with maximal symmetry (s-wave). The electron pairs then have higher angular momentum, and the energy gap has a generally more complicated dependence on the relative momentum $\boldsymbol{k}$, showing point or line nodes. Due to this reduced symmetry in the interaction, a wealth of interesting new phenomena is expected for these materials. Within mean-field (Ginzburg-Landau) theory, one of these new phenomena is the existence of induced order parameters of different symmetry. To investigate such admixtures, we determine the vortex structure in $d_{x^2-y^2}$-wave superconductors with tetragonal (D_{4h}) and orthorhombic (D_{2h}) symmetry on the basis of a Ginzburg-Landau theory. This order parameter symmetry has turned out in the recent years to be the most probable candidate for the high temperature superconductors (HTSC). For the case of a tetragonal symmetry, a d-wave vortex was found to drive an s-wave component with a characteristic four-fold structure, comprising 4 off-center vortices on each of the half-axes and a counter-rotating central vortex. Decreasing the Ginzburg-Landau parameter below the critical value $\kappa = 2$ leads to the collapse of the off-center vortices. An orthorhombic distortion modifies this structure significantly, with 6, 4, 2, or 0 off-center induced s-wave vortices present, depending on the magnitude of the distortion.

In contrast to the HTSC case, in Sr_2RuO_4 the most promising candidate for the order parameter symmetry is p-wave and corresponds to an inherently two dimensional representation of the tetragonal crystal group (Γ_{5u}^-). Based on this odd-parity superconducting order parameter, we investigate the single vortex structure in a weak-coupling model with anisotropic Fermi surface. Ginzburg-Landau calculations for a single vortex show a fourfold structure with an orientation depending on the microscopic Fermi surface properties. Near the lower critical field H_{c1}, an extended London theory is developed to determine the vortex lattice structure in this field region. We find near H_{c1} a centered rectangular vortex lattice, which shows a second order transition to a square vortex lattice for increasing field. This situation is similar to the case of the borocarbide superconductors, where the transition is due to nonlocal effects in the current-field relation. In the intermediate field range, where the vortex lattice has

square symmetry, we performed high precision Ginzburg-Landau solutions to investigate the detailed structure of the B-field distribution. Our results agree qualitatively well with the experiments, and we predict values for the Ginzburg-Landau parameter κ and the Fermi surface anisotropy ν.

In the second part, we use a Bogoliubov-de Gennes hamiltonian to determine the excitation spectrum in the circular symmetric vortices of p-wave superconductors. We introduce both screening in charge and current on the length scales $\lambda_{TF} \sim 1/k_F$ and λ_L, respectively. We find the predicted energy spectrum $E_n = n\omega_0$, where ω_0 is the minigap energy. Since we are working at low values for $k_F\xi_0$, we find at low temperatures a strong Kramer-Pesch effect as in the s-wave cores. The most interesting difference between s- and time-reversal symmetry breaking p-wave vortices is obtained in the vortex core charging: whereas the s-wave case shows a substantial core charge screened on the length scale $1/k_F$, the core charge for the energetically stable p-wave vortex is reduced by a large factor (~ 40). This finding is qualitatively consistent with Chern-Simons physics introduced in the Ginzburg-Landau theory due to the fundamental time-reversal symmetry breaking.

In the last chapter, preliminary results are shown for a solution of the Bogoliubov-de Gennes (BdG) problem on a vortex lattice. A singular gauge transformation is used to gauge the topological vortex phases away and to obtain formally a zero average field $\bar{B}$. The resulting BdG problem can be solved subject to Bloch-von Karmann boundary conditions. Since the numerical effort is considerable, the specific results so far have to be considered as preliminary. The good qualitative agreement with the Ginzburg-Landau solutions and the limiting case of isolated vortices however shows the potential of the method.

Kurzfassung

Das Thema der vorliegenden Dissertation ist die Struktur von isolierten Vortices und von deren Gittern in unkonventionellen Supraleitern. Im ersten Teil ziehen wir vorwiegend phänomenologische Ginzburg-Landau Theorien bei, um die detaillierte Form der individuellen Flusslinien und die Symmetrie der Vortex-Gitter zu untersuchen. Im zweiten Teil befassen wir uns mit den elementaren Quasiteilchen-Anregungen in der Kernzone von solchen Vortices. Wir benützen den Bogoliubov-de Gennes Formalismus, um die Energiespektren und die lokale Zustandsdichte selbstkonsistent zu berechnen.

Unkonventionelle Supraleiter sind Materialien, in denen die Elektronenpaarbildung nicht über den Wechselwirkungskanal mit maximaler Symmetrie (s-Kanal) geschieht. Die Elektronenpaare haben vielmehr höhere Drehimulse, und die Lücke in der Anregungsenergie hat generell eine kompliziertere Abhängigkeit vom Relativimpuls $\boldsymbol{k}$. Die Bandlücke kann für spezielle Richtungen des Relativimpulses Knotenlinien oder Knotenpunkte haben, das heisst die Lücke verschwindet an diesen Stellen. Diese reduzierte Symmetrie in der Wechselwirkung lässt eine Vielfalt von neuen Effekten erwarten. Im Rahmen einer Theorie von gemittelten Feldern (Ginzburg-Landau Theorie) ist einer dieser neuen Effekte die Existenz von induzierten Ordnungsparametern verschiedener Symmetrie. Um solche Zumischungen zu studieren, bestimmen wir auf der Basis einer Ginzburg-Landau Theorie die Struktur von isolierten Vortices des $d_{x^2-y^2}$-Typs sowohl für tetragonale (D_{4h}), wie auch für orthorhombische (D_{2h}) Kristalle. Diese spezielle Symmetrie des Ordnungsparameter ($d_{x^2-y^2}$) hat sich in den letzten Jahren als vielversprechendster Kandidat für die Beschreibung von Hochtemperatur-Supraleitern herausgestellt. Für den Fall der tetragonalen Symmetrie treibt der $d_{x^2-y^2}$-Wellen Vortex eine kleine Zumischung eines s-Wellen Supraleiters, die eine charakteristische vierzählige Struktur hat. Nebst einem Knoten mit gegenläufiger Phasenrotation im Vortex-Kern zeigt sie weitere vier Knoten auf den Achsen mit normaler Phasendrehung. Senkt man den Ginzburg-Landau Parameter unterhalb einen kritischen Wert $\kappa = 2$, so verschwinden diese zusätzlichen nichtzentralen Vortices. Eine orthorombische Deformation des Kristalls führt zu einer Vielfalt von ähnlichen Strukturen mit 6, 4, 2, oder gar keinen nichtzentralen Vortices, die abhängig ist von der Grösse und Art der orthorhombischen Störung.

Im Gegensatz zum Fall der Hochtemperatur-Supraleiter ist für den keramischen Supraleiter Sr_2RuO_4 der wahrscheinlichste Kandidat für den Ordnungsparameter eine p-Wellen Symmetrie, die zu einer zweidimensionalen Darstellung der Kristallgruppe gehört (Γ_{5u}^-). Wir untersuchen diesen Ordnungsparameter mit ungerader Parität im Rahmen einer Ginzburg-Landau Theorie mit Koeffizienten, die unter Annahme von schwacher Kopplung hergeleitet wurden. Um die Phänomene zu erklären, führen wir

eine Anisotropie in der Fermi-Fläche ein. Ginzburg-Landau Rechnungen zeigen für isolierte Vortices ähnliche vierzählige Strukturen wie im obigen Fall. Die Orientierung dieser Strukturen hängt von der Anisotropie der Fermi-Fläche ab. In der Nähe des unteren kritischen Felds H_{c1} entwickeln wir eine erweiterte London-Theorie um die Symmetrie des Vortex-Gitters zu bestimmen. Für die tiefsten Felder erhalten wir zentriert rechteckige Gitter, die in einem Phasenübergang zweiter Ordnung zu quadratischen Gittern übergehen, wenn man das Feld erhöht. Diese Resultate sind ähnlich denjenigen für die Borocarbid-Supraleiter, wo dieser Phasenübergang durch eine nichtlokale Beziehung zwischen Strom und Vektorpotential erklärt werden kann. Im mittleren Feldbereich, wo das Vortex-Gitter quadratische Symmetrie aufweist, haben wir präzise Ginzburg-Landau Rechnungen durchgeführt um die detaillierte Verteilung des B-Feldes zu bestimmen. Die Resultate stimmen gut mit den Experimenten überein, und wir können daraus Werte für den Ginzburg-Landau Parameter κ und für die Anisotropie ν der Fermi-Fläche bestimmen.

Im zweiten Teil dieser Dissertation berechnen wir das Energiespektrum der angeregten Zustände in den zirkulärsymmetrischen p-Wellen Vortices. Wir beschreiben das Problem durch einen Bogoliubov-de Gennes Hamiltonoperator, in dem die auftauchenden nichtlokalen Matrixelemente durch eine Gradientenentwicklung ausgedrückt werden. In unseren Rechnungen berücksichtigen wir die Abschirmung der Ladungen wie auch der Ströme. Wir finden numerisch das vorhergesagte Spektrum $E_n = n\omega_0$, wobei ω_0 den Abstand benachbarter Energieniveaux beschreibt. Da wir bei kleinen Werten für $k_F\xi_0$ arbeiten, finden wir auch im p-Wellen Fall bei tiefen Temperaturen einen starken Kramer-Pesch Effekt. Der interessanteste Unterschied zwischen s- und zeitumkehrverletzenden p-Wellen tritt beim Vergleich der Vortexladungen auf: während man in s-Wellen Fall eine klar erkennbare positive Vortexladung findet, ist diese für p-Wellen durch einen grossen Faktor (~ 40) unterdrückt. Dieses Resultat stimmt qualitativ gut überein mit Resultaten, die innerhalb einer erweiterten Ginzburg-Landau Theorie für zeitumkehrverletzende Systeme erwartet werden.

Im letzten Kapitel besprechen wie erste Resultate zu einer Lösung des Bogoliubov-de Gennes Problems für ein Vortex-Gitter. Eine singuläre Eichtransformation wird verwendet um die topologischen Phasendrehungen bei den Vortexkernen wegzueichen. Gleichzeitig erhält man eine Theorie mit formal verschwindendem mittlerem B-Feld. Dieses Problem kann mit einfachen Bloch-von Karmann Randbedingungen gelöst werden. Der numerische Aufwand ist aber dennoch beträchtlich, und die Resultate müssen als vorläufig gewertet werden. Die gute Übereinstimmung dieser Lösungen mit entsprechenden Resultaten aus der Ginzburg-Landau Theorie oder aus den Rechnungen für isolierte Vortices zeigt aber das Potential der Methode auf.

Contents

Chapter 1

Introduction

The discovery of the high temperature superconductors (HTSC) in 1986 by Bednorz and Müller[1] marks a milestone in the physics of superconductivity. Not only did it show the experimentalists the way to a whole class of new materials exhibiting extremely high critical temperatures compared to the conventional metallic superconductors, it also initiated intense theoretical research towards an understanding of the quality of these materials. And, last but not least, since their critical temperatures of the order of $T_c \sim 100$ K are markedly higher than the temperature of liquid nitrogen ($T = 77.3$ K), these materials are not only of academic interest, but found their application quite soon also in technology.

The HTSC are layered crystalline compounds containing one or more copper oxide planes, separated by nonmetallic layers. The crystal structure is in most cases tetragonal, with large anisotropy in the electronic properties along the z-axis. All known HTSC are strong type-II superconductors, which means that a large part of their phase diagram is dominated by the coexistence of magnetic field and superconducting order parameter. The interplay between magnetic fields and superconducting order parameter is described by the ratio of two length scales. The typical length scale for the decay of magnetic fields in a superconductor is the penetration depth $\lambda \sim 1500$Å. The healing length of the superconducting condensate is the coherence length $\xi \sim 20$Å. The ratio $\kappa = \lambda/\xi$ is called Ginzburg-Landau parameter and is a measure for the surface energy of the boundary between superconductor and field: in the type II case, where $\kappa \geq 1/\sqrt{2}$, the surface energy is negative, and a magnetic field penetrating the superconductor tends to split into small portions to maximize the length of the boundary. The field then penetrates in form of flux tubes, so called vortices, carrying one superconducting flux quantum $\Phi_0 = hc/2e$. The individual flux lines repel and usually form regular two-dimensional lattices.

The attempts to understand the physics of the HTSC has led to considerable extensions of the concept of the original BCS-superconductors. Already before the discovery

of HTSC, first experimental facts were presented, that certain heavy fermion superconductors as *e. g.* UBe_{13}[2] or UPt_3[3] did not fit into the picture of *s*-wave pairing. These materials were believed to show an electron pairing in an anisotropic channel like a *p*-wave spin triplet or a *d*-wave spin singlet state. It turned out, that also the HTSC belong to this class of so-called unconventional superconductors: evidence has grown in the recent years, that the copper-oxide superconductors are of $d_{x^2-y^2}$ symmetry. In the following, we briefly introduce the concept of unconventional superconductivity, and how to set up a corresponding Ginzburg-Landau theory. We follow the Review of Sigrist and Ueda (Ref. [4]).

The pairing wavefunction, also called gap function, is given in a generalized BCS theory as a mean-field expression of the generic matrix form

$$\Delta_{ss'}(\boldsymbol{k}) = \sum_{\boldsymbol{k}',s_3,s_4} V_{s',s,s_3,s_4}(\boldsymbol{k},\boldsymbol{k}')\langle a_{\boldsymbol{k}',s_3} a_{\boldsymbol{k},s_4}\rangle, \tag{1.1}$$

where V is the interaction potential, the $a_{\boldsymbol{k},s}$ are usual second quantized annihilation operators in reciprocal and spin space, and $\langle\rangle$ denotes the quantum expectation value. This pairing wavefunction describing the condensate of Cooper-pairs is the central quantity in the theory of superconductivity. As will be shown below, it is intimately related to both the order parameter describing superconducting density and the excitation energy gap. The antisymmetric nature of the fermions requires for the gap function matrix the symmetry $\hat{\Delta}(\boldsymbol{k}) = -\hat{\Delta}^T(-\boldsymbol{k})$. Therefore, for singlet pairing, the gap function can be described by a single even function $\psi(\boldsymbol{k})$

$$\hat{\Delta}(\boldsymbol{k}) = i\hat{\sigma}_y\psi(\boldsymbol{k}) = \begin{pmatrix} 0 & \psi(\boldsymbol{k}) \\ -\psi(\boldsymbol{k}) & 0 \end{pmatrix}, \tag{1.2}$$

whereas in the triplet case we need an odd vector function $\boldsymbol{d}(\boldsymbol{k})$

$$\hat{\Delta}(\boldsymbol{k}) = i(\boldsymbol{d}(\boldsymbol{k})\hat{\boldsymbol{\sigma}})\hat{\sigma}_y = \begin{pmatrix} -d_x(\boldsymbol{k}) + id_y(\boldsymbol{k}) & d_z(\boldsymbol{k}) \\ d_z(\boldsymbol{k}) & d_x(\boldsymbol{k}) + id_y(\boldsymbol{k}) \end{pmatrix}. \tag{1.3}$$

Restricting to unitary gap functions (*i. e.* $\hat{\Delta}\hat{\Delta}^\dagger \propto \hat{\sigma}_0$ where $\hat{\sigma}_0$ is the unit matrix), the energy spectrum in the bulk is given by

$$E_k = \sqrt{\epsilon^2(\boldsymbol{k}) + \frac{1}{2}\mathrm{tr}\hat{\Delta}\hat{\Delta}^\dagger(\boldsymbol{k})}. \tag{1.4}$$

The kinetic energy of the free particles is denoted by $\epsilon(\boldsymbol{k})$. In the case of *s*-wave symmetry, the function $\psi(\boldsymbol{k})$ is equal to a constant Δ_0, and the expression for the excitation energies takes the well known form $\sqrt{\epsilon^2(\boldsymbol{k}) + |\Delta_0|^2}$.

The whole electron system is subject to a symmetry group $G \times U(1) \times \mathcal{T}$, consisting of the point symmetry group G of the crystal, the gauge symmetry group $U(1)$ and the

time reversal symmetry $\mathcal{T}$. Thus it makes sense to expand the gap function into the irreducible representations of this symmetry group. Since the point symmetry group of a crystal is discrete, there is a finite number of irreducible representations. To generate basis functions in the invariant subspaces of these irreducible representations, one often takes the projections onto these spaces of basis states belonging to the representations of $SO(3)$ to fixed angular momentum l. The type of gap function is then called s-, p-, d-wave if the $\boldsymbol{k}$-scaling is $\hat{\Delta}(\lambda\boldsymbol{k}) = \lambda^l\hat{\Delta}(\boldsymbol{k})$ with $l = 0, 1, 2, \ldots$. However, this terminology has not to be confused with the effective form of the basis functions, which is only determined by symmetry and can be any superposition of terms with higher angular momentum[5].

The gap function can now be written as expansion in these symmetry compatible basis functions $\hat{\Delta}(\Gamma, m; \boldsymbol{k})$

$$\hat{\Delta}(\boldsymbol{k}) = \sum_{m,\Gamma} \eta(\Gamma, m)\hat{\Delta}(\Gamma, m; \boldsymbol{k}), \tag{1.5}$$

where Γ denotes the irreducible representation and m runs over the dimension of the representation. Usually one of these representations has the largest critical temperature T_c and thus dominates the rest, however, different representations can be admixed in principle (see Chapter 2). Finally, the quantities $\eta(\Gamma, m)$ are taken as space dependent order parameters $\eta(\boldsymbol{r}, \Gamma, m)$, which transform under the symmetry group like coordinates with respect to the basis function space given by the $\hat{\Delta}(\Gamma, m; \boldsymbol{k})$.

Having established the connections between pairing wave function, order parameter and energy gap, we have the choice between several methods to describe the structure of vortex lines in unconventional superconductors. Leaving the microscopical level in favor of a more phenomenological description, the free energy density of the superconducting system can be expanded near T_c in the (small) order parameter. The corresponding expansion, called Ginzburg-Landau free energy density, consist of all lowest order terms in the order parameter components and the gradient operators, which are invariant under the total symmetry group. The generic Ginzburg-Landau equation for an s-wave superconductor with order parameter η_s has in dimensionless units the form

$$f = -|\eta_s|^2 + |\eta_s^4| + |\boldsymbol{D}\eta_s|^2 + B^2, \tag{1.6}$$

where $\boldsymbol{D}$ stands for the gauge invariant derivative $-i\boldsymbol{\nabla} - \boldsymbol{A}$. Minimizing the free energy density with respect to order parameter and vector potential subject to boundary conditions leads to the spatial structure of the order parameter and the fields.

While the Ginzburg-Landau theory describes very well the physics of the vortex lines and the superconducting condensate, many experiments in the last years have measured the low energy behavior of unconventional superconductors. Among this wealth

of experimentally probed quantities which are sensitive to the low energy states are specific heat, London penetration depth[6, 7], nuclear magnetic resonance (NMR) relaxation rates[8], STM tunneling spectra[9, 10, 11, 12] and angular resolved photon emission spectroscopy data (ARPES)[13, 14]. It is therefore of great importance to determine the low energy spectrum of the vortex phase, especially for isolated vortices or regular vortex arrays. A very successful method to solve this problem is the Hartree-like self-consistent solution due to Bogoliubov and de Gennes. The superconducting order parameter thereby acts as a mean-field potential for the solution of the individual quasiparticles and is connected to these by a self-consistency relation. In the s-waves, such theoretical investigations have a long tradition and turned out to be very successful. The problem especially in $d_{x^2-y^2}$-wave symmetry however is far more involved: for the single vortex solution, the presence of the gap nodes destroys the circular symmetry of the problem, and analytic as well as numeric solutions are difficult.

The experimental evidence for HTSC points very clearly towards $d_{x^2-y^2}$-symmetry for the order parameter. Almost all experiments show signatures of line nodes in the gap, and a beautiful series of phase sensitive experiments showed clear agreement with this idea[15, 16, 17, 18, 19, 20]. However, a very interesting material does not fit into this scheme: in 1994, Sr_2RuO_4 was shown to have a superconducting transition at 1.5K[21]. Structurally, the strontium compound resembles strongly the HTSC. It is also a layered crystal, however with RuO planes instead of the CuO planes for the HTSC's. Theoretical and experimental progress for this compound during the last years points clearly towards a time reversal breaking p-wave superconductor. The direct test via a phase sensitive experiment is still missing, but the indirect hints are quite strong. Inspired by these two important cases, we restrict in this work to the cases of s-, p- and d-wave symmetry. The s-wave case is mainly taken as a reference to reveal the differences to the unconventional case. Where it is clear from the context, we will use the short notation d-wave for $d_{x^2-y^2}$-wave and p-wave for the specific representation Γ_{5u}^- investigated for the Sr_2RuO_4-system.

In this thesis, we use mainly the two viewpoints mentioned above to describe the unconventional superconductivity in HTSC and Sr_2RuO_4. In Chapter 2, we derive the free energy density for a $d_{x^2-y^2}$-wave superconductor with tetragonal symmetry and possible admixtures of s- and d_{xy}-wave symmetry. Although these admixtures are taken as vanishing in the bulk state, they can be induced by inhomogeneities in the main $d_{x^2-y^2}$ order parameter (s-admixtures) or by coupling to magnetic fields (d_{xy}-admixtures). We investigate the case of an isolated vortex line, where the admixed components turned out to show a very rich topological structure. The case of orthorhombic crystal symmetry is also discussed. In Chapter 3, a similar calculation is presented for the most promising p-wave order parameter symmetry to describe

Sr_2RuO_4. Basing on a weak coupling free energy density derived by Agterberg, we discuss the single vortex structure of this two-component order parameter. Near H_{c1}, we derive an extended London model to describe the vortex lattice, and find for $B \parallel c$ a second order transition between the hexagonal low field phase and a square lattice at higher fields, provided the Fermi surface has a square-shaped anisotropy. Within a precision Ginzburg-Landau solution, the detailed B-field distribution in the vortex lattice phase is determined and compared with recent experiments. Chapter 4 is dedicated to the solution of the single vortex problem within Bogoliubov-de Gennes theory for the circular symmetric s- and p-wave cases. For the latter case, a continuum model is derived basing on a gradient expansion of the nonlocal matrix elements. Finally, in Chapter 5 a self-consistent solution for the vortex lattice case for s-, p- and d-wave is presented within the Bogoliubov-de Gennes formalism. Although the numerical results are still preliminary, the method certainly shows the potential to furnish interesting results.

Chapter 2

Ginzburg-Landau Theory for d-Wave Superconductors

The content of the following chapter has been published in Physical Review B in October 1996[22].

2.1 Introduction

The discovery of high-temperature superconductors (HTSC) [1] has initiated a considerable effort in exploring their exotic properties. In recent years, a subject of intense discussion has been the symmetry of the superconducting order parameter. Nowadays, a large number of experiments provide good evidence for an order parameter with d-wave symmetry, *i. e.*, the gap function has the generic form $\Delta(\mathbf{k}) = \Delta_0(k_x^2 - k_y^2)$ in momentum space. Theoretical and experimental work has focused on the questions which physical properties will distinguish a d-wave from a conventional s-wave superconductor. An important issue is the presence of nodes in the gap at $k_x = \pm k_y$ which influence the low-temperature properties due to the presence of low-lying quasiparticle excitations. A second issue is the direct observation of the internal phase structure of the order parameter. In a beautiful series of phase sensitive experiments a phase structure has been observed which is compatible with d-wave symmetry in some HTSC[15, 18, 16, 17].

In the recent years, the problem of the structure of vortex lines in d-wave superconductors has attracted much attention. Vortices are topological defects in the superconducting order parameter, *i. e.* local zeros of the superconducting density, where screened flux tubes penetrate the superconductor[23]. Both, isolated vortices and their arrangement in a lattice have been investigated. Soininen *et al.*[24] applied the

Bogoliubov-de Gennes theory to electrons on a square lattice with attractive nearest-neighbor interaction. An admixture of the s-wave component to the d-wave order parameter was found in the vicinity of the vortex core. Berlinsky *et al.*[25] analyzed the structure of the admixed s-wave order parameter using the Ginzburg-Landau (GL) theory. Neglecting the effects of the magnetic field they observed that the s-wave component develops a four-lobe structure around a central counter-rotating vortex, where in each lobe a vortex appears with a positive winding. Very recently, Franz *et al.*[26] presented a more detailed discussion of the structure of d-wave vortices that includes the magnetic field effects self-consistently, which to a large extent is confirmed by our results below about tetragonal symmetry. Ren *et al.*[27] derived the GL equation from a phenomenological microscopic model and reached similar conclusions for the vortex structure. In a newer work, Xu *et al.*[28] present numerical calculations of a single vortex solution that do not show the external s-wave vortices. Below, we present an explanation of this result. Using the quasi-classical Eilenberger equations, Ichioka *et al.*[29] recently also reported the four-fold vortex structures found in the previous works.

It is not clear at present whether it is experimentally feasible to observe the structure of a single vortex. Therefore the influence of the single vortex structure on the arrangement of many vortices is an important issue. Berlinsky *et al.*[25, 26] concluded from their GL treatment that in the high-field limit the vortices should form an oblique lattice instead of the standard triangular one[9, 30], the four-fold symmetry of the vortex structure being incompatible with the triangular lattice symmetry. Similar results were achieved by Won and Maki[31] studying the Abrikosov-parameter on the basis of a quasi-classical treatment using linearized Gorkov-equations, and by Xu *et al.*[28] using a GL-energy functional derived from a phenomenological microscopic model.

In the present work we extend the investigation of the single vortex structure in three ways: (1) The structure of the s-wave component is analyzed including the effects due to the presence of a magnetic field. (2) Whereas previous works have been limited to tetragonal crystal symmetry, here, we study the effects of orthorhombic distortions. Note that various HTSC's, *e. g.* $YBa_2Cu_3O_7$, have this lattice structure. (3) We investigate the admixture of a d_{xy}-wave component as driven by the coupling to the magnetic field.

The coupling strength between the order parameter and the magnetic field is given by the GL-parameter $\kappa = \lambda/\xi_d$ (λ denotes the London penetration depth and ξ_d is the coherence length of the d-wave component). The case $\kappa = \infty$ ($e = 0$) corresponds to vanishing coupling, which was the limit considered in the works mentioned above[25, 27]. A finite coupling κ has two main consequences: The off-center vortices of the s-wave order parameter are suppressed. As a function of κ the position of these

four vortices moves gradually away from the center. The effect becomes appreciable, however, only in the range $0 < \kappa < 10$. For $\kappa < 2$, close to the type I regime, the off-center vortices disappear completely. The study of the asymptotic long distance behavior shows a difference between the cases $\kappa = \infty$ ($e = 0$) and $\kappa < \infty$. In the former case the admixed s-wave component η_s vanishes algebraically, while in the latter case screening effects lead to an exponential decay beyond the London penetration depth λ. Following Franz *et al.*[26], there exists an intermediate region, $\xi_d \ll r \ll \lambda$, where the algebraic decay $|\eta_s| \sim 1/r^2$ is still valid. This is due to the weak variation of the field in the range $r \ll \lambda$.

If the tetragonal lattice is distorted orthorhombically leaving the x- and y-axis as the main axes, we cannot distinguish s- and d-wave by symmetry anymore. The two components couple and a finite d-wave order parameter always induces a finite s-wave component everywhere in the bulk. This property has been applied to explain the Josephson tunneling currents measured by Sun *et al.*[32] in a Pb-YBCO junction with the surface perpendicular to the c-axis. If YBCO were a pure $d_{x^2-y^2}$-superconductor, one would expect a zero tunneling current. The induced s-wave component in the orthorhombic YBCO however couples to the s-wave superconductor and produces an observable tunneling current (for a more detailed discussion including heavily twinned materials see[33].) The non-vanishing s-wave component has consequences for the vortex structure as well, particularly for the position of the off-center vortices. For small distortions, we find that more vortices can appear with the original vortices displaced away from the center along one and towards the center along the other main axis.

The $d_{x^2-y^2}$- and d_{xy}-wave states can combine into $d_{x^2-y^2} + id_{xy}$, *i. e.* a complex state which breaks time reversal symmetry, and which has an intrinsic magnetic moment along the z-axis. Therefore, we can find an admixture of the d_{xy}-wave component in the vicinity of a $d_{x^2-y^2}$-wave vortex due to the presence of the magnetic field. It is shown that the both components have the same phase winding structure and no vortices in the admixed order parameter appear away from the center.

2.2 Ginzburg-Landau free energy density

In Ginzburg-Landau theory, superconductivity is described by a free energy functional that depends on a complex order parameter $\eta(\boldsymbol{r}, \boldsymbol{k})$ (gap function). Here, $\boldsymbol{r}$ and $\boldsymbol{k}$ denote the center of mass and the relative momentum of the two electrons forming a Cooper-pair. We are interested in vortex structures of layered materials with small interlayer-coupling. Assuming the external field to be perpendicular to the layers, we restrict ourselves to a two-dimensional problem. In addition, we require the free

D_{4h}-invariant terms	
2^{nd} order	: $\lvert\eta_s\rvert^2,\ \lvert\eta_d\rvert^2,\ \lvert\eta_{d'}\rvert^2$
4^{th} order	: $\lvert\eta_s\rvert^4,\ \lvert\eta_d\rvert^4,\ \lvert\eta_{d'}\rvert^4,\ \lvert\eta_s\rvert^2\lvert\eta_d\rvert^2,\ \lvert\eta_s\rvert^2\lvert\eta_{d'}\rvert^2,\ \lvert\eta_d\rvert^2\lvert\eta_{d'}\rvert^2,$
	: $\eta_s^2\eta_d^{*2},\ \eta_s^2\eta_{d'}^{*2},\ \eta_d^2\eta_{d'}^{*2}$
grad. terms	: $\lvert\boldsymbol{D}\eta_s\rvert^2,\ \lvert\boldsymbol{D}\eta_d\rvert^2,\ \lvert\boldsymbol{D}\eta_{d'}\rvert,^2$
	: $D_x^*\eta_s^* D_x\eta_d - D_y^*\eta_s^* D_y\eta_d,\ D_x^*\eta_s^* D_y\eta_{d'} + D_y^*\eta_s^* D_x\eta_{d'},$
	: $D_x^*\eta_{d'}^* D_y\eta_d - D_y^*\eta_{d'}^* D_x\eta_d$
D_{2h}-invariant terms	
2^{nd} order	: $\lvert\eta_s\rvert^2,\ \lvert\eta_d\rvert^2,\ \lvert\eta_{d'}\rvert^2,\ \eta_s\eta_d^*$
4^{th} order	: $\lvert\eta_s\rvert^4,\ \lvert\eta_d\rvert^4,\ \lvert\eta_{d'}\rvert^4,\ \lvert\eta_s\rvert^2\lvert\eta_d\rvert^2,\ \lvert\eta_s\rvert^2\lvert\eta_{d'}\rvert^2,\ \lvert\eta_d\rvert^2\lvert\eta_{d'}\rvert^2,$
	: $\eta_s^2\eta_d^{*2},\ \eta_s^2\eta_{d'}^{*2},\ \eta_d^2\eta_{d'}^{*2},\ \lvert\eta_{d'}\rvert^2\eta_s\eta_d^*,\ \eta_{d'}^2\eta_s^*\eta_d^*,$
	: $\lvert\eta_s\rvert^2\eta_s\eta_d^*,\ \lvert\eta_d\rvert^2\eta_s\eta_d^*$
grad. terms	: $D_x\eta_s D_x^*\eta_s^*,\ D_y\eta_s D_y^*\eta_s^*,\ D_x\eta_d D_x^*\eta_d^*,\ D_y\eta_d D_y^*\eta_d^*,$
	: $D_x\eta_{d'} D_x^*\eta_{d'}^*,\ D_y\eta_{d'} D_y^*\eta_{d'}^*,\ D_x^*\eta_s^* D_x\eta_d,\ D_y^*\eta_s^* D_y\eta_d,$
	: $D_x^*\eta_s^* D_y\eta_{d'},\ D_y^*\eta_s^* D_x\eta_{d'},\ D_x^*\eta_{d'}^* D_y\eta_d,\ D_y^*\eta_{d'}^* D_x\eta_d.$

Table 2.1: Invariant terms of Ginzburg-Landau free energy densities up to fourth order for tetragonal (D_{4h}) and orthorhombic (D_{2h}) symmetry. Addition of hermitian conjugate terms to guarantee reality is not explicitly written. The most general FED up to fourth order compatible with D_{4h} is the sum of all D_{4h}-invariant terms, each one multiplied by a real coefficient.

energy and also the free energy density (FED) to be invariant under the symmetry group $G \times U(1) \times K$, where G denotes the point group of the crystal (G is either D_{4h} (tetragonal symmetry) or D_{2h} (orthorhombic symmetry)), $U(1)$ is the gauge symmetry group and K represents the time reversal operation. We expand the order parameter $\eta(\boldsymbol{r}, \boldsymbol{k})$ in $\boldsymbol{k}$-dependent basis functions of the irreducible representations of the point group

$$\eta(\boldsymbol{r}, \boldsymbol{k}) = \eta_s(\boldsymbol{r}) + \eta_d(\boldsymbol{r})\,(\hat{k}_x^2 - \hat{k}_y^2) + \eta_{d'}(\boldsymbol{r})\,(\hat{k}_x\,\hat{k}_y). \tag{2.1}$$

which corresponds to even parity (spin singlet) pairs and $l \leq 2$. The FED is a scalar expansion in the order parameter components $\eta_s(\boldsymbol{r})$, $\eta_d(\boldsymbol{r})$ and $\eta_{d'}(\boldsymbol{r})$ up to fourth order including gradient terms (see Ref. [4]). In Table 2.1 we list all invariant terms for D_{4h} and D_{2h}, where we use the covariant gradient

$$\boldsymbol{D} \equiv (-i\boldsymbol{\nabla} - 2e\boldsymbol{A}) \tag{2.2}$$

to guarantee gauge invariance. In this way we can construct the most general scalar FED, where each invariant term has a material dependent real coefficient. As an example, we give here the FED for tetragonal symmetry with η_s and η_d, neglecting

$\eta_{d'}$, as was discussed *e. g.* by Joynt[34]:

$$\begin{aligned} f &= \alpha_s|\eta_s|^2 + \frac{\beta_s}{2}|\eta_s|^4 + \frac{1}{2m_s}|\boldsymbol{D}\eta_s|^2 \\ &\quad + \alpha_d|\eta_d|^2 + \frac{\beta_d}{2}|\eta_d|^4 + \frac{1}{2m_d}|\boldsymbol{D}\eta_d|^2 \\ &\quad + \gamma_1|\eta_s|^2|\eta_d|^2 + \gamma_2(\eta_s^2\eta_d^{*2} + \eta_s^{*2}\eta_d^2) \\ &\quad + \delta\Big((D_x^*\eta_s^*)(D_x\eta_d) - (D_y^*\eta_s^*)(D_y\eta_d) + h.c.\Big) + \frac{\boldsymbol{B}^2}{8\pi}. \end{aligned} \tag{2.3}$$

With

$$D_\alpha^*\eta_s^* D_\beta\eta_d = \eta_s^* D_\alpha D_\beta\eta_d + i\nabla_\alpha(\eta_s^* D_\beta\eta_d) \tag{2.4}$$

and neglecting surface effects (see below), we can replace the term $(D_x^*\eta_s^*)(D_x\eta_d) - (D_y^*\eta_s^*)(D_y\eta_d)$ by $\eta_s^*(D_x^2 - D_y^2)\eta_d$ in the FED.

2.3 Tetragonal symmetry D_{4h}: η_s-admixtures

In this section, we restrict the analysis to η_s and η_d. Furthermore, η_d shall be the dominant order parameter component ($T_c^d > T_c^s$). We introduce the units $\xi_d = (2m_d|\alpha_d|)^{-1/2}$ for the length, $(e\xi_d)^{-1}$ for the $\boldsymbol{A}$-field, $2\alpha_d^2/\beta_d$ for the energy density and $\sqrt{2|\alpha_i|/\beta_i}$ for the order parameters η_i in order to obtain a dimensionless Ginzburg-Landau free energy density

$$\begin{aligned} f &= \tilde{\alpha}|\eta_s|^2 + \tilde{\alpha}|\eta_s|^4 + \tilde{\mu}|\boldsymbol{D}\eta_s|^2 - |\eta_d|^2 + |\eta_d|^4 + |\boldsymbol{D}\eta_d|^2 \\ &\quad + \tilde{\gamma}_1|\eta_s|^2|\eta_d|^2 + \tilde{\gamma}_2(\eta_s^2\eta_d^{*2} + \eta_s^{*2}\eta_d^2) \\ &\quad + \tilde{\delta}(\eta_s^*(D_x^2 - D_y^2)\eta_d + h.c.) + 2\kappa^2\boldsymbol{B}^2. \end{aligned} \tag{2.5}$$

The rescaled parameters $\tilde{q}$ expressed in terms of the original parameters q in Eq. (2.3) are

$$\begin{aligned} &\tilde{\alpha} = \frac{\beta_d\alpha_s^2}{\beta_s\alpha_d^2}, \qquad \tilde{\mu} = \frac{m_d\beta_d|\alpha_s|}{m_s\beta_s|\alpha_d|}, \quad \kappa^2 = \frac{\lambda^2}{\xi_d^2} = \frac{\beta_d m_d^2}{8\pi e^2}, \\ &\tilde{\gamma}_1 = 2\frac{\gamma_1|\alpha_s|}{\beta_s|\alpha_d|}, \quad \tilde{\gamma}_2 = 2\frac{\gamma_2|\alpha_s|}{\beta_s|\alpha_d|}, \quad \tilde{\delta} = 2\delta m_d\sqrt{\frac{\beta_d|\alpha_s|}{\beta_s|\alpha_d|}}. \end{aligned} \tag{2.6}$$

Also, we have introduced the screening length $\lambda = \sqrt{m_d\beta_d}/(16\pi e^2|\alpha_d|)$. In the absence of a microscopic theory, we treat $\tilde{\alpha}, \tilde{\mu}, \tilde{\gamma}_i, \tilde{\delta}$, and κ as the phenomenological parameters of our theory. Working in a temperature range where the lowest order Taylor expansion in T/T_c^i for α_i and β_i is valid, we have

$$\begin{aligned} \alpha_i &= \alpha_i^0\Big(\frac{T}{T_c^i} - 1\Big), \quad \alpha_i^0 > 0, \\ \beta_i &= \text{const.}, \end{aligned} \tag{2.7}$$

and therefore

$$\begin{aligned} \tilde{\alpha} &= \frac{\beta_d}{\beta_s}\Big(\frac{\alpha_s^0\, T_c^d}{\alpha_d^0\, T_c^s}\Big(\frac{T-T_c^s}{T-T_c^d}\Big)\Big)^2, \\ \tilde{\mu} &= \frac{m_d\,\beta_d\,\alpha_s^0\,T_c^d}{m_s\,\beta_s\,\alpha_d^0\,T_c^s}\Big|\frac{T-T_c^s}{T-T_c^d}\Big|. \end{aligned} \tag{2.8}$$

We find $\tilde{\alpha}$ to be large at temperatures close to T_c^d and small at temperatures close to T_c^s. We will further restrict ourselves to the first case, *e. g.* the temperature range where $\tilde{\alpha} > 1$. This excludes homogeneous solutions with non-zero s-waves (note, that in the parameter range $0 < \tilde{\alpha} < 1$, $2\tilde{\alpha} < 2|\tilde{\gamma}_2| - \tilde{\gamma}_1 < 2\sqrt{\tilde{\alpha}}$ a global minimum with $|\eta_s|^2 \neq 0$ can exist.) Assuming $m_d \approx m_s$ and $\beta_d \approx \beta_s$ (compare Ref. [27]), we find the relation

$$\tilde{\alpha} \approx \tilde{\mu}^2. \tag{2.9}$$

The parameters $\tilde{\gamma}_1$, $\tilde{\gamma}_2$, and $\tilde{\delta}$ are treated here as essentially free phenomenological parameters (see Refs. [27, 35, 36] for values derived from different microscopical models). Restrictions on them can be obtained by demanding the FED to be bounded from below,

$$\sqrt{4\tilde{\alpha}} > (2|\tilde{\gamma}_2| - \tilde{\gamma}_1). \tag{2.10}$$

Together with $\tilde{\alpha} > 1$, this condition is equivalent to Eq. (2) in Ref. [26]. Under the conditions $\tilde{\alpha} > 1$ and Eq. (2.10), we find the homogeneous solution for pure d-waves

$$|\eta_s|^2 = 0, \qquad |\eta_d|^2 = \frac{1}{2}, \tag{2.11}$$

which is stable with respect to global changes of the order parameters. Furthermore, we consider the stability of this solution against spatial modulations, and the corresponding linear stability analysis provides the condition

$$\tilde{\mu} > \tilde{\delta}^2 \tag{2.12}$$

ruling out spontaneous small-scale modulations of the order parameters.

2.3.1 Vortex solution in the limit $|\eta_s| \ll |\eta_d|$

We now study the single vortex solution for $|\eta_s| \ll |\eta_d|$. In this limit, we may neglect the feedback of the s-wave component and assume the zero order solution for η_d and $\boldsymbol{A}$, which is the single vortex solution of the pure d-wave case

$$\begin{aligned} \eta_d &= d(r)e^{i\theta} \qquad\qquad d(r) \in \mathbb{R} \\ \boldsymbol{A} &= A(r)\hat{\boldsymbol{e}}_{\boldsymbol{\theta}}. \end{aligned} \tag{2.13}$$

The functions $d(r)$ and $A(r)$ are still unknown. For η_s, we perform a partial wave expansion

$$\eta_s = \sum_{n=-\infty}^{+\infty} s_n(r) e^{in\theta}, \tag{2.14}$$

where the $s_n(r)$ are complex functions. We obtain a coupled set of second order differential equations for the functions $d(r), A(r)$, and $s_n(r)$. In Appendix A.1, we show by minimization of the free energy functional, that only the real parts of the functions $s_{-1}(r)$ and $s_3(r)$ are non-zero. The remaining equations in $d(r), A(r), s_{-1}(r)$, and $s_3(r)$ have to be solved both for $\kappa = \infty$ ($e = 0$) and $\kappa < \infty$. To obtain analytical results, we consider the Ginzburg-Landau-equation for η_s,

$$\eta_s = -2|\eta_s|^2\eta_s - \frac{\tilde{\mu}}{\tilde{\alpha}}(\boldsymbol{D}^2\eta_s) - \frac{\tilde{\gamma}_1}{\tilde{\alpha}}|\eta_d|^2\eta_s - 2\frac{\tilde{\gamma}_2}{\tilde{\alpha}}\eta_d^2\eta_s^* - \frac{\tilde{\delta}}{\tilde{\alpha}}(D_x^2 - D_y^2)\eta_d. \tag{2.15}$$

We first state, that for $\tilde{\delta} \equiv 0$, the pure d-solution is stable against admixture of η_s through the $\tilde{\gamma}_1$- and $\tilde{\gamma}_2$-terms, as can be shown by a linear stability analysis. Thus, the $\tilde{\gamma}_1$- and $\tilde{\gamma}_2$-terms are not relevant to generate an s-wave component. The gradient term in η_s is of order $|\eta_s|\tilde{\mu}/\tilde{\alpha}$, which is small compared to η_s in the temperature range considered, as $\tilde{\mu}/\tilde{\alpha} \ll 1$. Furthermore, we can neglect the terms of third order in η_s. Obviously, the mixed gradient term proportional to $\tilde{\delta}$ is crucial for our problem. Using $\eta_d = d(r)e^{i\theta}$, we arrive at the source term

$$\begin{aligned}
\eta_s &\approx -\frac{\tilde{\delta}}{\tilde{\alpha}}(D_x^2 - D_y^2)d(r)e^{i\theta} \\
&= -\frac{\tilde{\delta}}{\tilde{\alpha}}\Big(-\frac{1}{2}d'' + \frac{3}{2r}d' - 2Ad' - \frac{3}{2r^2}d + \frac{3A}{r}d - 2A^2d - A'd\Big)e^{3i\theta} \\
&\quad -\frac{\tilde{\delta}}{\tilde{\alpha}}\Big(-\frac{1}{2}d'' - \frac{1}{2r}d' + 2Ad' + \frac{1}{2r^2}d + \frac{A}{r}d - 2A^2d + A'd\Big)e^{-i\theta} \\
&= -\frac{\tilde{\delta}}{\tilde{\alpha}}\mathcal{K}_3(d,A)e^{3i\theta} - \frac{\tilde{\delta}}{\tilde{\alpha}}\mathcal{K}_{-1}(d,A)e^{-i\theta} \equiv \Sigma_A,
\end{aligned} \tag{2.16}$$

generating a finite order parameter η_s. Note that the only θ-dependences are of the form $e^{-i\theta}$ or $e^{3i\theta}$. In cylindrical coordinates, the tetragonal symmetry of the operator $(D_x^2 - D_y^2)$ is essentially reflected by an angular dependence of the form $\cos 2\theta$ or $\sin 2\theta$, which, combined with the vortex phase turn $e^{i\theta}$, gives the phase factors discussed above. A qualitative understanding of the induced s-wave is based on the structure of this source term. If we neglect the vector potential A, we can interpret the derivatives as a discrete sum of four shifted copies of the d-wave-vortex,

$$\eta_s \approx l^2(\nabla_x^2 - \nabla_y^2)d(x,y) \approx d(x+l,y) + d(x-l,y) - d(x,y+l) - d(x,y-l), \tag{2.17}$$

where $l^2 = \tilde{\delta}/\tilde{\alpha}$ has to be $\ll 1$ in order to provide a good approximation to the derivatives. Choosing for $d(x,y)$ an approximative solution of the d-wave problem,

we already find a qualitatively correct behavior for the s-wave. For example a fit

$$d(x,y) \equiv d(r)e^{i\theta} = \begin{cases} \frac{r}{c\sqrt{2}}e^{i\theta} & r \leq c \\ \frac{1}{\sqrt{2}}e^{i\theta} & r \geq c \end{cases} \tag{2.18}$$

produces for $c < d$ an s-wave exhibiting a central counter-rotating vortex and four off-center vortices with positive phase turn on the half-axes (see Figs. 2.1,2.4). Note, that the position of the off-center s-wave vortices does not trivially match up with the shift vector l, but depends on the details of the d-wave solution. Using a more reasonable fit

$$d(x,y) \equiv d(r)e^{i\theta} = \frac{1}{\sqrt{2}} \tanh\left(\frac{r}{c}\right) e^{i\theta}, \tag{2.19}$$

we obtain quantitatively correct results.

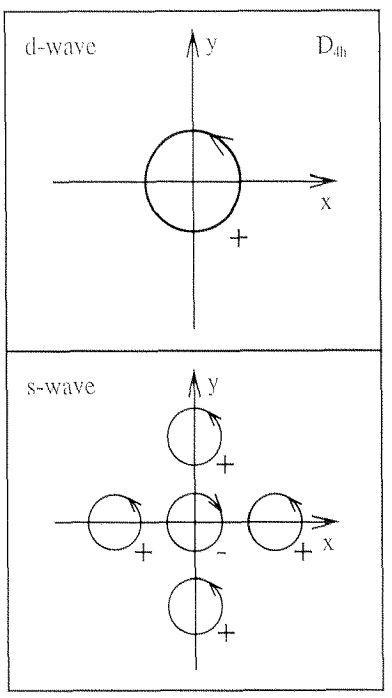

Figure 2.1: Schematic illustration of the topology of the d-wave and the admixed s-wave in the single-vortex case of a tetragonal d-wave superconductor for $\kappa = \infty$ ($e = 0$). The phase turns of the vortices are marked with little arrows and a sign (+ for positive phase turn).

The positions of the off-center vortices lie for this fit at the roots r_0 of the equation

$$\tanh\left(\frac{r+l}{c}\right) + \tanh\left(\frac{r-l}{c}\right) - 2\frac{r}{\sqrt{r^2+l^2}} \tanh\left(\frac{\sqrt{r^2+l^2}}{c}\right) = 0. \tag{2.20}$$

We choose $c = 1.715$, which correctly reproduces the initial slope of the d-wave at $r = 0$ (see Hu[37]). In the limit $l \ll 1$, we find the vortex positions at $r_0 = 2.81$. Although this result is in good accordance with the value $r_0 = 2.80$, which we obtain by numerical solution of the full problem (see Fig. 2.3), one has to be careful with quantitative results based on this simple explanation, since the value 2.81 strongly depends on the behavior of the fit near $r = 3$.

In the following, we will investigate this source term more closely for the two cases $\kappa = \infty$ ($e = 0$) and $\kappa < \infty$.

Solutions in the limit $\kappa = \infty$ ($e = 0$)

We start with the simpler case $\kappa = \infty$ ($e = 0$). Based on the previous discussion and the asymptotics calculated in Appendix A.2, we analyze the properties of the source term $\Sigma \equiv \Sigma_{A=0}$. We are interested in the topological structure of the s-wave component, in particular in the location of the s-wave vortices and their phase structure. Since the order parameter $\eta_s = \Sigma$ vanishes in the core of a vortex, we look for point-like zeros of the source term Σ.

For this purpose, the amplitude of the s-wave component is not important and we ignore the prefactor $\tilde{\delta}/\tilde{\alpha}$ in Σ for convenience.

Reviewing Eq. (2.16) for $\kappa = \infty$ ($e = 0$), we find

$$\Sigma = -\mathcal{K}_3(d)e^{3i\theta} - \mathcal{K}_{-1}(d)e^{-i\theta}, \tag{2.21}$$

which can have point-like zeros at $r = r_0$ only if one of two conditions is fulfilled ($k \in \mathbb{Z}$)

$$\begin{aligned} \theta &= k\tfrac{\pi}{2}, & 0 &= -\mathcal{K}_3(d(r)) - \mathcal{K}_{-1}(d(r))|_{r=r_0} \\ & & &= d''(r) - \tfrac{1}{r}d'(r) + \tfrac{1}{r^2}d(r)|_{r=r_0}, \\ \theta &= \tfrac{\pi}{4} + k\tfrac{\pi}{2}, & 0 &= -\mathcal{K}_3(d(r)) + \mathcal{K}_{-1}(d(r))|_{r=r_0} \\ & & &= -\tfrac{2}{r}d'(r) + \tfrac{2}{r^2}d(r)|_{r=r_0}. \end{aligned} \tag{2.22}$$

On the diagonals $x = \pm y$ (*i. e.* $\theta = \frac{\pi}{4} + k\frac{\pi}{2}$), Eq. (2.22) reduces to

$$rd'(r) = d(r). \tag{2.23}$$

The d-wave component has a monotonically decreasing derivative $d'(r)$,

$$rd'(r) < r\frac{d(r) - d(0)}{r} = d(r), \tag{2.24}$$

and we find that Eq. (2.23) is satisfied only at $r = 0$.

Thus, no vortices appear on the diagonals ($x = \pm y$). On the x- and y-axis ($\theta = k\frac{\pi}{2}$), Eq. (2.22) reads

$$d''(r) - \frac{1}{r}d'(r) + \frac{1}{r^2}d(r) = 0. \tag{2.25}$$

From the asymptotic behavior of $d(r)$ at $r \to 0$ we find

$$d(r) = d_1 r - \frac{1}{8} d_1 r^3 + O(r^4), \tag{2.26}$$

so that Eq. (2.25) leads to

$$d''(r) - \frac{1}{r} d'(r) + \frac{1}{r^2} d(r) = -\frac{1}{2} d_1 r + O(r^3) < 0, \tag{2.27}$$

since we have $d_1 > 0$. On the other hand, with the r-dependence of $d(r)$ for $r \to \infty$ given in Eq. (A.18) we find

$$d''(r) - \frac{1}{r} d'(r) + \frac{1}{r^2} d(r) = \frac{1}{\sqrt{2} r^2} - \frac{9}{2\sqrt{2} r^4} + O(\frac{1}{r^6}) > 0. \tag{2.28}$$

Therefore, at least one zero appears at a finite r_0. (Generally an odd number of zeros, if we count degenerate zeros with their degeneracy.) In addition, we can determine the phase portrait in the regions around any zero of Σ. We consider the behavior of the phase on the positive x-axis ($r \neq 0$). An off-center vortex shows a positive (negative) phase turn, if $-\mathcal{K}_3 - \mathcal{K}_{-1}$ changes sign from $-$ to $+$ ($+$ to $-$) for increasing r. In the extreme type II case with only one zero (one external vortex), we find a positive phase turn at the off-center vortices at $r = r_0$. On the y-axis, the picture is not changed qualitatively (the phase turn has the same sign) but the overall phase is shifted by $3\pi/2$. Combined with the negative phase turn at the central vortex $r = 0$ as $\eta_s \sim \mathcal{K}_{-1}(d) e^{-i\theta}$ for small r, this leads to an overall phase turn of 6π at large r (Fig. 2.1). Similar results were obtained by Berlinsky *et al.*[25, 26].

A further remark concerns the parameter $\tilde{\delta}$. The source term Σ (Eq. (2.21)) is proportional to $\tilde{\delta}$. Thus, a sign change in $\tilde{\delta}$ shifts the phase of Σ by π and has no other influence. We also investigated the problem by numerical minimization of the FED Eq. (A.6) obtained from the partial wave expansion. According to the results in the beginning of Section 2.3, we have chosen $\tilde{\alpha}$ significantly larger than 1 (typically $\tilde{\alpha} = 100$), and $\tilde{\mu} = \sqrt{\tilde{\alpha}}$ following Eq. (2.9). In the limit $|\eta_s| \ll |\eta_d|$ and $\kappa = \infty$ ($e = 0$), the analytic results are reproduced (Fig. 2.2; $\tilde{\delta}$ is chosen close to the maximal allowed value, *i. e.* $\tilde{\delta} \lessapprox \sqrt{\tilde{\mu}} = \sqrt{10}$). If $\tilde{\delta} = 0$, no s-waves occur, independent of the values of the other parameters. Moreover, the amplitudes of the s_i-partial waves are roughly proportional to $\tilde{\delta}$, provided that the values of $\tilde{\gamma}_1$ and $\tilde{\gamma}_2$ are small with respect to $\tilde{\alpha}$. Large $\tilde{\gamma}_i$-values influence the form of the solution, but they do not generate a non-trivial s-wave component. In all the simulations we performed, one external vortex along each half-axis appears. As long as the parameter $\tilde{\alpha}$ is taken to be large enough, the location of these external vortices is only weakly dependent on the parameters $\tilde{\mu}, \tilde{\gamma}_1, \tilde{\gamma}_2$ and $\tilde{\delta}$. Smaller $\tilde{\alpha}$ tend to push the vortices to larger r-values.

The relative size of the resulting s-wave admixture depends on the values of the parameters. Since $\max|\eta_s|$ is roughly proportional to $\tilde{\delta}/\tilde{\alpha}$, large s-waves occur for

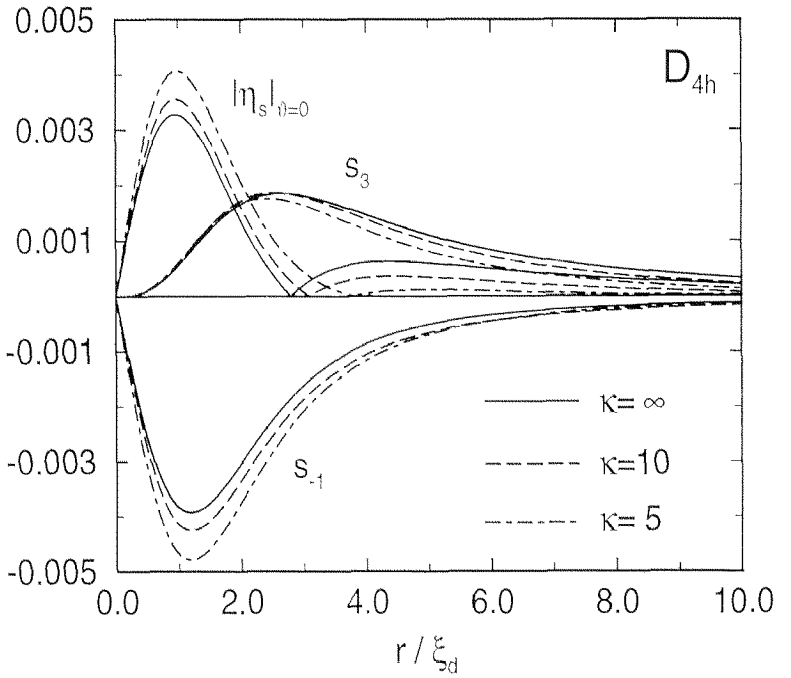

Figure 2.2: Absolute value of the admixed order parameter η_s at angle $\theta = 0$, as well as s_3 and s_{-1} plotted versus the radius r for different values of the Ginzburg-Landau parameter κ. The values of the parameters are $\tilde{\alpha} = 100$, $\tilde{\mu} = \sqrt{\tilde{\alpha}} = 10$, $\tilde{\gamma}_1 = \tilde{\gamma}_2 = 0$, $\tilde{\delta} = 3.16$. Choosing $\tilde{\delta} = 3.16$ corresponds to maximal s-waves due to $\tilde{\mu} \geq \tilde{\delta}^2$.

large $\tilde{\delta}$ and small $\tilde{\alpha}$. Because of the relations $1 < \tilde{\alpha} < \tilde{\mu}^2$ and $\tilde{\mu} \leq \tilde{\delta}^2$ we find the largest s-wave components for $\tilde{\mu} \approx \tilde{\alpha} \approx \tilde{\delta} \approx 1$. Numerical results in this range show the relative size of $|\eta_s|$ to be of the order of 0.1. Ignoring the restriction $\tilde{\alpha} > 1$, even larger s-waves can be obtained.

Solutions for $\kappa < \infty$

Again, we first study the problem analytically. According to the results of Appendix A.2, we find along the x-axis the behavior

$$\begin{aligned} r \to 0 \quad &: \quad \Sigma_A = 4r(d_3 - a_1 d_1) < 0, \\ r \to \infty \quad &: \quad \eta_s = s^+(r) \sim C_1 \mathrm{sign}\left(\tfrac{4-\kappa^2}{2-\kappa^2}\right) r^{-1} e^{-2Kr}, \end{aligned} \tag{2.29}$$

while along the diagonals, we have

$$\begin{aligned} r \to 0 \quad &: \quad \Sigma_A = -4r(d_3 - a_1 d_1) e^{\frac{3}{4}i\pi}, \\ r \to \infty \quad &: \quad \eta_s = -s^-(r) e^{\frac{3}{4}i\pi} \sim -C_2 A_\infty r^{-\frac{1}{2}} e^{-Kr} e^{\frac{3}{4}i\pi}, \end{aligned} \tag{2.30}$$

where C_1 and C_2 are positive constants. Note, that for the large-r limit we considered directly the asymptotics of η_s calculated in Appendix A.2 instead of the source term.

As in the previous section, we determine whether there is an even or an odd number of vortices on the axes and on the diagonals by comparing the phases of $\eta_s = \Sigma$ for small and large r. With $A_\infty < 0$ (as explained in Appendix A.2) we find an even number (generally 0) on the diagonals. This agrees with the $\kappa = \infty$ ($e = 0$) case discussed above. On the half-axes, however, the situation is more interesting: due to the sign factor in the large-r asymptotics, we find an odd number of vortices if $\kappa > 2$, and an even number if $\sqrt{2} < \kappa < 2$. This means, that for large κ, we expect to find one vortex as in the extreme type II case, whereas for small enough κ these vortices will vanish as a result of the coupling to the A-field. This effect may be the explanation for the absence of vortices in the numerical calculations recently published by Xu *et al.*[28] at $\kappa = 2$, which is exactly the critical value for κ following our above argumentation.

An analysis of the phase behavior shows, that the phase turn of the n-th vortex (located at r_n, where the labeling goes from small to large r omitting the central vortex) in the direction of a half-axis is equal to $(-1)^{n+1}\,\mathrm{sign}(\mathcal{K}_{-1}(r_n))2\pi$. Assuming $\mathcal{K}_{-1}$ to be strictly positive, we find the overall phase turns

$$\begin{aligned} \kappa > 2 \quad &\rightarrow \quad 6\pi, \\ \sqrt{2} < \kappa < 2 \quad &\rightarrow \quad -2\pi. \end{aligned} \tag{2.31}$$

This result for the overall phase turn is equivalent to the result obtained by integrating the gradient of the complex phase of η_s along a circle of large radius. We have calculated the solutions for finite κ also numerically. To investigate the influence of decreasing κ, we have chosen all other parameters to be constant. As a result, we find in our simulations either one or no external vortex in each direction $\pm x$ and $\pm y$ (Fig. 2.2). A closer investigation of the dependence of the vortex position on the Ginzburg-Landau parameter κ is shown in Fig. 2.3. One notices, that a small κ, *i. e.* a strong coupling to the A-field, tends to push the location of this vortex to large r. The critical value of κ can be estimated numerically as roughly 2, *i. e.* the same value as predicted by the analytical treatment.

2.3.2 Numerical results

The main difference between the general solution and the limiting case $|\eta_s| \ll |\eta_d|$ is, that as soon as $|\eta_s| \sim |\eta_d|$, the influence of η_s on η_d and A can no longer be neglected. This has two consequences: first, the equation $\eta_s = \Sigma_A$ is no longer valid. Although the considerations above regarding the source term remain true, we loose much information about the form of η_s, since gradient and coupling terms are not

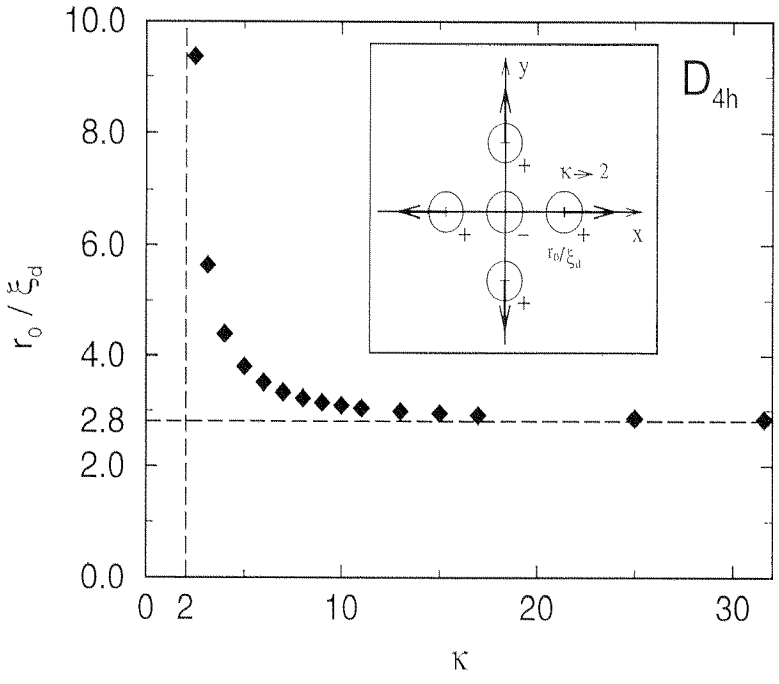

Figure 2.3: Dependence of the induced s-wave vortex position r_0 on the Ginzburg-Landau parameter κ in a tetragonal symmetry. The parameters are the same as in Fig. 2.2. One notices, that the vortex moves to infinity for $\kappa \to 2$, whereas the large κ value for the vortex position is $r_0 = 2.8$.

negligible. second, the ansatz $\eta_d = d(r)e^{i\theta}$, $\boldsymbol{A} = A(r)\hat{\boldsymbol{e}}_{\boldsymbol{\theta}}$ is no longer valid. For example, a large s_3-partial wave favors the existence of a d_5-wave, *i. e.* a partial wave of η_d with the phase $e^{5i\theta}$, which consists of the single phase turn $e^{i\theta}$ times a fourfold anisotropy. Therefore, the general problem is much more complex than the small-$|\eta_s|$ case. Results in this range of parameters can be obtained only numerically. We use a minimization method for the full FED discretized on a two dimensional grid. We have calculated two significant cases, one with large $\tilde{\alpha}$ and large κ ($\to$ small η_s and A, Fig. 2.4)) and one with small $\tilde{\alpha}$ and small κ ($\to$ large η_s and A). The most interesting result is that indeed in the case of large s-waves, the d-wave is no longer radially symmetric but shows a tetragonal deformation. In both cases, we find for the s-waves four external vortices (Fig. 2.4). The vector plot of the s-wave corresponding to the first data set (Fig. 2.5) shows the phase portrait with a negative phase turn at the origin and positive phase turns at the external vortices, leading to an overall phase turn of 6π at large values of r. Thus, all the statements about the phase predicted from our asymptotic analysis are reproduced in the numerical results. Similar figures were recently published by Franz *et al.*[26] neglecting the magnetic field in their numerical calculations, and by Xu *et al.*[28]. As we showed above, the absence of external s-wave

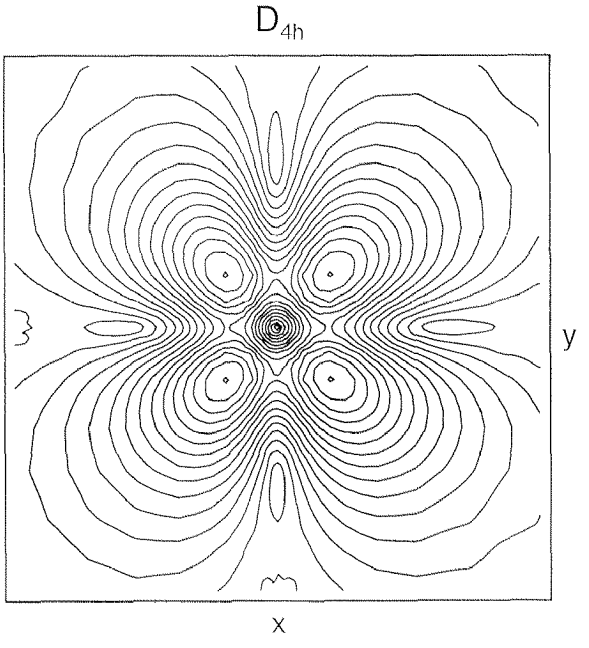

Figure 2.4: Contour plot of the absolute value of the order parameter η_s for tetragonal symmetry. The parameters are $\tilde{\alpha} = 100$, $\tilde{\mu} = 10$, $\tilde{\gamma}_1 = 0$, $\tilde{\gamma}_2 = 5$, $\tilde{\delta} = 3.16$, and $\kappa = 10$. There are 15 equidistant contours ranging from 0 to 0.006. The external vortices appear as zeros on the half-axes.

vortices in the latter work is most probably due to the fact that they work with $\kappa = 2$.

2.4 Tetragonal symmetry D_{4h}: $\eta_{d'}$-admixtures

In this section, we consider a d-wave superconductor with tetragonal symmetry, that shows admixtures of the $\eta_{d'}$-component.

The FED then differs from the η_d-η_s-case only in the important gradient-gradient coupling term (Table 2.1), which is now

$$D_x^* \eta_{d'}^* D_y \eta_d - D_y^* \eta_{d'}^* D_x \eta_d. \tag{2.32}$$

A partial integration leads to a coupling to the B_z-field of the form $\propto (iB_z \eta_{d'}^* \eta_d + h.c.)$. Performing the same scaling as in the η_d-η_s-case (Eq. 2.6), we find the rescaled FED (corresponding to the FED Eq. (2.5))

$$\begin{aligned} f \;=\; & \tilde{\alpha}|\eta_{d'}|^2 + \tilde{\alpha}|\eta_{d'}|^4 + \tilde{\mu}|\boldsymbol{D}\eta_{d'}|^2 - |\eta_d|^2 + |\eta_d|^4 + |\boldsymbol{D}\eta_d|^2 \\ & + \tilde{\gamma}_1 |\eta_{d'}|^2 |\eta_d|^2 + \tilde{\gamma}_2 (\eta_{d'}^2 \eta_d^{*2} + \eta_{d'}^{*2} \eta_d^2) \\ & + 2i\tilde{\delta} B_z (\eta_{d'}^* \eta_d - \eta_{d'} \eta_d^*) + 2\kappa^2 \boldsymbol{B}^2. \end{aligned} \tag{2.33}$$

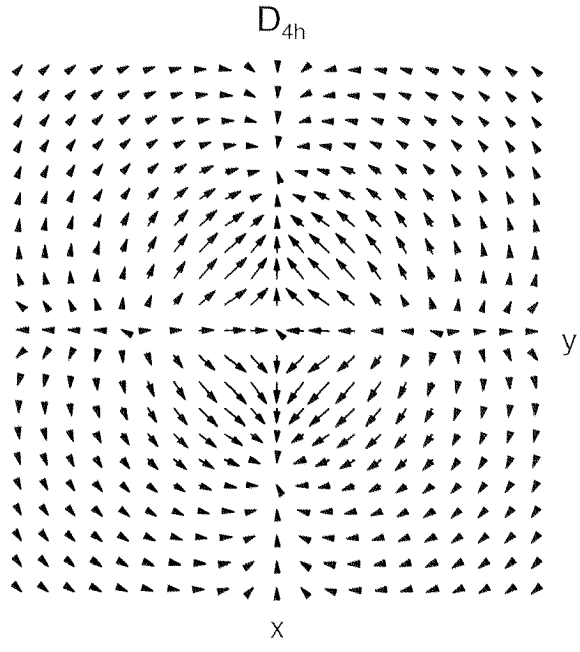

Figure 2.5: Vector plot of the order parameter η_s for tetragonal symmetry. The parameters are the same as in Fig. 2.4. The central vortex shows a negative phase turn and the four off-center vortices have positive phase turns, leading to an overall phase turn of 6π.

Due to the coupling to the B_z-field, we see that there is no $\eta_{d'}$-admixture in the extreme type II limit ($\kappa = \infty$, $e = 0$), since we have $\boldsymbol{B} = 0$. (Note that $\boldsymbol{B}$ is a rescaled field which is zero for $e = 0$.) For $\kappa < \infty$, we make the ansatz (2.13) for small admixtures and perform a partial wave expansion for $\eta_{d'}$

$$\eta_{d'} = \sum_{n=-\infty}^{+\infty} t_n(r) e^{in\theta}. \tag{2.34}$$

A minimization argument explained in the Appendix A.1 gives the only non-vanishing component of $\eta_{d'}$ to be the imaginary part of the t_1-partial wave, further denoted by $t(r) \in \mathbb{R}$,

$$\eta_{d'} = it(r)e^{i\theta}. \tag{2.35}$$

Since there is only one non-trivial partial wave component $t(r)$, $|\eta_{d'}|$ is independent of the angle. Consequently, point-like zeros cannot occur but in the origin, and a zero in $t(r)$ at $r = r_0$ corresponds to a vanishing order parameter component $\eta_{d'}$ on a circle of radius r_0.

Investigating the asymptotics, we find that no off-centered zeros are possible. For

small r, one finds a linear behavior

$$t(r) = b_1 r + O(r^3). \tag{2.36}$$

The sign of the coefficient b_1 can be determined from the coupling term $4\tilde{\delta}B_z td$, which has to be negative. Assuming that B_z and d are positive, b_1 has the opposite sign of the parameter $\tilde{\delta}$. For large-r asymptotics, we find (compare with Appendix A.2)

$$\begin{aligned} A(r) &\sim \frac{1}{2r} + A_\infty r^{-\frac{1}{2}} e^{-Kr}, \\ t(r) &\sim T_\infty r^{-\frac{1}{2}} e^{-Kr}, \\ d(r) &\sim \frac{\sqrt{2}}{2} - D_\infty r^{-1} e^{-2Kr}, \end{aligned} \tag{2.37}$$

with

$$T_\infty = A_\infty \frac{2\sqrt{2}\kappa\tilde{\delta}}{G^-\kappa^2 - 2\tilde{\mu}} + O(\tilde{\delta}^2), \tag{2.38}$$

and an exponent K given for small $\tilde{\delta}$ by

$$K^2 = \frac{1}{\kappa^2}\Big(1 + \frac{2\tilde{\delta}^2}{G^-\kappa^2 - 2\tilde{\mu}} + O(\tilde{\delta}^4)\Big), \tag{2.39}$$

where $G^- = 2\tilde{\alpha} + \tilde{\gamma}_1 - 2\tilde{\gamma}_2$. Since $A_\infty < 0$ (see Appendix A.2), we find that $t(r)$ has for large r also the opposite sign of the parameter $\tilde{\delta}$. From this result, we would expect an even number of radial zeros. For small $\eta_{d'}$ and small fields, $t(r)$ is proportional to the product $B_z(r)d(r)$ and therefore has no zeros. It is reasonable to assume that there are no qualitative changes for larger $\eta_{d'}$, which is also confirmed numerically. The central $\eta_{d'}$-vortex shows the same phase turn as the η_d-vortex, but with a relative phase of $\pm\pi/2$.

2.5 Orthorhombic symmetry D_{2h}

We consider the change in the FED due to orthorhombic distortions of the tetragonal symmetry, *i. e.* we keep the notion of s- and d-wave components and take their additional coupling due to the distortion into account. As in Section 2.3, we assume $\eta_{d'} = 0$. We arrive at the unscaled FED

$$\begin{aligned} f \;=\; & \alpha_s|\eta_s|^2 + \frac{\beta_s}{2}|\eta_s|^4 + \frac{1}{2m_s^x}|D_x\eta_s|^2 + \frac{1}{2m_s^y}|D_y\eta_s|^2 \\ & + \alpha_d|\eta_d|^2 + \frac{\beta_d}{2}|\eta_d|^4 + \frac{1}{2m_d^x}|D_x\eta_d|^2 + \frac{1}{2m_d^y}|D_y\eta_d|^2 \\ & + \gamma_0(\eta_s\eta_d^* + \eta_s^*\eta_d) + \gamma_1|\eta_s|^2|\eta_d|^2 + \gamma_2(\eta_s^2\eta_d^{*2} + \eta_s^{*2}\eta_d^2) \\ & + \gamma_3|\eta_s|^2(\eta_s\eta_d^* + \eta_s^*\eta_d) + \gamma_4|\eta_d|^2(\eta_s\eta_d^* + \eta_s^*\eta_d) \\ & + \delta_x(D_x^*\eta_s^* D_x\eta_d + h.c) + \delta_y(D_y^*\eta_s^* D_y\eta_d + h.c.) + \frac{\boldsymbol{B}^2}{8\pi}. \end{aligned} \tag{2.40}$$

Note, that the tetragonal FED (Eq. 2.3) is a special case of this FED, namely for $\gamma_0 = \gamma_3 = \gamma_4 = 0$ and $\delta_x = -\delta_y$. As a simplification, we assume

$$\frac{m_s^x}{m_s^y} = \frac{m_d^x}{m_d^y} = \varepsilon^2. \tag{2.41}$$

Since the terms with coefficients γ_1, γ_2, and γ_3 are not relevant for the qualitative behavior, we neglect them in the further analysis. With the definition $m_s \equiv m_s^x (= \varepsilon^2 m_s^y)$, $m_d \equiv m_d^x (= \varepsilon^2 m_d^y)$, and the reparametrization

$$\begin{aligned} \tilde{y} &= \frac{y}{\varepsilon}, \\ (r, \theta) &= (\sqrt{x^2 + \tilde{y}^2}, \arctan \frac{\tilde{y}}{x}), \\ \tilde{A}_y &= \varepsilon A_y, \end{aligned} \tag{2.42}$$

we find that the free energy density again has a structure that allows for a partial wave expansion in the limit $\kappa = \infty$ ($e = 0$). Performing the same scaling as in the tetragonal case (Eqs. (2.5,2.6)), we obtain the rescaled FED

$$\begin{aligned} f &= \tilde{\alpha}|\eta_s|^2 + \tilde{\alpha}|\eta_s|^4 + \tilde{\mu}|\boldsymbol{D}\eta_s|^2 - |\eta_d|^2 + |\eta_d|^4 + |\boldsymbol{D}\eta_d|^2 \\ &\quad + \tilde{\gamma}_0(\eta_s \eta_d^* + \eta_s^* \eta_d) + \tilde{\gamma}_4 |\eta_d|^2 (\eta_s \eta_d^* + \eta_s^* \eta_d) \\ &\quad + \tilde{\delta}_x(\eta_s^* D_x^2 \eta_d + h.c.) + \tilde{\delta}_y(\eta_s^* D_y^2 \eta_d + h.c.) + 2\tilde{\kappa}^2 \boldsymbol{B}^2, \end{aligned} \tag{2.43}$$

with the parameters

$$\begin{aligned} &\tilde{\gamma}_0 = \frac{\gamma_0}{|\alpha_d|}\sqrt{\frac{\beta_d|\alpha_s|}{\beta_s|\alpha_d|}}, \quad \tilde{\gamma}_4 = 2\frac{\gamma_4}{\beta_d}\sqrt{\frac{\beta_d|\alpha_s|}{\beta_s|\alpha_d|}}, \quad \tilde{\kappa}^2 = \frac{1}{\varepsilon^2}\frac{\lambda^2}{\xi_d^2} = \frac{\beta_d m_d^2}{8\pi e^2 \varepsilon^2}, \\ &\tilde{\delta}_x = 2\delta_x m_d \sqrt{\frac{\beta_d|\alpha_s|}{\beta_s|\alpha_d|}}, \quad \tilde{\delta}_y = 2\frac{\delta_y m_d}{\varepsilon^2}\sqrt{\frac{\beta_d|\alpha_s|}{\beta_s|\alpha_d|}}. \end{aligned} \tag{2.44}$$

The parameters $\tilde{\alpha}$ and $\tilde{\mu}$ are defined as in the tetragonal case. Notice that the redefinitions of the parameters $\tilde{\kappa}$ and $\tilde{\delta}_y$ include the parameter ε describing the anisotropy of the effective masses of the charge carriers.

2.5.1 Homogeneous solution

As in the tetragonal case, we want to find first the minimal homogeneous solutions. We notice that the homogeneous FED depends only on the absolute values $|\eta_d|$ and $|\eta_s|$ and the relative phase θ of η_s and η_d. Choosing the phase of η_d to be zero, we find via minimization:

$$\begin{aligned} 0 &= -|\eta_d| + 2|\eta_d|^3 + \tilde{\gamma}_0|\eta_s|\cos\theta + 3\tilde{\gamma}_4|\eta_d|^2|\eta_s|\cos\theta, \\ 0 &= \tilde{\alpha}|\eta_s| + 2\tilde{\alpha}|\eta_s|^3 + \tilde{\gamma}_0|\eta_d|\cos\theta + \tilde{\gamma}_4|\eta_d|^3\cos\theta, \\ 0 &= -\tilde{\gamma}_0|\eta_s||\eta_d|\sin\theta - \tilde{\gamma}_4|\eta_s||\eta_d|^3\sin\theta. \end{aligned} \tag{2.45}$$

The third equation has solutions at

$$\begin{array}{rcll} \theta & = & k\pi & \Rightarrow \quad \eta_s \in \mathbb{R}, \\ \eta_s & = & 0 & \Rightarrow \quad |\eta_d|^2 = \frac{1}{2}, \\ \eta_d & = & 0 & \Rightarrow \quad \eta_s \equiv \eta_d \equiv 0, \end{array} \tag{2.46}$$

and

$$\tilde{\gamma}_0 + \tilde{\gamma}_4 |\eta_d|^2 = 0. \tag{2.47}$$

We consider only the $\theta = k\pi$ solutions, thus we choose $\eta_d = |\eta_d|$ real and positive and absorb the sign of the $\cos\theta$ terms by replacing $|\eta_s|$ by $\eta_s \in \mathbb{R}$. Restricting ourselves to the interesting solutions $\eta_s, \eta_d \neq 0$ and introducing the ratio of amplitudes x,

$$\eta_s = x\eta_d, \tag{2.48}$$

we obtain a polynomial equation of fourth order in x from Eqs. (2.45):

$$2\tilde{\gamma}_0\tilde{\alpha}x^4 - 2\tilde{\alpha}x^3 - 3\tilde{\alpha}\tilde{\gamma}_4 x^2 - (2\tilde{\gamma}_0\tilde{\gamma}_4 + 2\tilde{\alpha})x - (\tilde{\gamma}_4 + 2\tilde{\gamma}_0) = 0. \tag{2.49}$$

The condition for the solution describing a local minimum is, that the matrix $\mathcal{S}$ of second derivatives of the FED with respect to the fields is positive definite. Calculating the matrix elements, one finds

$$\begin{array}{rcl} \mathcal{S}_{\eta_d\eta_d} & = & -1 + 6\eta_d^2 + 6\tilde{\gamma}_4\eta_d^2 x, \\ \mathcal{S}_{\eta_d\eta_s} & = & \tilde{\gamma}_0 + 3\tilde{\gamma}_4\eta_d^2, \\ \mathcal{S}_{\eta_s\eta_s} & = & \tilde{\alpha} + 6\tilde{\alpha}\eta_d^2 x^2, \\ \mathcal{S}_{\eta_d\theta} & = & \mathcal{S}_{\eta_s\theta} = 0, \\ \mathcal{S}_{\theta\theta} & = & -\tilde{\gamma}_0\eta_d^2 x - \tilde{\gamma}_4\eta_d^4 x. \end{array} \tag{2.50}$$

Thus, the conditions for an (at least locally) stable minimum are

$$\mathcal{S}_{\eta_d\eta_d},\ \mathcal{S}_{\eta_s\eta_s},\ \mathcal{S}_{\theta\theta} > 0 \quad \text{and} \quad \mathcal{S}_{\eta_d\eta_d}\mathcal{S}_{\eta_s\eta_s} > \mathcal{S}^2_{\eta_d\eta_s}. \tag{2.51}$$

Assuming $\tilde{\gamma}_0, \tilde{\gamma}_4 \ll \tilde{\alpha}$, which means $x \ll 1$, we find the approximate solution $x = -(2\tilde{\gamma}_0 + \tilde{\gamma}_4)/(2\tilde{\alpha} + 2\tilde{\gamma}_0\tilde{\gamma}_4)$, which corresponds to a stable minimum. We will later use numerical determination of the lowest stable minimum using Eqs. (2.49-2.51) to find the correct asymptotic values for the numerical simulations in the orthorhombic case. A last remark concerns the allowed parameter range. Assuming vanishing $\tilde{\gamma}_1$, $\tilde{\gamma}_2$, and $\tilde{\gamma}_3$, the relation

$$\tilde{\alpha} > \frac{27}{16}|\tilde{\gamma}_4|^4 \tag{2.52}$$

is sufficient for the FED to be bounded from below.

2.5.2 Vortex solution in the limit $|\eta_s| \ll |\eta_d|$

As in the tetragonal case (Section 2.3.1), we use the Ansatz (2.13) for η_d and A and perform a partial wave expansion for η_s. The resulting coupled system of radial equations obtained by minimization (Appendix A.1) involves only the functions $d(r)$, $A(r)$, and the real parts of the partial waves $s_{-1}(r)$, $s_3(r)$ and $s_1(r)$. The additional $s_1(r)$ partial wave appears due to the orthorhombic distortions. To obtain analytical results, we again consider the Ginzburg-Landau-equation for η_s, which reads

$$\begin{aligned} \eta_s &= -2|\eta_s|^2\eta_s - \frac{\tilde{\mu}}{\tilde{\alpha}}(\boldsymbol{D}^2\eta_s) - \frac{\tilde{\gamma}_0}{\tilde{\alpha}}\eta_d - \frac{\tilde{\gamma}_4}{\tilde{\alpha}}|\eta_d|^2\eta_d \\ &\quad - \frac{\tilde{\delta}_x}{\tilde{\alpha}}({D_x}^2\eta_d) - \frac{\tilde{\delta}_y}{\tilde{\alpha}}({D_y}^2\eta_d). \end{aligned} \tag{2.53}$$

We restrict ourselves to the case of small orthorhombic distortions, choosing

$$\tilde{\gamma}_0,\ \tilde{\gamma}_4 \ll \tilde{\alpha}. \tag{2.54}$$

Using further the arguments leading to Eq. (2.16), we find the relevant source term for η_s

$$\begin{aligned} \eta_s &\approx -\Big(\frac{\tilde{\gamma}_0}{\tilde{\alpha}} + \frac{\tilde{\gamma}_4}{\tilde{\alpha}}d^2 + \frac{\tilde{\delta}_x}{\tilde{\alpha}}{D_x}^2 + \frac{\tilde{\delta}_y}{\tilde{\alpha}}{D_y}^2\Big)d(r)e^{i\theta} \\ &= -\Big(\frac{\tilde{\gamma}_0}{\tilde{\alpha}}d + \frac{\tilde{\gamma}_4}{\tilde{\alpha}}d^3\Big)e^{i\theta} - +\Big(\frac{\tilde{\delta}_x + \tilde{\delta}_y}{\tilde{\alpha}}\Big)\Big(-\frac{1}{2}d'' - \frac{1}{2r}d' + \frac{1}{2r^2}d - \frac{2A}{r}d + 2A^2d\Big)e^{i\theta} \\ &\quad -\Big(\frac{\tilde{\delta}_x - \tilde{\delta}_y}{2\tilde{\alpha}}\Big)\Big(-\frac{1}{2}d'' + \frac{3}{2r}d' - 2Ad' - \frac{3}{2r^2}d + \frac{3A}{r}d - 2A^2d - A'd\Big)e^{3i\theta} \\ &\quad -\Big(\frac{\tilde{\delta}_x - \tilde{\delta}_y}{2\tilde{\alpha}}\Big)\Big(-\frac{1}{2}d'' - \frac{1}{2r}d' + 2Ad' + \frac{1}{2r^2}d + \frac{A}{r}d - 2A^2d + A'd\Big)e^{-i\theta} \\ &\equiv -\Big(\frac{\tilde{\gamma}_0}{\tilde{\alpha}}d + \frac{\tilde{\gamma}_4}{\tilde{\alpha}}d^3 + \frac{\tilde{\delta}_x + \tilde{\delta}_y}{\tilde{\alpha}}\mathcal{K}_1(d,A)\Big)e^{i\theta} \\ &\quad -\Big(\frac{\tilde{\delta}_x - \tilde{\delta}_y}{2\tilde{\alpha}}\mathcal{K}_3(d,A)\Big)e^{3i\theta} - \Big(\frac{\tilde{\delta}_x - \tilde{\delta}_y}{2\tilde{\alpha}}\mathcal{K}_{-1}(d,A)\Big)e^{-i\theta} \equiv \Sigma_A^{orth}. \end{aligned} \tag{2.55}$$

For simplicity, we drop in the following the fields $A(r)$, *i. e.* work in the limit $\tilde{\kappa} = \infty$ ($e = 0$). From the last expression in Eq. (2.55), we notice, that the terms proportional to $e^{-i\theta}$ and $e^{3i\theta}$ have the same structure as in the tetragonal case. The part that breaks tetragonal symmetry (proportional to $e^{i\theta}$) splits up into two parts. The first is of the form

$$-\Big(\frac{\tilde{\gamma}_0}{\tilde{\alpha}}d + \frac{\tilde{\gamma}_4}{\tilde{\alpha}}d^3\Big)e^{i\theta}. \tag{2.56}$$

This term adds a (slightly deformed) central vortex with positive phase turn to the tetragonal solution. For $r \to \infty$, the term reflects the finite bulk value of η_s: The exact asymptotic value of η_s is

$$\eta_s = \frac{|\eta_s|_{hom}}{|\eta_d|_{hom}}d(r)e^{i\theta}, \tag{2.57}$$

where $|\eta_i|_{hom}$ are the homogeneous bulk solutions for the same phenomenological parameters. To investigate the influence of this term in detail, we simplify the problem by setting $\tilde{\gamma}_4 = 0$, since the $\tilde{\gamma}_0$- and the $\tilde{\gamma}_4$-term act qualitatively the same way. Further, we fix $\tilde{\delta}_x = -\tilde{\delta}_y$, $\tilde{\delta}_x > 0$ and $\tilde{\gamma}_0 > 0$. From Section 2.3.1 we know, that on the x-axis, the tetragonal source term Σ has negative sign at small r, then crosses the x-axis at the core of the external vortex and has positive sign at large r. To this source term, the orthorhombic contribution $-\tilde{\gamma}_0/\tilde{\alpha}d$ has to be added. For small enough $\tilde{\gamma}_0$, the external vortex is then moved to larger r-values and a second vortex is generated at larger r with negative phase turn. For larger $\tilde{\gamma}_0$, this vortex-antivortex pair shrinks and finally annihilates (see Fig. 2.6).

On the y-axis, the tetragonal solution has the same radial behavior as on the x-axis, multiplied by a global phase $e^{3i\pi/2}$. In addition to this tetragonal result, the orthorhombic part contributes $(\tilde{\gamma}_0/\tilde{\alpha})de^{3i\pi/2}$, such that the vortex moves towards the center, and no other vortices appear. The total phase turn of the s-wave is therefore 2π, as is expected from the asymptotic solution Eq. (2.57). The second symmetry breaking term has the form

$$-\Big(\frac{\tilde{\delta}_x + \tilde{\delta}_y}{\tilde{\alpha}}\Big)\mathcal{K}_1(d)e^{i\theta}. \tag{2.58}$$

We assume $\tilde{\gamma}_0 = \tilde{\gamma}_4 = 0$ and $\tilde{\delta}_x > -\tilde{\delta}_y > 0$. $\mathcal{K}_1(d)$ is everywhere positive, such that on the x-axis, the tetragonal vortex position is again moved to larger r-values and on the y-axis towards the center. Since no additional antivortices appear on the x-axis, the overall phase turn in this situation is 6π as in the tetragonal case.

2.5.3 Numerical results

Again we compare our analytical results to a numerical simulation. First, we discuss the results of the partial wave approach restricted to the extreme type II case. Note, that all results and plots are expressed in the reparametrized units of Eqs. (2.42). To obtain the original unscaled result, one has to scale the plots along the y-axis with the factor ε. The anisotropy of the original parameter δ is larger by the factor ε^2: $\delta_x/\delta_y = \varepsilon^2\tilde{\delta}_x/\tilde{\delta}_y$. In the following we fix the parameters $\tilde{\alpha} = 100$, $\tilde{\mu} = 10$, $\tilde{\delta}_x = 3.16$ and $\tilde{\gamma}_4 = 0$. The values for $\tilde{\alpha}$, $\tilde{\mu}$, and $\tilde{\delta}_x$ are chosen as in Section 2.3.1. As discussed above, the influence of non-vanishing $\tilde{\gamma}_0$ and $\tilde{\gamma}_4$ is qualitatively the same, therefore we restrict ourselves to the case $\tilde{\gamma}_4 = 0$. The values of $\tilde{\delta}_y$ and $\tilde{\gamma}_0$ are variable. First, we examine the modifications when the system is gradually distorted to orthorhombic symmetry by variation of the parameter $\tilde{\gamma}_0$. We therefore keep the tetragonal mixed gradient coupling $\tilde{\delta}_y = -\tilde{\delta}_x$.

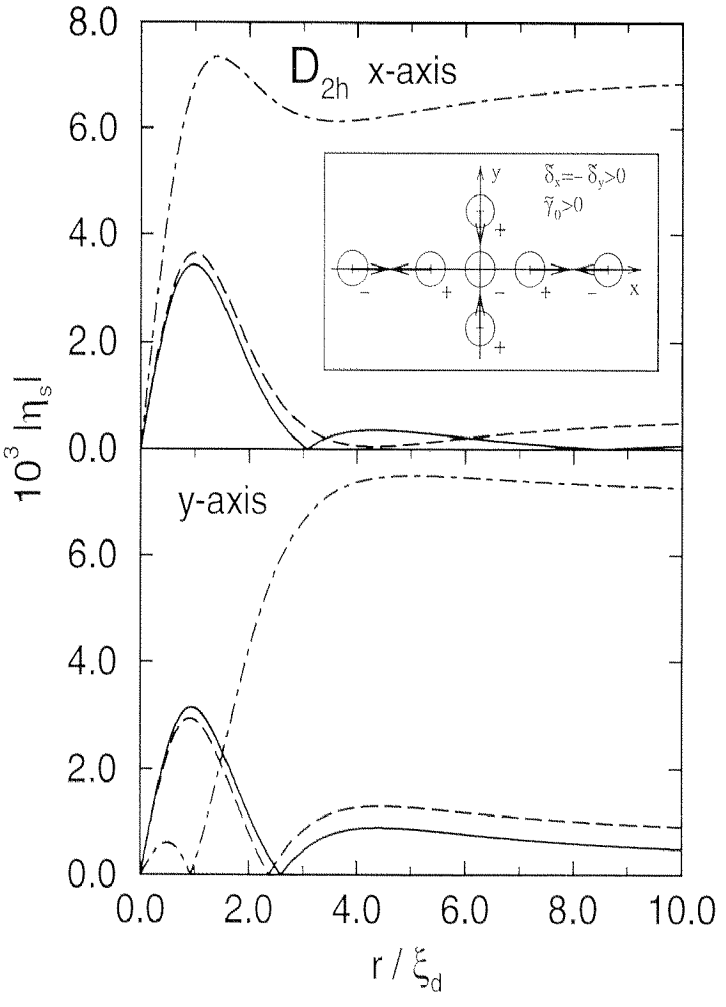

Figure 2.6: Absolute value of the order parameter η_s along the x-axis (upper graph) and along the y-axis (lower graph) for different values of $\tilde{\gamma}_0$ in orthorhombic symmetry. The parameters are $\tilde{\alpha} = 100$, $\tilde{\mu} = 10$, $\tilde{\gamma}_4 = 0$, $\tilde{\delta}_x = -\tilde{\delta}_y = 3.16$, $\tilde{\kappa} = \infty$, and $\tilde{\gamma}_0 = 0.04$ (solid), 0.1 (dashed) and 1 (dot-dashed). The case $\tilde{\gamma}_0 = 0$ corresponds to tetragonal symmetry, *i. e.* symmetric vortex positions on the x- and y-axis. A larger $\tilde{\gamma}_0$ leads to a non-vanishing large-r value of η_s and to the formation of antivortices on the x-axis, which annihilate with the external vortices on the x-axis for larger $\tilde{\gamma}_0$. The position of the vortex-antivortex pairs for increasing $\tilde{\gamma}_0$ is indicated by the arrows in the inset.

As we expect from the discussion in the previous section, the existence of small $\tilde{\gamma}_0$ does not change the form of the s_{-1}- and s_3-waves, but induces a finite s_1-wave due to the strong coupling to the d-wave. We see in Fig. 2.6 that the vortices on the x-axis move to larger r-values and soon annihilate with the second vortex generated by the orthorhombic deformation. E.g. for $\tilde{\gamma}_0 = 0.04$, we still have two vortices on the x-axis, whereas for $\tilde{\gamma}_0 = 0.1$ they both have disappeared. On the y-axis, we find the vortices

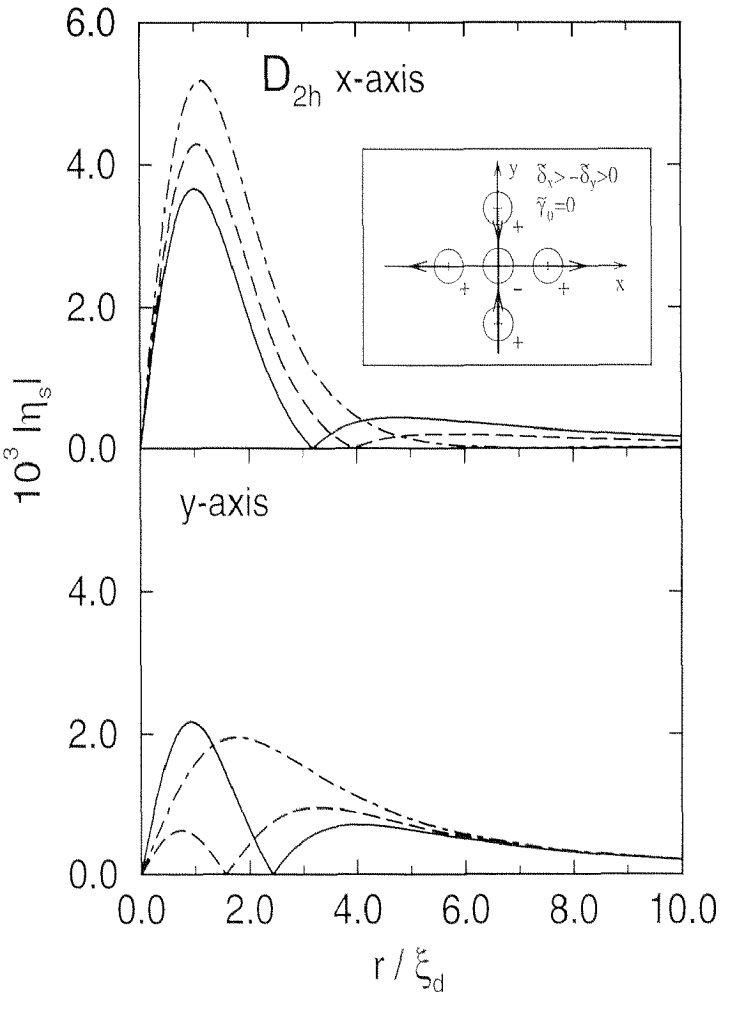

Figure 2.7: Absolute value of the order parameter η_s along the x-axis (upper graph) and along the y-axis (lower graph) for different values of $\tilde{\delta}_y$ in orthorhombic symmetry. The parameters are $\tilde{\alpha} = 100$, $\tilde{\mu} = 10$, $\tilde{\gamma}_0 = \tilde{\gamma}_4 = 0$, $\tilde{\delta}_x = 3.16$, $\tilde{\kappa} = \infty$, and $\tilde{\delta}_y = -0.8\ \tilde{\delta}_x$ (solid), $\tilde{\delta}_y = -0.5\ \tilde{\delta}_x$ (dashed) and $\tilde{\delta}_y = -0.1\ \tilde{\delta}_x$ (dot-dashed). Choosing $\tilde{\delta}_y = -\tilde{\delta}_x$ corresponds to the tetragonal case. An asymmetry between $\tilde{\delta}_x$ and $\tilde{\delta}_y$ leads to asymmetric vortex positions on the x- and y-axis, but not to a non-vanishing bulk-value of η_s.

moving towards the origin (Fig. 2.6). Results for the total s-wave at $\theta = \pi/4$ show that no vortices appear on the diagonals.

For the second set of calculations we use $\tilde{\gamma}_0 = 0$, but vary $\tilde{\delta}_y$. The s_3- and s_{-1}-waves change substantially with respect to the tetragonal case. This is not surprising, since by changing $\tilde{\delta}_y$, we change also the tetragonal source term Σ (see Eqs. (2.21) and (2.55)) and therefore directly the s_{-1}- and s_3-components. As in the first case, we find the s_1-component having larger amplitude, the more $\tilde{\delta}_y$ differs from the tetragonal value $-\tilde{\delta}_x$. The consequence is that as in the first set of calculations, the vortices on

the x-axis move to larger r-values, while the vortices on the y-axis move towards the origin (Fig. 2.7). For small $\tilde{\delta}_y$, the vortex on the x-axis moves towards infinity, while the vortex on the y-axis disappears towards zero. If we interchange the role of $\tilde{\delta}_y$ and $\tilde{\delta}_x$, *e. g.* $\tilde{\delta}_y = -3.16$ and changing $\tilde{\delta}_x$, we simply invert the sign of the s_1-component (Eq. (2.55)) without changing the tetragonal part. This relative sign between the s_1-component and the tetragonal part determines the different behavior along the x- and y-axis. With the proposed values $\tilde{\delta}_y = -3.16$ and $\tilde{\delta}_x < 3.16$, we would get the same results as before (up to an irrelevant phase factor), rotated by $\pi/2$ (*i. e.* x and y interchanged). Finally, we solved the full problem also for the orthorhombic case with $\tilde{\kappa} < \infty$ by minimization of the FED discretized on a two dimensional grid. In Figs. 2.8 and 2.9, we show a typical contour plot (surface plot) of η_s for the values $\tilde{\alpha} = 100, \tilde{\mu} = 10, \tilde{\gamma}_0 = 0.5, \tilde{\delta}_x = -\tilde{\delta}_y = 3.16, \tilde{\kappa} = 10$ and all other parameters equal to zero. One clearly recognizes the results discussed above: the vortices on the x-axis have disappeared, while the y-vortices are still clearly visible.

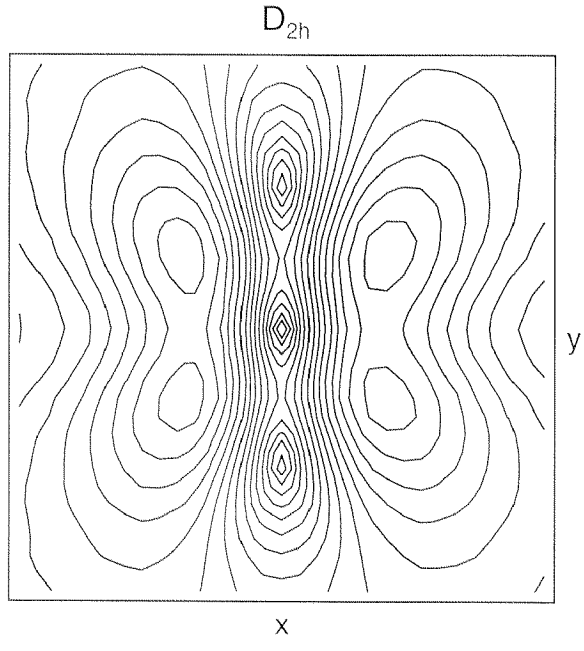

Figure 2.8: Contour plot of the absolute value of the order parameter η_s for orthorhombic symmetry. The parameters are $\tilde{\alpha} = 100$, $\tilde{\mu} = 10$, $\tilde{\gamma}_0 = 0.5$, $\tilde{\gamma}_4 = 0$, $\tilde{\delta}_x = -\tilde{\delta}_y = 3.16$, and $\tilde{\kappa} = 10$. There are 15 equidistant contours ranging from 0 to 0.0065. On the y-axis, there are two off-center vortices, whereas on the x-axis, the vortex-antivortex-pairs have annihilated.

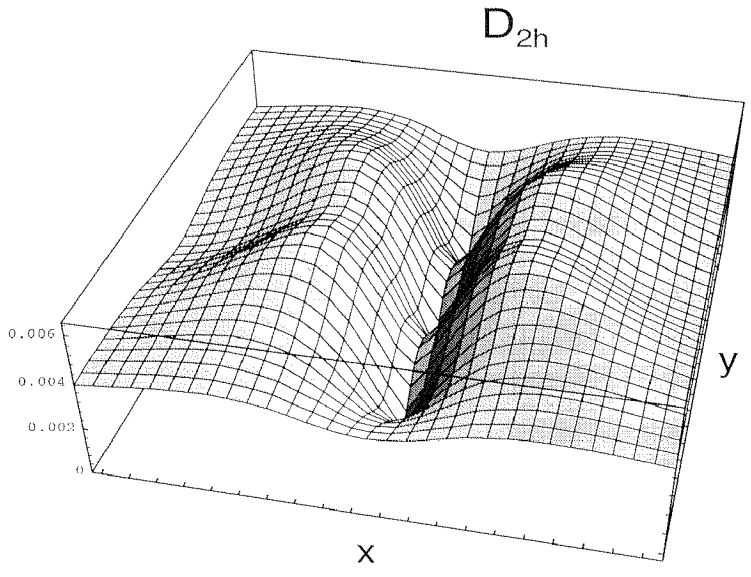

Figure 2.9: Surface plot of the absolute value of the order parameter η_s for orthorhombic symmetry. The parameters are the same as in Fig. 2.8. Notice the finite bulk value of the η_s-wave.

2.6 Conclusion

We have analyzed both analytically and numerically the properties of single-vortex solutions of several Ginzburg-Landau models for d-wave superconductivity. The η_d-component of the superconductor is always assumed to be the main superconducting component. The results depend qualitatively on the Ginzburg-Landau parameter κ. For tetragonal symmetry, we have found for the extreme type II limit ($\kappa = \infty$, $e = 0$) possible s-wave admixtures showing the well-known[24, 25, 26, 27, 28] four-lobe structure with one counter-rotating vortex at the center and four vortices with positive phase turn ~ 2.8 coherence lengths away from the central vortex on the half-axes. The decay for large r is proportional to $1/r^2$, as found by Berlinsky *et al.*[24]. For large κ ($\kappa < \infty$), the location of the off-center vortices moves to larger r-values and the asymptotic decay turns to an exponential behavior for $r \gg \lambda$, suppressing the visibility of the off-center vortices considerably.

As discussed by Franz *et al.*[26], the s-wave decays still algebraically $\sim 1/r^2$ in the intermediate region $\xi_d \ll r \ll \lambda$. For $\kappa < 2$, we have shown analytically and numerically that the off-center vortices disappear, which explains the absence of external

s-wave vortices in the numerical calculations of Xu *et al.*[28].

Possible $\eta_{d'}$-admixtures in tetragonal symmetry couple via a B_z-field to the η_d component and thus do not appear in the extreme type II limit (*i. e.* $\kappa = \infty$, $e = 0$). For $\kappa < \infty$, the absolute value $|\eta_{d'}|$ is independent of the angle and shows no off-center zeros. The central $\eta_{d'}$-vortex has a positive phase turn.

Finally, the influence of orthorhombic distortions on the s-wave admixtures has been studied. Two qualitatively different kinds of orthorhombic distortion have been considered. Introduction of coupling terms of the form $\eta_d\eta_s^* + \eta_d^*\eta_s$ leads to homogeneous solutions with a non-vanishing η_s-component. This homogeneous s-wave admixture can explain non-vanishing Josephson tunneling currents between s-wave superconductors and orthorhombically distorted $d_{x^2-y^2}$-wave superconductors[32]. Moreover, measurements of the tunneling current could provide a possibility of determining the ratios $\tilde{\gamma}_0/\tilde{\alpha}$ and $\tilde{\gamma}_4/\tilde{\alpha}$. Turning to the vortex solution in D_{2h}-symmetry, the non-vanishing homogeneous bulk-value of η_s leads to an asymptotically non-vanishing η_s-component. As a consequence, we find zero, one or two vortices on the axes. The four-fold symmetry is reduced to a two-fold symmetry. Orthorhombic distortions can also be realized by choosing an asymmetric gradient-gradient-coupling, $\tilde{\delta}_x \neq -\tilde{\delta}_y$. The solutions then decay to zero for large r and show zero or one vortices on each axis direction. The two mechanisms can also occur together, the prediction of the solutions (vortex positions) is then more difficult.

Chapter 3

Phenomenological Approach for Sr_2RuO_4

Sections 3.1 - 3.3 of this chapter have been published in Physical Review B in March 1999[38], however with a minor, but conceptually important difference. When this paper was written, the experimental orientation of the vortex lattice was reported to be aligned with the crystal axes of Sr_2RuO_4[39]. In the meantime, it turned out that this finding was wrong and the two lattices are misaligned by an angle of 45°[40]. In contrast to the original paper, we rely in the text below on the correct orientation of the vortex lattice. The numerical results of Section 3.4 are part of a collaboration with an experimental group and will be published in Physical Review Letters[41].

3.1 Introduction

With the observation of zero resistivity in Sr_2RuO_4 below $T_c = 0.93$K, Maeno *et al.*[21] discovered the first layered perovskite compound without CuO_2 planes showing superconductivity. Recent experimental and theoretical research provides considerable evidence that the superconducting state of Sr_2RuO_4 is of an odd-parity p-wave symmetry.

Classifying the superconducting states of a generalized BCS theory[4], the mean fields

$$\Delta_{s,s'}(\boldsymbol{k}) = -\sum_{\boldsymbol{k}',\sigma,\sigma'} V_{s's\sigma\sigma'}(\boldsymbol{k},\boldsymbol{k}')\langle c_{\boldsymbol{k}',\sigma} c_{-\boldsymbol{k}',\sigma'}\rangle \tag{3.1}$$

are split into singlet and triplet pairing states making use of the antisymmetry condition $\hat{\Delta}(\boldsymbol{k}) = -\hat{\Delta}^T(-\boldsymbol{k})$. While singlet states are described through an even scalar function $\psi(\boldsymbol{k})$ in the form $\hat{\Delta}(\boldsymbol{k}) = i\hat{\sigma}_y\psi(\boldsymbol{k})$, triplet states take the form

$$\hat{\Delta}(\boldsymbol{k}) \propto i(\boldsymbol{d}(\boldsymbol{k})\cdot\hat{\boldsymbol{\sigma}})\hat{\sigma}_y, \tag{3.2}$$

where $\boldsymbol{d}(\boldsymbol{k}) = -\boldsymbol{d}(-\boldsymbol{k})$ is an odd vector function[42]. Taking into account the crystal symmetry, the $\boldsymbol{k}$-dependent functions $\psi(\boldsymbol{k})$ and $\boldsymbol{d}(\boldsymbol{k})$ have to belong to an irreducible representation of the lattice point group, in our case the tetragonal point group D_{4h}.

Initial proposals of odd parity superconductivity in Sr_2RuO_4 were founded on the itinerant ferromagnetism of related ruthenate compounds and on the similarities between Sr_2RuO_4 and ^{3}He in the Fermi liquid corrections produced by electronic correlations[43]. Recently, muon spin rotation (μSR) measurements[44] have revealed that a spontaneous magnetization begins to develop below T_c. This finding is most naturally explained in terms of a time-reversal ($\mathcal{T}$) symmetry breaking state implying a multiple component (*i. e.* higher dimensional) representation of the D_{4h} point group. Furthermore, since the electronic structure of Sr_2RuO_4 is quasi-two dimensional, a gap function with a strong k_z-dependence is unlikely. Of the remaining two odd or even two-component representations of D_{4h}, the odd Γ_{5u}^- representation with basis functions $\{\boldsymbol{d}_1(\boldsymbol{k}), \boldsymbol{d}_2(\boldsymbol{k})\} = \{\hat{\boldsymbol{z}}k_x, \hat{\boldsymbol{z}}k_y\}$ is the only without nodes at $k_z = 0$ and therefore is most likely to be realized in Sr_2RuO_4.

In Ginzburg-Landau (GL) theory, we deal with order parameters $\eta_j(\boldsymbol{R})$ depending only on the center-of-mass coordinate $\boldsymbol{R}$, defined through

$$\hat{\Delta}(\boldsymbol{R}, \boldsymbol{k}) = \sum_{j=1}^{2} \eta_j(\boldsymbol{R})\; i(\boldsymbol{d}_j(\boldsymbol{k}) \cdot \hat{\boldsymbol{\sigma}})\hat{\sigma}_y. \tag{3.3}$$

As usual[4] we switch the transformation behavior from the basis functions $\boldsymbol{d}_j(\boldsymbol{k})$ to the order parameter components η_j. The components (η_1, η_2) then share the rotation-inversion symmetry properties of (k_x, k_y), and the broken $\mathcal{T}$-state is $(\eta_1, \eta_2) \propto (1, \pm i)$. Based on this order parameter, Agterberg[45] examined the vortex lattice structures of Sr_2RuO_4 near H_{c2}: for an applied finite field H along a high symmetry direction in the basal ab-plane, two vortex lattice phases have been found with a second superconducting transition between them, while a square vortex lattice has minimal energy when the field is along the c-axis. Band structure calculations[46, 47, 48] reveal that the density of states near the Fermi surface is mainly due to the four Ru $4d$ electrons, which hybridize strongly with the O $2p$ orbitals and give rise to three bands crossing the Fermi surface, labeled α, β and γ (see Ref.[46]). The measured values of the penetration depth λ and the coherence length ξ[39] indicate that the γ sheet (due to the xy-Wannier functions) of the Fermi surface shows the superconducting transition[45]. Assuming that ferromagnetic spin fluctuations are responsible for the superconducting state, this finding is in agreement with ^{17}O NMR experiments[49] showing strong ferromagnetic spin enhancements only in the Ru $4d_{xy}$ orbitals. Within the model of orbital dependent superconductivity [50], the orientation of the square lattice mentioned above depends on the sign of the square anisotropy ν of the Fermi surface sheet relevant for superconductivity. Band structure calculations first pointed

towards $\nu > 0$ for the α, β bands and $\nu < 0$ for the γ band[51]. Recent experiments using SANS[40, 41] show a square vortex lattice aligned with the diagonals of the crystal lattice in a wide range of the phase diagram, which suggest a positive anisotropy ν (see below). This would be inconsistent with the assumption of γ-band superconductivity pointed out above. However, newer band structure calculations obtain also a positive sign for the anisotropy ν of the γ-band[52].

In this chapter we investigate the single vortex core structure and the geometry of the vortex lattice near the lower critical field H_{c1}. We start from the Ginzburg-Landau theory for the two-component order parameter (η_1, η_2) and solve numerically for the vortex core structure of an isolated vortex. The individual vortex cores show square deformations. This vortex core structure is observable through scanning tunneling microscopy (STM) measurements since the in-plane coherence length of 900 Å is well within the spatial resolution required by STM. In Section 3.3, we derive an extended London model valid for fields near H_{c1} and large GL parameters κ and determine the geometric structure of the vortex lattice. We find hexagonal lattices near H_{c1}, deforming into square lattices upon increasing the applied field. The transition to the square lattice is of second order, as predicted also for borocarbides earlier[53, 54]. Taking the γ sheet as relevant for superconductivity, the orientation of the square lattices is in agreement with experiments[40, 41]. Bitter decoration studies near H_{c1} can be used to detect the predicted field dependent transition between hexagonal and square lattice, which would complete the picture found by SANS-measurements for higher applied fields[39, 40, 41]. A further characteristic of the hex-to-square transition is the peak splitting in the field distribution calculated in Sec. 3.3.2 and measurable in μSR experiments. As mentioned already, a similar transition has been predicted in borocarbide [53, 54] and high-T_c superconductors [55] and has been observed recently in the borocarbide materials [56]. Finally in Section 3.4 we investigate the detailed structure of the local field B at arbitrary applied fields within two-component Ginzburg-Landau theory. Fitting the lowest two Fourier components of B for different applied fields to the experimentally determined values[41], we find reasonable values for the fitting parameters κ and ν. Moreover, the structure of the local B-field shows field minima between nearest neighbor vortices within our two-component approach, a feature which is also found experimentally[41]. Since single component Ginzburg-Landau theories do not seem to be able to explain this qualitative feature, this finding is a strong point in favor of a two-component order parameter.

3.2 Isolated vortices: Ginzburg-Landau theory

We start from the Ginzburg-Landau free-energy density (f) for the two-dimensional representation Γ_{5u}^{--} of the tetragonal point group, with the Ginzburg-Landau coefficients determined within a weak-coupling approximation in the clean limit. These two approximations seem reasonable for Sr_2RuO_4 given the ratios[57] $T_c/\epsilon_F \sim 10^{-4}$ and $l/\xi \approx 8$ (here T_c denotes the critical temperature, ϵ_F the Fermi energy, l the mean free path and ξ the coherence length). In usual dimensionless units, we have[58]

$$\begin{aligned} f &= -(|\eta_+|^2+|\eta_-|^2)+\frac{1}{2}\left(|\eta_+|^4+|\eta_-|^4\right)+2\,|\eta_+|^2|\eta_-|^2+\frac{\nu}{2}\left[(\eta_-\eta_+^*)^2+(\eta_-^*\eta_+)^2\right] \\ &\quad +B^2+|\boldsymbol{D}\eta_+|^2+|\boldsymbol{D}\eta_-|^2 \\ &\quad +\frac{1+\nu}{2}\left[(D_x\eta_+)(D_x\eta_-)^*+(D_x\eta_-)(D_x\eta_+)^*\right] \\ &\quad -\frac{1+\nu}{2}\left[(D_y\eta_+)(D_y\eta_-)^*+(D_y\eta_-)(D_y\eta_+)^*\right] \\ &\quad +\frac{1-\nu}{2\,i}\left[(D_x\eta_+)(D_y\eta_-)^*+(D_y\eta_+)(D_x\eta_-)^*\right] \\ &\quad -\frac{1-\nu}{2\,i}\left[(D_x\eta_+)^*(D_y\eta_-)+(D_y\eta_+)^*(D_x\eta_-)\right], \end{aligned} \tag{3.4}$$

where $\eta_\pm=(\eta_1\pm i\eta_2)/\sqrt{2}$, $\boldsymbol{B}=\nabla\wedge\boldsymbol{A}$, $D_\mu=-i\,\nabla_\mu/\kappa-A_\mu$, f is in units $B_c^2/4\pi$, lengths are in units of the penetration depth λ, $\boldsymbol{B}$ is in units $\sqrt{2}B_c=\Phi_0/(2\pi\lambda\xi)$, $\alpha=\alpha_0(T-T_c)$, and $\kappa=\lambda/\xi$. The anisotropy $\nu=(\langle v_x^4\rangle-3\langle v_x^2v_y^2\rangle)/(\langle v_x^4\rangle+\langle v_x^2v_y^2\rangle)$ is a parameter that measures the tetragonal distortion of the Fermi surface ($\langle\cdot\rangle$ denotes averaging over the Fermi surface; note $|\nu|\le 1$ and $\nu=0$ for a cylindrical geometry). The free energy f is invariant under a simultaneous rotation of 45° around the c-axis and changing sign of ν. This implies that all results derived below for $\nu>0$ can be transformed into the corresponding results for negative $\nu<0$ by a simple rotation, and we limit ourselves to the case $\nu>0$. Further we deal only with external fields applied along the c-axis allowing us to omit all terms containing z-derivatives.

At zero applied field the two degenerate solutions $(\eta_+,\eta_-)=(1,0)$ and $(\eta_+,\eta_-)=(0,1)$ minimize the free energy f. For nonzero applied field, the degeneracy is lifted, and depending on the direction of the applied field only one component $\eta_\pm$ is stable. Throughout this section we will fix the dominant order parameter to be η_- and discuss the differences between the stable and the unstable case. The asymptotic vorticity of the dominant η_--component determines the (vortex generated) field direction along the positive or negative z-axis. In the spatially inhomogeneous situations considered below, the second component η_+ is driven through the mixed gradient terms [gradient terms such as $(D_x\eta_+)^*(D_y\eta_-)$] and decays far away from the defect. Note, that to each solution $\{\eta_-,\eta_+,\boldsymbol{B}\}$ a symmetric counterpart with reversed field direction exists

$$\{\eta_-,\eta_+,\boldsymbol{B}\} \quad\rightarrow\quad \{\eta_+^*,\eta_-^*,-\boldsymbol{B}\}. \tag{3.5}$$

3.2.1 Asymptotic solution

Below, we first examine the asymptotic solutions of the GL-equations for $\nu = 0$. Second, we use the $\nu = 0$-solution and carry out perturbation theory in ν to obtain the asymptotic solutions for $\nu \neq 0$ (we ignore the coupling to the vector potential in the latter case). We are interested mainly in the qualitative behavior of the solutions for small and large r. In the cylindrical case ($\nu = 0$) the problem exhibits rotational

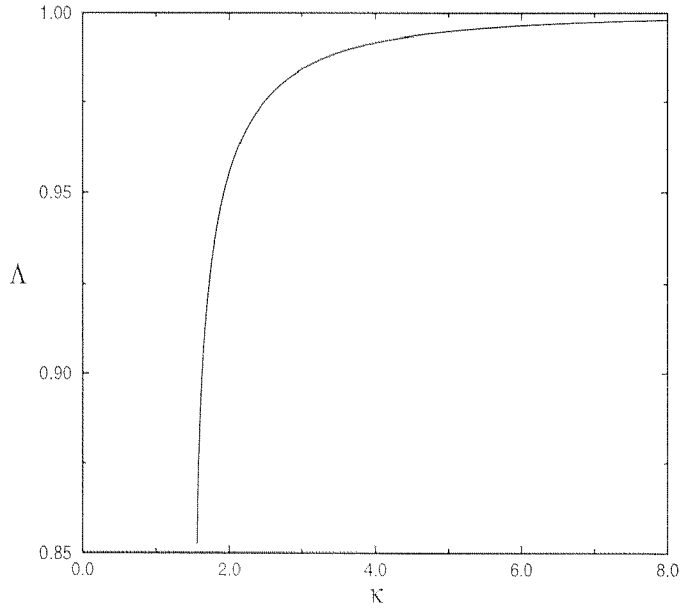

Figure 3.1: Exponent Λ governing the decay of $\nu = 0$ solutions.

symmetry. Restricting to fields $\boldsymbol{B} = B(r)\boldsymbol{e}_z$, the solution has the structure

$$\begin{aligned} \eta_-(\boldsymbol{r}) &= e^{in\theta}\eta_-(r), \\ \eta_+(\boldsymbol{r}) &= e^{i(n+2)\theta}\eta_+(r), \\ \boldsymbol{A}(\boldsymbol{r}) &= A(r)\boldsymbol{e}_\theta, \end{aligned} \tag{3.6}$$

where (r, θ) are polar coordinates and n denotes the phase winding of the topological defect driving the vortex in the main superconducting component. The relative phase $e^{i2\theta}$ between η_- and η_+ corresponds to an angular momentum difference $\Delta l = 2$ and comes in through the specific form $(D_x + iD_y)^2$ of the mixed gradient terms for $\nu = 0$. The solutions for $n = \pm 1$ are the most stable ones. We expect the $n = 1$ case to be energetically slightly favored, since the counter-rotating current contribution of the admixed order parameter component tends to reduce the kinetic energy of the currents. The small r expansion to cubic order takes the form

$$n = 1: \qquad \eta_-(\boldsymbol{r}) \sim \left(m_1^0 r - \left(\frac{3}{2} p_3^0 + \frac{\kappa^2}{8} m_1^0 \left(1 + \frac{2}{\kappa} a_1^0 \right) \right) r^3 \right) e^{i\theta},$$

$$\begin{aligned} \eta_+(\boldsymbol{r}) &\sim p_3^0 r^3\, e^{3i\theta}, \\ A(r) &\sim a_1^0 r - \frac{(m_1^0)^2}{8\kappa}\, r^3, \end{aligned} \tag{3.7}$$

$$\begin{aligned} n=-1: \quad \eta_-(\boldsymbol{r}) &\sim \left(m_1^0 r + \frac{\kappa^2}{6}\left(\frac{1}{2}p_1^0 - m_1^0 + \frac{3}{\kappa} a_1^0 \left(m_1^0 + p_1^0\right)\right) r^3 \right) e^{-i\theta}, \\ \eta_+(\boldsymbol{r}) &\sim \left(p_1^0 r + \frac{\kappa^2}{6}\left(\frac{1}{2}m_1^0 - p_1^0 - \frac{3}{\kappa} a_1^0 \left(m_1^0 + p_1^0\right)\right) r^3 \right) e^{i\theta}, \\ A(r) &\sim a_1^0 r - \frac{(p_1^0)^2 - (m_1^0)^2}{8\kappa}\, r^3, \end{aligned} \tag{3.8}$$

where m_1^0, $p_{1,3}^0$, and a_1^0 are the first expansion coefficients of η_-, η_+, and A, to be determined by matching this small r expansion to the asymptotics at $r \to \infty$. The latter reads

$$\begin{aligned} \eta_-(\boldsymbol{r}) &= (1 - m(r))\, e^{in\theta}, \\ \eta_+(\boldsymbol{r}) &= p(r)\, e^{i(n+2)\theta}, \\ A(r) &= \pm\frac{1}{\kappa r} + a(r), \end{aligned} \tag{3.9}$$

where the $\pm$ stands for $n = \pm 1$. The asymptotic form of the GL-equations requires the three functions $m(r)$, $p(r)$, and $a(r)$ to be of the form

$$\begin{aligned} \eta_-(\boldsymbol{r}) &\sim \left(1 - \frac{(n+2)^2}{2\kappa^2 r^2}\right) e^{in\theta}, \\ \eta_+(\boldsymbol{r}) &\sim \frac{n^2+2n}{2\kappa^2 r^2}\, e^{i(n+2)\theta}, \end{aligned} \tag{3.10}$$

if we ignore the vector potential $A(r) = 0$ ($a(r) = 0$). For the general case ($A(r) \neq 0$) the main asymptotics is an exponential decay

$$a(r), m(r), p(r) \sim e^{-r/\Lambda}, \tag{3.11}$$

which is a consequence of transverse screening. From Fig. 3.1 we see, that for reasonably large κ this exponent Λ approaches 1, which equals the usual penetration depth in dimensionless units.

We proceed now with the anisotropic case $\nu \neq 0$ (here we neglect the vector potential). An expansion to first order in ν produces the following result for small r

$$\begin{aligned} n=1: \quad \eta_-(\boldsymbol{r}) &\sim \left(m_1^0 r - \frac{\kappa^2 m_1^0 + 12 p_3^0}{8}\, r^3 \right) e^{i\theta} + \nu \left(\frac{\kappa^2 m_1^0 + 12 p_3^0}{16} - \frac{3 g_{-,3}^0}{2} \right) r^3 e^{-i\theta}, \\ \eta_+(\boldsymbol{r}) &\sim p_3^0 r^3\, e^{3i\theta} + \nu g_{-,3}^0 r^3\, e^{-i\theta}, \end{aligned} \tag{3.12}$$

$$\begin{aligned} n=-1: \quad \eta_-(\boldsymbol{r}) &\sim \left(m_1^0 r + \frac{\kappa^2}{12}(p_1^0 - 2m_1^0) r^3 \right) e^{-i\theta} + \nu g_{+,3}^0 r^3\, e^{3i\theta}, \\ \eta_+(\boldsymbol{r}) &\sim \left(p_1^0 r + \frac{\kappa^2}{12}(m_1^0 - 2p_1^0) r^3 \right) e^{i\theta} + \nu f_{-,3}^0 r^3\, e^{-3i\theta}, \end{aligned} \tag{3.13}$$

and for large r

$$\eta_-(\boldsymbol{r}) \sim \left(1 - \frac{(n+2)^2}{2\kappa^2 r^2}\right) e^{in\theta} - \nu \frac{n}{2\kappa^2 r^2} \left(e^{i(n+4)\theta} + 3e^{i(n-4)\theta}\right),$$
$$\eta_+(\boldsymbol{r}) \sim \frac{n^2+2n}{2\kappa^2 r^2} e^{i(n+2)\theta} + \nu \frac{n}{\kappa^2 r^2} \left(e^{i(n+6)\theta} + e^{i(n-2)\theta}\right). \quad (3.14)$$

The additional coefficients $g^0_{\pm,3}$ and $f^0_{\pm,3}$ are the first expansion coefficients of the higher angular momentum states ($f^0_{\pm,3}$ from $\eta_+ \sim e^{i(n+2\pm4)\theta}$ and $f^0_{\pm,3}$ from $\eta_- \sim e^{i(n\pm4)\theta}$), which arise for $\nu \neq 0$. Comparing the condensation energy for the two cases $n = \pm 1$ we find that the $(n = -1)$-case is energetically favored: as mentioned earlier, the current contribution of the admixed order parameter opposes the main current direction and lowers thus the kinetic energy. Further, the admixed η_+ order parameter rises linearly in the center rather than cubic as is the case for $n = 1$, and the asymptotic phase turns of η_+ are the same in the center and for large r (which is also an argument against off-centered zeroes as seen for example in $d_{x^2-y^2}$-superconductors). Both points lead to a higher gain in condensation energy, which should stabilize the $(n = -1)$-solution. Our numerical Ginzburg-Landau results (described in the next paragraph) for the critical fields $H_{c1} = \epsilon_l \kappa / 4\pi$ confirm this finding: for $\kappa = 2.5$ and

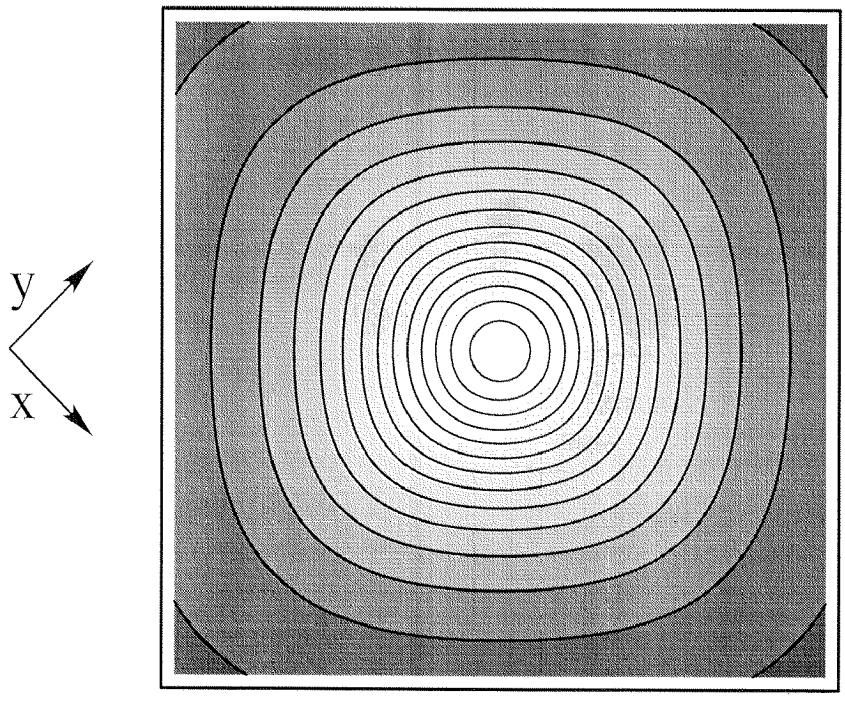

Figure 3.2: Contour plot of the absolute value of the $|B|$-field for the same parameters as in Fig. 3.4. Notice the strong square deformations of the vortex core along the axes of the crystal lattice. The contours are 0.03, 0.06, ..., 0.42.

$\nu = 0.3$, we obtain

$$\begin{aligned} H_{c1}(n=-1) &= 0.43B_c, \\ H_{c1}(n=1) &= 0.47B_c, \end{aligned}$$

demonstrating the stability of the $(n = -1)$-solution compared to $(n = 1)$. The corresponding s-wave result is $H_{c1} = 0.48B_c$.

3.2.2 Numerical solution for isolated vortices

To obtain complete numerical solutions, we minimize the free energy density on a two-dimensional grid. The minimization is carried out by relaxing an initial configuration $\eta_+ = 0$, $\eta_- = \tanh(r)\, e^{\pm i\theta}$ and $\boldsymbol{A} = 0$ iteratively. The phase turn of the dominant order parameter η_- determines the field direction along the z axis. Indeed we find that the energetically favorable $(n = -1)$-solution shows no off-centered zeroes in η_+ (Fig. 3.4). The admixed η_+ solution shows a fourfold structure with a maximal amplitude along the diagonals.
On the other hand, in the unstable $(n = 1)$-case the admixed component η_+ exhibits a negative phase turn around the center, and consequently four off-centered zeroes with positive phase turn are needed to match up this phase $e^{-i\theta}$ at small r to the asymptotic phase $e^{3i\theta}$ at large r (Fig. 3.6). In addition the vortex core center of the dominant order parameter (Fig. 3.3) is distorted with marked elongations along the axes of the crystal lattice for $\nu > 0$ (and analogously along the diagonals for $\nu < 0$). This behavior is understood recalling the properties of the Fermi surface. For $\nu > 0$, the density of states (DOS) at the Fermi surface is larger along the diagonals than along the axes. A larger DOS however implies also a larger effective mass, which reduces the coherence length and thus the size of the vortex. Finally, the distribution of the absolute value of the B_z-field (Fig. 3.2) also shows clear square deformations rotated by 45° with respect to the underlying crystal lattice. This pattern is qualitatively well known from analog GL-calculations for s-admixture in $d_{x^2-y^2}$ high-T_c superconductors[22, 24, 25, 26, 29]. The dominant component η_- and the B_z-field show similar features as in the stable case discussed above (Fig. 3.5).

3.3 Vortex lattice: London theory

3.3.1 Extended London theory

We wish to determine the form of the vortex lattice close to H_{c1}. Instead of solving the Ginzburg-Landau free energy directly, here we follow an idea recently developed in the

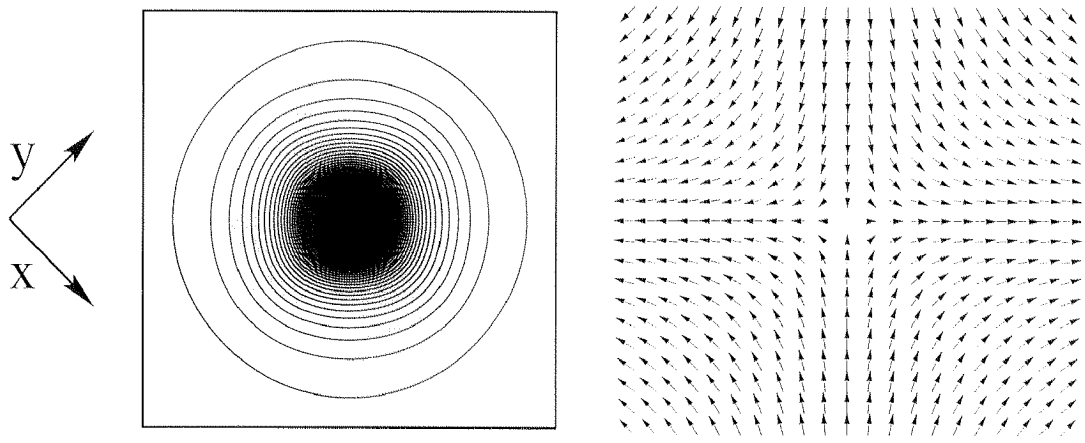

Figure 3.3: Dominant order parameter η_- for the stable configuration (negative phase turn of η_-) for the parameters $\kappa = 2.5$ and $\nu = 0.3$. Contour plot (left) of the absolute value $|\eta_-|$, and vector plot (right) of η_-. The contours in the contour plot of $|\eta_-|$ are 0.99, 0.975, ...

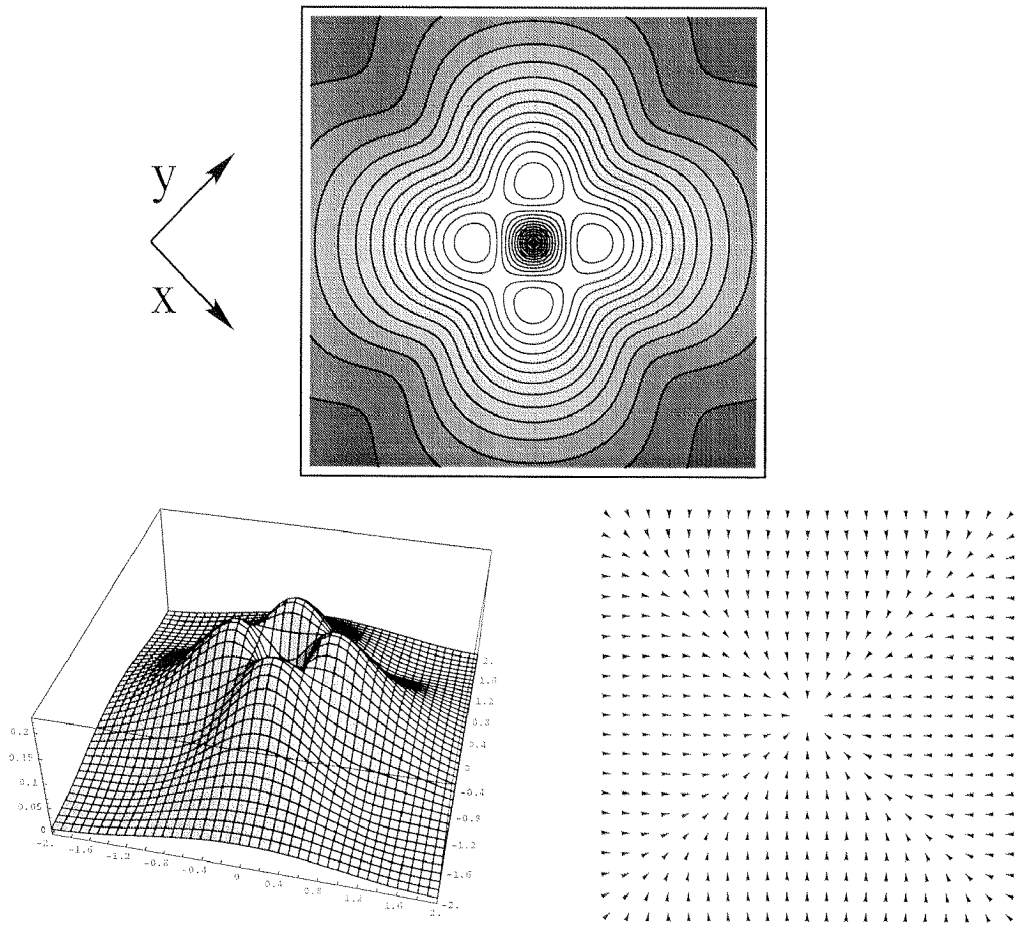

Figure 3.4: Admixed order parameter η_+ for the same parameters as Fig. 3.3. Contour (above) and surface plot (left) of the absolute value $|\eta_+|$, and vector plot (right) of η_+. The contours in the contour plot of $|\eta_+|$ are 0.03, 0.045, ..., 0.225.

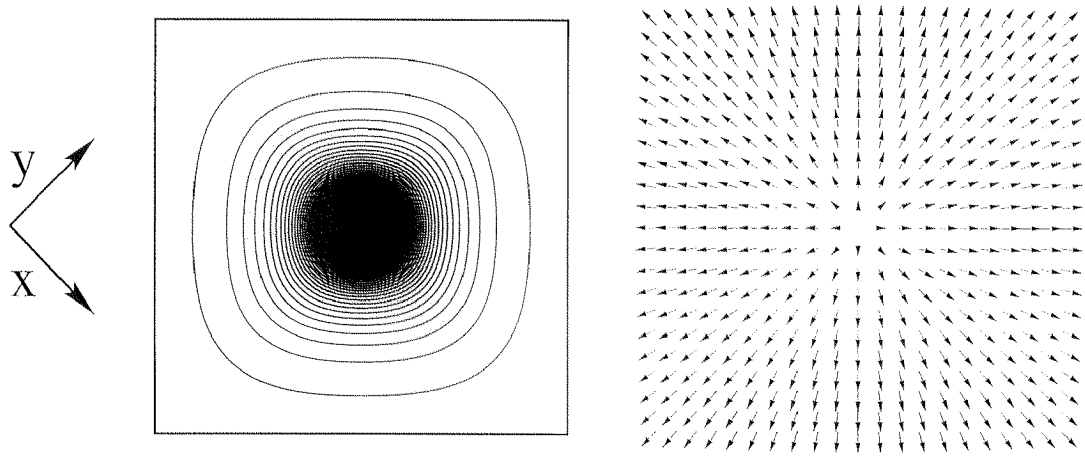

Figure 3.5: Dominant order parameter η_- for the unstable configuration (positive phase turn of η_-) for the parameters $\kappa = 2.5$ and $\nu = 0.3$. Contour plot (left) of the absolute value $|\eta_-|$, and vector plot (right) of η_-. The contours in the contour plot of $|\eta_-|$ are 0.99, 0.975, ...

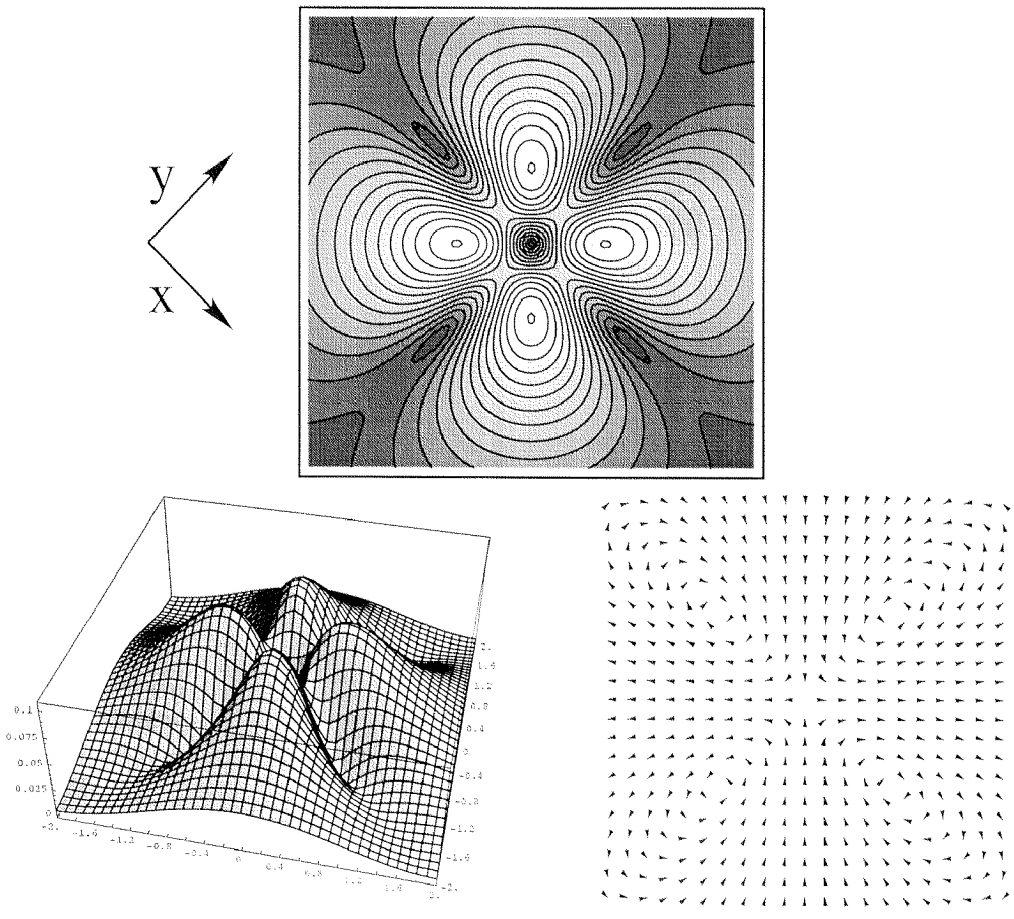

Figure 3.6: Admixed order parameter η_+ for the same parameters as Fig. 3.5. Contour (above) and surface plot (left) of the absolute value $|\eta_+|$, and vector plot (right) of η_+. The contours in the contour plot of $|\eta_+|$ are 0.03, 0.045, ..., 0.225.

context of $d_{x^2-y^2}$-wave superconductors with a weak admixing of an s-component[55]. We first integrate out the admixed component, leading to a one-component free energy density. We assume $\kappa \gg 1$ to be able to use London approximation and expand in $\nu \ll 1$. We obtain an effective free energy density which depends only on the field B and which can be minimized with respect to the geometry of the vortex lattice. Though our results will be quantitatively inaccurate for the low-κ Sr_2RuO_4 material, we still expect to obtain a qualitatively correct picture. The Ginzburg-Landau equation for η_+ to first order in $|\eta_+|/|\eta_-|$ reads

$$0 = -\eta_+ + 2\,|\eta_-|^2\eta_+ + \boldsymbol{D}^2\,\eta_+ + \frac{1+\nu}{2}\,(D_x^2 - D_y^2)\,\eta_- - \frac{1-\nu}{2\,i}\,(D_xD_y + D_yD_x)\,\eta_-. \quad (3.15)$$

Within London theory the dominant component η_- has modulus unity (see Eq. (3.18)) and the first three terms lead to the expression $(1+\boldsymbol{D}^2)\,\eta_+$. Solving formally for η_+ and substituting this expression into the free energy density, we obtain the effective one-component Ginzburg-Landau free energy

$$f = -|\eta_-|^2 + \frac{1}{2}\,|\eta_-|^4 + |\boldsymbol{D}\eta_-|^2 - \eta_-^*\,\mathcal{P}(\boldsymbol{D},\nu)\,\left(1+\boldsymbol{D}^2\right)^{-1}\mathcal{P}(\boldsymbol{D},\nu)\,\eta_- + B^2, \quad (3.16)$$

with

$$\mathcal{P}(\boldsymbol{D},\nu) = \frac{1+\nu}{2}\,(D_x^2 - D_y^2) - \frac{1-\nu}{2\,i}\,(D_xD_y + D_yD_x). \quad (3.17)$$

Here we have consistently neglected all terms of order η_+^4, $\nu\eta_+^2$, and higher. Following the usual scheme for London approximation we replace the order parameter η_- and its derivative by the superfluid velocity $\boldsymbol{v}$

$$\begin{aligned} \eta_- &= e^{i\phi(\boldsymbol{x})}, \\ \boldsymbol{D}\eta_- &= (\frac{1}{\kappa}\,\boldsymbol{\nabla}\phi(\boldsymbol{x}) - \boldsymbol{A})\,e^{i\phi(\boldsymbol{x})} \equiv \frac{1}{\kappa}\,\boldsymbol{v}\,e^{i\phi(\boldsymbol{x})}. \end{aligned} \quad (3.18)$$

Keeping only terms up to second order in $\boldsymbol{v}$ and up to first order in the anisotropy parameter ν, we obtain the London free energy in Fourier representation

$$\begin{aligned} f(\boldsymbol{k}) &= -\frac{1}{2} + \frac{1}{\kappa^2}\,\boldsymbol{v}^2 + B^2 \\ &\quad -\frac{1}{4\kappa^4}\,\frac{1}{1+k^2/\kappa^2}\left(k^2\boldsymbol{v}^2 + 2\nu\left[(k_x^2-k_y^2)\,(v_x^2-v_y^2) - (2\,k_xk_y)\,(2\,v_xv_y)\right]\right). \end{aligned} \quad (3.19)$$

Here, all quadratic expressions in $\boldsymbol{v}$ and B have to be understood as $v_iv_j = v_i(\boldsymbol{k})v_j(-\boldsymbol{k})$ (the results for vorticity $n = \pm 1$ are the same on this level of calculation; they would differ if one included higher orders in $\boldsymbol{v}$).

Next, we eliminate $\boldsymbol{v}$. We obtain an equation connecting B and $\boldsymbol{v}$ by variation of the London free energy Eq. (3.19) with respect to the vector potential $\boldsymbol{A}$. The corresponding Euler-Lagrange equation reads

$$\begin{aligned} &i\,\kappa^3\,\boldsymbol{k}\wedge\boldsymbol{B} = \\ &\quad \kappa^2\,\boldsymbol{v} - \frac{1}{4}\,\frac{1}{1+k^2/\kappa^2}\left(k^2\boldsymbol{v} + 2\nu\left[(k_x^2-k_y^2)\,(v_x\hat{\boldsymbol{x}} - v_y\hat{\boldsymbol{y}}) - (2\,k_xk_y)\,(v_x\hat{\boldsymbol{y}} + v_y\hat{\boldsymbol{x}})\right]\right). \end{aligned} \quad (3.20)$$

We solve this equation for $\boldsymbol{v}$ up to first order in ν and substitute the solution back into the London free energy density (Eq. (3.19)), to obtain

$$\begin{aligned} f(\boldsymbol{q}) &= -\frac{1}{2} + \left[1 + q^2\kappa^2 \frac{1+q^2}{(1+\frac{3}{4}q^2)^2}\left(1 + \frac{3}{4}q^2 - \frac{\nu}{2}\left(\frac{(q_x^2-q_y^2)^2}{q^2} - \frac{(2\,q_x q_y)^2}{q^2}\right)\right)\right] B^2 \\ &\equiv -\frac{1}{2} + J(\boldsymbol{q},\nu,\kappa)\,B^2, \end{aligned} \tag{3.21}$$

where we introduced the short notation $\boldsymbol{q} = (1/\kappa)\boldsymbol{k}$. The variation with respect to $B(\boldsymbol{k})$ leads to the extended London equation

$$J(\boldsymbol{q},\nu,\kappa)B(\boldsymbol{k}) = 0 \tag{3.22}$$

where we recover in the limit $\kappa \to \infty$ the well-known result $(1+k^2)B(\boldsymbol{k}) = 0$ (no sources).

3.3.2 Vortex lattice close to H_{c1}

We parameterize the unit cell in real space through the angles θ_1 and θ_2, the ratio of the lengths of the unit vectors ζ and the average field $\bar{B}$ (see Fig. 3.7), where the first three parameters describe the geometry and $\bar{B}$ the size of the cell. The lattice geometry depends on the applied field H and is determined by minimizing the Gibbs free energy $\mathcal{G}(H)$ given in Eq. (3.24) with respect to the unit cell parameters. We generate the vortex lattice by introducing the corresponding source terms at the vortex core positions into the London equations. A convenient form for these source

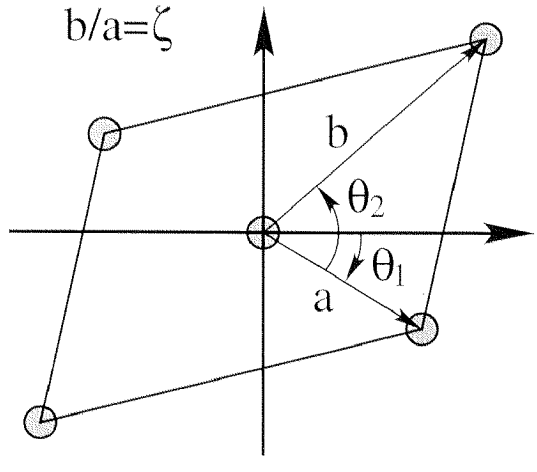

Figure 3.7: Schematic illustration of the real unit cell. θ_2 denotes the opening angle between the primitive basis vectors, whereas θ_1 denotes the orientation of $\boldsymbol{a}$ with respect to the crystal x-axis.

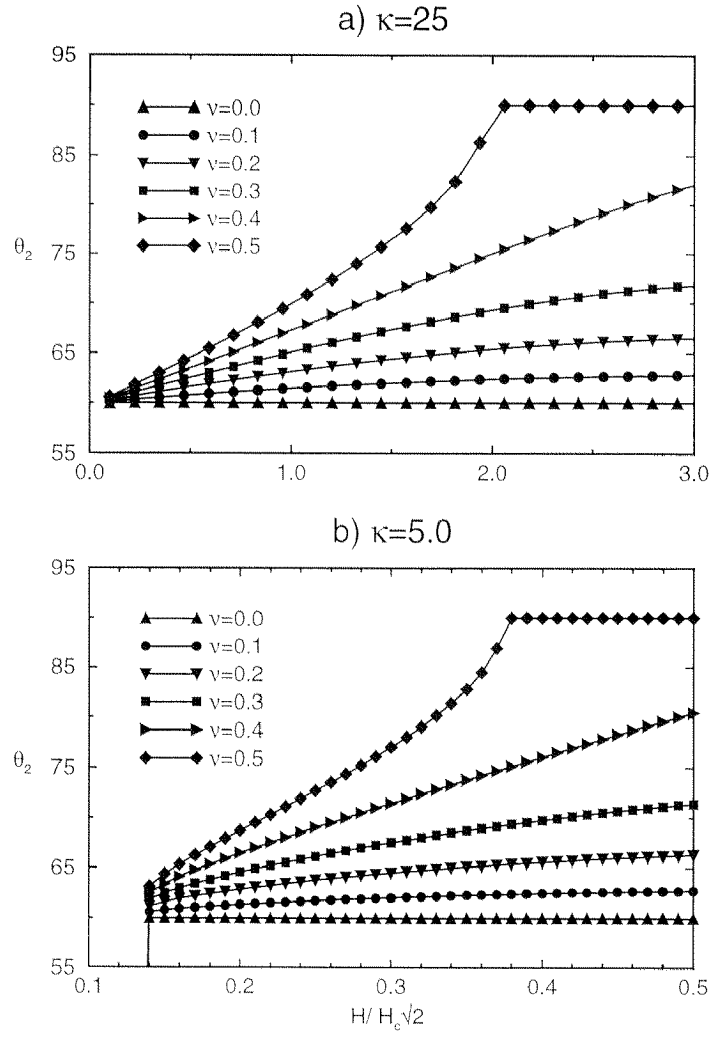

Figure 3.8: Vortex lattice structure as function of the applied field H. The GL-parameter is $\kappa = 25$ (a) and $\kappa = 5$ (b), and θ_2 denotes the angle between the unit cell vectors minimizing the free energy density given in Eq. (3.24). Note that in the small field range necessary for our approach, the second order transition to the square lattice is visible only for high values of the anisotropy ν.

terms is[59]

$$\sigma(\boldsymbol{r}) = \kappa \sum_j e^{-\kappa^2(\boldsymbol{r}-\boldsymbol{r}_j)^2/2}, \tag{3.23}$$

where the sum runs over all positions $\boldsymbol{r}_j$ of the vortex lattice. The magnetic field and the Gibbs free energy for the vortex lattice read

$$B(\boldsymbol{r}) = \bar{B} \sum_{\boldsymbol{q}_j} \frac{e^{i\kappa \boldsymbol{q}_j r}\, e^{-q_j^2/2}}{J(\boldsymbol{q}_j, \nu, \kappa)}$$

$$\mathcal{G}(H) = \bar{B}^2 \sum_{\boldsymbol{q}_j} \frac{e^{-q_j^2}}{J(\boldsymbol{q}_j, \nu, \kappa)} - 2H\bar{B}, \tag{3.24}$$

where the specific form of the vortex lattice is given by the reciprocal lattice vectors $\boldsymbol{q}_j$. Writing the operator $J(\boldsymbol{q}, \nu, \kappa)$ in the form

$$J(\boldsymbol{q}, \nu, \kappa) = 1 + \kappa^2 \frac{1+q^2}{(1+\frac{3}{4}q^2)^2} \left(q^2 + \frac{3}{4}q^4 - \frac{\nu}{2} q^4 \cos 4\phi_q \right), \tag{3.25}$$

it is obvious that a change of sign in ν still corresponds to a rotation in real and reciprocal space by 45°. We thus restrict the discussion again to positive values of ν. The resulting vortex lattices exhibit a centered rectangular unit cell with the main axes aligned along the axes of the underlying crystal. Without loss of generality we thus assume $\theta_1 = -\theta_2/2$ and $\zeta = 1$ in the remainder of this section. In Fig. 3.8 we plot the angle θ_2 minimizing the Gibbs free energy for different values of ν versus the field H (Fig. 3.8a: $\kappa = 25.0$, Fig. 3.8b: $\kappa = 5.0$). For large enough values of the anisotropy parameter ν, the vortex lattice evolves from hexagonal at low applied fields to square at high fields. The lattices found in our calculations ($\nu > 0$) are always

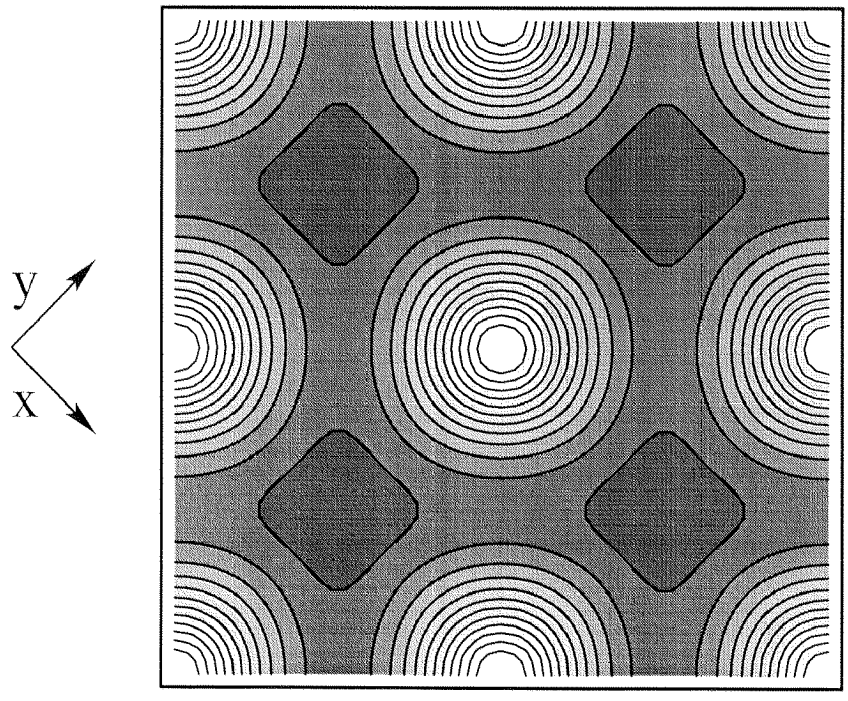

Figure 3.9: Contour plot of the field distribution for $\nu = 0.4, \kappa = 2.5, H = 0.25$. The horizontal and vertical axes of the plot correspond to the diagonals of the underlying crystal lattice. The field distribution shows a square lattice rotated by 45° with respect to the crystal axes, with weak square shaped deformations of the vortex cores.

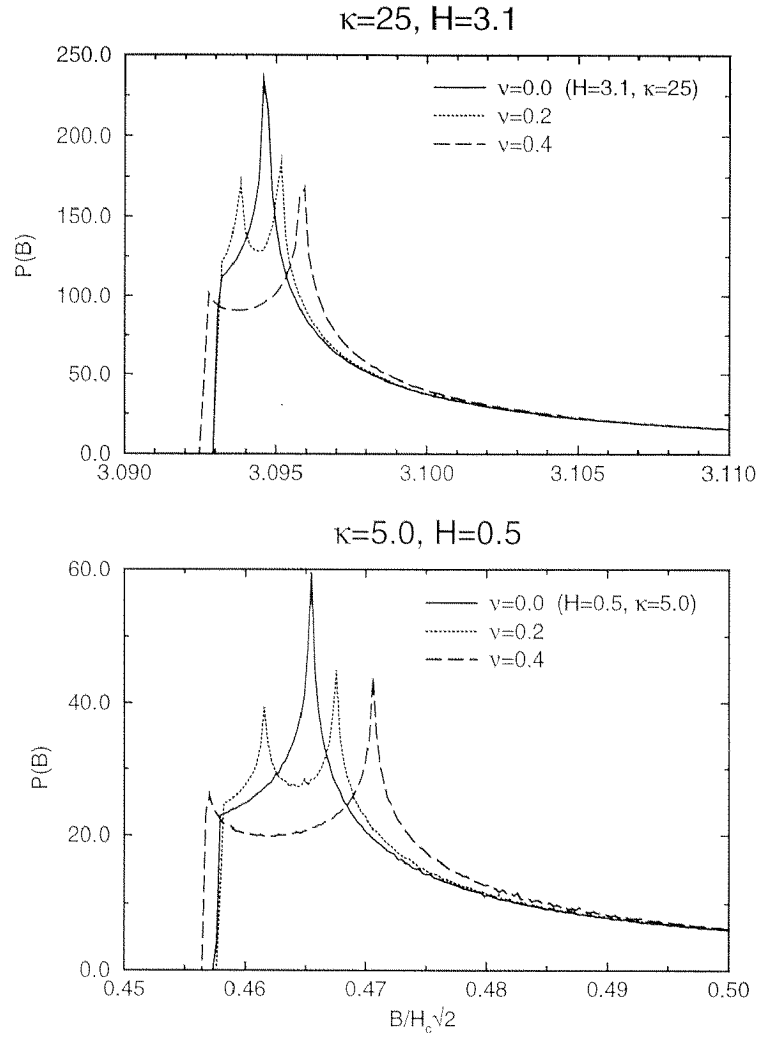

Figure 3.10: Field distribution $P(B)$ for different values of the anisotropy ν at $\kappa = 2.5, H = 0.3$ (a) and $\kappa = 25.0, H = 3.1$ (b).

aligned with the diagonals of the underlying lattice (see Fig. 3.9). For decreasing κ, the crossover to a square lattice approaches to the lower critical field H_{c1} and occurs at lower anisotropies ν, an effect which is believed to be even stronger if one would include all nonlinearities into the theory. These results are in good agreement with recent experimental data of Forgan *et al.*[40, 41], who find in Sr_2RuO_4 a square lattice rotated by 45° with respect to the crystal lattice down to very small fields in the phase diagram. (This is is contrast to the earlier results of the same group[39].) The shape of the individual B-field flux lines around the vortex core is perfectly circular for $\nu = 0$ over the whole range of the applied field H, whereas we find square deformations of the B-field for positive values of ν (see Fig.3.9). This is in agreement with the single vortex results obtained in the previous section.

Apart form the vortex lattice symmetry, the corresponding field distributions are of

interest. Experiments using μSR can observe the field distribution

$$P(B) = \frac{1}{V_{\rm uc}} \int_{V_{\rm uc}} d^2\boldsymbol{r}\, \delta\left(B - B(\boldsymbol{r})\right). \tag{3.26}$$

In Fig. 3.10, characteristic results are shown for two cases $\kappa = 25.0, H = 3.1$ (a) and $\kappa = 5.0, H = 0.5$ (b). While at $\nu = 0$ the field distribution shows only one peak with a small shoulder towards the minimal field value, the situation for $\nu \neq 0$ is quite different. With increasing $|\nu|$ the $\nu = 0$-peak splits into two due to the appearance of two nonequivalent classes of saddle points in the B-field. Upon further increase of $|\nu|$, the low field peak gradually vanishes and finally develops into a broad shoulder.

3.4 Vortex lattice: Ginzburg-Landau theory

3.4.1 Free energy density in gauge invariant fields

In the preceding sections we have calculated the structure of isolated vortices as well as the properties of the vortex lattice near the square-to-hex transition. Both calculations correspond to the situation with low vortex density near the lower critical field H_{c1}. In the meantime, the experimental progress has drawn the attention also to the situation with intermediate applied fields. Very high quality small angle neutron scattering (SANS) experiments[39, 40, 41] have made it possible to determine the lower few Fourier components of the B-field distribution in the vortex lattice within a large range of applied fields H. It is an interesting question whether these values for the Fourier coefficients can be reproduced within our simple Ginzburg-Landau theory. To solve the vortex lattice problem within Ginzburg-Landau theory, we first tried to extend the numerical solution designed for s-wave superconductors[60] to the p-wave FED. In contrast to the s-wave case, where this method converges very efficiently, it turned out in the p-wave case that the method was eventually unstable. However, the first few iteration steps converge very fast towards the physical solution and lead to a very good starting point for a conventional minimization algorithm using Fourier decomposition. This combination of two minimization methods turned out to be efficient enough to produce good results on the vortex lattice parameters.

In this chapter we will first describe the basic ideas of this minimization technique introduced by Brandt, the details of which are described in Appendix B. Since this minimization assumes a given mean penetrating field $\bar{B}$, the following minimization with constant applied field H has to make use of some interesting scaling relations of the free energy density, introduced for s-waves by Doria *et al.*[61, 62]. We then will compare our results with the recent SANS measurements of Kealey *et al.*[41].

We start with the Ginzburg-Landau FED Eq. (3.4) in dimensionless units as introduced in Section 3.2

$$\begin{aligned} f &= -(|\eta_+|^2+|\eta_-|^2)+\frac{1}{2}\left(|\eta_+|^4+|\eta_-|^4\right)+2\,|\eta_+|^2|\eta_-|^2+\frac{\nu}{2}\left[(\eta_-\eta_+^*)^2+(\eta_-^*\eta_+)^2\right] \\ &\quad +B^2+|\boldsymbol{D}\eta_+|^2+|\boldsymbol{D}\eta_-|^2 \\ &\quad +\frac{1+\nu}{2}\left[(D_x\eta_+)(D_x\eta_-)^*+(D_x\eta_-)(D_x\eta_+)^*\right] \\ &\quad -\frac{1+\nu}{2}\left[(D_y\eta_+)(D_y\eta_-)^*+(D_y\eta_-)(D_y\eta_+)^*\right] \\ &\quad +\frac{1-\nu}{2\,i}\left[(D_x\eta_+)(D_y\eta_-)^*+(D_y\eta_+)(D_x\eta_-)^*\right] \\ &\quad -\frac{1-\nu}{2\,i}\left[(D_x\eta_+)^*(D_y\eta_-)+(D_y\eta_+)^*(D_x\eta_-)\right], \end{aligned} \tag{3.27}$$

where the gauge invariant derivative is given as before by $D_\mu=-i\,\nabla_\mu/\kappa-A_\mu$. To write the whole free energy density in gauge invariant quantities, we introduce

$$\begin{aligned} \omega &= |\eta_-|^2 \\ \eta_- &= |\eta_-|e^{i\phi(\boldsymbol{x})} \\ \eta_+ &= (\eta+i\sigma)e^{i\phi(\boldsymbol{x})} \\ \boldsymbol{Q} &= \boldsymbol{A}-\frac{\boldsymbol{\nabla}\phi}{\kappa}, \end{aligned} \tag{3.28}$$

where η and σ are real quantities to describe the admixed component, and obtain the gauge invariant form

$$\begin{aligned} f &= -\omega+\frac{\omega^2}{2}+\frac{(\boldsymbol{\nabla}\omega)^2}{4\kappa^2\omega}+\omega\boldsymbol{Q}^2+h^2 \\ &\quad -(\eta^2+\sigma^2)+\frac{1}{2}(\eta^2+\sigma^2)^2+2\omega(\eta^2+\sigma^2)+\nu\omega(\eta^2-\sigma^2) \\ &\quad +\left(\frac{\boldsymbol{\nabla}\sigma}{\kappa}-\boldsymbol{Q}\eta\right)^2+\left(\frac{\boldsymbol{\nabla}\eta}{\kappa}+\boldsymbol{Q}\sigma\right)^2 \\ &\quad +(1+\nu)\left(Q_x\omega^{\frac{1}{2}}\left(Q_x\eta-\frac{\partial_x\sigma}{\kappa}\right)+\frac{1}{2\kappa}\frac{\partial_x\omega}{\omega^{\frac{1}{2}}}\left(\frac{\partial_x\eta}{\kappa}+Q_x\sigma\right)\right)-(x\leftrightarrow y) \\ &\quad +(1-\nu)\left(Q_y\omega^{\frac{1}{2}}\left(Q_x\sigma+\frac{\partial_x\eta}{\kappa}\right)-\frac{1}{2\kappa}\frac{\partial_y\omega}{\omega^{\frac{1}{2}}}\left(Q_x\eta-\frac{\partial_x\sigma}{\kappa}\right)\right)+(x\leftrightarrow y). \end{aligned} \tag{3.29}$$

We derive Ginzburg-Landau equations in the gauge invariant quantities by derivation of f with respect to ω,η,σ and $\boldsymbol{Q}$. By taking the rotation of the GL-equation for $\boldsymbol{Q}$, we end up with an equation including the B-field. The resulting set of four equations can be written in the form

$$\begin{aligned} (-\boldsymbol{\nabla}^2+2\kappa^2)\omega &= g_1(\omega,\eta,\sigma,\boldsymbol{Q}) \\ (-\boldsymbol{\nabla}^2+\bar{\omega})B &= g_2(\omega,\eta,\sigma,\boldsymbol{Q}) \\ (-\boldsymbol{\nabla}^2+2\kappa^2)\eta &= g_3(\omega,\eta,\sigma,\boldsymbol{Q}) \\ (-\boldsymbol{\nabla}^2+2\kappa^2)\sigma &= g_4(\omega,\eta,\sigma,\boldsymbol{Q}) \end{aligned} \tag{3.30}$$

where $\bar{\omega}$ is the average order parameter and the detailed form of the expressions g_i are given in Appendix B (Eq. (B.3)).

In contrast to the calculation of the vortex lattice symmetry of the last section, we parametrize the vortex lattice in a slightly adapted form. Starting from the results of the London theory, we concentrate on lattices occurring in the square-to-hex transition, which are of centered rectangular symmetry with respect to the diagonals (axes) for negative (positive) anisotropy ν. Aware of the symmetry between positive and negative ν mentioned above (Sec. 3.2), we restrict ourselves to $\nu < 0$ in the following. In contrast to actual understanding[40, 41], this was the experimentally favored value when we performed our calculations.

For a given lattice unit cell (which implies a given $\bar{B}$ and a definite lattice symmetry), we expand the order parameters and the B-field in the corresponding reciprocal lattice vectors

$$\begin{aligned}
\omega(\boldsymbol{r}) &= {\sum_{m,n}}' a_{m,n}(1-\cos \boldsymbol{k}_{m,n}\boldsymbol{r}) \\
B(\boldsymbol{r}) &= \bar{B} + {\sum_{m,n}}' b_{m,n} \cos \boldsymbol{k}_{m,n}\boldsymbol{r} \\
\boldsymbol{Q}(\boldsymbol{r}) &= \boldsymbol{Q}_A(\boldsymbol{r}) + {\sum_{m,n}}' b_{m,n} \frac{\hat{\boldsymbol{z}} \wedge \boldsymbol{k}_{m,n}}{\boldsymbol{k}_{m,n}^2} \sin \boldsymbol{k}_{m,n}\boldsymbol{r} \\
\eta(\boldsymbol{r}) &= {\sum_{m,n}}' c_{m,n}(1-\cos \boldsymbol{k}_{m,n}\boldsymbol{r}) \\
\sigma(\boldsymbol{r}) &= {\sum_{m,n}}' d_{m,n}(1-\cos \boldsymbol{k}_{m,n}\boldsymbol{r}),
\end{aligned} \tag{3.31}$$

where the primed sum stands for summation over all $(m,n) \neq (0,0)$. $\boldsymbol{Q}_A$ is the gauge invariant velocity field of an s-wave Abrikosov solution, which satisfies

$$\boldsymbol{\nabla} \wedge \boldsymbol{Q}_A = \left(\bar{B} - \Phi_0 \sum_{i,j} \delta^{2D}(\boldsymbol{r} - \boldsymbol{R}_{i,j}) \right) \hat{\boldsymbol{z}}. \tag{3.32}$$

The singular contribution comes from the vortex phase field and produces a vanishing average rotation of $\boldsymbol{Q}$ and $\boldsymbol{Q}_A$. Further we have $\boldsymbol{\nabla}\boldsymbol{Q} = \boldsymbol{\nabla}\boldsymbol{Q}_A = 0$. As initial condition for the minimization we use the Abrikosov solution near B_{c2} for the main order parameter component and the B-field, and zero for the admixed component (see App. B, Refs. [63, 64]).

The above set of equations leads to a very efficient minimization algorithm for s-waves[60]. For p-waves, the first few iterations also converge very fast towards the physical solution, however further iteration leads in most cases to oscillations between several locally minimal solutions. We use therefore the first few Brandt minimization

steps only to obtain good initial solutions for a conventional GL minimization scheme (see App. B).

3.4.2 Minimization of Gibbs free energy

An expansion in reciprocal vectors of a fixed vortex lattice geometry as it was performed above assumes a knowledge of the mean penetrating field $\bar{B}$. All length scales connected to the lattice unit cell are determined basically by $1/\sqrt{\bar{B}}$. However, in typical experiments measuring vortex lattice properties, the externally applied field H is controlled rather than $\bar{B}$, which means that the Gibbs free energy has to be minimized. Generalizing the scaling argument to the p-wave case, which was presented originally for s-waves by Doria *et al.*[61, 62], we deduce a simple equation governing the average field $\bar{B}$. Together with the Ginzburg-Landau equations of the last section, the minimization of the Gibbs free energy is then possible.

We start with a typical Ginzburg-Landau free energy per volume

$$F(\boldsymbol{\psi}(\boldsymbol{x}), \boldsymbol{A}(\boldsymbol{x}), \bar{B}) = \frac{1}{V}\int_V d^3\boldsymbol{x}\left(f^2(\boldsymbol{\psi}(\boldsymbol{x})) + f^4(\boldsymbol{\psi}(\boldsymbol{x})) + f^{kin}(\boldsymbol{D}\boldsymbol{\psi}(\boldsymbol{x})) + B(\boldsymbol{x})^2\right) \tag{3.33}$$

where f^2, f^4 are quadratic and fourth order terms in the order parameters and f^{kin} denotes the second order gradient term. Be aware that this free energy depends on the multi-component order parameter $\boldsymbol{\psi}(\boldsymbol{x})$, the vector potential $\boldsymbol{A}(\boldsymbol{x})$ and the mean field $\bar{B}$, provided that the form of the vortex lattice is given. We perform the following scaling transformation

$$\begin{aligned} \boldsymbol{x} &\rightarrow \frac{\boldsymbol{x}}{\lambda} \equiv \boldsymbol{x}' \\ \psi_\lambda(\boldsymbol{x}') &= \psi(\lambda\boldsymbol{x}') \\ \boldsymbol{A}_\lambda(\boldsymbol{x}') &= \lambda\boldsymbol{A}(\lambda\boldsymbol{x}'). \end{aligned} \tag{3.34}$$

It can be shown[61, 62], that $\bar{B}$ (defined as a contour integral and thus basically a topological quantity) transforms as

$$\bar{B}_\lambda = \lambda^2\bar{B}. \tag{3.35}$$

Under this transformation, the GL free energy is

$$\begin{aligned} F(\psi_\lambda(\boldsymbol{x}), \boldsymbol{A}_\lambda(\boldsymbol{x}), \bar{B}_\lambda) &= \frac{1}{V'}\int_{V'} d^3\boldsymbol{x}'\Big(f^2(\psi_\lambda(\boldsymbol{x}')) + f^4(\psi_\lambda(\boldsymbol{x}')) \\ &\quad + \frac{1}{\lambda^2}f^{kin}(\boldsymbol{D}_\lambda\psi_\lambda(\boldsymbol{x}')) + \frac{1}{\lambda^4}B_\lambda(\boldsymbol{x}')^2\Big). \end{aligned} \tag{3.36}$$

The functional form of F has changed only in the prefactors $1/\lambda^2$ and $1/\lambda^4$ and the fact that $\bar{B} \to \bar{B}_\lambda = \lambda^2 \bar{B}$. On the other hand, the constrained minimum is still the same by construction. Thus, differentiation with respect to λ leads to

$$0 = -2F^{kin} - 4F^{field} + \frac{\partial F}{\partial \bar{B}} 2\bar{B}, \tag{3.37}$$

and together with the thermodynamic relation

$$H = \frac{1}{2}\frac{\partial F}{\partial \bar{B}} \tag{3.38}$$

we obtain

$$\bar{B} = \frac{1}{2H}(F^{kin} + 2F^{field}) = \frac{1}{2H}(2F^{field} - F^2 - 2F^4). \tag{3.39}$$

The last equation makes use of $F^{tot} = F^2 + F^4 + F^{kin} + F^{field}$ and $F^{tot} = -F^4 + F^{field}$ (see Eq. (B.7)). To find the minimal vortex lattice configuration for given applied field H, we have to minimize the Gibbs free energy

$$G = \frac{1}{V_{uc}} \int_{V_{uc}} d^3\boldsymbol{x} \left(f(\psi(\boldsymbol{x}), \boldsymbol{D}\psi(\boldsymbol{x}), B(\boldsymbol{x}), \bar{B}) - 2HB(\boldsymbol{x}) \right) = F - 2H\bar{B}. \tag{3.40}$$

Compared to the case with constant $\bar{B}$, we have identical Ginzburg-Landau equations for $\psi(\boldsymbol{x})$ and $\boldsymbol{A}(\boldsymbol{x})$, and an additional equation for $\bar{B}$

$$\frac{\partial G}{\partial \bar{B}} = \frac{\partial}{\partial \bar{B}} F - 2H. \tag{3.41}$$

Using Eq. (3.37), we find

$$\frac{\partial G}{\partial \bar{B}} = \frac{F^{kin}}{\bar{B}} + 2\frac{F^{field}}{\bar{B}} - 2H, \tag{3.42}$$

and the Gibbs-GL equation for $\bar{B}$ can thus be written as

$$F^{kin} + 2\langle B^2 \rangle - 2H\bar{B} = 0. \tag{3.43}$$

This equation, which governs the average size of the magnetic field when the applied field H is given, completes the set of Ginzburg-Landau equations given in the last section.

3.4.3 Results

Recently, the group of E. M. Forgan[39, 40, 41] has performed measurements of higher order Bragg reflections from the scattering of neutrons from the flux line lattice of Sr_2RuO_4 (see Fig. 3.11). In earlier experiments, they found a square lattice in the whole temperature and field range. Due to an alignment error, the orientation of this

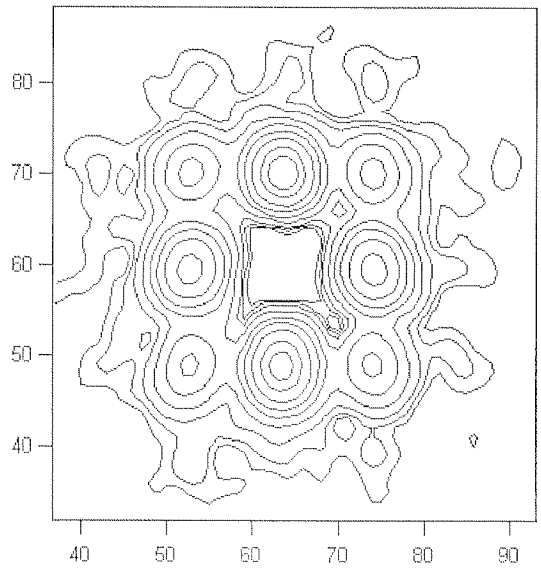

Figure 3.11: Contour plot of the small angle neutron scattering results for the flux line lattice of Sr_2RuO_4 at $H = 20$mT and $T = 100$mK[41]. The [110] axis of the crystal is parallel to the vertical axis of the plot.

square lattice was first claimed to be parallel to the crystal lattice[39]. Later, this error was corrected and the lattice was found to be rotated by 45° with respect to the crystal lattice[40, 41]. The following discussion of exact higher order Fourier components is therefore restricted to this specific symmetry of the vortex lattice. (Note that our results are still symmetric under simultaneous change of sign of ν and rotation of the vortex lattice by 45°.) Given a reciprocal lattice vector $\boldsymbol{k}_{m,n}$ (see Appendix B), the corresponding diffracted neutron Bragg peak has an integrated intensity $I_{m,n}$

$$I_{m,n} \propto \frac{|F_{m,n}|^2}{|\boldsymbol{k}_{m,n}|}, \tag{3.44}$$

where $F_{m,n}$ is a spatial Fourier component of the local B field

$$B(\boldsymbol{r}) = \sum_{m,n} F_{m,n} e^{i\boldsymbol{k}_{m,n}\boldsymbol{r}}. \tag{3.45}$$

In the Abrikosov solution for a single component Ginzburg-Landau (SC-GL) theory near the upper critical field H_{c2}, these coefficients are given for a square lattice by

$$F^A_{m,n} \propto -(-1)^{m^2+mn+n^2} e^{-\pi\frac{(m^2+n^2)}{2}} \tag{3.46}$$

and decay very quickly, whereas the single component London solution valid for large κ and lower fields leads to

$$F^L_{m,n} \propto \frac{1}{1+\boldsymbol{k}^2_{m,n}}. \tag{3.47}$$

Model	$I_{1,1}/I_{1,0}$	$I_{2,0}/I_{1,0}$	$I_{2,1}/I_{1,0}$
London (SC)	0.1768	0.0313	0.0179
Abrikosov (SC)	0.0306	0.00004	0.000002
SC-GL ($B = 20$ mT)	0.0783	0.00091	0.000298
TC-GL near B_{c2} ($\nu = 0.0$)	0.2263	0.00552	0.00056
TC-GL near B_{c2} ($\nu = -0.2$)	0.4205	0.00222	0.00113
TC-GL ($B = 20$ mT), best fit	0.1658	0.00018	0.00093
Exp. ($B = 20$ mT, $T = 100$ mK)	0.197(2)	0.011(3)	0.007(1)

Table 3.1: Neutron scattering intensities from several theoretical models compared to the experimental values[41]. The single component (SC) models have generally very small intensities, whereas the two component GL (TC-GL) solutions show satisfactory agreement at least in the lowest order Bragg peaks.

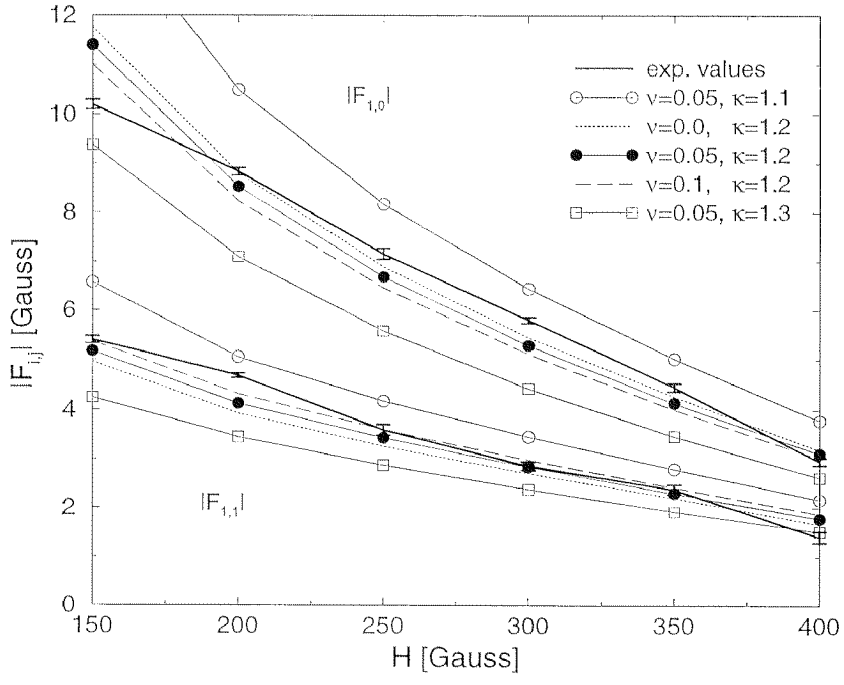

Figure 3.12: Numerical results for Fourier components $F_{1,0}$ and $F_{1,1}$ of local B-field versus applied field H compared with the measured values (thick lines). The set of lines with $\kappa = 1.2$ fits the experiments best, the dependence on ν is only weak.

Using the exact numerical solution for the single component case at intermediate fields[60], more realistic values for intermediate fields can be calculated. Specific values for such a single component GL theory at field $H = 20$mT are given in Ta-

ble 3.1. Within the two component order parameter theory (TC-GL) for Sr_2RuO_4, Agterberg[45, 58] determined the solution near the upper critical field, corresponding to the Abrikosov solution for s-waves. With our solution of the full Ginzburg-Landau problem, we could calculate the Fourier components of the B-fields at arbitrary applied field H and could do a systematic fit in the parameters κ and ν. The results of Agterberg's calculations as well as our best fit values are displayed in Table 3.1. For our fit, we used the experimental values for the Fourier components $F_{1,0}$ and $F_{1,1}$ at $T = 100\text{mK}$ and applied fields $H = 15, 20, \ldots, 40\text{mT}$. In Fig. 3.12 we show the results for the unrescaled Fourier components $F_{1,0}$ and $F_{1,1}$ compared with the experimental values (thick line). The unrescaled Fourier components depend more strongly on κ rather than on ν, and the comparison with the experiment suggests a value $\kappa \approx 1.2$. On the other hand, the rescaled Fourier coefficients $|F_{1,1}|/|F_{1,0}|$ turned out to be more sensitive to changes in ν. Comparing with the experimental results leads to a very small value of $\nu \lesssim 0.05$ (see Fig. 3.13). We did not include higher order Fourier

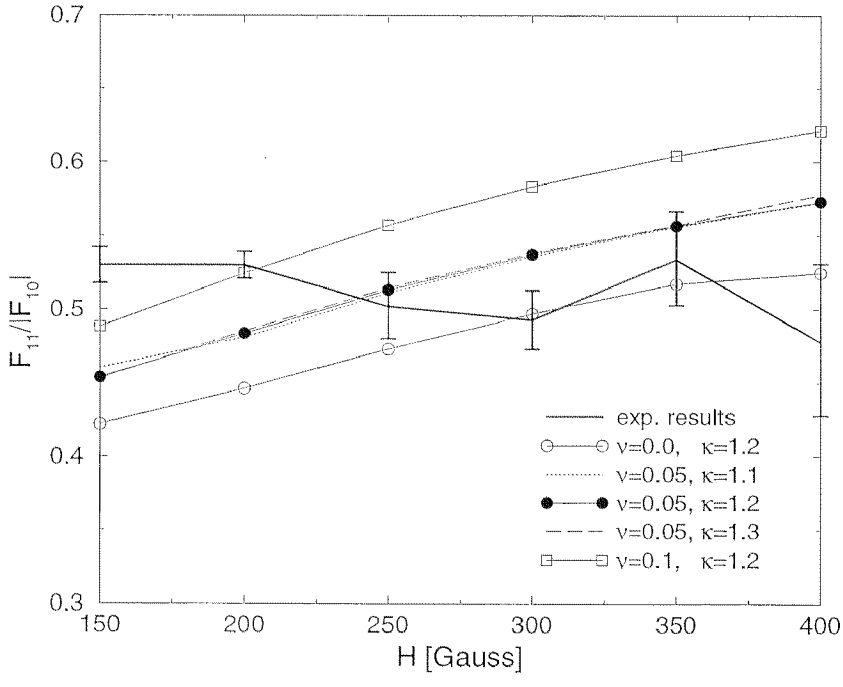

Figure 3.13: Numerical results for the ratio $F_{1,1}/|F_{1,0}|$ versus applied field H compared with the measured values (thick line). Determining the anisotropy parameter ν in the higher field region where our results are expected to describe the experiments best leads to a value $\nu \lesssim 0.05$. The dependence on κ is very weak.

components into our fitting. Although the numerical results reproduce the measured values qualitatively and also quantitatively very well, there are some drawbacks to these results. From Table 3.1 we learn that the results for higher order Bragg peaks

are generally much too small for TC-GL theories. In our results, the $(2,0)$ peak is even more suppressed than in the H_{c2} results of Agterberg. As can be seen from Fig. 3.14, this is due to a sign change: in all two component theories, the sign of $F_{2,0}$ for high fields is negative, whereas for fields near H_{c1} the London signs are valid (positive signs for all components). In our best fit results, we are exactly in the intermediate field

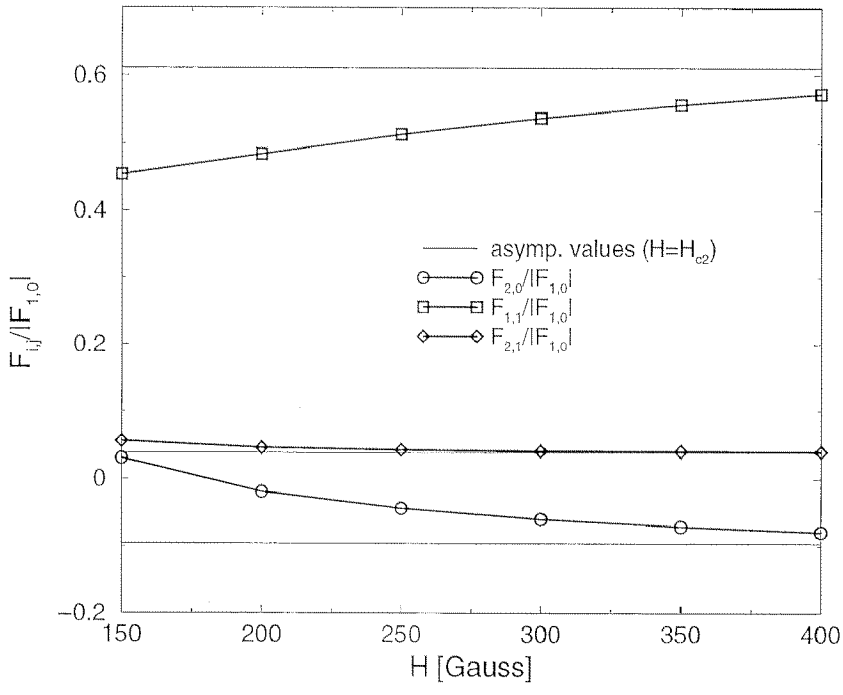

Figure 3.14: Numerical results for the ratios $F_{1,1}/|F_{1,0}|$, $F_{2,0}/|F_{1,0}|$ and $F_{2,1}/|F_{1,0}|$ versus applied field H compared with the asymptotic values for applied field $H \approx H_{c2}$ (solid lines). The parameters used are $\nu = 0.05$ and $\kappa = 1.2$.

region where the $(2,0)$ component is almost zero. The second drawback concerns the low field results. It turned out, that in the experiments, there is basically no difference between applied field H and mean penetrating field $\bar{B}$ also at low applied fields. This is most probably due to vortex pinning, which prevents an adjustment to the thermodynamic equilibrium state in the field cooled samples. Our numerical results however are thermally equilibrated solutions and show marked suppression of $\bar{B}$ for low external fields ($H \lesssim 20$mT). While this discrepancy certainly influences the quantitative comparison of our results to this specific experiment for the lowest fields, the results obtained from fitting in the high field region are not affected. An interesting detail in this context is, that our calculations show the transition to the Meissner state at fields $10\text{mT} \lesssim H < 15\text{mT}$. Recent measurements[65] point towards an experimental result of the same size, in accordance with earlier estimates ($H_{c1||c} = 11$mT[66].) A reconstruction of the local B-field shows, that the two component solutions are also

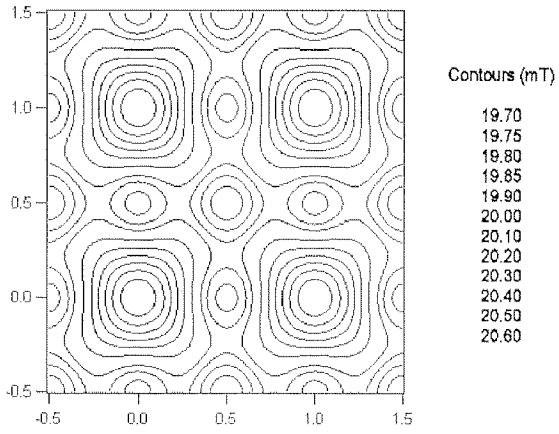

a) Experimental values at $H = 20\text{mT}$, $T = 100\text{mK}$

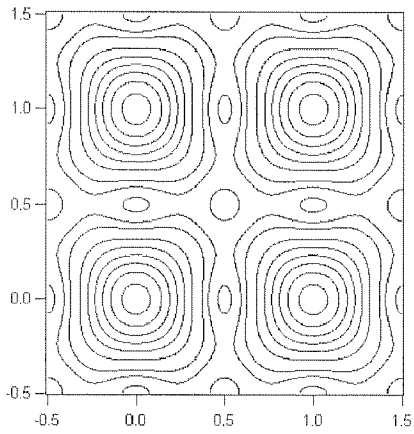

b) Two-component GL (TC-GL) values at $H = 20\text{mT}$, $T = 100\text{mK}$

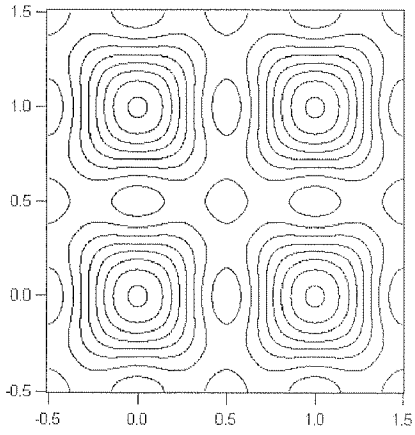

c) TC-GL-values at H_{c2} for $\nu = 0.0$

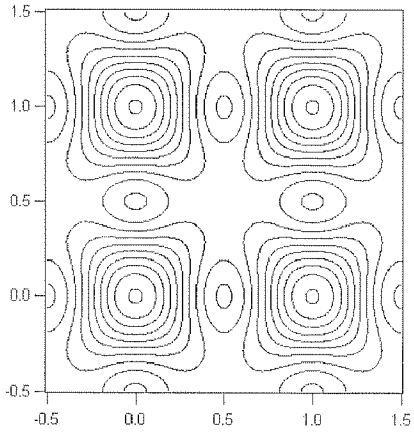

d) TC-GL-values at H_{c2} for $\nu = 0.2$

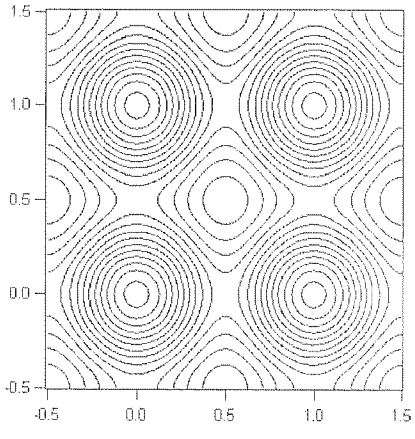

e) Abrikosov solution for a single component order parameter

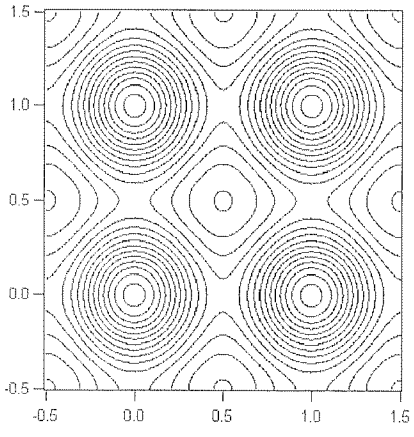

f) Brandt values at for single component GL theory at $H = 20\text{mT}$

Figure 3.15: Different fits for experimental B-field distributions.

qualitatively quite different from single component solutions (Fig. 3.15). While in the latter case the minimum field points lies in the center of a square of four vortices, in the two component case it lies between adjacent vortices. This feature is qualitatively independent of the anisotropy parameter ν and can thus be regarded as inherent to this two component model. These intervortex minima are even more prominent in the reconstruction of the experimental data, which is a strong point in favor of a two component theory.

3.5 Conclusion

We have investigated the single vortex and vortex lattice structure of Sr_2RuO_4, assuming a weak-coupling, clean limit description of the 2D odd-parity Γ_{5u}^- symmetry of the superconducting state in Sr_2RuO_4. Assuming the leading order parameter to be η_-, the stable single vortex solution (denoted $(1,-1)$) takes the asymptotic form $(\eta_+,\eta_-) = (p(r)e^{i\theta},[1-m(r)]e^{-i\theta})$. A second low energy vortex solution has the asymptotic form $(\eta_+,\eta_-) = (p(r)e^{3i\theta},[1-m(r)]e^{i\theta})$ (denoted $(3,1)$). Solutions of the latter type appear to be the minimal ones for d-wave superconductors with an admixed s-wave component. Here, the symmetry allows for the competing $(1,-1)$-solution which has lower energy as it has reduced currents, contains fewer nodes and decays slower near the vortex core. The stable $(1,-1)$-solution shows clear four-fold deformations due to the anisotropy of the density of states at the Fermi surface. Current experimental results on the vortex lattice structure point towards an elongation of the vortex along the crystal lattice axes, in agreement with our theoretical analysis. A direct proof of such a structure should be observable through STM measurements.

The structure of the vortex lattice near H_{c1} has been determined using an extended London approach where the admixed η_+ component has been integrated out. The resulting London theory predicts that with increasing field the vortex lattice will continuously deform from a hexagonal to a square lattice. The orientation of the square vortex lattice depends on the anisotropy parameter ν: For $\nu < 0$ the square vortex lattice is aligned with the crystal lattice whereas for $\nu > 0$ the orientation of the vortex lattice is rotated by 45°. Comparing to recent experimental results of Kealey *et al.*[40, 41], who found the vortex and crystal lattices misaligned by an angle of 45° in almost the entire field range, we conclude that $\nu > 0$. The second order hex-to-square transition should be observable through Bitter decoration experiments. An alternative signature of this transition is given through the splitting in the peak of the field distribution $P(B)$. These field distributions should be observable in μSR experiments.

Finally, the detailed structure of the square vortex lattice at arbitrary applied fields

$H_{c1} < H < H_{c2}$ was examined using a full Ginzburg-Landau approach. Calculating the Fourier components of the local B-field for several applied fields H, we determined the free parameters κ and ν by fitting to experimental results[41]. The most promising values are $\kappa \approx 1.2$ and $\nu \lesssim 0.05$. Experimental results for κ obtained from determining λ and ξ range from $\kappa \approx 1.2$[66, 67] to $\kappa \approx 1.9$[39]. (Note that the result $\kappa_{exp} = 2.6$ obtained in the latter publication within the framework of an s-wave superconductor has to be corrected by a factor $\sqrt{e_H} \approx 0.74$[58]). The calculated value for the anisotropy parameter ν is still a matter of controversy[51, 52]. Although the detailed comparison between experiment and our calculation may be influenced by the presence of vortex pinning in the experiments, the structure of the local B-field distribution shows the same qualitative features in the experiments as in our numerical results. Since this is not true for single component Ginzburg-Landau theories, this makes for a strong point in favor of the two-component theory.

Chapter 4

Quasiparticles in p-Wave Vortex Cores

4.1 Introduction

While the two-component Ginzburg-Landau theory for p-wave superconductors has intensively been studied in the last years and has been shown to describe the experimental findings at least qualitatively well, the properties of quasiparticle excitations in the vortex core have not gained much attention. In the s-wave case, extensive quasiclassical ($k_F\xi_0 \gg 1$) and quantum limit ($k_F\xi_0 \gtrsim 1$) calculations have successfully explained many features found by scanning tunneling microscopy (STM) measurements. We present in this chapter a self-consistent solution of the Bogoliubov-de Gennes vortex problem for a p-wave superconductor near the quantum limit.

In 1968, Eilenberger[68] managed to overcome the substantial complexities the Gorkhov theory poses for the solution of spatially inhomogeneous situations by transforming the Gorkhov equations into a set of first-order equations, later usually referred to as Eilenberger or quasiclassical equations. This was done through integrating out the energy variable of the Green's function. Many important quantities as for example currents, local density of states, or the order parameter can be determined from this quasiclassical approach, as long as the parameter $k_F\xi_0 \gg 1$. This method was later used by Kramer and Pesch[69] to determine the detailed structure of the s-wave vortex core numerically, finding that the effective vortex core size ξ_1 is substantially suppressed for low temperatures compared with the BCS-coherence length $\xi_0 = v_F/\Delta_0$. This work contrasted an earlier analytical approach by de Gennes, Caroli and Matricon[70, 71], who assumed the coherence length to be temperature-independent and found analytically the famous low energy level spectrum in the s-wave vortex core $E_n = \omega_0(n + \frac{1}{2})$ with $n = 0, 1, 2, \ldots$ and the minigap $\omega_0 \sim \Delta_0^2/E_F$.

Kramer and Pesch suggested this minigap to be modified by a factor $\propto \ln \xi_0/\xi_1$ due to the vortex core narrowing. In the early years of this decade, the beautiful series of STM experiments on $NbSe_2$ by Hess and coworkers[72, 73, 74] gave a strong new impact to the field. They measured local density of states (LDOS) patterns which showed clear zero bias peaks at the vortex cores which split up into two peaks at higher energies upon leaving the vortex core center. At the same time, the problem of an isolated vortex was reexamined numerically within Bogoliubov-de Gennes theory first by Shore *et al.*[75] who managed to explain the zero bias peak, and later in a beautiful work by Gygi and Schlüter[76, 77]. Determining the electronic properties of an isolated vortex core fully self-consistently at intermediate values $k_F\xi_0 \approx 40$, they could verify the earlier quasiclassical calculations about the Kramer-Pesch effect, finding also a strong reduction of the vortex core size at low temperatures. Their results for the LDOS profile using the parameters of the experiment was qualitatively very satisfying. Adding sixfold perturbations to the crystal potential and vector field[78], they obtained a good agreement with the sixfold starlike LDOS patterns measured by Hess *et al.*. These successes initiated further work in the field. Using quasiclassical theory, Hayashi *et al.*[79, 80] presented a more detailed analysis of the tunneling conductance in $NbSe_2$. To explain finer details in the measured LDOS such as a splitting of the lobes of the starlike LDOS pattern and several additional ridges, they introduced a sixfold gap-anisotropy (anisotropic s-wave pairing), which was showed to be crucial for the reproduction of these effects. In a different work, they considered also the situation in the vortex lattice[81]. Very recently, the earlier work of Gygi *et al.* was reexaminated very close to the quantum limit in a more systematic way by Hayashi and coworkers[82, 83]. They show a detailed study of the Kramer-Pesch effect at very low $k_F\xi_0$ and temperatures.

An interesting new aspect in the discussion of s-wave vortices is a possible vortex charging effect[84, 85]. Blatter *et al.*[86] pointed out, that for an s-wave superconductor with particle-hole asymmetry, the main contribution to the vortex charge is proportional to the slope of the density of states at the Fermi level. Assuming a 3D parabolic dispersion, they determined the line charge accumulation within a vortex core of size ξ to be of the order $Q \sim ek_F(\lambda_{TF}/\xi)^2$, where $1/k_F$ enters the expression as typical value for the interlayer spacing. In a later work, Hayashi *et al.*[87] calculated vortex charges within the Bogoliubov-de Gennes formalism self-consistently for a single vortex line without screening. Working in two dimensions with a dispersion with vanishing slope of the density of states, they considered the vortex charge to be mainly determined by the detailed electronic structure in the vortex core, at least for the small values of $k_F\xi_0$ used in their calculation.

For the nodeless p-wave superconductors as discussed in the context of Sr_2RuO_4 (*cf.* Chapter 3), the interest in electronic properties arose only recently. Pioneer-

ing work on the low energy excitations was done in the context of the superfluid ^{3}He-A phase[88]. Volovik used Sommerfeld quantization on a quasiclassical fundament to show that the low energy spectrum for p-wave superconductors with vorticity ± 1 has the form $E_n = \omega_0 n$ rather than $E_n = \omega_0(n + \frac{1}{2})$ as for the s-wave case. The expression for the minigap ω_0 is formally the same in both cases and depends only on the specific radial form and size of the dominant order parameter and on k_F and ξ. Within Bogoliubov-de Gennes theory, a non-selfconsistent calculation for the isolated vortex was presented recently by Matsumoto and Sigrist[89]. The authors showed, that in principle a distinction of s- and p-wave superconductivity is possible through chiral optical absorption measurements. Very recently, several authors pointed out that in addition to the GL-free energy density presented in the last sections, P- and T-violating terms in the electromagnetic potentials are important for p-wave superconductors[90, 91, 92, 93]. These contributions are bilinear in the electromagnetic potentials and of first order in derivative and are equivalent to the Chern-Simons terms in the static limit. For time-reversal breaking gap functions, unusual couplings between charge, current and the electromagnetic potentials are expected[93]. Goryo pointed out[90, 91, 92], that these Chern-Simons terms lead to an exactly quantized vortex charge of size $-ne/4$, where n is the vorticity of the dominant order parameter. Since this charge depends on the sign of the vorticity, it should be distinguishable from other vortex charging effects as for example due to the zero energy state[94]. However, within the light that the total vortex charge is zero, it is rather questionable whether this concept of fractional charge is meaningful in the context of p-wave superconductors.

In the following chapters, we present a numerical self-consistent investigation of the isolated p-wave vortex core within the two-component order parameter theory of Agterberg[50, 45, 58] near the quantum limit. Since the parameter $k_F\xi_0$ for Sr_2RuO_4 is believed to be large (of the order of 1000), our work does certainly not give quantitative predictions for this specific material. However, on a more qualitative level we believe to gain a closer insight into the consequences of the p-wave symmetry of the order parameter on the electronic properties of an isolated vortex line. Note that we use throughout the whole chapter the convention $e = |e|$.

4.2 Bogoliubov-de Gennes formalism

We start with the textbook effective hamiltonian for interacting electrons[95]. Defining the mean-field gap function in the usual way following *e. g.* Ref. [95], we obtain after

a standard Bogoliubov transformation the generic Bogoliubov-de Gennes equations

$$\begin{pmatrix} h_0(\boldsymbol{r})\hat{\sigma}_0\hat{u}_n(\boldsymbol{r}) + \int d^3\boldsymbol{r}'\hat{\Delta}(\boldsymbol{r},\boldsymbol{r}')\hat{v}_n(\boldsymbol{r}') \\ \int d^3\boldsymbol{r}'\hat{\Delta}^\dagger(\boldsymbol{r}',\boldsymbol{r})\hat{u}_n(\boldsymbol{r}') - h_0^*(\boldsymbol{r})\hat{\sigma}_0\hat{v}_n(\boldsymbol{r}) \end{pmatrix} = E_n \begin{pmatrix} \hat{u}_n(\boldsymbol{r}) \\ \hat{v}_n(\boldsymbol{r}) \end{pmatrix}, \tag{4.1}$$

where $h_0(\boldsymbol{r})$ is the single particle hamiltonian, $\hat{u}_n, \hat{v}_n$ are the space dependent Bogoliubov transformation matrices between particle and quasiparticle operators, and $\hat{\sigma}_0$ denotes the unit matrix. The gap matrix $\hat{\Delta}(\boldsymbol{r},\boldsymbol{r}')$ is defined as mean field pairing wavefunction in real space ($\Psi(\boldsymbol{r},s)$ being the usual electron field operator)

$$\Delta_{ss'}(\boldsymbol{r},\boldsymbol{r}') = \sum_{s_3,s_4} V_{s',s,s_3,s_4}(\boldsymbol{r},\boldsymbol{r}')\langle\Psi(\boldsymbol{r}',s_3)\Psi(\boldsymbol{r},s_4)\rangle. \tag{4.2}$$

As demonstrated in the introduction (*cf.* Chapter 1), the spin properties of the spin singlet case (s-, d-wave) as well as the triplet case with $s_z = 0$ (p-wave for Sr_2RuO_4) can be described by an off-diagonal gap matrix

$$\hat{\Delta}(\boldsymbol{r},\boldsymbol{r}') = \begin{pmatrix} 0 & \Delta(\boldsymbol{r},\boldsymbol{r}') \\ \pm\Delta(\boldsymbol{r},\boldsymbol{r}') & 0 \end{pmatrix}, \tag{4.3}$$

where the upper (lower) sign stands for the triplet (singlet) state. Due to the special form of the gap matrix, and making use of the spin reversal symmetry, the Bogoliubov-de Gennes equations can be considerably simpified to the form

$$\begin{pmatrix} h_0(\boldsymbol{r})u_n(\boldsymbol{r}) + \int d^3\boldsymbol{r}'\Delta(\boldsymbol{r},\boldsymbol{r}')v_n(\boldsymbol{r}') \\ \mp\int d^3\boldsymbol{r}'\Delta^*(\boldsymbol{r},\boldsymbol{r}')u_n(\boldsymbol{r}') - h_0^*(\boldsymbol{r})v_n(\boldsymbol{r}) \end{pmatrix} = E_n \begin{pmatrix} u_n(\boldsymbol{r}) \\ v_n(\boldsymbol{r}) \end{pmatrix}, \tag{4.4}$$

where the single particle hamiltonian is given through

$$h_0(\boldsymbol{r}) = \frac{1}{2m}\left(\frac{\hbar}{i}\boldsymbol{\nabla} + \frac{e}{c}\boldsymbol{A}(\boldsymbol{r})\right)^2 - E_F - e\Phi(\boldsymbol{r}). \tag{4.5}$$

We have used the relation $\Delta^*(\boldsymbol{r}',\boldsymbol{r}) = -\Delta^*(\boldsymbol{r},\boldsymbol{r}')$. Zeeman-terms have been neglected in all cases investigated below. This form of the Hamiltonian is valid for both triplet and singlet superconductors as long as the gap matrix in spin-space is off-diagonal. Again, the upper (lower) sign corresponds to the p-wave (s/d-wave). We assume for the interaction potential a universal form

$$V_{s',s,s_3,s_4}(\boldsymbol{r},\boldsymbol{r}') = \frac{1}{2}V_s(\boldsymbol{r},\boldsymbol{r}')(\delta_{s',s_4}\delta_{s,s_3} - \delta_{s',s_3}\delta_{s,s_4}) + \frac{1}{2}V_t(\boldsymbol{r},\boldsymbol{r}')(\delta_{s',s_4}\delta_{s,s_3} + \delta_{s',s_3}\delta_{s,s_4}), \tag{4.6}$$

where the potentials V_s and V_t for the singlet and triplet case have the form

$$V_{s,t}(\boldsymbol{r},\boldsymbol{r}') = v_0 f_l(\boldsymbol{r},\boldsymbol{r}'), \tag{4.7}$$

where $v_0 = |v_0|$ stands for the interaction strength and the index l for the type of superconductivity (s = s-wave, d = d-wave, p = p-wave). Inserting the Bogoliubov transformations into the self-consistency relation and thus expressing it in terms of the quasiparticle wavefunctions, we obtain

$$\begin{aligned}\Delta(\boldsymbol{r},\boldsymbol{r}') &= \frac{v_0}{2} f_l(\boldsymbol{r},\boldsymbol{r}') \sum_n \Big(\mp u_n(\boldsymbol{r}) v_n^*(\boldsymbol{r}') + v_n^*(\boldsymbol{r}) u_n(\boldsymbol{r}') \Big) \tanh\left(\frac{\beta E_n}{2}\right) \\ &\equiv v_0 f_l(\boldsymbol{r},\boldsymbol{r}') D(\boldsymbol{r},\boldsymbol{r}') \end{aligned} \tag{4.8}$$

where the plus sign stands for p-waves and the minus sign for s/d-waves.

We assume now a model potential of the form $V_{s,t}(\boldsymbol{r},\boldsymbol{r}') = v_0 f_l(\boldsymbol{\rho})$ where $\boldsymbol{\rho} = \boldsymbol{r} - \boldsymbol{r}'$ is the relative coordinate, with

$$\begin{aligned} f_s(\boldsymbol{\rho}) &= \textstyle\sum_{\boldsymbol{k}} e^{i\boldsymbol{\rho}\boldsymbol{k}} &&= \frac{V}{(2\pi)^3} \int d^3\boldsymbol{k}\; e^{i\boldsymbol{\rho}\boldsymbol{k}} \\ f_p(\boldsymbol{\rho}) &= \textstyle\sum_{\boldsymbol{k}} e^{i\boldsymbol{\rho}\boldsymbol{k}} \frac{\boldsymbol{k}^2}{2k_F^2} &&= \frac{V}{(2\pi)^3} \int d^3\boldsymbol{k}\; e^{i\boldsymbol{\rho}\boldsymbol{k}} \frac{\boldsymbol{k}^2}{2k_F^2} \\ f_d(\boldsymbol{\rho}) &= \textstyle\sum_{\boldsymbol{k}} e^{i\boldsymbol{\rho}\boldsymbol{k}} \frac{(k_x^2-k_y^2)^2}{4k_F^4} &&= \frac{V}{(2\pi)^3} \int d^3\boldsymbol{k}\; e^{i\boldsymbol{\rho}\boldsymbol{k}} \frac{(k_x^2-k_y^2)^2}{4k_F^4} \end{aligned} \tag{4.9}$$

The detailed forms of the potentials have to be understood as a generic model. We concentrate on the derivation of the p-case, which shows all relevant techniques. A corresponding analysis of the s- and d-wave case is found in Appendix C.1.1. In order to obtain a Bogoliubov-de Gennes problem depending on one real-space coordinate only, we transform the self-consistency relation for the order parameter to center of mass coordinates in real space $\boldsymbol{R}$ and relative coordinates in Fourier space $\boldsymbol{k}$. After Fourier transformation in the relative coordinate $\boldsymbol{\rho}$, we obtain for the above p-wave model potential ($\boldsymbol{\nabla}_{1,2}$ denotes the derivative of $D(\boldsymbol{R},\boldsymbol{R})$ with respect to the first/second argument)

$$\begin{aligned}
&\Delta_p(\boldsymbol{R},\boldsymbol{k}) = \\
&= \frac{1}{V}\int d^3\boldsymbol{\rho}\; \Delta_p(\boldsymbol{r},\boldsymbol{r}') e^{-i\boldsymbol{\rho}\boldsymbol{k}} \\
&= \frac{v_0}{(2\pi)^3}\int d^3\boldsymbol{\rho}\; d^3\boldsymbol{k}'\; \frac{\boldsymbol{k}'^2}{2k_F^2} e^{i\boldsymbol{\rho}\boldsymbol{k}'} D(\boldsymbol{R}+\frac{1}{2}\boldsymbol{\rho},\boldsymbol{R}-\frac{1}{2}\boldsymbol{\rho}) e^{-i\boldsymbol{\rho}\boldsymbol{k}} \\
&= \frac{v_0}{(2\pi)^3}\int d^3\boldsymbol{\rho}\; d^3\boldsymbol{k}'\; \frac{\boldsymbol{k}'^2}{2k_F^2} e^{i\boldsymbol{\rho}\boldsymbol{k}'} \left(1+\frac{1}{2}\boldsymbol{\rho}\boldsymbol{\nabla}_1 - \frac{1}{2}\boldsymbol{\rho}\boldsymbol{\nabla}_2 + O(\rho^2\partial_i\partial_j)\right) D(\boldsymbol{R},\boldsymbol{R}) e^{-i\boldsymbol{\rho}\boldsymbol{k}} \\
&= \frac{v_0}{(2\pi)^3}\int d^3\boldsymbol{\rho}\; d^3\boldsymbol{k}'\; \left(1+(\boldsymbol{\nabla}_1-\boldsymbol{\nabla}_2)\frac{i\boldsymbol{\nabla}_k}{2} + O\Big(i^2\partial_{k_i}\partial_{k_j}\partial_i\partial_j\Big)\right) D(\boldsymbol{R},\boldsymbol{R}) \frac{\boldsymbol{k}'^2}{2k_F^2} e^{i\boldsymbol{\rho}(\boldsymbol{k}'-\boldsymbol{k})} \\
&= v_0\left(\frac{\boldsymbol{k}^2}{2k_F^2} + \frac{i\boldsymbol{k}}{2k_F^2}(\boldsymbol{\nabla}_1-\boldsymbol{\nabla}_2) - \frac{1}{8k_F^2}\boldsymbol{\nabla}_1^2 - \frac{1}{8k_F^2}\boldsymbol{\nabla}_2^2 + \frac{1}{4k_F^2}(\boldsymbol{\nabla}_1\cdot\boldsymbol{\nabla}_2)\right) D(\boldsymbol{R},\boldsymbol{R}) \\
&= v_0 \frac{i\boldsymbol{k}}{2k_F^2}(\boldsymbol{\nabla}_1-\boldsymbol{\nabla}_2) D(\boldsymbol{R},\boldsymbol{R}).
\end{aligned} \tag{4.10}$$

In the last step, the even terms in $\boldsymbol{k}$ vanish because of the specific symmetry of the expression $D(\boldsymbol{R},\boldsymbol{R})$ due to the spin triplet interaction, and we obtain the desired form of the order parameter (Eq. (4.11)) as expected from symmetry classification (see Chapter 1). The two component order parameter $\boldsymbol{\eta}(\boldsymbol{R}) = (\eta_x(\boldsymbol{R}), \eta_y(\boldsymbol{R}))$ is thus defined through

$$\Delta_p(\boldsymbol{R},\boldsymbol{k}) \equiv \frac{1}{Vk_F}\boldsymbol{\eta}(\boldsymbol{R})\cdot\boldsymbol{k}. \tag{4.11}$$

Going over to the chiral combinations

$$\eta_\pm(\boldsymbol{R}) = \frac{1}{\sqrt{2}}\Big(\eta_x(\boldsymbol{R}) \pm i\eta_y(\boldsymbol{R})\Big), \tag{4.12}$$

this order parameter corresponds exactly to the order parameter dealt with in the Ginzburg-Landau calculations presented earlier (see Chapter 3). In terms of the quasiparticle amplitudes, this definition leads to the self-consistency relation ($\Box_\pm \equiv (\partial_x \pm i\partial_y)$)

$$\eta_\pm(\boldsymbol{R}) = -\frac{iV}{2\sqrt{2}k_F}v_0\sum_n\Big(v_n^*(\boldsymbol{R})\Box_\pm u_n(\boldsymbol{R}) - u_n(\boldsymbol{R})\Box_\pm v_n^*(\boldsymbol{R})\Big)\tanh\left(\frac{\beta E_n}{2}\right). \tag{4.13}$$

In the same manner we can transform also the off-diagonal integrals, which then read in the case of p-wave

$$\begin{aligned}
&\int d^3\boldsymbol{r}'\Delta_p(\boldsymbol{r},\boldsymbol{r}')v(\boldsymbol{r}') = \\
&= \frac{1}{(2\pi)^3}\int d^3\boldsymbol{r}'d^3\boldsymbol{k}\;\boldsymbol{\eta}(\boldsymbol{R})\frac{\boldsymbol{k}}{k_F}e^{i\boldsymbol{\rho}\boldsymbol{k}}v(\boldsymbol{r}') \\
&= \frac{1}{(2\pi)^3}\int d^3\boldsymbol{r}'d^3\boldsymbol{k}\;v(\boldsymbol{r}')\boldsymbol{\eta}(\boldsymbol{R})\frac{i\boldsymbol{\nabla}_{\boldsymbol{r}'}}{k_F}e^{i\boldsymbol{\rho}\boldsymbol{k}} \\
&= -\frac{i}{(2\pi)^3k_F}\int d^3\boldsymbol{r}'d^3\boldsymbol{k}\;e^{i\boldsymbol{\rho}\boldsymbol{k}}\left(v(\boldsymbol{r}')\frac{1}{2}(\boldsymbol{\nabla}\boldsymbol{\eta})\Big|_{\boldsymbol{R}} + \boldsymbol{\eta}(\boldsymbol{R})(\boldsymbol{\nabla}v)\Big|_{\boldsymbol{r}'}\right) \\
&= -\frac{i}{k_F}\left(v(\boldsymbol{r})\frac{1}{2}\boldsymbol{\nabla}\boldsymbol{\eta}(\boldsymbol{r}) + \boldsymbol{\eta}(\boldsymbol{r})\boldsymbol{\nabla}v(\boldsymbol{r})\right),
\end{aligned} \tag{4.14}$$

or, using the more convenient order parameters $\eta_\pm$

$$\int d^3\boldsymbol{r}'\Delta_p(\boldsymbol{r},\boldsymbol{r}')v(\boldsymbol{r}') = -\frac{i}{\sqrt{2}k_F}\sum_\pm\left(\eta_\pm(\boldsymbol{r})\Box_\mp + \frac{1}{2}\Big(\Box_\mp\eta_\pm(\boldsymbol{r})\Big)\right)v(\boldsymbol{r}). \tag{4.15}$$

The derivation presented above makes only sense, if it respects the gauge invariance. For the s-wave case, this is immediately clear, however for the higher order symmetries it is not obvious. In Appendix C.1.2, we show at the example of the p-wave case that gauge transformations commute with the gradient expansion performed above, and thus the gauge invariance is indeed respected.

4.2.1 Bogoliubov-de Gennes equations in center-of-mass coordinates

With the work done above we are ready to write down the full self-consistent problem. Since we want to discuss purely 2-dimensional problems, it is convenient to restrict to the xy-plane and neglect all z-dependencies. There are several possibilities to do this, either by enhancing m_z, which leads basically to a delta peak in density of states at $E_z = 0$, or by letting m_z go to zero, which (together with the energy cutoff) would allow only the $k_z = 0$ mode and thus lead to L_z-dependent results. In our approach, we basically follow the first method, taking into account the density of states in z-direction in all summations over the quasiparticle states as an additional factor $n_z = N_z/L_z$. Having the original quasiparticles normalized to unity (denoted here by $\tilde{u}, \tilde{v}$)

$$\int d^3\boldsymbol{r}\Big(|\tilde{u}_n(\boldsymbol{r})|^2 + |\tilde{v}_n(\boldsymbol{r})|^2\Big) = 1 \tag{4.16}$$

we change to quasiparticles normalized to unity in two dimensions ($\boldsymbol{x} = (x, y)$)

$$\begin{pmatrix} \tilde{u}_n(\boldsymbol{r}) \\ \tilde{v}_n(\boldsymbol{r}) \end{pmatrix} = \frac{1}{\sqrt{L_z}} \begin{pmatrix} 1 & 0 \\ 0 & e^{i\alpha} \end{pmatrix} \begin{pmatrix} u_n(\boldsymbol{x}) \\ v_n(\boldsymbol{x}) \end{pmatrix}. \tag{4.17}$$

The matrix transformation is purely for convenience, we choose $\alpha = 0$ for s- and d-waves and $\alpha = \pi/2$ for p-waves to get rid of imaginary parts. Additionally, we write the problem in dimensionless units, using the following scalings

$$\begin{aligned} E_{sc} &= |\Delta|_\infty(T = 0) \equiv \Delta_0 \\ x_{sc} &= \xi_0 = \frac{v_F}{\Delta_0} \\ A_{sc} &= \frac{\hbar e \mu_p n_z}{m\xi_0} \\ j_{sc} &= \frac{e\hbar n_z}{m\xi_0^3} \\ \Phi_{sc} &= \frac{e n_z}{\epsilon_p} \\ \rho_{sc} &= \frac{e n_z}{\xi_0^2}. \end{aligned} \tag{4.18}$$

Here Δ_0 denotes the spectral energy gap at zero temperature, ξ_0 is the BCS coherence length, and ϵ_p and μ_p dielectric constant and permeability, respectively. In addition, we have the relations

$$\begin{aligned} E_F^0 &\equiv \frac{k_F^2}{2mE_{sc}} = \frac{k_F}{2} \\ \frac{e}{\hbar c} A_{sc} &= \frac{1}{\lambda_L^2 n_s} \frac{1}{\xi_0} \equiv \gamma_A \frac{1}{\xi_0} \end{aligned}$$

$$e\Phi_{sc} = \frac{\xi_0^2}{\lambda_{TF}^2}\frac{1}{k_F\xi_0}\Delta_0 \equiv \gamma_\Phi E_F^0, \tag{4.19}$$

where n_s is the two dimensional electron density. The self-consistency relations for current and charge are derived directly from the $(\Phi, \boldsymbol{A})$-dependent part of the hamiltonian by variation with respect to $(\Phi, \boldsymbol{A})$

$$\begin{aligned}
\boldsymbol{j}(\boldsymbol{r}) &= -c\,\frac{\delta H_{\text{eff}}}{\delta \boldsymbol{A}(\boldsymbol{r})} \\
&= -\frac{e\hbar n_z}{2m\xi_0^3}\frac{1}{j_{sc}}\sum_n \left[u_n^*\left(\frac{\boldsymbol{\nabla}}{i}+\gamma_A\boldsymbol{A}\right)u_n f(E_n) + v_n\left(\frac{\boldsymbol{\nabla}}{i}+\gamma_A\boldsymbol{A}\right)v_n^*\Big(1-f(E_n)\Big)\right] \\
&\qquad\qquad +h.c. \\
&= -\frac{1}{2}\sum_n \left[u_n^*\left(\frac{\boldsymbol{\nabla}}{i}+\gamma_A\boldsymbol{A}\right)u_n f(E_n) + v_n\left(\frac{\boldsymbol{\nabla}}{i}+\gamma_A\boldsymbol{A}\right)v_n^*\Big(1-f(E_n)\Big)\right] + h.c. \\
\rho_e(\boldsymbol{r}) &= -c\frac{\delta H_{\text{eff}}}{\delta\Phi(\boldsymbol{r})} \\
&= -\frac{en_z}{\xi_0^2}\frac{1}{\rho_{sc}}\sum_n u_n^*u_n f(E_n) + v_n^*v_n\Big(1-f(E_n)\Big) \\
&= -\sum_n u_n^*u_n f(E_n) + v_n^*v_n\Big(1-f(E_n)\Big)
\end{aligned} \tag{4.20}$$

The factor n_z stems from the summation over the states in z-direction (N_z) and the norm of the tilded states ($1/L_z$). Together with the Maxwell relations (using $\boldsymbol{\nabla}\boldsymbol{A}=0$) we obtain a complete set of equations

$$\begin{aligned}
j &= \boldsymbol{\nabla}\wedge\boldsymbol{\nabla}\wedge\boldsymbol{A} \\
&= -\boldsymbol{\nabla}^2\boldsymbol{A}
\end{aligned} \tag{4.21}$$

and

$$\rho = \rho_+ + \rho_e = -\boldsymbol{\nabla}^2\Phi \tag{4.22}$$

where $\rho_+ = -\frac{1}{V_{2D}}\int d^2\boldsymbol{r}\rho_e(\boldsymbol{r})$ is the uniform charge density of the positive background and is held fixed to the corresponding normal state value ρ_0 by adjusting the Fermi energy. These self-consistency equations are independent on the symmetry of the order parameter, since they rely only on the kinetic part of the Bogoliubov-de Gennes hamiltonian and not on the off-diagonal parts. Together with the relations for the order parameters presented in the next three paragraphs, we have a full set of self-consistent equations. Note that we define below an effective interaction constant as $v = v_0 N_z$.

s-wave case

Bogoliubov-de Gennes equations:

$$\begin{pmatrix} h_0 & \eta_s \\ \eta_s^* & -h_0^* \end{pmatrix} \begin{pmatrix} u_n \\ v_n \end{pmatrix} = E_n \begin{pmatrix} u_n \\ v_n \end{pmatrix} \tag{4.23}$$

with

$$h_0(\boldsymbol{r}) = \frac{E_F^0}{k_F^2} \left(\frac{1}{i} \boldsymbol{\nabla} + \gamma_A \boldsymbol{A}(\boldsymbol{r}) \right)^2 - E_F - \gamma_\Phi \Phi(\boldsymbol{r}). \tag{4.24}$$

Self-consistency relation for the gap function:

$$\eta_s(\boldsymbol{r}) = V_{2D} \upsilon \sum_n v_n^*(\boldsymbol{r}) u_n(\boldsymbol{r}) \tanh\left(\frac{\beta E_n}{2}\right) \tag{4.25}$$

p-wave case

Bogoliubov-de Gennes equations:

$$\begin{pmatrix} h_0 & \frac{1}{\sqrt{2}k_F} \sum_\pm \left(\eta_\pm \Box_\mp + \frac{1}{2}(\Box_\mp \eta_\pm) \right) \\ -\frac{1}{\sqrt{2}k_F} \sum_\pm \left(\eta_\pm^* \Box_\pm + \frac{1}{2}(\Box_\pm \eta_\pm^*) \right) & -h_0^* \end{pmatrix} \begin{pmatrix} u_n \\ v_n \end{pmatrix} = E_n \begin{pmatrix} u_n \\ v_n \end{pmatrix}. \tag{4.26}$$

Self-consistency relation for the gap function:

$$\eta_\pm(\boldsymbol{r}) = -\frac{V_{2D}}{2\sqrt{2}k_F} \upsilon \sum_n \left(v_n^*(\boldsymbol{x}) \Box_\pm u_n(\boldsymbol{x}) - u_n(\boldsymbol{x}) \Box_\pm v_n^*(\boldsymbol{x}) \right) \tanh\left(\frac{\beta E_n}{2}\right) \tag{4.27}$$

d-wave case

Bogoliubov-de Gennes equations:

$$\begin{pmatrix} h_0 & -\frac{1}{k_F^2}\eta_d(\partial_x^2 - \partial_y^2) + \left((\partial_x \eta_d)\partial_x - (\partial_y \eta_d)\partial_y \right) + \frac{1}{4}\left((\partial_x^2 - \partial_y^2)\eta_d^* \right) \\ -\frac{1}{k_F^2}\eta_d^*(\partial_x^2 - \partial_y^2) + \left((\partial_x \eta_d^*)\partial_x - (\partial_y \eta_d^*)\partial_y \right) + \frac{1}{4}\left((\partial_x^2 - \partial_y^2)\eta_d^* \right) & -h_0^* \end{pmatrix} \begin{pmatrix} u_n \\ v_n \end{pmatrix} = E_n \begin{pmatrix} u_n \\ v_n \end{pmatrix}.$$

Self-consistency relation for the gap function:

$$\eta_d(\boldsymbol{r}) = -\frac{V_{2D}}{4k_F^2} \upsilon \sum_n \Big(v_n^*(\partial_x^2 - \partial_y^2) u_n + u_n(\partial_x^2 - \partial_y^2) v_n^* - 2\left(\partial_x v_n^* \partial_x u_n - \partial_y v_n^* \partial_y u_n \right) \Big) \tanh\left(\frac{\beta E_n}{2}\right) \tag{4.28}$$

Summation Convention

To obtain a self-consistent solution, we have furthermore to fix the summation range in all the sums above. Following general ideas, we can write the Bogoliubov Hamiltonian either in quasiparticles with definite spin direction and positive as well as negative energies, or by spin reversal symmetry

$$\tilde{u}_n, \tilde{v}_n, E_n, s \rightarrow -\tilde{v}_n^*, \tilde{u}_n^*, -E_n, -s \tag{4.29}$$

in quasiparticles with both up and down spins but only positive energy. We use in the whole approach the first convention, so we always sum over all positive and negative quasiparticle energies occurring in the solution of the BdG-problem. On the other hand, we have to define the range of the attractive interactions between the electrons forming Cooper-pairs. Here we adopt the usual convention, limiting the interaction to the plane wave states with energies smaller than a cutoff energy $E_c = \hbar\omega_c$ measured with respect to the Fermi energy

$$|\xi_{\boldsymbol{k}}| = |E_{\boldsymbol{k}} - E_F^0| \leq E_c. \tag{4.30}$$

In our numerical simulations we conveniently take $E_c = E_F^0$.

4.3 Bulk solution

Within Ginzburg-Landau theory, it has been shown that the homogeneous bulk solution in the p-wave case has two degenerate solutions where only either η_+ or η_- is present and equal to the bulk value η_∞

$$(\eta_\pm, \eta_\mp) = (\eta_\infty, 0). \tag{4.31}$$

We take plane waves in a finite box for the quasiparticle amplitudes

$$\begin{pmatrix} u_{\boldsymbol{k}}(\boldsymbol{x}) \\ v_{\boldsymbol{k}}(\boldsymbol{x}) \end{pmatrix} = \frac{1}{\sqrt{V_{2D}}} \begin{pmatrix} u_{\boldsymbol{k}} \\ v_{\boldsymbol{k}} \end{pmatrix} e^{i\boldsymbol{k}\boldsymbol{x}}. \tag{4.32}$$

The hamiltonian reads

$$\begin{pmatrix} \xi_{\boldsymbol{k}} & \frac{1}{\sqrt{2}} \sum_\pm \eta_\pm \left(\frac{ik_x \pm k_y}{k_F} \right) \\ -\frac{1}{\sqrt{2}} \sum_\pm \eta_\pm^* \left(\frac{ik_x \mp k_y}{k_F} \right) & -\xi_{\boldsymbol{k}} \end{pmatrix} \begin{pmatrix} u_{\boldsymbol{k}} \\ v_{\boldsymbol{k}} \end{pmatrix} = E_{\boldsymbol{k}} \begin{pmatrix} u_{\boldsymbol{k}} \\ v_{\boldsymbol{k}} \end{pmatrix}, \tag{4.33}$$

and diagonalization of the eigenvalue problem leads to

$$\xi_{\boldsymbol{k}} = E_F \left(\frac{k^2}{k_F^2} - 1 \right)$$

$$
\begin{aligned}
E_{\boldsymbol{k}} &= \pm\sqrt{\xi_{\boldsymbol{k}}^2 + \frac{1}{2}|\eta_\infty|^2\frac{k^2}{k_F^2}} \\
u_{\boldsymbol{k}} &= \sqrt{\frac{1}{2}\left(1 \pm \frac{\xi_{\boldsymbol{k}}}{|E_{\boldsymbol{k}}|}\right)} \\
v_{\boldsymbol{k}} &= \pm e^{i\alpha}\sqrt{\frac{1}{2}\left(1 \mp \frac{\xi_{\boldsymbol{k}}}{|E_{\boldsymbol{k}}|}\right)},
\end{aligned} \tag{4.34}
$$

where the phase is determined through

$$
\frac{\eta_\infty}{|\eta_\infty|}e^{i\alpha} = \frac{(-ik_x \pm k_y)}{k}. \tag{4.35}
$$

Inserting this result into the gap equation, we obtain (using $v = v_0 N_z$)

$$
\begin{aligned}
\eta_\infty &= -\frac{1}{\sqrt{2}}v\sum_{E_{\boldsymbol{k}}}\left(u_{\boldsymbol{k}}v_{\boldsymbol{k}}^*\frac{ik_x \mp k_y}{k_F}\right)\tanh\left(\frac{\beta E_{\boldsymbol{k}}}{2}\right) \\
&= \frac{1}{4}v\sum_{E_{\boldsymbol{k}}}\frac{k^2}{k_F^2}\frac{\eta_\infty}{E_{\boldsymbol{k}}}\tanh\left(\frac{\beta E_{\boldsymbol{k}}}{2}\right).
\end{aligned} \tag{4.36}
$$

Thus the self-consistency equation for the bulk energy gap $\Delta_0 = |\eta_\infty|/\sqrt{2}$ at zero temperature reads

$$
\begin{aligned}
1 &= \frac{v}{2}\sum_{E_{\boldsymbol{k}}}\frac{k^2}{k_F^2}\frac{1}{2|E_{\boldsymbol{k}}|} = \frac{v}{2}\sum_{E_{\boldsymbol{k}}\geq 0}\frac{k^2}{k_F^2}\frac{1}{E_k} \\
&= \frac{v}{2}\frac{N^{2D}(0)}{2}\int_{-E_c}^{E_c} d\xi_{\boldsymbol{k}}\frac{\xi_{\boldsymbol{k}}+1}{\sqrt{\xi_{\boldsymbol{k}}^2 + \Delta_0^2(\xi_{\boldsymbol{k}}+1)}} \\
&= \frac{vN^{2D}(0)}{4}\left(\frac{1}{E_F}(W_+ - W_-) + \left(1 - \frac{\Delta_0^2}{2E_F^2}\right)\ln\left|\frac{2E_c + \frac{\Delta_0^2}{E_F} + 2W_+}{-2E_c + \frac{\Delta_0^2}{E_F} + 2W_-}\right|\right) \\
&\sim \frac{vN^{2D}(0)}{2}\ln\frac{2E_c}{\Delta_0},
\end{aligned} \tag{4.37}
$$

where $N^{2D}(0) = V_{2D}k_F^2/2\pi E_F^0 = V_{2D}k_F/\pi\Delta_0$ is the density of states at E_F^0 including the spin values, and

$$
W_\pm = \sqrt{E_c^2 + \Delta_0^2\left(1 + \frac{E_c}{E_F}\right)}. \tag{4.38}
$$

In rescaled units, we have simply to put $\Delta_0 = 1$. For comparison we add the result for the s-wave case which reads

$$
1 = \frac{vN^{2D}(0)}{2}\left(\ln\left|\frac{E_c + W}{-E_c + W}\right|\right), \tag{4.39}
$$

where

$$
W = \sqrt{E_c^2 + \Delta_0^2}. \tag{4.40}
$$

Note that this result is equivalent to the usual result if $E_c \gg \Delta_0$.

4.4 Vortex solutions

Assuming a circular Fermi surface, the s-wave as well as the p-wave single vortex problem on a disk shows perfect rotational invariance due to the absence of gap nodes. This means, that angular momentum is a good quantum number and the problem actually can be written as a set of one-dimensional radial problems in different subspaces with constant angular momentum. Consequently, all physical quantities occur in rotationally invariant form

$$\begin{aligned} \boldsymbol{A}(\boldsymbol{r}) &= A(r)\boldsymbol{e}_\phi \\ \boldsymbol{B}(\boldsymbol{r}) &= B(r)\boldsymbol{e}_z \\ \boldsymbol{j}(\boldsymbol{r}) &= j(r)\boldsymbol{e}_\phi \\ \Phi(\boldsymbol{r}) &= \Phi(r) \\ \boldsymbol{E}(\boldsymbol{r}) &= E(r)\boldsymbol{e}_r \\ \rho(\boldsymbol{r}) &= \rho(r) \end{aligned} \tag{4.41}$$

and the corresponding Maxwell equations read in dimensionless form

$$\begin{aligned} B &= \frac{1}{r}\partial_r\left(rA\right) \\ j &= -\partial_r\left(\frac{1}{r}\partial_r\left(rA\right)\right) \\ E &= -\partial_r\Phi \\ \rho &= -\frac{1}{r}\partial_r\left(r\partial_r\Phi\right). \end{aligned} \tag{4.42}$$

Note that the E-fields occurring due to charging effects are radial and thus orthogonal to the currents, which means that they do not contribute to ohmic resistance. To be able to solve the Maxwell equations, we need to have reasonable boundary conditions. For A and B we take the well known conditions

$$A(0) = 0, \qquad B(R) = 0 \tag{4.43}$$

and the fact that the A-field is linear near $r = 0$. For the potential Φ and the E-field it is convenient to take

$$\int \Phi(r) r dr = 0, \qquad E(0) = 0. \tag{4.44}$$

The first equation basically defines Φ as a fluctuation of the electrostatic potential with respect to a constant background included in the chemical potential (Fermi energy) due to charging effect. As mentioned above, we keep the total positive background charge fixed to the value of the normal state and adjust the Fermi energy correspondingly to obtain charge neutrality.

In p-wave superconductors, we have for a fixed B-field orientation two possible vortex states. This is due to the two dimensional representation of the point group and due to the fact, that in the bulk state the two solutions $(\eta_\pm, \eta_\mp) = (\eta_\infty, 0)$ are degenerate. Fixing $B \parallel +\hat{\boldsymbol{z}}$, we have either

$$\begin{array}{ll} (S) & \eta_-(r,\varphi) \propto \hat{\eta}_-(r)e^{-i\varphi}, \qquad \eta_+(r,\varphi) \propto \hat{\eta}_+(r)e^{i\varphi}, \\ (U) & \eta_+(r,\varphi) \propto \hat{\eta}_+(r)e^{-i\varphi}, \qquad \eta_-(r,\varphi) \propto \hat{\eta}_-(r)e^{-3i\varphi}, \end{array} \tag{4.45}$$

where the components with phase turn $e^{-i\varphi}$ are the dominant component for our fixed field orientation. We denote the two possible orientations of the p-wave case by S (stable) and U (unstable) according to the results of the GL-single vortex calculations, where the S-case turned out to be energetically favored. In the s-wave we have simply one possibility

$$\eta(r,\varphi) \propto \hat{\eta}(r)e^{-i\varphi}. \tag{4.46}$$

Solving the two dimensional single vortex problem on a disk of radius R, we can choose different basis sets with different boundary conditions. The two boundary conditions investigated by us are vanishing basis functions or vanishing normal derivatives of the basis functions at the boundary. We work with the usual Bessel-function basis sets

$$\phi_{l,j}(r,\varphi) = \frac{1}{\sqrt{2\pi}} e^{il\varphi} f_{l,j}(r) = \frac{1}{\sqrt{2\pi}} e^{il\varphi} N_{l,j} J_{|l|}(\frac{Z_{l,j}}{R} r). \tag{4.47}$$

The $J_{|l|}(r)$ are Bessel functions of order $|l|$, whereas $N_{l,j}$ is a normalization factor and $Z_{l,j}$ are specific constants to fulfill the boundary conditions mentioned above. We have

$$\begin{aligned} N_{l,j} &= \frac{\sqrt{2}}{R|J_{|l|+1}(Z_{l,j})|} \\ Z_{l,j} &= j\text{-th zero of } J_{|l|}(r) \end{aligned} \tag{4.48}$$

for the case with vanishing functions at the boundary, and

$$\begin{aligned} N_{l,j} &= \frac{\sqrt{2}}{R|J_{|l|}(Z_{l,j})|} \left(\sqrt{1 - \frac{l^2}{Z_{l,j}^2}}\right)^{-\frac{1}{2}} \\ Z_{l,j} &= j\text{-th zero of } \partial_r J_{|l|}(r) \end{aligned} \tag{4.49}$$

for the case with vanishing derivatives. Both systems are complete orthonormal function sets on a disk of radius R. It was checked that the choice of the basis is completely irrelevant for the behavior of the results near the vortex core, thus all results presented below are calculated within the first basis set (vanishing wavefunctions at the boundary). We expand the quasiparticles in this basis

$$u_n(\boldsymbol{r}) = \sum_{l,j} u_{l,j}^n \phi_{l,j}(r,\varphi)$$

$$
\begin{aligned}
&= \frac{1}{\sqrt{2\pi}} e^{il\varphi} \sum_j u^n_{l,j} f_{l,j}(r) \\
&\equiv \frac{1}{\sqrt{2\pi}} e^{il\varphi} u_{n,l}(r),
\end{aligned} \tag{4.50}
$$

with $v_n(\boldsymbol{r})$ treated analogously. In the second step we have used, that due to rotational symmetry the problem splits into different subspaces with constant angular momentum. The off-diagonal blocks in the hamiltonian due to the gap function then define, which specific angular momentum components of $u(\boldsymbol{r})$ and $v(\boldsymbol{r})$ are coupled. For our three cases we find

$$
\begin{array}{lccl}
s\text{-wave} & u_l & \leftrightarrow & v_{l+1} \\
p\text{-wave (S)} & u_l & \leftrightarrow & v_l \\
p\text{-wave (U)} & u_{l-1} & \leftrightarrow & v_{l+1}
\end{array} . \tag{4.51}
$$

Using the spin reversal symmetry, we find the following transformations for the radial quasiparticle wavefunctions between negative and positive l

$$
\begin{array}{lccccccccc}
s\text{-wave} & u^n_l & v^n_{l+1} & E^n_l & l & \rightarrow & -v^n_{-l} & u^n_{-l-1} & -E^n_{-l-1} & -l \\
p\text{-wave (S)} & u^n_l & v^n_l & E^n_l & l & \rightarrow & v^n_{-l} & u^n_{-l} & -E^n_{-l} & -l \\
p\text{-wave (U)} & u^n_{l-1} & v^n_{l+1} & E^n_l & l & \rightarrow & -v^n_{-l+1} & u^n_{-l-1} & -E^n_{-l} & -l
\end{array} . \tag{4.52}
$$

which allows us to restrict ourselves to $l \geq 0$ in all three cases. The detailed implementation of the Bogoliubov hamiltonian and the self-consistency equations can be found in Appendix C.3.

4.4.1 Numerical results

In the following section, we present the results of our calculations for single vortex lines in p-wave superconductors. The corresponding, mostly well known results for s-wave symmetry are given as a reference. As mentioned above, we work on a circular disk with radius R. Since the boundary effects for the p-wave case are long ranged, the calculations had to be done on a large radial interval. This is mainly due to the fact that the boundary stabilizes in the p-wave case an order parameter combination different from the homogeneous bulk case. In quasiclassical calculations dealing with a one-dimensional boundary, Matsumoto *et al.*[96] found the order parameter component perpendicular to the boundary to be suppressed to zero. For our circular boundary with normal vector $(\cos\varphi, \sin\varphi)$ this condition reads $\eta_x \cos\varphi + \eta_y \sin\varphi = 0$. Indeed, we find numerically

$$
\hat{\eta}_+ + \hat{\eta}_- = \eta_+ e^{-i\varphi} + \eta_- e^{i\varphi} = \eta_x \cos\varphi + \eta_y \sin\varphi = 0 \tag{4.53}
$$

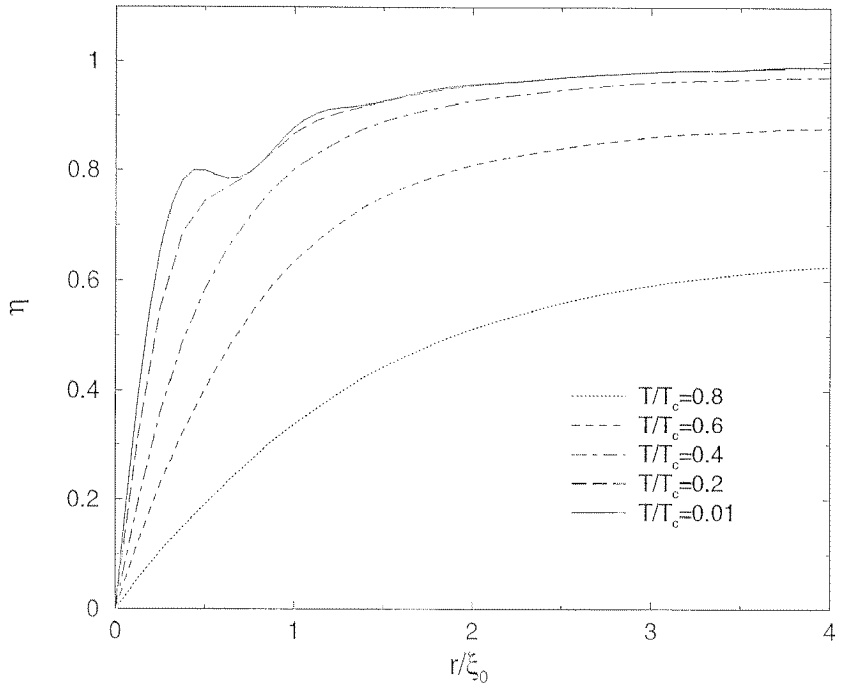

Figure 4.1: Order parameter for the s-wave case for different temperatures and $k_F\xi_0 = 4$.

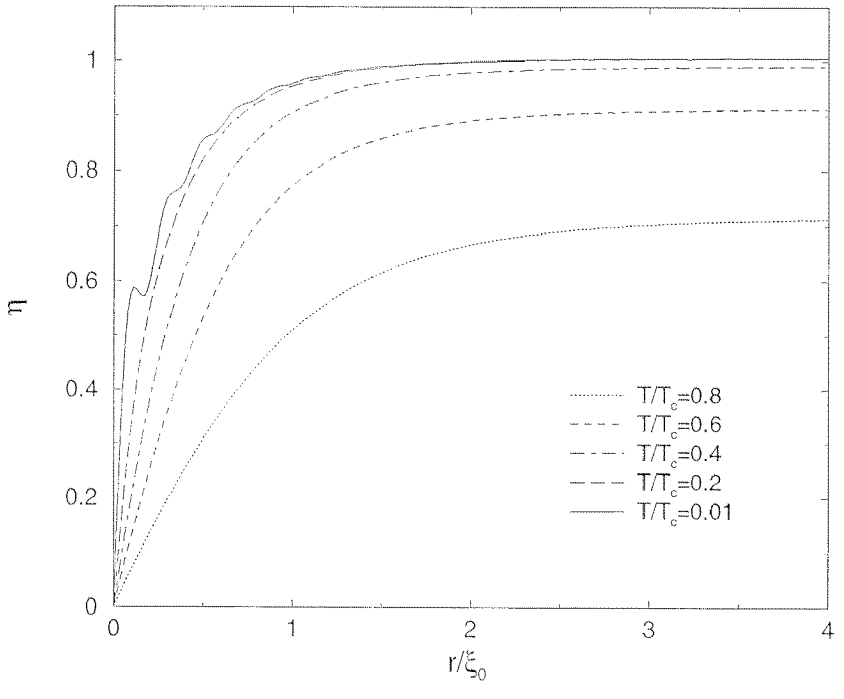

Figure 4.2: Order parameter for the s-wave case for different temperatures and $k_F\xi_0 = 16$. Note the narrowing of the vortex core for decreasing temperature (Kramer-Pesch effect). For very low temperatures, the effects of individual quasiparticles become visible as oscillations on the lengths scale $1/k_F\xi_0$ (compare also Fig. 4.1).

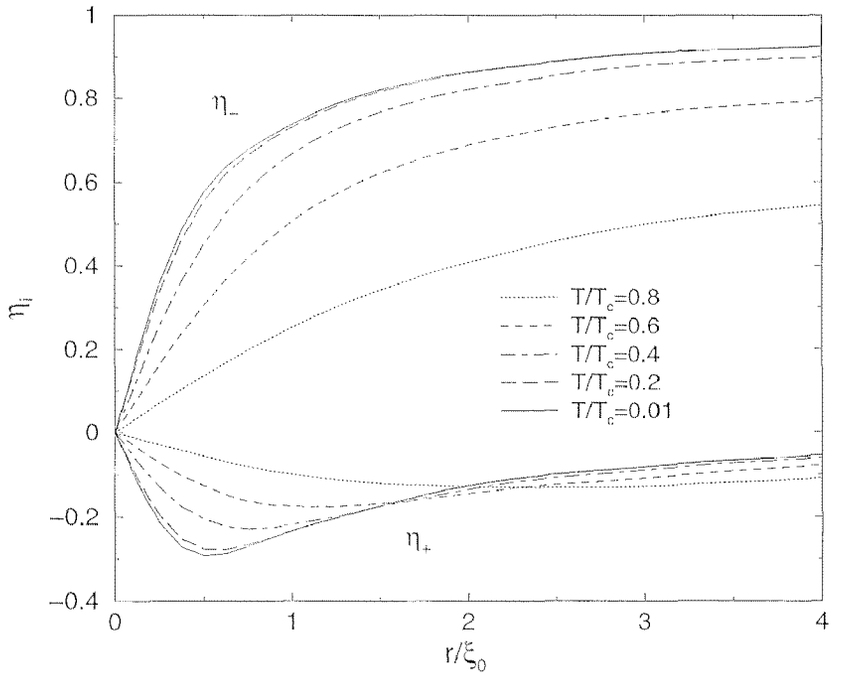

Figure 4.3: Order parameter for the stable (S) p-wave case for different temperatures and $k_F\xi_0 = 4$.

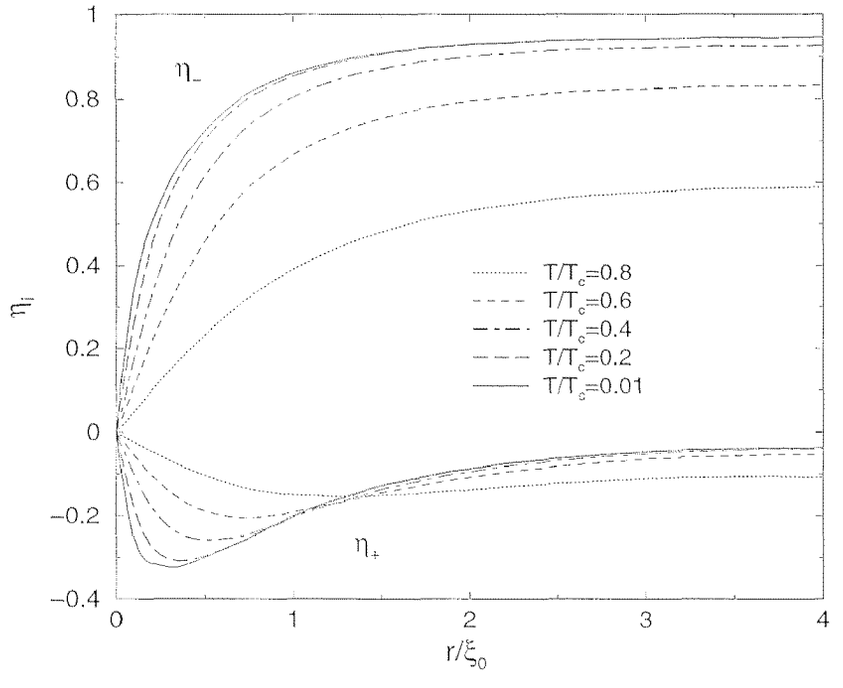

Figure 4.4: Order parameter for the stable (S) p-wave case for different temperatures and $k_F\xi_0 = 16$. As in the s-wave case, at low temperatures a shrinking of the core size is visible. The admixed component shows a linear rise near the core (compare also Fig. 4.3).

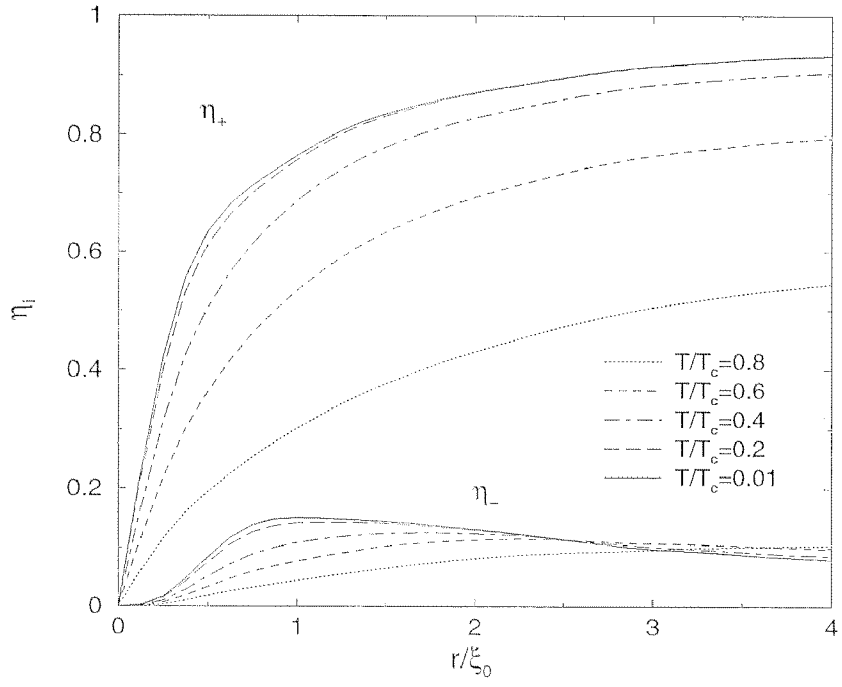

Figure 4.5: Order parameter for the unstable (U) p-wave case for different temperatures and $k_F\xi_0 = 4$.

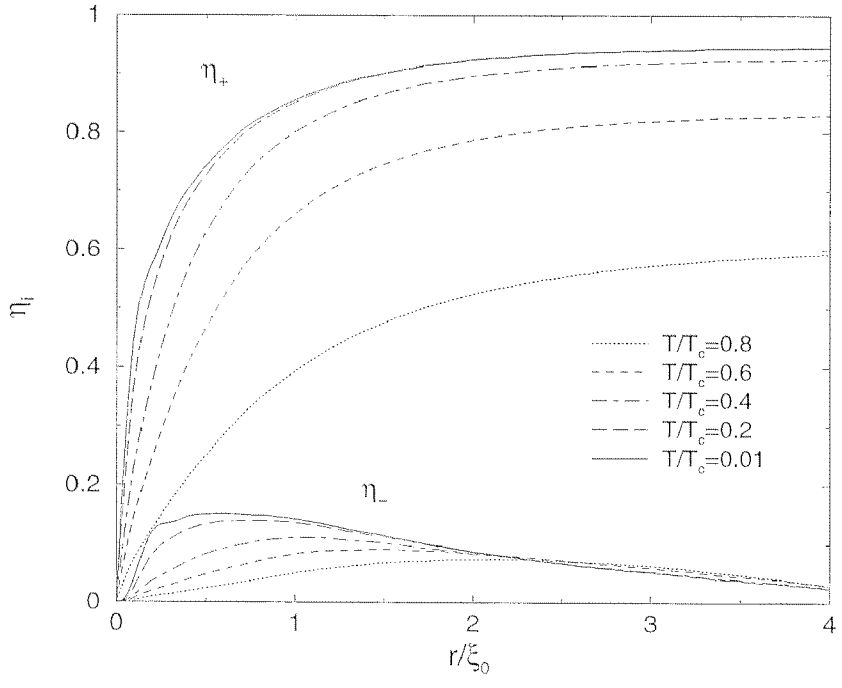

Figure 4.6: Order parameter for the unstable (U) p-wave case for different temperatures and $k_F\xi_0 = 16$. As in the s-wave case, at low temperatures a shrinking of the core size is visible. The admixed component shows a cubic rise near the core (compare also Fig. 4.5).

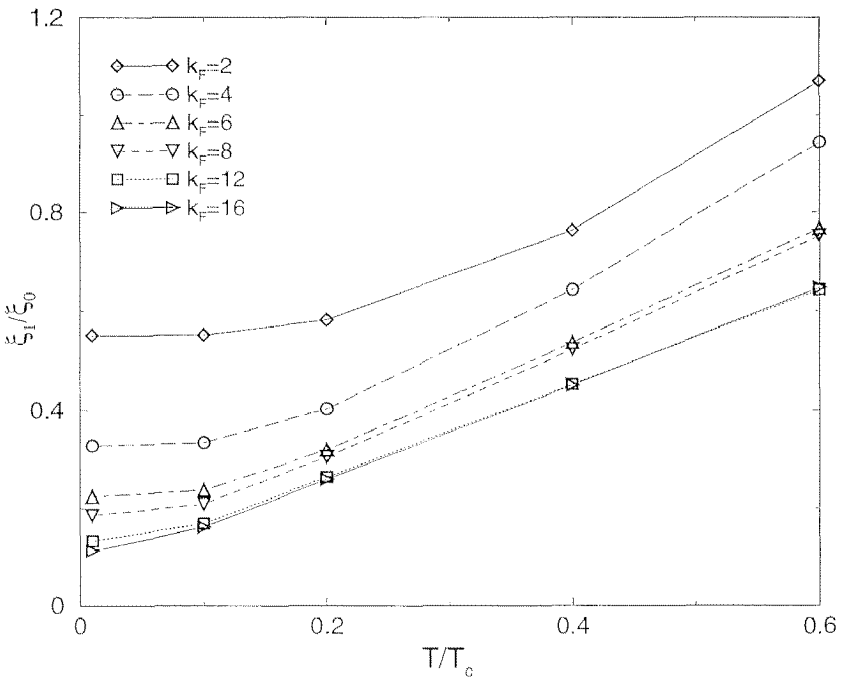

Figure 4.7: Kramer-Pesch effect for s-wave case: Effective vortex size ξ_1/ξ_0 versus normalized temperature T/T_c for different $k_F\xi_0$.

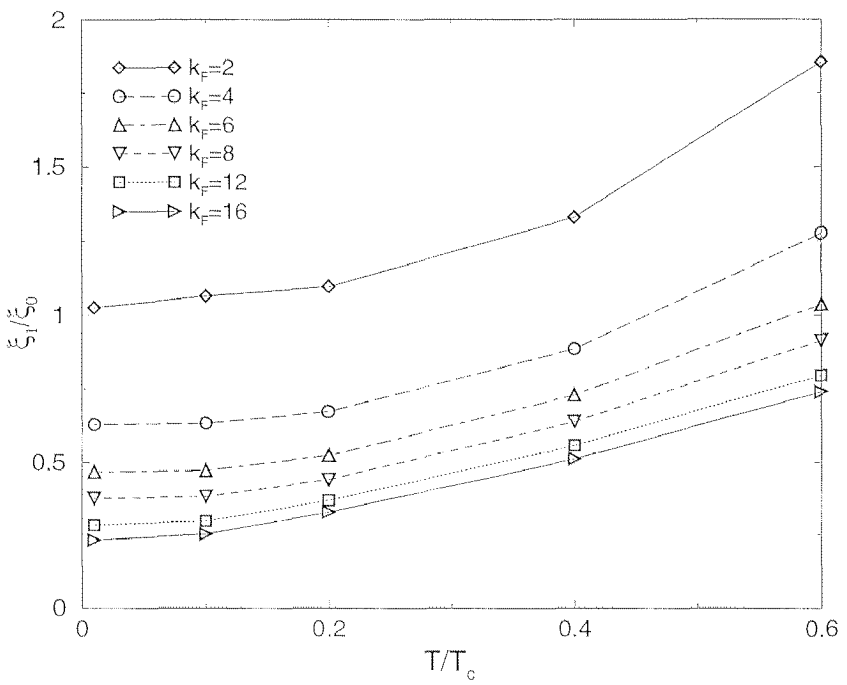

Figure 4.8: Kramer-Pesch effect for stable (S) p-wave case: Effective vortex size ξ_1/ξ_0 versus normalized temperature T/T_c for different $k_F\xi_0$.

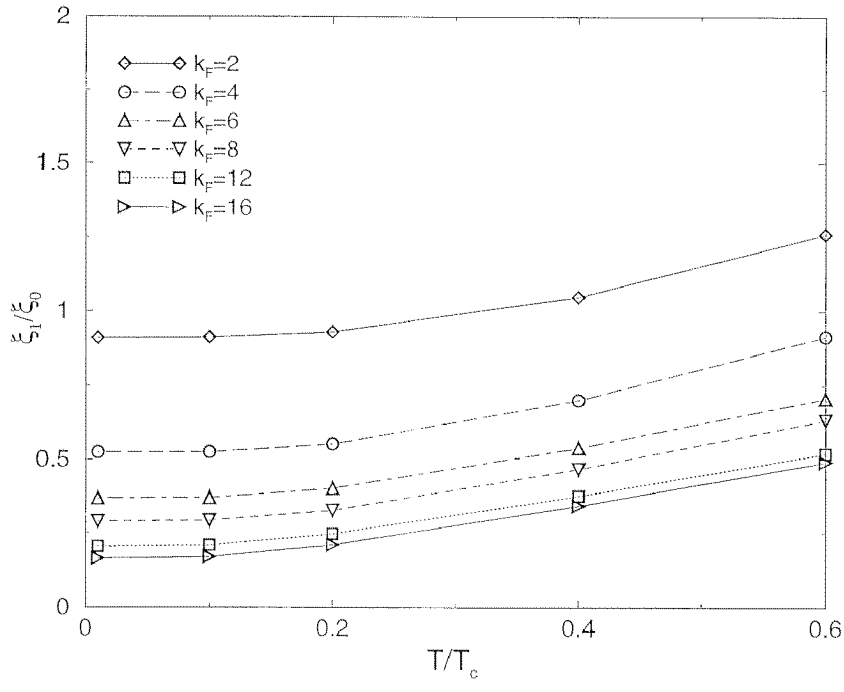

Figure 4.9: Kramer-Pesch effect for unstable (U) p-wave case: Effective vortex size ξ_1/ξ_0 versus normalized temperature T/T_c for different $k_F\xi_0$.

near the boundary, thus a suppressed perpendicular component in accordance with the quasiclassical results and in contrast to the bulk solution. Using large radial intervals depending on the value for $k_F\xi_0$ (typically $R/\xi_0 = 32$ for $k_F\xi_0 = 2, 4$, $R/\xi_0 = 16$ for $k_F\xi_0 = 6, 8$, and $R/\xi_0 = 8$ for $k_F\xi_0 = 12, 16$), the vortex core properties turn out to be independent on the disk radius with the order parameters saturating to the bulk solution in the intermediate region. For simplicity, for this model calculations we have chosen our cutoff energy to be $E_c = E_F^0$, and the temperatures are measured in units of $T_c = \Delta_0/1.764$. In contrast to earlier results, we have included full screening in both current (London screening) and charge (Thomas-Fermi screening). For the screening lengths we chose $\lambda_L = 2$ and $\lambda_{TF} = 1/k_F$. The total electronic charge is fixed to the normal state value, and charge neutrality is achieved by iteratively adjusting the Fermi energy. In Figs. 4.1-4.6 we show the order parameters η_s (s-wave) and $\eta_\pm/\sqrt{2}$ (p-wave) for different temperatures and $k_F\xi_0 = 4, 16$. (Note that with our definition of the order parameter, the asymptotic bulk value in the p-wave case is $\sqrt{2}$, whereas the spectral gap at $T = 0$ is $\Delta_0 = 1$.) In the p-wave case, the results show nicely the asymptotic behavior of the admixed components $\eta_+ \propto r$ ($\eta_- \propto r^3$) for the stable (unstable) case. The admixed component decays on a length scale of the order of ξ_0, as is expected from the fact that these admixtures are driven by the inhomogeneity of the main dominant parameter. In accordance with this effect, the decay is slower for higher temperatures, where ξ_0 increases. The reduction of the bulk

value of the order parameter follows nicely the BCS-law also for p-waves. The s-wave results show for low temperatures oscillations on the scale of $1/k_F$ reported already in earlier works[82, 83], whereas these oscillations are almost absent in the p-wave case.

In Figs. 4.7-4.9 we show an analysis of the Kramer-Pesch effect for the three cases. Unlike other references, where the effective vortex size is defined as

$$\xi_1^u = \left(\lim_{r\to 0} \frac{\eta(r)}{r\eta_\infty(0)} \right)^{-1}, \tag{4.54}$$

we use the more comfortable definition (in dimensionless units)

$$\xi_1 = \left(\lim_{r\to 0} \frac{\eta(r)}{r\eta_\infty(T)} \right)^{-1}, \tag{4.55}$$

which gives the effective vortex core size. For low temperatures where the bulk gap equals the bulk gap at zero temperature, the two definitions coincide. According to Kramer and Pesch, this effective core size should follow the law

$$\xi_1(T) \ln \left(\frac{\xi_0}{\xi_1(T)} \frac{\eta_\infty(0)}{\eta_\infty(T)} \right) \sim \frac{T}{T_c} \left(\frac{\eta_\infty(0)}{\eta_\infty(T)} \right)^2. \tag{4.56}$$

for temperatures larger than $T_0 \approx \Delta_0^2/E_F \sim 2/k_F$, and

$$\xi_1(T) \sim \frac{1}{k_F} \tag{4.57}$$

for lower temperatures. The expression Eq. (4.56) can be simplified in the region $T_0 < T \ll T_c$ to the leading behavior

$$\xi_1(T) \sim \frac{T}{T_c}. \tag{4.58}$$

In Figs. 4.7-4.9 we observe that this effect is reproduced in the numerical results. For temperatures $T < 0.6T_c$ the dependence of $\xi_1(T)$ is linear and saturates to a value roughly proportional to $1/k_F$ (see Fig. 4.10). This saturation is due to the lowest energy states, which have oscillations on the scale $1/k_F$ and thus their significant contributions to the gap function at position $r \sim 1/k_F$. The saturation takes place at higher temperatures if $k_F\xi_0$ is small, in accordance with the predicted $T_0 \sim 2/k_F$. Note further that the vortex core size $\xi_1(T)$ is by roughly a factor two larger in the p-wave system than in the s-wave case.

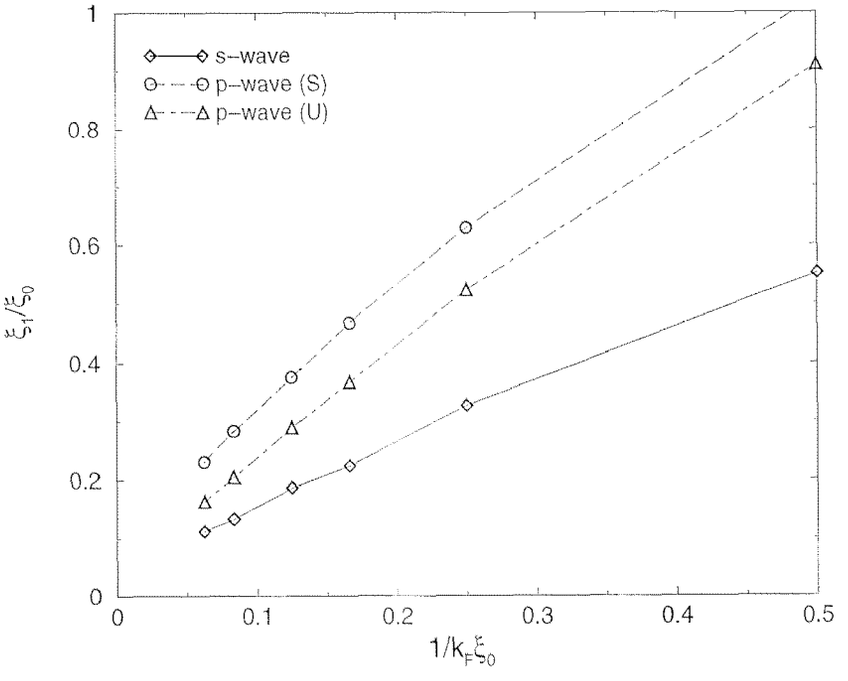

Figure 4.10: Vortex core size at very low temperature $T = 0.01T_c$ versus $1/k_F\xi_0$.

Looking at the energy spectra at low temperatures $T = 0.01T_c$ (Figs. 4.11-4.13), we find that for these small values of $k_F\xi_0$, the lowest few eigenstates differ considerably from the naively expected results $E_n = \omega_0(n + 1/2)$ for s-wave and $E_n = \omega_0 n$ for p-wave symmetry, with $\omega_0 \sim \Delta_0^2/E_F^0 = 2/k_F\xi_0$ (note that we work in dimensionless units). Using a quasiclassical derivation with additional Sommerfeld-quantization, Volovik obtained for the minigap the expression[94]

$$\omega_0 = \frac{\int_{-\infty}^{\infty} ds|\Psi_0(s)|^2 \frac{\Delta(|s|)}{k_F|s|}}{\int_{-\infty}^{\infty} ds|\Psi_0(s)|^2} \tag{4.59}$$

with $\Psi_0(s) = \exp(-\int_0^s ds'\Delta(s')/v_F)$, in accordance with earlier results for the s-wave case[70, 69]. Using $\Delta(s) = \Delta_0 \tanh(s/\xi_0)$, we obtain the minigap $\omega_0 = 0.85/k_F\xi_0$. Compared with our numerical data, this naive expectation predicts far too low energies especially for larger values of $k_F\xi_0$. The mistake is obvious: due to the Kramer-Pesch effect, the reduced vortex core size for low temperatures enhances the effective minigap in the low energy spectrum. This was pointed out by several authors[69, 82, 83] for the s-wave case. In Fig. 4.14 we show, that the qualitative dependence of the lowest energies of $k_F\xi_0$ is quite well described by the formula

$$E_n = f(n)\frac{\ln c\, k_F\xi_0}{k_F\xi_0} \propto f(n)\omega_0 \tag{4.60}$$

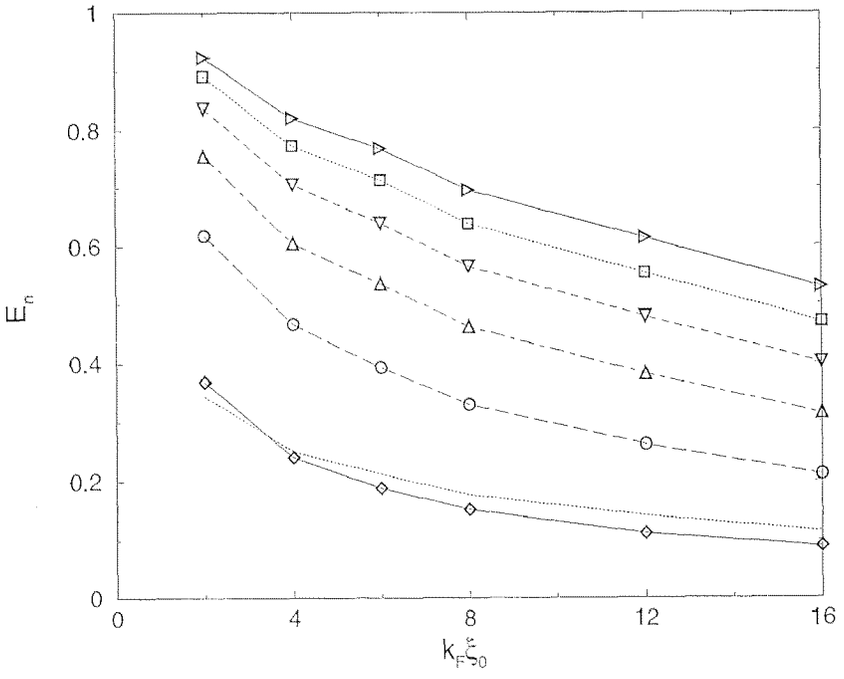

Figure 4.11: Lowest few quasiparticle energies for s-wave case at low temperature $T = 0.01T_c$ versus $k_F\xi_0$. The energies are considerably increased with respect to the expected behavior $E_n = \omega_0(n + 1/2)$ due to the narrowing of the vortex core.

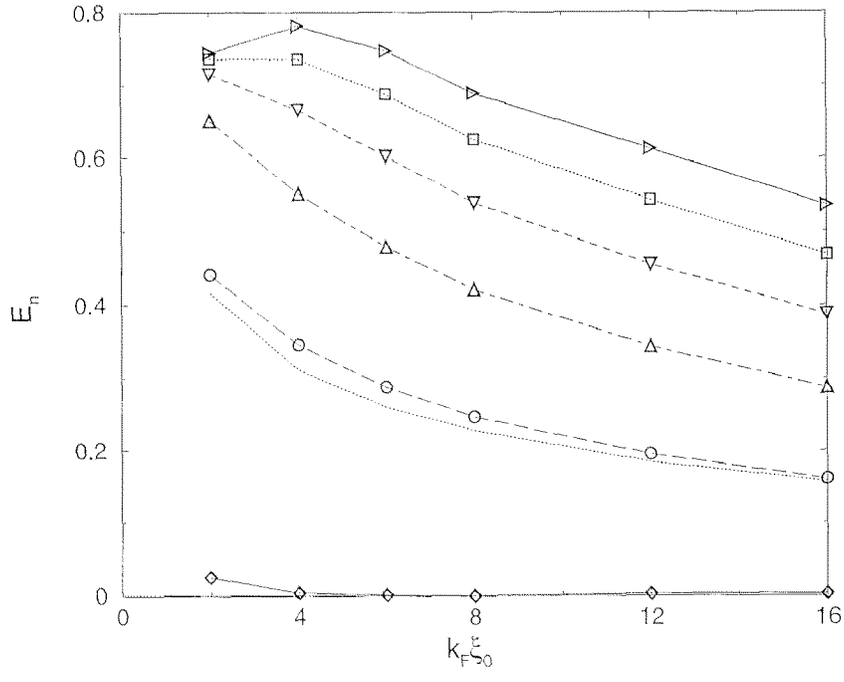

Figure 4.12: Lowest few quasiparticle energies for the stable (S) p-wave case at low temperature $T = 0.01T_c$ versus $k_F\xi_0$. The energies are considerably larger than the expected behavior $E_n = \omega_0 n$ due to the narrowing of the vortex core.

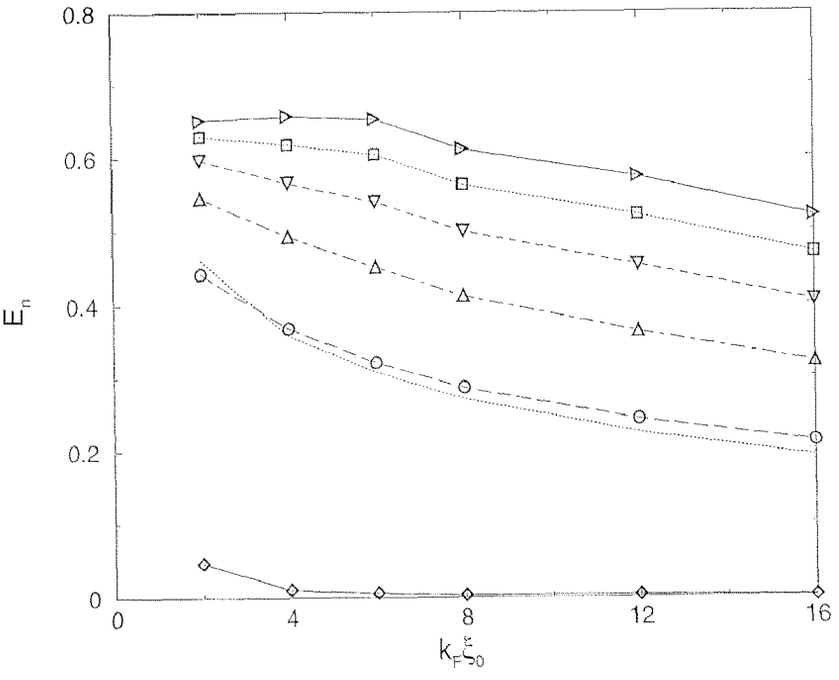

Figure 4.13: Lowest few quasiparticle energies for the unstable (U) p-wave case at low temperature $T = 0.01T_c$ versus $k_F\xi_0$. The energies are considerably larger than the expected behavior $E_n = \omega_0 n$ due to the narrowing of the vortex core.

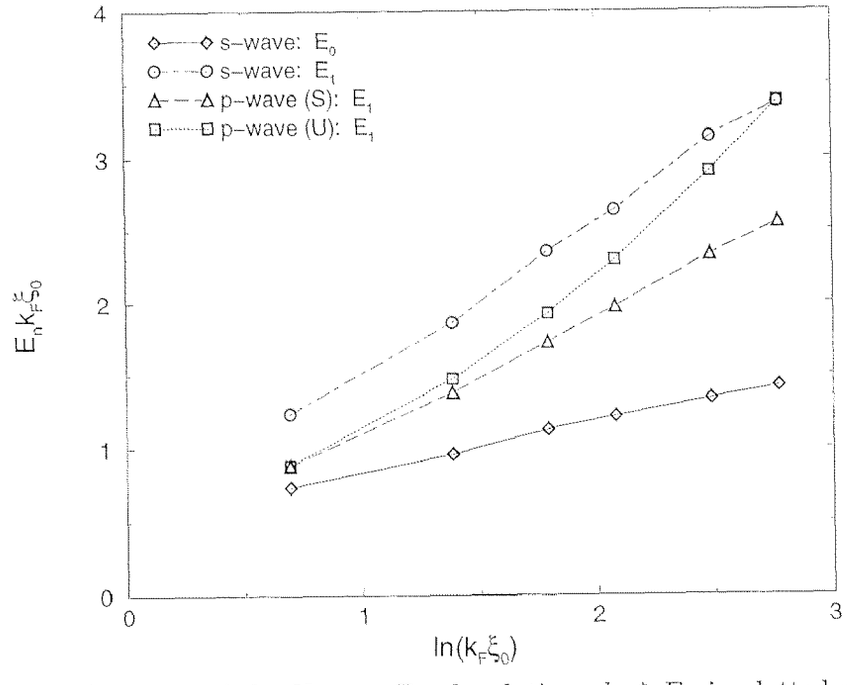

Figure 4.14: Test of the Kramer-Pesch relation: $k_F\xi_0 E_n$ is plotted versus $\ln k_F\xi_0$ for the lowest two states of the s-wave and the lowest non-zero state for the two p-wave cases. As expected from Kramer-Pesch at low temperatures, one finds a linear behavior.

where c is a constant of order unity. This expression is the Kramer-Pesch result for the minigap energy ω_0 for temperatures lower than ω_0, which is an approximation to Eq. (4.59) for very small vortex cores $\xi_1 \ll \xi_0$. For a more quantitative result, we should use Eq. (4.59) directly. Assuming a vortex $\Delta(r) = \Delta_0 \tanh(r/\xi_1)$ with reduced size ξ_1, we obtain near $T = 0$ for the minigap the expression

$$\omega_0 = \frac{1}{k_F \xi_0} f\left(\frac{\xi_1}{\xi_0}\right) \tag{4.61}$$

with

$$f(x) = \frac{\int_1^\infty dt\, t^{-2x-1} / \ln\left(t + \sqrt{t^2-1}\right)}{x \int_1^\infty dt\, t^{-2x}/\sqrt{t^2-1}}. \tag{4.62}$$

Inserting the values obtained numerically for the effective vortex size ξ_1, we find an excellent agreement with the numerical lowest non-zero energy states. For E_0 in the s-wave and E_1 in the p-wave case, the corresponding results are shown as dotted lines in Figs. 4.11-4.13. Since this approach is limited to energies $E_n \ll \Delta_0$, the higher energy states are not as well described by this formula. As is expected, the zero energy state occurring in the p-wave case does not show such energy shifts. Its small enhancement in energy for the lowest values of $k_F\xi_0$ is rather an artifact of the calculation, since the zero energy state strongly hybridizes with its counterpart at the boundary and thus is more sensitive to boundary effects.

Finally, in Figs. 4.15-4.17, we show the results for the vortex core charging. As mentioned above, in contrast to the results presented by Hayashi *et al.*[87], our results are calculated including current and charge screening on the length scales $\lambda_L = 2$ and $\lambda_{TF} = 1/k_F$. Since we work with a 2D parabolic energy spectrum which has vanishing slope of the density of states at the Fermi level, the main contribution to the vortex charge following Blatter *et al.*[86] gives no contribution. The positive vortex charge is rather due to the electric field compensating the centripetal force of the rotating superfluid[86, 84]. For p-waves, the interesting new feature is the strong suppression of vortex charge for the stable vortex configuration. Compared with the unstable solution, which shows vortex charging of similar size as the s-wave system, the stable p-wave case has a vortex charge which is a factor 30 smaller. The reason for this feature is not yet completely clear. However, this finding seems to be intimately related to the time reversal breaking property of the superconducting state. Recently, it has been shown[90, 91, 92, 93] that integrating out the particle fields of an effective hamiltonian for the p-wave system leads to an anomalous coupling between charges, current and electromagnetic potentials. These anomalous terms are proportional to the chirality of the superconducting state. The chirality χ is defined as the winding of the gap function in $\boldsymbol{k}$-space along the Fermi surface, or in terms of the superconducting order parameters as $\chi = \mathrm{sgn}(|\eta_-|^2 - |\eta_+|^2)$. In time reversal symmetric cases (*e. g.*

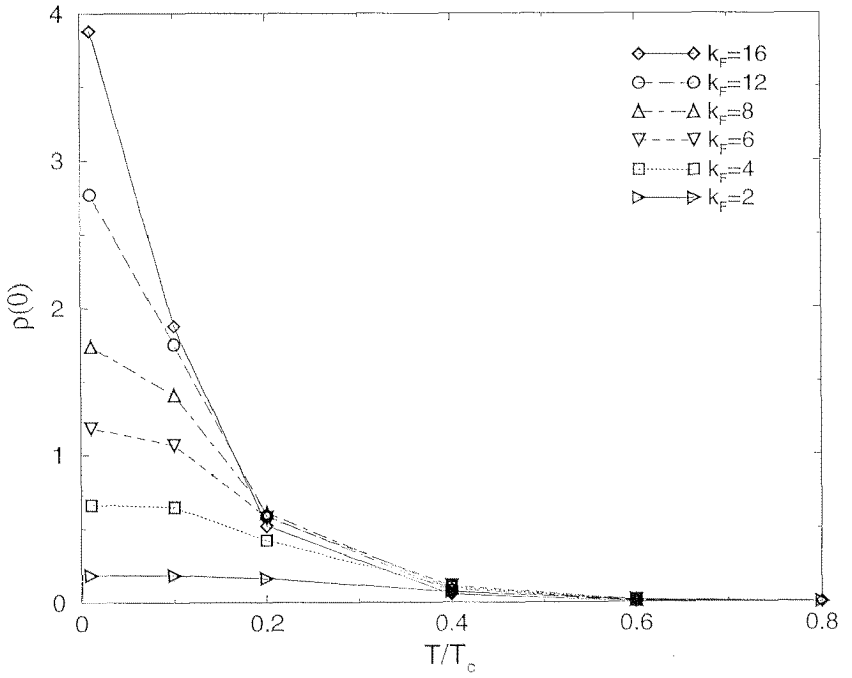

Figure 4.15: Charge density at $r = 0$ for s-wave case versus T for different $k_F r$.

$(\eta_x, \eta_y) = (1, 0)$), the chirality is zero and the anomalous terms are absent. Within Ginzburg-Landau theory, this effect appears if one includes in the free energy density all symmetry-allowed terms containing the scalar potential A_0 and its derivatives to lowest order ($\boldsymbol{E} = -\boldsymbol{\nabla} A_0$)[93]. In addition to the usual screening contributions to the charge and current equations, one then finds in the bulk situation terms proportional to the chirality of the state. In our single vortex situation, these terms take the form

$$\rho_{anom}(r) \propto \begin{cases} -K\partial_r\Big((\eta_+^2 + \eta_-^2)\frac{1}{r} - (\eta_+^2 - \eta_-^2)A(r)\Big) & \text{for (S)} \\ -K\partial_r\Big((-\eta_+^2 + 3\eta_-^2)\frac{1}{r} - (\eta_+^2 - \eta_-^2)A(r)\Big) & \text{for (U)} \end{cases}, \tag{4.63}$$

where K is a phenomenological parameter, and

$$j_{anom}(r) \propto 2K(\eta_+^2 - \eta_-^2)E(r). \tag{4.64}$$

Note, that due to these terms, the B-field contributes to the charge screening and an electric field generates a perpendicular current. Within a weak-coupling derivation, the phenomenological parameter K has been shown to be positive[93]. For our vortex situation, inserting the asymptotic behavior of the order parameter components, we find

$$\rho_{anom}(0) \propto \begin{cases} -K(2 - \chi O(r^2)) & \text{for (S)} \\ K(1 + \chi O(r^2)) & \text{for (U)} \end{cases} \tag{4.65}$$

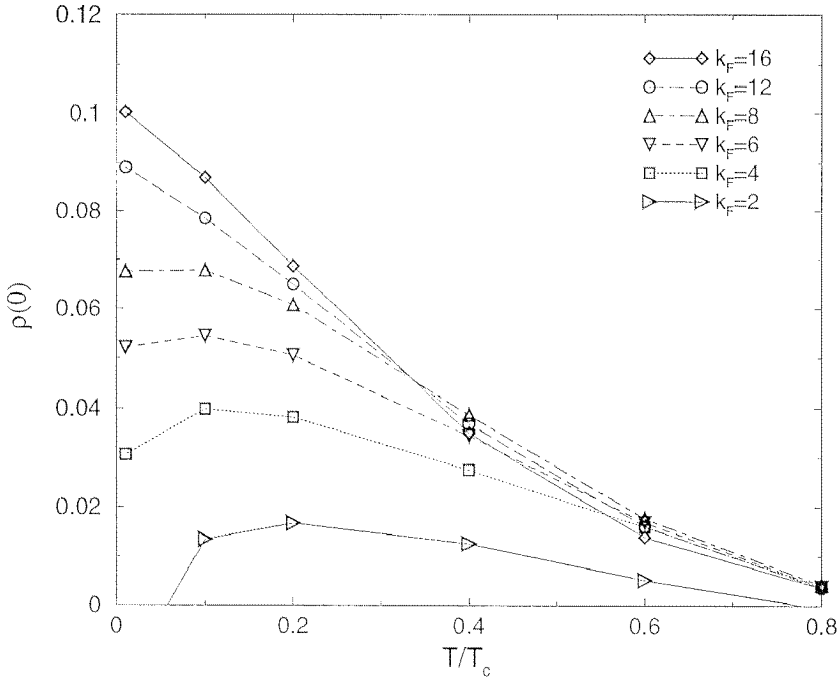

Figure 4.16: Charge density at $r = 0$ for stable (S) p-wave case versus T for different k_F.

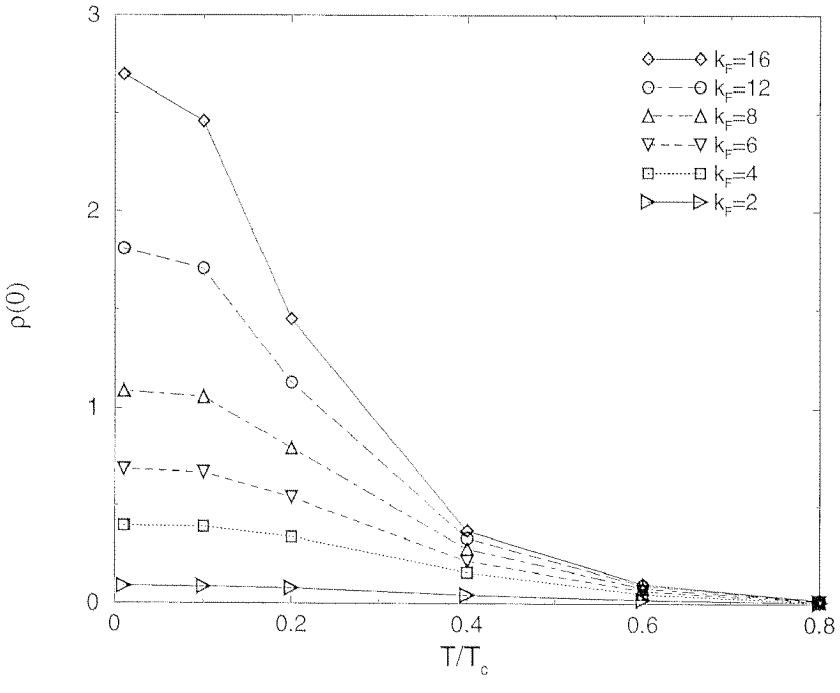

Figure 4.17: Charge density at $r = 0$ for unstable (U) p-wave case case versus T/T_c for different k_F.

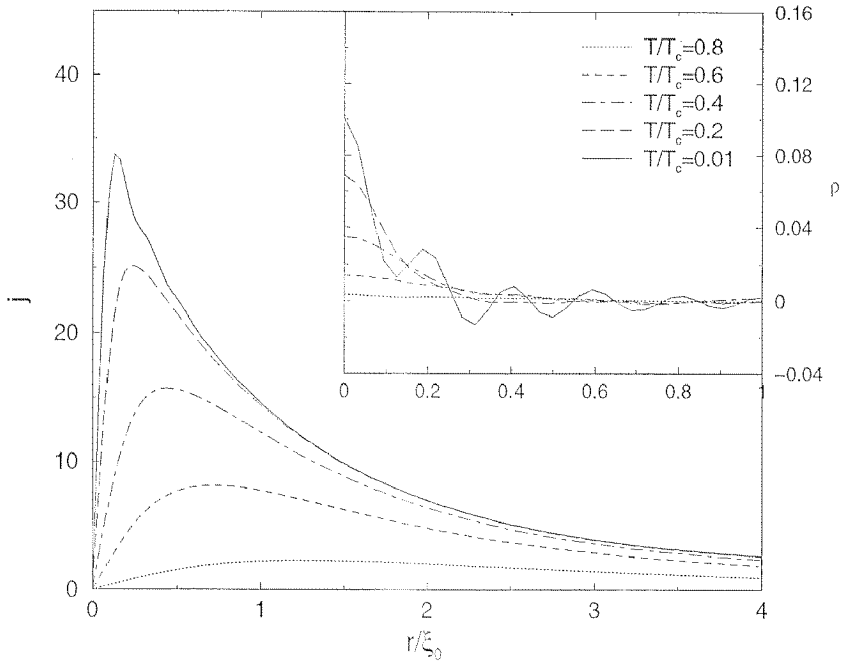

Figure 4.18: Current density for the stable (S) p-wave case for $k_F\xi_0 = 16$ and different T. In the inset, the charge density is shown for the same parameters.

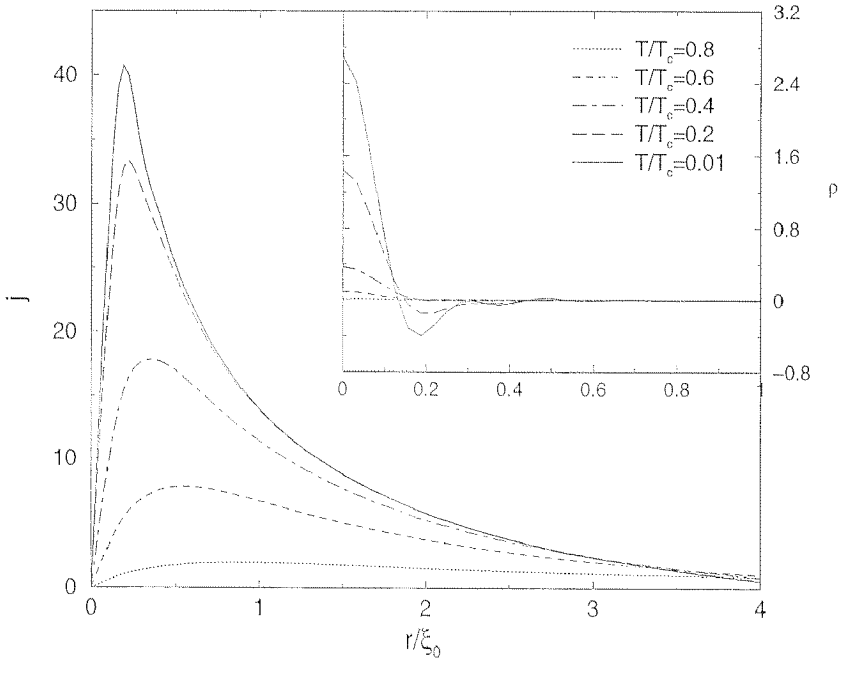

Figure 4.19: Current density for the unstable (U) p-wave case for $k_F\xi_0 = 16$ and different T. In the inset, the charge density is shown for the same parameters. Note the different scale with respect to Fig. 4.18.

and

$$j_{anom}(r) \propto \begin{cases} 2K(r^2 - r^2)E(r) \approx 0 & \text{for (S)} \\ 2Kr^2E(r) & \text{for (U)} \end{cases} . \tag{4.66}$$

The numerical results are in qualitative accordance with these findings. Looking at the charge distribution, we expect from Eq. (4.65) a stronger positive vortex charging for the unstable case than the stable, which is easily seen in Figs. 4.18,4.19. In the stable case, this results in an almost vanishing vortex charge. The electric field therefore is close to zero, and according to Eq. (4.66), no anomalous current contribution is expected. On the other hand, the electric field in the unstable case shows a positive peak at roughly $r = 0.1\xi_0$ (*cf.* Fig. 4.20), and thus we expect a positive anomalous contribution to the current in this region. Indeed, the comparison of Fig. 4.18 and Fig. 4.19 shows that the current in the unstable case is enhanced in this region with respect to the stable case. It is important to note, that in contrary to the bulk situation, the effect on the vortex charge does not come directly from the terms proportional to the chirality χ, but from terms which describe the asymptotic behavior of the order parameters in the core.

An alternative explanation to the difference in the vortex core charge could be given in terms of the individual energy levels in the cores. Assuming $T = 0$, in the stable

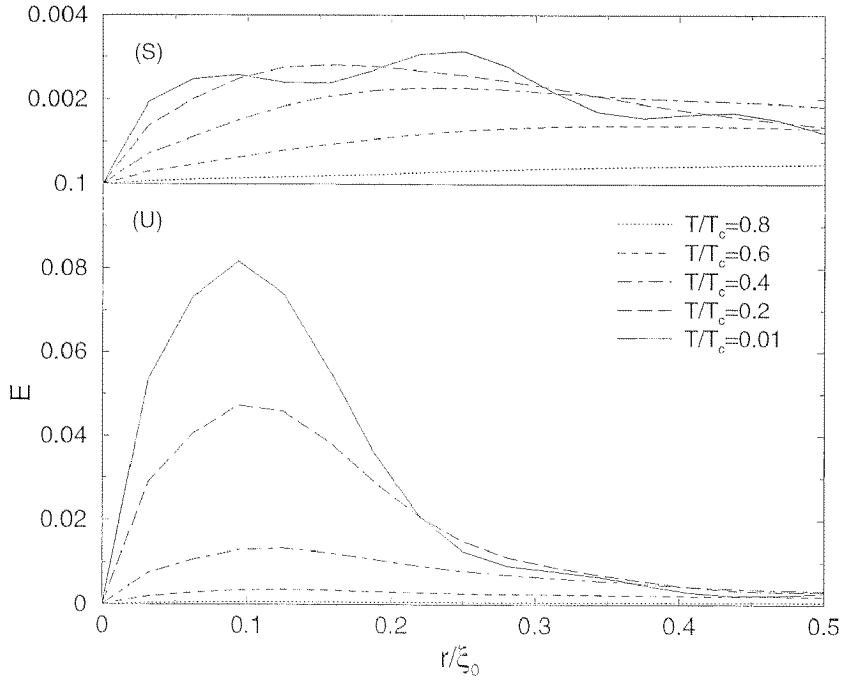

Figure 4.20: Radial electric field $E(r)$ for the stable (S) and unstable (U) p-wave case for $k_F\xi_0 = 16$ and different T. Note that the scale for the (S) case is a factor 10 smaller than for (U).

p-wave case (S), the zero energy level $(u_{0,l}, v_{0,l})$ has angular momentum $l = 0$ and thus has a contribution proportional to a Bessel-function $|J_0(0)|^2$ to the charge density $\rho = -\sum_{E_n=0} |v_n|^2 - 2\sum_{E_n>0} |v_n|^2$. In the unstable case (U), all quasiparticle amplitudes with positive energy which contribute to the charge density have higher angular momentum, and thus vanish at the core. Compared with the unstable case, one therefore expects an extra negative charge in the core of the stable case due to the $l = 0$-contribution, in qualitative agreement with the numerics. This discussion is closely related to a treatment of the s-wave case[87].

At the moment both explanations are certainly only of a qualitative nature. A more quantitative approach to decide between the two ideas is subject of current research.

4.5 Conclusion

In this chapter, we have solved the problem of a single p-wave vortex corresponding to the Γ_{5u}^- symmetry self-consistently within Bogoliubov-de Gennes theory. Our results include full screening in both charge and current and are performed near the quantum limit (values $k_F\xi_0 \leq 16$). The two component order parameter shows near the core the expected behavior found already in the Ginzburg-Landau calculations of the last chapter (*cf.* Chapter 3): for fixed direction of the B-field in positive z-direction, the dominant order parameter η_- (η_+) for the stable (unstable) case shows a linear rise in the core and saturates to the bulk value for large r. The admixed order parameters rises linearly for the stable case and cubic for the unstable case, decaying to zero at large radii r. At low temperatures, the vortex core size shrinks considerably according to the Kramer-Pesch effect. As in the s-wave case, the temperature dependence of this effective vortex size ξ_1 is given by the Kramer-Pesch result $\xi_1 \sim T/T_c$, saturating at $\xi_1 \sim 1/k_F$ for very low temperatures. This narrowing of the vortex core affects directly the quasiparticle energy spectrum. Instead of an equidistant energy spectrum $E_n = \omega_0 n$ with a minigap $\omega_0 \approx \Delta_0^2/E_F$, we observe the first non-zero energy state to be substantially enhanced in energy. The numerical results for the energies E_1 agree perfectly with a quasiclassical calculation using the reduced vortex size ξ_1. We conclude that the shift in energy is primarily due to the Kramer-Pesch effect. A surprising result is obtained for the vortex charging in these p-wave systems. While one finds a substantial vortex charging in the s-wave case and the unstable p-wave case, the vortex charge in the stable p-wave case is suppressed by a large factor. Most probably this effect can be explained in terms of anomalous charge and current contributions reflecting the time reversal symmetry breaking of this superconducting order parameter. While a qualitative explanation of the reduced vortex charging is possible, further investigation is needed for a more quantitative comparison.

Chapter 5

Vortex Lattices within Bogoliubov de Gennes Theory

5.1 Introduction

The problem of a single isolated vortex as presented in the last chapter is numerically quite easily solvable for situations with perfect or at least approximate circular symmetry. If this circular symmetry is broken either due to anisotropic pairing as for example in the $d_{x^2-y^2}$ system or due to periodic boundary conditions occurring in vortex lattices, the problem is far more involved. If gap nodes are present as in the case of a $d_{x^2-y^2}$-wave superconductor, the question arises whether the low energy excitations in a vortex core are localized as in the fully gapped s-wave case, or extended along the gap nodes. Since the nature of the quasiparticle excitations is crucial for the understanding of the low-energy physics of the mixed state, this question is of great importance.

Early theoretical investigations on the $d_{x^2-y^2}$-wave spectrum were performed by Volovik, using quasiclassical arguments[97]. In the limit of small applied fields H and large $k_F\xi_0$, he determined the averaged density of states at the Fermi level $N(0)$ to be proportional to $\sqrt{H}$ instead of H found for the s-wave system. In its simplest form, the $\sqrt{H}$ behavior can be derived by observing that the supercurrent around each individual vortex Doppler-shifts the local quasiparticle spectrum $E_{\boldsymbol{k}} \rightarrow E_{\boldsymbol{k}} - \boldsymbol{v}_s(\boldsymbol{r})\boldsymbol{k}$. This results in a finite local density of states $N(0,\boldsymbol{r}) \propto v_s(\boldsymbol{r}) \propto 1/r$. Integrating the LDOS up to the intervortex distance $R \sim \sqrt{H_{c2}/H}$ and multiplying with the vortex density H/Φ_0 leads to the $\sqrt{H}$-behavior. This prediction was experimentally confirmed by early measurements of the specific heat at low temperatures[98]. After first calculations due to Soininen *et al.*[24], Wang and MacDonald presented a numerical investigation of the $d_{x^2-y^2}$-wave Bogoliubov de-Gennes equations for a vortex

lattice[99]. Using a single band lattice hamiltonian, they found a local density of states which showed a broad peak in the vortex core. Their average local density of states $N(0)$ seemed to fit the predicted $\sqrt{H}$-law. In a refined quasiclassical calculation, Schopohl and Maki[100, 101] showed the local density of states of a single vortex to have a significant fourfold structure, in sharp contrast to the s-wave case. Following Ichioka *et al.*[29], this fourfold pattern is due to four specific quasiclassical particle orbits which follow asymptotically the directions of the gap nodes. A very important contribution to the discussion about the local density of states in $d_{x^2-y^2}$-wave vortex cores were the scanning tunneling microscopy (STM) measurements by the Geneva group[10, 9, 11, 12]. The tunneling conductance of the STM tip dI/dV is in first approximation proportional to the (thermally broadened) local density of states. Scanning a vortex at fixed bias eV leads therefore to a complete map of the LDOS at this energy. The dI/dV spectra at zero applied field are clearly different for BiSCCO and YBCO. While the first shows a DOS which is rather close to a simple $d_{x^2-y^2}$-wave spectrum, in YBCO a very large zero bias conductance is measured, and several nontrivial subpeaks at energies smaller than the gap are observed. The LDOS in the vortex core shows for YBCO two characteristic peaks at energies $\sim \pm\Delta_0/4$. These measured subgap peaks in the LDOS of a vortex core were first tentatively identified as the lowest bound states of a s-wave like spectrum for the very low number $k_F\xi_0 \sim 2$, suggesting an essentially localized character of the lowest excitations in the $d_{x^2-y^2}$-wave core. Unfortunately, the STM-method has still not enough spatial resolution to decide about the predicted fourfold anisotropy in the LDOS[100, 101].

After some quite controversial attempts to solve the Bogoliubov-de Gennes equations approximatively[102, 103, 104], Franz and Tešanović[105] presented a first self-consistent solution of the single vortex problem. Using an interaction potential with a fourfold structure in the relative coordinate $V(r,\varphi) = V\cos^2(2\varphi)\delta(r-a)/a$, they found the lowest energy states to be strongly peaked near the vortex core, however extended along the gap nodes. Their calculated LDOS showed a series of peaks at very low energies, in direct contradiction to the experimental finding. Suggesting a fully gapped mixed $d_{x^2-y^2} + i\epsilon d_{xy}$ order parameter with a magnetic field induced d_{xy} component ($\epsilon < 1$) led them to qualitatively satisfying LDOS spectra showing a small minigap to the lowest energy peaks. Very recently, the field has gained new impulse through several interesting works. Gorkhov and Schrieffer made a remarkable prediction, that in a $d_{x^2-y^2}$-wave superconductor at intermediate fields $H_{c1} \ll H \ll H_{c2}$, the quasiparticles will form Landau levels (LL) with a discrete energy spectrum $E_n = \pm\hbar\omega_H\sqrt{n}$ where $\omega_H = 2\sqrt{\omega_c\Delta_0/\hbar}$ with $\omega_c = eB/mc$ being the cyclotron frequency. However, in this approach the influence of the spatially varying supercurrents is neglected, which, following Melnikov[106], strongly mix the individual Landau levels. Based on a systematic group theoretical treatment of the magnetic translation group[107, 108, 109],

Yasui and Kita presented a fully self-consistent calculation of the energy spectrum of a continuum $d_{x^2-y^2}$ model[110]. They expanded the Bogoliubov-de Gennes hamiltonian into eigenstates of the magnetic translation group, determined by a Landau level index and a magnetic Bloch vector. While the s-wave case shows for low magnetic fields an essentially flat quasiparticle dispersion corresponding to the hopping bands of localized states, for the $d_{x^2-y^2}$-wave system they obtain energy bands reaching zero energy and showing large dispersion. The results for the LDOS in the vortex core show a large zero bias peak for low applied fields $B/H_{c2} = 0.05$, which splits into two peaks at fields $B/H_{c2} = 0.3$. Introducing a field induced time reversal symmetry breaking id_{xy} component does not alter the picture also for substantially high values for this admixture. While the qualitative picture resembles the experimental findings quite well, the STM results were taken at considerably smaller fields. Recently, Franz and Tešanović[111] proposed an interesting approach using a singular gauge transformation (see below) to get rid of the order parameter phase singularities at the vortex cores. The resulting problem is formally equivalent to a problem of quasiparticles in zero average field and can be treated by band structure techniques. In a non-selfconsistent approach to the low energy spectrum, the authors found a vanishing LDOS at the Fermi level, in contrast to the works using Landau levels, and a series of peaks due to van Hove singularities. They concluded, that the superfluid response of a superconductor ensures that the effective magnetic field B_{eff} seen by a fermionic quasiparticle is zero on average, even in the vortex state. This notion is not correct, as we will show later, since the singular contributions of the gauge transformation have no effect on the quasiparticles at all.

In this chapter we extend the singular gauge method to solve the Bogoliubov-de Gennes problem for a vortex lattice self-consistently. The main problem of the description of magnetic flux lattices is, that a non-vanishing average B-field leads to vector potentials which are fundamentally not periodic. Thus, the whole system formulated in quasiparticles cannot be expanded in usual Bloch-states (see Ref.[111] for a nice outline of the problem). Thus one is either bound to a description within basis functions of the magnetic translation group (see Ref.[110]), or one uses a singular gauge transformation to be able to expand in usual Bloch vectors. The idea to apply such gauge transformations in the description of electronic properties near periodic magnetic fields was presented by Nielsen and Hedegård[112, 113]. They introduced the method to investigate a two dimensional electron gas subject to periodic or disordered distributions of magnetic flux quanta. The basic idea is, that a particle with charge e can not feel an infinitely thin solenoid carrying a flux equal to an integer multiple of the electronic flux quantum $\Phi_0^e = h/e$ (corresponding to an even multiple of the superconducting flux quantum $\Phi_0 = h/2e$). The reason is the vanishing spatial extent of the B-field on the one hand and the vanishing of Aharonov-Bohm type effects

due to the special size of the enclosed flux on the other hand. This point goes apparently back to Dirac[114, 115], and consequently such string-like objects carrying single flux quanta are usually called Dirac vortices. We will apply this method on our Bogoliubov-de Gennes problem on the vortex lattice introduced in this chapter and outline the structure of the gauge transformed problem. It turns out, that despite of the decomposition of the problem into subspaces with constant Bloch vector, the numerical effort to solve the model is considerable and requires more efficient algorithms. Preliminary results on smaller systems are presented in the last section, which demonstrate the principal applicability of the method.

5.2 Bogoliubov-de Gennes equations for vortex lattices

5.2.1 Introduction

As starting point we use the Bogoliubov-de Gennes formalism in dimensionless units developed in the last chapter (Section 4.2). Note that we use slightly different scales for length, energy and vector potential

$$\begin{aligned} r_{sc} &= \xi_a \\ E_{sc} &= E_F \\ A_{sc} &= \frac{\Phi_0}{\pi\xi_a} = \frac{\hbar c}{e\xi_a}. \end{aligned} \tag{5.1}$$

where ξ_a is a length of the order of the BCS coherence length. The kinetic part of the hamiltonian in these scales then reads

$$h_0(\boldsymbol{r}) = \frac{1}{k_F^2}\left(\frac{1}{i}\boldsymbol{\nabla} + \boldsymbol{A}(\boldsymbol{r})\right)^2 - 1. \tag{5.2}$$

A further difference to former sections occurs in the p-wave case: since for lattice solutions we loose the circular symmetry, it is more convenient to use the order parameter components (η_x, η_y) rather than (η_+, η_-). Instead of Eqs. (4.17,4.26), we use therefore

$$\begin{pmatrix} \tilde{u}_n(\boldsymbol{r}) \\ \tilde{v}_n(\boldsymbol{r}) \end{pmatrix} = \frac{1}{\sqrt{L_z}} \begin{pmatrix} u_n(\boldsymbol{x}) \\ v_n(\boldsymbol{x}) \end{pmatrix} \tag{5.3}$$

and

$$\begin{pmatrix} h_0 & -\frac{i}{k_F}\left(\boldsymbol{\eta}\boldsymbol{\nabla} + \frac{1}{2}(\boldsymbol{\nabla}\boldsymbol{\eta})\right) \\ -\frac{i}{k_F}\left(\boldsymbol{\eta}^*\boldsymbol{\nabla} + \frac{1}{2}(\boldsymbol{\nabla}\boldsymbol{\eta}^*)\right) & -h_0^* \end{pmatrix} \begin{pmatrix} u_n \\ v_n \end{pmatrix} = E_n \begin{pmatrix} u_n \\ v_n \end{pmatrix}. \tag{5.4}$$

The self-consistency relation for the gap function reads

$$\begin{aligned}\boldsymbol{\eta}(\boldsymbol{r}) &= -\frac{iV}{2k_F}\upsilon_0\sum_n\Big(\tilde{v}_n^*(\boldsymbol{r})\boldsymbol{\nabla}\tilde{u}_n(\boldsymbol{r})-\tilde{u}_n(\boldsymbol{r})\boldsymbol{\nabla}\tilde{v}_n^*(\boldsymbol{r})\Big)\tanh\left(\frac{\beta E_n}{2}\right)\\ &= -\frac{iV_{2D}}{2k_F}\upsilon\sum_n\Big(v_n^*(\boldsymbol{x})\boldsymbol{\nabla}u_n(\boldsymbol{x})-u_n(\boldsymbol{x})\boldsymbol{\nabla}v_n^*(\boldsymbol{x})\Big)\tanh\left(\frac{\beta E_n}{2}\right).\end{aligned}\tag{5.5}$$

Further, for simplicity we neglect self-consistent screenings in current and charge and work with a fixed vector potential corresponding to Gaussian B-field peaks (see below). The introduction of self-consistency in the electromagnetic quantities poses no principal problem in our formalism, since the physical quantities are periodic with respect to the vortex lattice and can easily be expanded in the corresponding unit vectors. However, self-consistent calculations including screening have to be relaxed very slowly and thus the calculation time increases considerably.

5.2.2 Geometry

The unit cell of the two-dimensional vortex lattice is determined by the two primitive vectors $\boldsymbol{a}_1$ and $\boldsymbol{a}_2$. Below we will see, that we have to work with a unit cell which is twice as large, called magnetic unit cell. We use for reasons of symmetry the diagonal unit cell defined through the vectors

$$\begin{aligned}\boldsymbol{c}_1 &= \boldsymbol{a}_1-\boldsymbol{a}_2\\ \boldsymbol{c}_2 &= \boldsymbol{a}_1+\boldsymbol{a}_2.\end{aligned}\tag{5.6}$$

We denote the opening angle measured from $\boldsymbol{c}_1$ in positive direction to $\boldsymbol{c}_2$ with θ and the angle between the x-axis and $\boldsymbol{c}_1$ with φ. Using

$$\begin{aligned}|\boldsymbol{c}_1\wedge\boldsymbol{c}_2| &= 2V_{uc}=|\boldsymbol{c}_1||\boldsymbol{c}_2|\sin\theta\\ \frac{|\boldsymbol{c}_2|}{|\boldsymbol{c}_1|} &= \zeta\end{aligned}\tag{5.7}$$

leads to the relations

$$\begin{aligned}\boldsymbol{c}_1 &= |\boldsymbol{c}_1|\Big(\cos\varphi,\sin\varphi\Big)\\ \boldsymbol{c}_2 &= |\boldsymbol{c}_2|\Big(\cos(\varphi+\theta),\sin(\varphi+\theta)\Big)\\ |\boldsymbol{c}_1| &= \sqrt{\frac{2V_{uc}}{\zeta\sin\theta}}\\ |\boldsymbol{c}_2| &= \sqrt{\frac{2V_{uc}\zeta}{\sin\theta}}.\end{aligned}\tag{5.8}$$

For the components of the reciprocal vectors we obtain

$$\begin{aligned} \boldsymbol{d}_1 &= \frac{2\pi}{2V_{uc}}(\boldsymbol{c}_2 \wedge \hat{\boldsymbol{z}}) = 2\pi\sqrt{\frac{\zeta}{2V_{uc}\sin\theta}}\Big(\sin(\varphi+\theta), -\cos(\varphi+\theta)\Big) \\ \boldsymbol{d}_2 &= -\frac{2\pi}{2V_{uc}}(\boldsymbol{c}_1 \wedge \hat{\boldsymbol{z}}) = 2\pi\sqrt{\frac{1}{2V_{uc}\zeta\sin\theta}}\Big(-\sin\varphi, \cos\varphi\Big). \end{aligned} \tag{5.9}$$

5.2.3 Self-consistent equations for the vortex lattice

As outlined above, the main idea of this approach is that we gauge away the topological phase singularities at the vortex cores through a singular gauge transformation. This gauge transformation has a fixed form and basically leads to an addition of Dirac δ-peaks of strength $-\Phi_0^e$ in the B-field, which exactly cancel out the average magnetic field. These δ-peaks in the B-field have no effect on the quasiparticles: since they have finite size and live on a vanishing area, they do not affect the quasiparticles directly, and a possible Aharonov-Bohm effect vanishes due to the flux being equal to the electronic flux quantum, which is given in our dimensionless units as

$$\Phi_0^e = \frac{hc}{e} = \frac{hc}{eA_{sc}r_{sc}} = 2\pi. \tag{5.10}$$

We start with the dominant order parameter component near a vortex core at position $\boldsymbol{r}_i$ given as

$$\eta(\boldsymbol{r}) \propto \hat{\eta}(\boldsymbol{r})e^{-i\phi_i(\boldsymbol{r})}, \tag{5.11}$$

where $\phi_i(\boldsymbol{r})$ is the pure topological phase singularity obeying

$$\boldsymbol{\nabla} \wedge \boldsymbol{\nabla}\phi_i(\boldsymbol{r}) = -2\pi\delta(\boldsymbol{r}-\boldsymbol{r}_i). \tag{5.12}$$

The order parameter $\hat{\eta}(\boldsymbol{r})$ may still carry a complex phase, but without topological defects. Having in mind the self-consistency relation $\eta(\boldsymbol{r}) \propto \sum_n u_n(\boldsymbol{r})v_n^*(\boldsymbol{r})$, it is obvious that the singular gauge transformation can be implemented as

$$\begin{pmatrix} u_n \\ v_n \end{pmatrix} = \begin{pmatrix} e^{i\phi_u(\boldsymbol{r})} & 0 \\ 0 & e^{-i\phi_v(\boldsymbol{r})} \end{pmatrix} \begin{pmatrix} \hat{u}_n \\ \hat{v}_n \end{pmatrix} \tag{5.13}$$

with $\phi_u(\boldsymbol{r}) + \phi_v(\boldsymbol{r}) = \phi_i(\boldsymbol{r})$. However, since the phase $\phi_i(\boldsymbol{r})$ corresponds to one phase turn, a splitting of $\phi_i(\boldsymbol{r})$ into two nonzero contributions would lead to quasiparticle wavefunctions $\hat{u}_n$ and $\hat{v}_n$ which are not single-valued. Therefore it is favorable to compensate every vortex phase turn either by a phase transformation in the particle or in the hole part. In principle one is free to choose such an assignment. It is convenient to decompose the vortex lattice into two sublattices A and B, where we choose for A the diagonal lattice formed through the vectors $\boldsymbol{c}_1$ and $\boldsymbol{c}_2$ and for B the

same lattice translated by $(\boldsymbol{c}_1 + \boldsymbol{c}_2)/2$. We define the unitary gauge transformation as

$$\begin{pmatrix} u_n \\ v_n \end{pmatrix} = \begin{pmatrix} e^{i\phi_A(\boldsymbol{r})} & 0 \\ 0 & e^{-i\phi_B(\boldsymbol{r})} \end{pmatrix} \begin{pmatrix} \hat{u}_n \\ \hat{v}_n \end{pmatrix} \tag{5.14}$$

where the phase functions $\phi_{A,B}$ carry now the topological phase singularities of the sublattice A (B analogously)

$$\boldsymbol{\nabla} \wedge \boldsymbol{\nabla}\phi_A(\boldsymbol{r}) = -2\pi \sum_{i \in A} \delta(\boldsymbol{r} - \boldsymbol{r}_i). \tag{5.15}$$

This term is actually the contribution of the singular gauge transformation to the vector potential $\boldsymbol{A}(\boldsymbol{r})$. Comparing with Eq. (5.10) we see that a Dirac vortex opposing the average field direction with the size of two superconducting flux quanta is induced in every sublattice cell. This contribution exactly cancels the average field $\bar{B} = \Phi_0/V_{uc}$. Having the average B-field now equal to zero, it is possible to perform a simple Bloch wave expansion in all occurring quantities. In the following we apply this gauge transformation to the Bogoliubov-de Gennes system of the last chapter.

Diagonal parts

First we implement this gauge transform on the diagonal blocks (kinetic energy terms), and obtain for the upper diagonal block

$$\begin{aligned} e^{-i\phi_A} h_0 e^{i\phi_A} &= e^{-i\phi_A} \frac{1}{k_F^2} \left(\frac{1}{i}\boldsymbol{\nabla} + \boldsymbol{A}(\boldsymbol{r}) \right)^2 e^{i\phi_A} - 1 \\ &= \frac{1}{k_F^2} \left(\frac{1}{i}\boldsymbol{\nabla} + \boldsymbol{\nabla}\phi_A(\boldsymbol{r}) + \boldsymbol{A}(\boldsymbol{r}) \right)^2 - 1 \\ &= \frac{1}{k_F^2} \left(\frac{1}{i}\boldsymbol{\nabla} - \boldsymbol{Q}_A(\boldsymbol{r}) \right)^2 - 1, \end{aligned} \tag{5.16}$$

where we defined the vector potential in this singular gauge as

$$\boldsymbol{Q}_A(\boldsymbol{r}) = -\boldsymbol{\nabla}\phi_A(\boldsymbol{r}) - \boldsymbol{A}(\boldsymbol{r}). \tag{5.17}$$

The equations for the lower diagonal are correspondingly

$$e^{i\phi_B}(-h_0^*)e^{-i\phi_B} = -\frac{1}{k_F^2} \left(-\frac{1}{i}\boldsymbol{\nabla} - \boldsymbol{Q}_B(\boldsymbol{r}) \right)^2 - 1 \tag{5.18}$$

with

$$\boldsymbol{Q}_B(\boldsymbol{r}) = -\boldsymbol{\nabla}\phi_B(\boldsymbol{r}) - \boldsymbol{A}(\boldsymbol{r}). \tag{5.19}$$

Note, that as outlined above, the vector potential has vanishing average curl, which means that the average B-field is zero

$$\left\langle \boldsymbol{\nabla} \wedge \boldsymbol{Q}_{A,B} \right\rangle_{2V_{uc}} = \left\langle -B(\boldsymbol{r}) + 2\pi \sum_{i \in A,B} \delta(\boldsymbol{r} - \boldsymbol{r}_i) \right\rangle_{2V_{uc}} = -\bar{B} + \frac{2\pi}{2V_{uc}} = 0. \tag{5.20}$$

This is true, since the superconducting flux quantum in our units is $\Phi_0 = \pi$ as derived earlier. Next, we implement the singular gauge transformation on the off-diagonal terms for the different symmetries of gap functions.

Off-diagonal parts: s-waves

The s-wave case is particularly easy to transform. For the off-diagonal terms we define

$$\eta_s = e^{i(\phi_A + \phi_B)} \hat{\eta}_s \tag{5.21}$$

and obtain

$$e^{-i\phi_A} \eta_s e^{-i\phi_B} = \hat{\eta}_s. \tag{5.22}$$

The lower left off-diagonal block consequently reads

$$e^{i\phi_B} \eta_s^* e^{i\phi_A} = \hat{\eta}_s^*, \tag{5.23}$$

and for the self-consistency equation we obtain

$$\begin{aligned} \hat{\eta}_s(\boldsymbol{r}) &= e^{-i(\phi_A + \phi_B)} V_{2D} v \sum_n e^{i\phi_B} \hat{v}_n^* e^{i\phi_A} \hat{u}_n \tanh\left(\frac{\beta E_n}{2}\right) \\ &= V_{2D} v \sum_n \hat{v}_n^* \hat{u}_n \tanh\left(\frac{\beta E_n}{2}\right). \end{aligned} \tag{5.24}$$

p-waves

The occurrence of derivatives in both the off-diagonal part of the Bogoliubov-de Gennes hamiltonian and the self-consistency relation for the order parameter complicates the situation considerably. For the off-diagonal terms we define as above

$$\boldsymbol{\eta} = e^{i(\phi_A + \phi_B)} \hat{\boldsymbol{\eta}} \tag{5.25}$$

and obtain

$$\begin{aligned} & e^{-i\phi_A} \left(-\frac{i}{k_F} \left(e^{i(\phi_A + \phi_B)} \hat{\boldsymbol{\eta}} \boldsymbol{\nabla} + \frac{1}{2} (\boldsymbol{\nabla} e^{i(\phi_A + \phi_B)} \hat{\boldsymbol{\eta}}) \right) \right) e^{-i\phi_B} \\ &= -\frac{i}{k_F} \left(\hat{\boldsymbol{\eta}} (\boldsymbol{\nabla} - i \boldsymbol{\nabla} \phi_B) + \frac{1}{2} \Big((\boldsymbol{\nabla} + i \boldsymbol{\nabla} \phi_A + i \boldsymbol{\nabla} \phi_B) \hat{\boldsymbol{\eta}} \Big) \right) \\ &= -\frac{i}{k_F} \left(\hat{\boldsymbol{\eta}} \boldsymbol{\nabla} + \frac{1}{2} (\boldsymbol{\nabla} \hat{\boldsymbol{\eta}}) - \frac{i}{2} \hat{\boldsymbol{\eta}} (\boldsymbol{\nabla} \phi_B - \boldsymbol{\nabla} \phi_A) \right) \\ &= -\frac{i}{k_F} \left(\hat{\boldsymbol{\eta}} \boldsymbol{\nabla} + \frac{1}{2} (\boldsymbol{\nabla} \hat{\boldsymbol{\eta}}) + \frac{i}{2} \hat{\boldsymbol{\eta}} (\boldsymbol{Q}_B - \boldsymbol{Q}_A) \right). \end{aligned} \tag{5.26}$$

The lower left off-diagonal block consequently reads

$$\begin{aligned} & e^{i\phi_B}\left(-\frac{i}{k_F}\left(e^{-i(\phi_A+\phi_B)}\hat{\boldsymbol{\eta}}^*\boldsymbol{\nabla}+\frac{1}{2}(\boldsymbol{\nabla}e^{-i(\phi_A+\phi_B)}\hat{\boldsymbol{\eta}}^*)\right)\right)e^{i\phi_A} \\ &= -\frac{i}{k_F}\left(\hat{\boldsymbol{\eta}}^*\boldsymbol{\nabla}+\frac{1}{2}(\boldsymbol{\nabla}\hat{\boldsymbol{\eta}}^*)+\frac{i}{2}\hat{\boldsymbol{\eta}}^*\left(\boldsymbol{Q}_B-\boldsymbol{Q}_A\right)\right), \end{aligned} \tag{5.27}$$

and for the self-consistency relation we obtain

$$\begin{aligned} \hat{\boldsymbol{\eta}}(\boldsymbol{r}) &= e^{-i(\phi_A+\phi_B)}\left(-\frac{iV_{2D}}{2k_F}\upsilon\right)\sum_n\left(e^{i\phi_B}\hat{v}_n^*\boldsymbol{\nabla}e^{i\phi_A}\hat{u}_n-e^{i\phi_A}\hat{u}_n\boldsymbol{\nabla}e^{i\phi_B}\hat{v}_n^*\right)\tanh\left(\frac{\beta E_n}{2}\right) \\ &= -\frac{iV_{2D}}{2k_F}\upsilon\sum_n\left(\hat{v}_n^*(\boldsymbol{\nabla}+i\boldsymbol{\nabla}\phi_A)\hat{u}_n-\hat{u}_n(\boldsymbol{\nabla}+i\boldsymbol{\nabla}\phi_B)\hat{v}_n^*\right)\tanh\left(\frac{\beta E_n}{2}\right) \\ &= -\frac{iV_{2D}}{2k_F}\upsilon\sum_n\left(\hat{v}_n^*\boldsymbol{\nabla}\hat{u}_n-\hat{u}_n\boldsymbol{\nabla}\hat{v}_n^*+i(\boldsymbol{Q}_B-\boldsymbol{Q}_A)\hat{v}_n^*\hat{u}_n\right)\tanh\left(\frac{\beta E_n}{2}\right). \end{aligned} \tag{5.28}$$

d-waves

Finally we calculate the d-wave case: with the definition

$$\eta_d = e^{i(\phi_A+\phi_B)}\hat{\eta}_d \tag{5.29}$$

we obtain for the upper right off-diagonal part

$$\begin{aligned} & e^{-i\phi_A}\left(-\frac{1}{k_F^2}\Big(e^{i(\phi_A+\phi_B)}\hat{\eta}_d(\partial_x^2-\partial_y^2)+\left((\partial_x e^{i(\phi_A+\phi_B)}\hat{\eta}_d)\partial_x-(\partial_y e^{i(\phi_A+\phi_B)}\hat{\eta}_d)\partial_y\right)\right. \\ &\qquad\left.+\frac{1}{4}\left((\partial_x^2-\partial_y^2)\,e^{i(\phi_A+\phi_B)}\hat{\eta}_d\right)\Big)\right)e^{-i\phi_B} \\ &= -\frac{1}{k_F^2}\left(\frac{1}{4}(\partial_x^2-\partial_y^2)\hat{\eta}_d+\Big((\partial_x\hat{\eta}_d)\partial_x-(\partial_y\hat{\eta}_d)\partial_y\Big)+\hat{\eta}_d(\partial_x^2-\partial_y^2)\right. \\ &\quad -i\hat{\eta}_d\Big((Q_A^x-Q_B^x)\partial_x-(Q_A^y-Q_B^y)\partial_y\Big)-\frac{i}{2}\Big((Q_A^x-Q_B^x)\partial_x\hat{\eta}_d-(Q_A^y-Q_B^y)\partial_y\hat{\eta}_d\Big) \\ &\quad -\frac{1}{4}\Big((Q_A^x-Q_B^x)^2-(Q_A^y-Q_B^y)^2\Big)\hat{\eta}_d \\ &\quad \left.-\frac{i}{2}\hat{\eta}_d\Big(\partial_x(Q_A^x-Q_B^x)-\partial_y(Q_A^y-Q_B^y)\Big)-\frac{i}{4}\hat{\eta}_d(\partial_x^2-\partial_y^2)(\phi_A+\phi_B)\right). \end{aligned} \tag{5.30}$$

The lower left off-diagonal block has almost exactly the same form, however with all $\hat{\eta}_d$ replaced by $\hat{\eta}_d^*$ and with the last sign reversed in front of the term proportional to $(\phi_A+\phi_B)$. The self-consistency equation finally reads

$$\hat{\eta}_d(\boldsymbol{r}) = -e^{-i(\phi_A+\phi_B)}\frac{V_{2D}\upsilon_0}{4k_F^2}\sum_n\left(e^{i\phi_B}\hat{v}_n^*(\partial_x^2-\partial_y^2)e^{i\phi_A}\hat{u}_n+e^{i\phi_A}\hat{u}_n(\partial_x^2-\partial_y^2)\hat{v}_n^*\right.$$

$$
\begin{aligned}
&\qquad -2\Big(\partial_x(e^{i\phi_B}\hat{v}_n^*)\partial_x(e^{i\phi_A}\hat{u}_n)-\partial_y(e^{i\phi_B}\hat{v}_n^*)\partial_y(e^{i\phi_A}\hat{u}_n)\Big)\Big)\tanh\left(\frac{\beta E_n}{2}\right)\\
&= -\frac{V_{2D}\upsilon_0}{4k_F^2}\sum_n\Bigg(\hat{v}_n^*(\partial_x^2-\partial_y^2)\hat{u}_n+\hat{u}_n(\partial_x^2-\partial_y^2)\hat{v}_n^*-2\Big((\partial_x\hat{v}_n^*)(\partial_x\hat{u}_n)-(\partial_y\hat{v}_n^*)(\partial_y\hat{u}_n)\Big)\\
&\quad -\hat{u}_n\hat{v}_n^*\Big((Q_A^x-Q_B^x)^2-(Q_A^y-Q_B^y)^2\Big)+i\hat{u}_n\hat{v}_n^*(\partial_x^2-\partial_y^2)(\phi_A+\phi_B)\\
&\quad -2i\hat{v}_n^*\Big((Q_A^x-Q_B^x)\partial_x-(Q_A^y-Q_B^y)\partial_y\Big)\hat{u}_n\\
&\quad +2i\hat{u}_n\Big((Q_A^x-Q_B^x)\partial_x-(Q_A^y-Q_B^y)\partial_y\Big)\hat{v}_n^*\Bigg)\tanh\left(\frac{\beta E_n}{2}\right).
\end{aligned}
\tag{5.31}
$$

Starting from here, we simplify the notation and let all hats away, dealing with the new quasiparticles and gap functions only.

5.2.4 Bloch ansatz

As mentioned already, in this gauge all physical quantities occurring in the Bogoliubov-de Gennes hamiltonian can be shown to be periodic with respect to the magnetic unit cells defined above. With other words, the hamiltonian commutes with the lattice translation group corresponding to the magnetic unit cell. It is therefore possible to use a Bloch ansatz to decouple the problem. We assume periodic boundary conditions over many magnetic unit cells

$$\psi(\boldsymbol{r})=\psi(\boldsymbol{r}+\boldsymbol{R}) \tag{5.32}$$

with $\boldsymbol{R}=(2N-1)\boldsymbol{c}_1+(2N-1)\boldsymbol{c}_2$. In this way, we obtain the magnetic Bloch vectors

$$\boldsymbol{K}=v\boldsymbol{D}_1+w\boldsymbol{D}_2 \qquad\qquad v,w\in\{-N+1,\ldots,N-1\} \tag{5.33}$$

where we defined the Bloch unit vectors as

$$
\begin{aligned}
\boldsymbol{D}_1 &= \frac{1}{2N-1}\boldsymbol{d}_1\\
\boldsymbol{D}_2 &= \frac{1}{2N-1}\boldsymbol{d}_2.
\end{aligned}
\tag{5.34}
$$

Given the Bloch vectors $\boldsymbol{K}$, we define the basis functions

$$\phi_{\boldsymbol{K},\boldsymbol{k}}(\boldsymbol{r})=\frac{1}{\sqrt{2(2N-1)^2V_{uc}}}e^{i(\boldsymbol{K}+\boldsymbol{k})\boldsymbol{r}}, \tag{5.35}$$

with the vectors of the reciprocal lattice

$$\boldsymbol{k} = \boldsymbol{k}_{m,n}=m\boldsymbol{d}_1+n\boldsymbol{d}_2. \tag{5.36}$$

As in the last chapter, we work with a two-dimensional circular Fermi surface. Since we have no self-consistency in charge and current, we could restrict our Hilbert space to the states contributing to the self-consistent order parameter. However, it turned out to be favorable to take the Hilbert space larger and introduce a smooth cutoff for the self-consistency equation. We take the Hilbert space as a sheet with thickness $\pm E_H$ around the Fermi surface. The necessary condition for a reciprocal vector $\boldsymbol{k}_{m,n}$ to belong to this Hilbert space is therefore

$$1 - E_H \leq \frac{1}{k_F^2}\boldsymbol{k}_{m,n}^2 = \frac{1}{k_F^2}(d_1^2 m^2 + d_2^2 n^2 + 2\boldsymbol{d}_1\boldsymbol{d}_2 mn) \leq 1 + E_H. \tag{5.37}$$

As an upper bound for the values for m and n, we determine

$$a = \sqrt{k_F^2(1+E_H)}\left(\frac{d_1^2+d_2^2}{2} - \frac{1}{2}\sqrt{(d_1^2-d_2^2)^2 + 4(\boldsymbol{d}_1\boldsymbol{d}_2)^2}\right)^{-\frac{1}{2}}. \tag{5.38}$$

5.2.5 Field distribution

For simplicity we assume a fixed B-field of Gaussian form for every vortex line, contributing one flux quantum

$$B = \frac{1}{2\kappa^2}\sum_i \exp\left(-\frac{(\boldsymbol{r}-\boldsymbol{r}_i)^2}{2\kappa^2}\right). \tag{5.39}$$

For the rotations of the vector potential in singular gauge we find

$$\boldsymbol{\nabla}\wedge\boldsymbol{Q}_A = 2\pi\sum_{i\in A}\delta(\boldsymbol{r}-\boldsymbol{r}_i) - \frac{1}{2\kappa^2}\sum_{i\in A,B} e^{-\frac{(\boldsymbol{r}-\boldsymbol{r}_i)^2}{2\kappa^2}}. \tag{5.40}$$

We calculate the Fourier components of the second part

$$\begin{aligned} -B_{\boldsymbol{k}_{m,n}} &= -\frac{1}{2V_{uc}}\int_{2V_{uc}}\frac{1}{2\kappa^2}\sum_{i\in A,B} e^{-\frac{(\boldsymbol{r}-\boldsymbol{r}_i)^2}{2\kappa^2}} e^{-i\boldsymbol{k}_{m,n}\boldsymbol{r}} d^2\boldsymbol{r} \\ &= -\frac{\pi}{2V_{uc}} e^{-\frac{\kappa^2\boldsymbol{k}_{m,n}^2}{2}}\left(1+e^{-i\pi(m+n)}\right), \end{aligned} \tag{5.41}$$

where we used ($\nu = 0$ for A and $\nu = 1$ for B)

$$\boldsymbol{r}_i\boldsymbol{k}_{m,n} = (p\boldsymbol{c}_1 + q\boldsymbol{c}_2 + \nu\frac{\boldsymbol{c}_1+\boldsymbol{c}_2}{2})(m\boldsymbol{d}_1 + n\boldsymbol{d}_2) = 2\pi(mp+qn) + \nu\pi(m+n). \tag{5.42}$$

The Fourier component of the first part is calculated analogously

$$c_{\boldsymbol{k}_{m,n}} = \frac{\pi}{V_{uc}} \qquad \left(\frac{\pi}{V_{uc}}e^{-i\pi(m+n)} \quad \text{for sublattice } B\right), \tag{5.43}$$

and we obtain for the curl of $\boldsymbol{Q}_{A,B}$

$$\boldsymbol{\nabla} \wedge \boldsymbol{Q}_{A,B} = \frac{\pi}{2V_{uc}} \sum_{m,n} e^{i\boldsymbol{k}_{m,n}\boldsymbol{r}} \left(2 - (1 + e^{-i\pi(m+n)}) e^{-\frac{\kappa^2 \boldsymbol{k}_{m,n}^2}{2}}\right) \begin{cases} 1 & \text{for } A \\ e^{-i\pi(m+n)} & \text{for } B \end{cases} \tag{5.44}$$

and for $\boldsymbol{Q}_{A,B}$ the expression

$$\boldsymbol{Q}_{A,B} = \frac{\pi}{2V_{uc}} \sum_{m,n\neq(0,0)} e^{i\boldsymbol{k}_{m,n}\boldsymbol{r}} \left(2 - (1 + e^{-i\pi(m+n)}) e^{-\frac{\kappa^2 \boldsymbol{k}_{m,n}^2}{2}}\right) \frac{i\boldsymbol{k}_{m,n} \wedge \hat{\boldsymbol{z}}}{\boldsymbol{k}_{m,n}^2} \begin{cases} 1 & \text{for } A \\ e^{-i\pi(m+n)} & \text{for } B \end{cases} . \tag{5.45}$$

In the conventional gauge, the phase factor of a superconducting vortex has a topological singularity, which suppresses the absolute value of the order parameter to zero in the vortex core. Since this is a topological effect, it is present also in microscopic approaches where the spatial resolution is given by the inverse Fermi wavevector $1/k_F$. In the singular gauge used above, this topological restriction has disappeared, and expanding the problem in a finite basis one could expect a non-zero order parameter in the vortex core on a length scale of $1/k_F$. However, it is easily seen that the $\boldsymbol{Q}_{A,B}^2(\boldsymbol{r} - \boldsymbol{r}_i)$ terms occurring in the diagonal blocks have divergencies for $\boldsymbol{r} \to \boldsymbol{r}_i$. To avoid infinite contributions to the eigenvalue problem, the quasiparticle wavefunction have to vanish at the location of the divergences. More precisely, due to the special form of the gauge transformation the electron part of the wavefunction has to vanish on the sublattice A, whereas the hole part vanishes on the sublattice B. For the s-wave case, this leads again to vortex cores which are exactly zero on both sublattices, since $\eta_s \propto \sum_n v_n^* u_n$. For the less simple self-consistency relations for the p- and d-wave case, this is no longer true. Indeed in the numerical results, the vortex cores do not vanish on length scales smaller than $1/k_F$. Similar arguments can be found for the expansion in Bloch wave states.

5.3 Vortex lattice results

5.3.1 Implementation

With the preparations outlined in the last sections, it is possible to implement the problem for numerical solution. We use the Bloch wave basis given in Eq. (5.35) with energies in a shell of width E_H around the Fermi energy $1 - E_H \leq E_{\boldsymbol{k}} \leq 1 + E_H$ (Note that $E_F = 1$ in dimensionless units). The problem decomposes into subspaces with basis functions having constant Bloch wavevector $\boldsymbol{K}$. The corresponding expressions for the matrix elements of the Bogoliubov-de Gennes problem are derived in Appendix D.1.

The order parameter and the vector potential are expanded in the reciprocal unit cell vectors

$$\begin{aligned} \eta(\boldsymbol{r}) &= \sum_{|\boldsymbol{k}|\leq k_H} \eta_{\boldsymbol{k}} e^{i\boldsymbol{k}\boldsymbol{r}} \\ \boldsymbol{Q}(\boldsymbol{r}) &= \sum_{|\boldsymbol{k}|\leq 2k_H} \boldsymbol{Q}_{\boldsymbol{k}} e^{i\boldsymbol{k}\boldsymbol{r}}. \end{aligned} \tag{5.46}$$

The cutoff for the vector potential components is given by $2k_H$, where $k_H = k_F\sqrt{1+E_H}$ is the maximal $|\boldsymbol{k}|$ in the Hilbert space. Components with larger $|\boldsymbol{k}|$ values do not interact with quasiparticles in the Hilbert space. For the order parameter components, a cutoff of the order k_H turned out to be sufficient. The range of the interaction leading to the superconducting order parameter was modeled by a smooth exponential cutoff centered at $E_c \equiv E_H/4$: quasiparticles with wave vectors $\boldsymbol{k}$ enter the self-consistency relation with a contribution proportional to $\exp\left[-((k^2-k_F^2)/E_c)^8\right]$. To reduce computational effort, we used the inversion symmetry of the lattice. All results presented in the next sections are calculated for square vortex lattices, although the method is implemented for the general case. For p-wave symmetry, we restrict to the stable case (*cf.* Chapters 3, 4).

5.3.2 Numerical results

The results described below are to a certain extent preliminary. It turned out, that although we restrict to small values of the Fermi wavelength, the scaling of the numerical effort is quite bad in our code. Given the average magnetic field $\bar{B}$ which determines the primitive reciprocal lattice vectors ($\propto \sqrt{\bar{B}}$), and the typical size of the Hilbert space $\propto k_F^2$, the number of basis vectors per Bloch quantum number is of the order of

$$N_b \propto \frac{k_F^2}{\bar{B}}. \tag{5.47}$$

Since the computing time increases at least with N_b^3 per Bloch quantum number, the problem is quite hard to solve and we are bound to small values of k_F and not too small average fields $\bar{B}$. In the following we present the results of these self-consistent calculations. We chose for all calculations a value $k_F\xi_a = 15$, which is reasonably large to avoid problems with the resolution of vortex cores (*cf.* the comments above), and small enough to handle small $\bar{B}$-fields. To obtain stable results for local density of states and order parameters, it turned out that only few Bloch vectors were needed. Most results were done with $N = 6$, corresponding to periodic boundary conditions over $2N-1 = 11$ magnetic unit cells in both x- and y-direction. The Hilbert space cutoff is taken as $E_H = 0.8$, and the interaction potential strength $vV_{2D} = 0.057$

leading to bulk energy gaps $\Delta_s^0 = 0.14E_F$, $\Delta_p^0 = 0.15E_F$, and $\Delta_d^0 = 0.18E_F$. The calculations are performed at temperatures near $T = 0$. In Fig. 5.2, we show

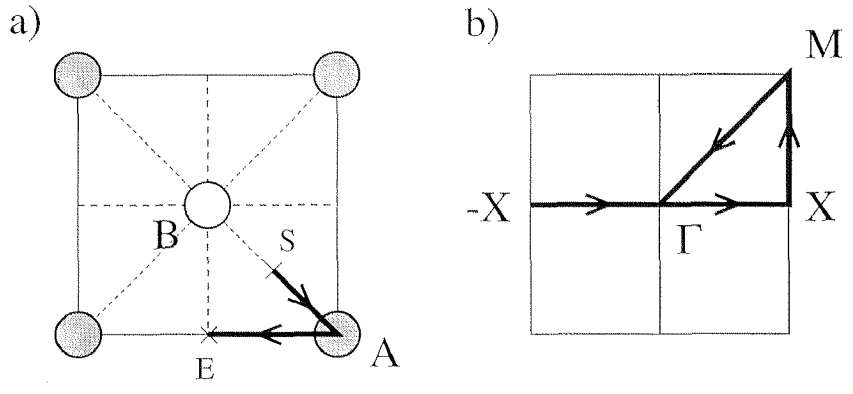

Figure 5.1: Schematic plot of the real space magnetic unit cell (a) and corresponding Brillouin zone (b). The path where the LDOS is calculated is marked by a thick line with arrows in (a), and the path in the Brillouin zone where the band energies are shown is marked by arrows in (b).

the calculated energy spectra for the p-wave case for different average fields ranging from $\bar{B} = 1.2 - 0.2$. Along the horizontal axis, the position of the Bloch vectors is indicated by the crystallographic symmetry points of the magnetic Brillouin zone (see Fig. 5.1 (b)). We encounter a situation which is in many respects close to the situation in an atomic crystal. Instead of atoms with a spectrum of electronic states which form energy bands through their overlap with states of neighboring atoms, we have a discrete spectrum of quasiparticles living in the fully gapped vortex cores. Since the intervortex distance is far larger than the typical crystal lattice constants, the corresponding Brillouin zone of the vortex lattice is much smaller. For small average fields, where the vortex density is small, we expect the Bloch bands to be centered at the bound state levels of the single vortex showing virtually no dispersion. As shown in Fig. 5.2, flat bands which qualitatively correspond to the single vortex energies (*cf.* Fig. 4.12) are observed. The zero energy state, however, is considerably enhanced to a finite energy (note that the states at exactly zero energy are artifacts of the calculation and have no physical meaning). The reason for this is not clear and is subject of current investigation. For increasing average field, the vortices come closer and the overlap of the bound state wavefunctions of neighboring vortices increases. Thus the bands show stronger dispersion (see Fig. 5.2, $B = 1.2, 1.0$) due to increased hopping probability, especially for energetically higher bands. It is important to note that for fields where the bands show nonzero dispersion, these band structures are very sensitive to the intervortex distance and thus to the average B field. This contrasts to the case in atomic lattices, where variations of a few percent in the lattice

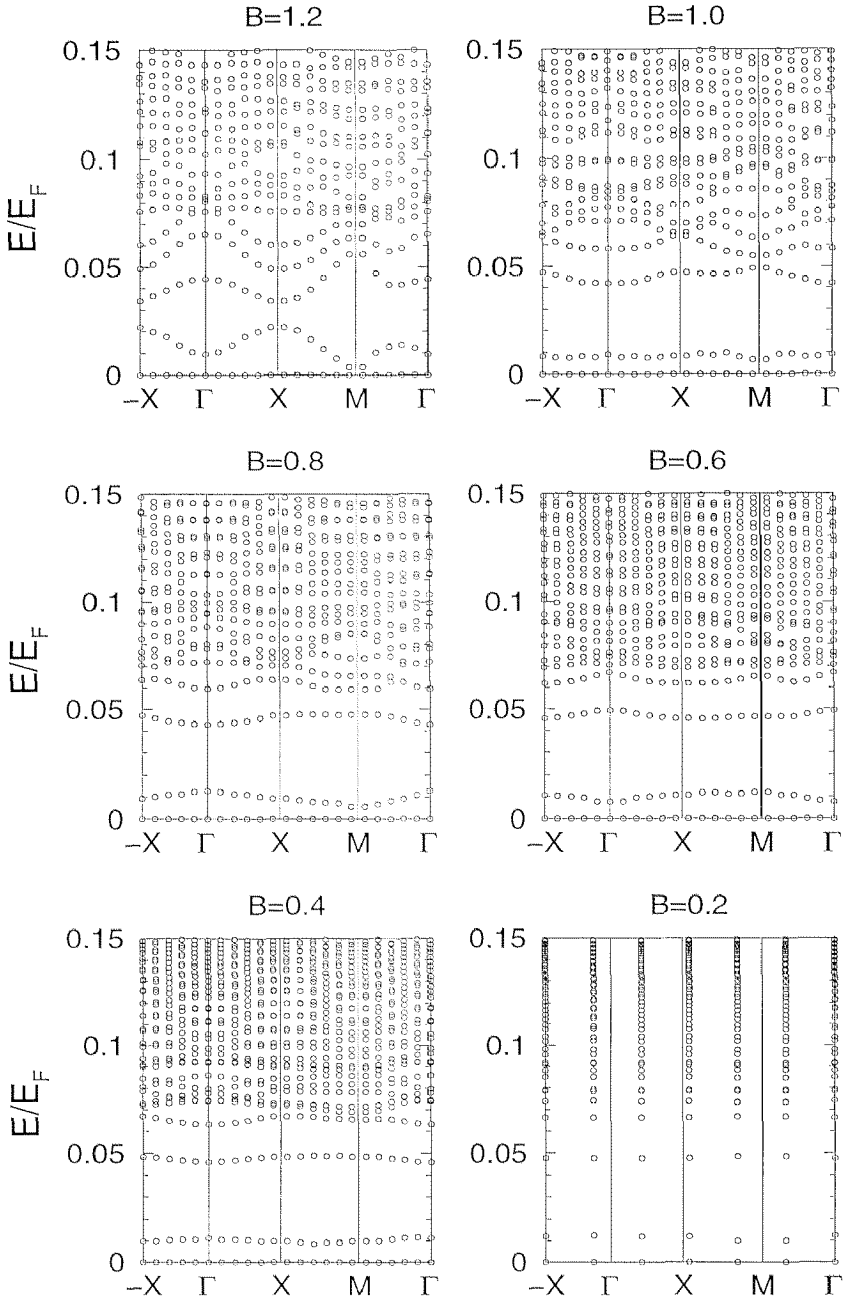

Figure 5.2: Quasiparticle spectra for the p-wave system for different average fields B and $k_F\xi_a = 15$. On the horizontal axis, the position within the magnetic Brillouin zone is marked by the crystallographic symmetry points (*cf.* Fig. 5.1). The range of the vertical axis denoting the particle energy corresponds to the bulk gap $\Delta_p = 0.15E_F$. Note, that the points at exactly zero energy are artifacts of the calculation and do not correspond to physical states.

constant does not change the band structure qualitatively. The reason for this feature

is clear: the band structure is defined through overlap integrals, which vary on a scale of the quasiparticle wavelength $\lambda \propto 1/k_F$. Thus the bands change qualitatively, if the lattice constant is changed by λ. Since the lattice constant for atomic lattices is also of the order $1/k_F$, substantial changes in the lattice constant are necessary to change the band structure considerably. In our vortex lattice band structures, the lattice constant is $a = \sqrt{2\pi/\bar{B}}$, which is much larger than $\lambda \propto 1/k_F$ for small enough $\bar{B}$. The band structures should be essentially constant only for changes in the lattice constant $\Delta a < 1/k_F$, which corresponds to small changes in the average B-field of

$$|\Delta \bar{B}| \ll \frac{1}{k_F}\sqrt{\pi \bar{B}^3}. \tag{5.48}$$

Indeed this behavior was verified in the field range $B \gtrsim 1.0$, where the vortices are close enough to show a significant dispersion. A similar behavior as in the p-wave case is found in the s-wave case (Fig. 5.3, upper graphs). The qualitative comparison of the low field results with the single vortex case shows good agreement. In the d-wave case the situation is completely different (Fig. 5.3, lower graphs): The presence of the gap nodes leads to a complicated low energy spectrum without clear bound states. Most probably, the low energy states are extended along the gap nodes, and lead thus to a substantial dispersion in the energy bands (*cf.* Ref. [110]), in contrast to the cases without gap nodes. With our resolution in the Brillouin zone, it is difficult to identify bandlike structures. To obtain more reliable results on the energy spectrum for the d-wave case, the number of Bloch vectors should be enhanced considerably.

In Fig. 5.4 the admixed order parameter for p-wave symmetry is shown for different average fields $\bar{B}$. For large fields $\bar{B} \geq 0.3$, the admixed order parameter shows distinct maxima on the bonds between neighboring vortices. Decreasing the average field reduces these maxima and leads finally to a lattice of distinct, approximately circular symmetric structures, which correspond to the form of the admixed order parameter for isolated vortices. The dominant order parameter (not shown here) shows increasing fourfold anisotropy for increasing average field. These structures of the dominant and admixed order parameter are qualitatively close to the corresponding results for the same average B-fields obtained within the two-component Ginzburg-Landau theory presented in Chapter 4. A quantitative comparison and a systematic investigation of the differences, giving information about corrections to the standard Ginzburg-Landau theory, is left for the future.

Finally, in Figs. 5.5 - 5.7, we present the results of our calculations for the local density of states (LDOS) in the vortex lattice at low average magnetic fields $\bar{B} = 0.2$. We show the LDOS along a path crossing the vortex core at the point A as indicated in Fig. 5.1 (a). As it is expected for the s-wave case (Fig. 5.5), two ridges of enhanced LDOS are visible connecting peaks at small energies near the core with the enhanced LDOS at

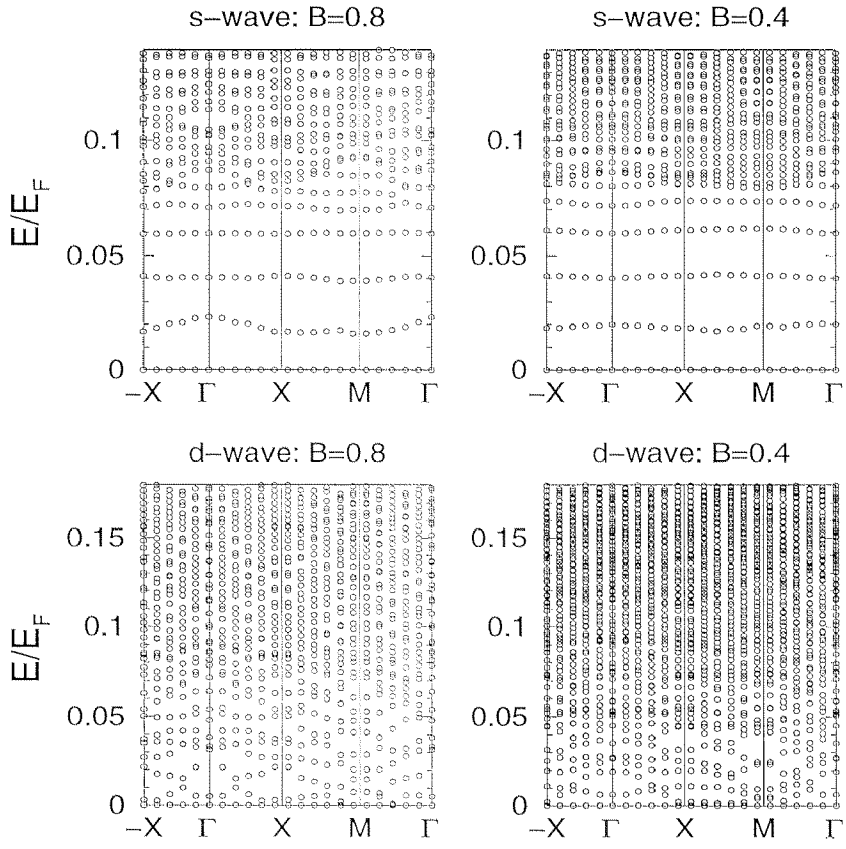

Figure 5.3: Quasiparticle spectra for the s-wave system (upper line) and the d-wave system (lower line) for average fields $B = 0.8, 0.4$ and $k_F\xi_a = 15$. On the horizontal axis, the position within the magnetic Brillouin zone is marked by the crystallographic symmetry points (*cf.* Fig. 5.1). The range of the vertical axis denoting the particle energy corresponds to the bulk gaps $\Delta_s = 0.14E_F$ and $\Delta_d = 0.18E_F$, respectively. Note, that the points at exactly zero energy are artifacts of the calculation and do not correspond to physical states.

the gap energy far from the core. These ridges are due to the bound states, which have their weight (*i. e.* their quasiclassical orbit) at larger radii for increasing energy. The results are in good qualitative agreement with calculations of single vortices for small values of $k_F\xi_0$[82]. The ridges of enhanced LDOS were investigated in great detail in STM-experiments of $NbSe_2$[72, 73, 74] and quasiclassical calculations[78, 79, 80]. For the p-wave case (Fig. 5.6), the LDOS shows similar ridges as in the s-wave case. This finding agrees with the quasiclassical expectation, since the main difference between s- and p-wave core states is the quantization of the energy at very low energies. The ridge phenomena, however, are due to quasiclassical pathes, which are basically the same for the two symmetries. The difference in orbital quantization should only be seen for isolated vortex cores, where one would expect a LDOS peak at exactly zero

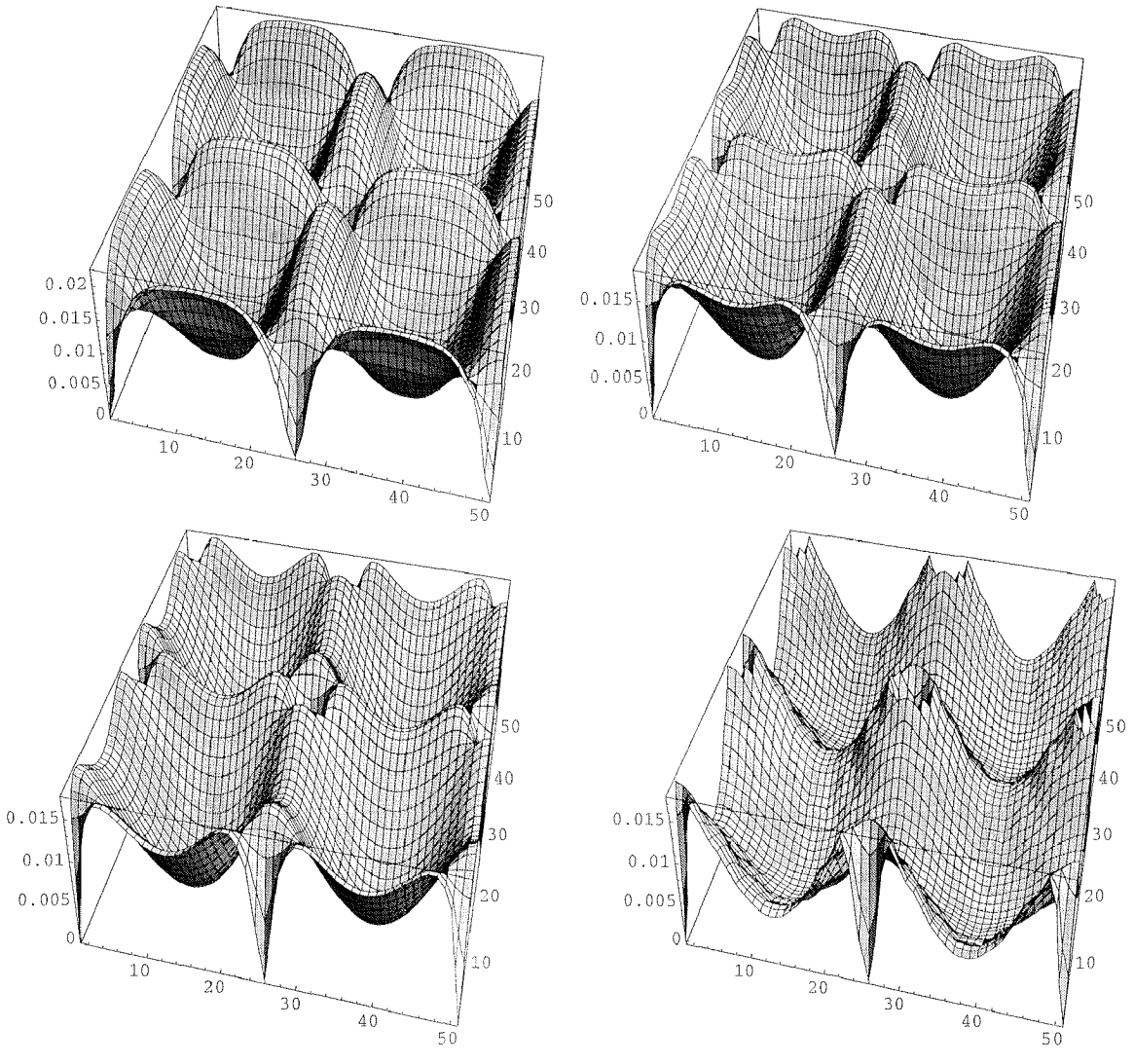

Figure 5.4: Admixed order parameter η_+ in the p-wave system for four different average fields (from upper left to lower right) $\bar{B} = 0.3, 0.2, 0.15, 0.08$ and $k_F\xi_a = 15$. For fields $\bar{B} \geq 0.3$, the admixed order parameter shows distinct maxima on the bonds between neighboring vortices. Reducing the average field gradually reduces these maxima and finally leads to a lattice of nearly isolated vortices.

energy due to the topological zero energy state. As mentioned above, this zero energy state is shifted to larger energies and therefore no zero energy peak is observed in our data. Finally, in Fig. 5.7, the result for the LDOS of a pure d-wave symmetry is shown. The situation here is completely different as in the preceding cases, since the gap nodes lead to different quasiclassical pathes. Although the low energy spectrum has shown to be complicated, the LDOS shows also quite distinct features which are stable against lowering the field or increasing calculation precision. Generally the LDOS shows Friedel-like oscillations in the whole energy range. Far from the core, the

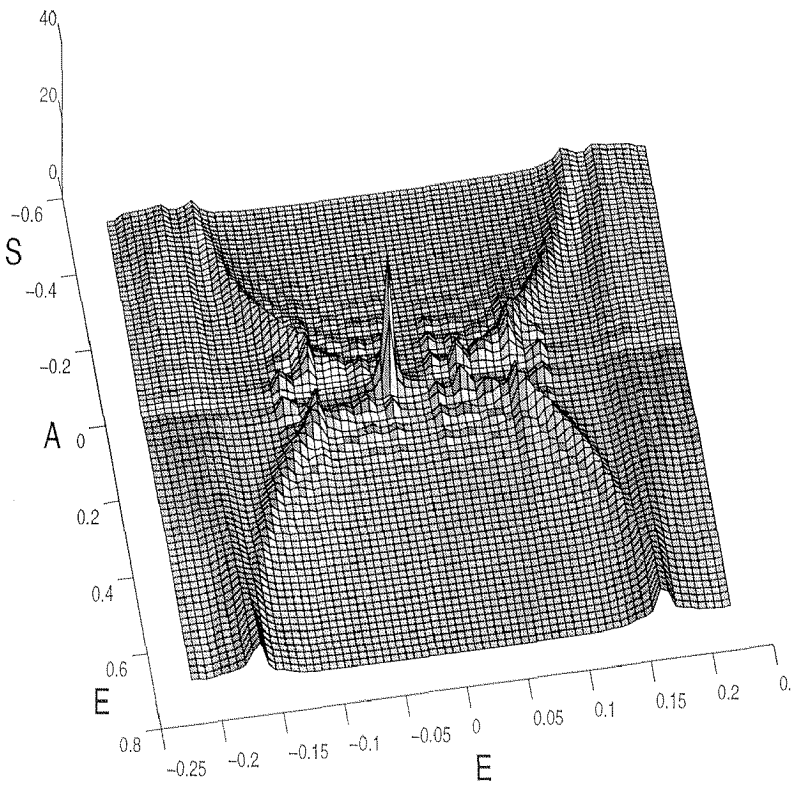

Figure 5.5: Local density of states (LDOS) for the s-wave system at the average field $\bar{B} = 0.2$. The path along which the LDOS is depicted in Fig. 5.1 (a).

influence of the low energy states in the gap nodes is seen in their nonzero contribution to the LDOS for energies lower than the gap energy. Approaching the vortex core, as in s- and p-waves two ridges of enhanced LDOS are visible. Qualitatively similar ridges were already presented based on quasiclassical calculations by Ichioka *et al.*[29]. These ridges are due to four quasiclassical pathes for fixed energy, which enter and leave the vortex core in the direction of the gap nodes. A future more systematic evaluation of the LDOS at different angles with respect to the vortex lattice should point out the difference between the d-wave case and the former cases more clearly.

5.4 Conclusion

In conclusion, we have presented in this chapter a self-consistent solution of the vortex lattice problem for s-, p- and d-wave symmetry within Bogoliubov-de Gennes theory. We used the singular gauge transformation introduced earlier[113, 112, 111] to gauge

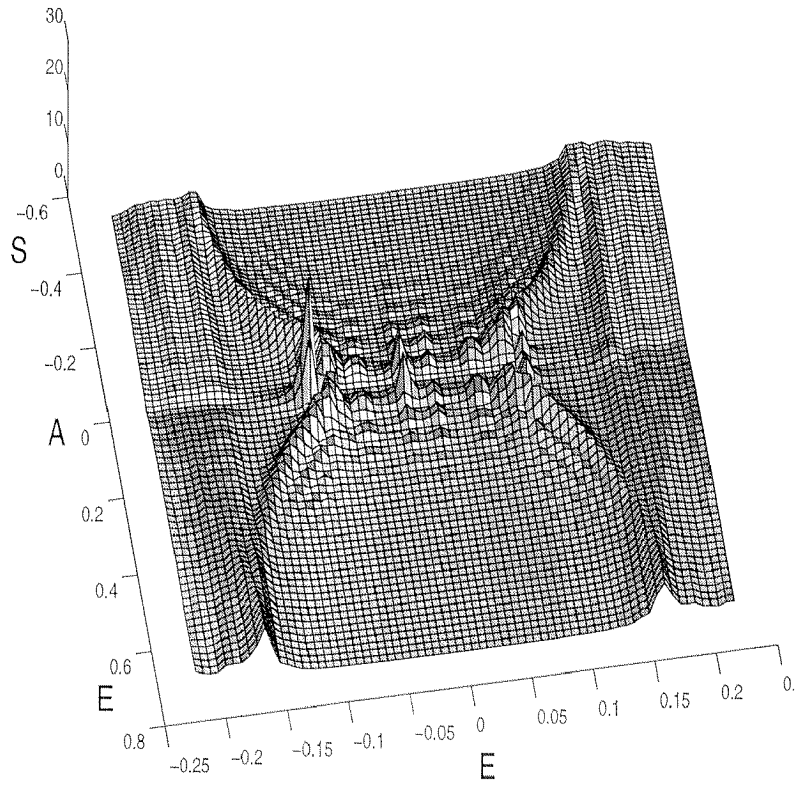

Figure 5.6: Local density of states for the p-wave system at the average field $\bar{B} = 0.2$. The path along which the LDOS is depicted in Fig. 5.1 (a).

away the topological vortex phase singularities and to obtain a zero average B-field simultaneously. Although the numerical effort to solve the problem in the interesting range of parameters is considerable, first results presented in this chapter reveal the method to be promising. The s-wave system merely was treated as a test system to check the main characteristics of the method. For the p-wave system, the results for the admixed order parameter, which is the more sensitive quantity than the dominant order parameter, shows very good qualitative agreement with corresponding two-component Ginzburg-Landau results. Maxima along the nearest neighbor bonds at large fields are gradually reduced for decreasing fields, until a lattice of virtually isolated vortices is achieved. The local density of states shows a similar picture as in the s-wave case with subgap ridges of enhanced LDOS due to the bound states. The energy spectrum at low magnetic fields shows the expected flat bands with energies comparable to the bound state levels of the single vortex problem. For higher magnetic fields, the bands show strong dispersion due to the overlap of the bound state wavefunctions. This band scheme lives on a very small Brillouin zone and is strongly dependent on the average magnetic field, since the overlap integrals determining the

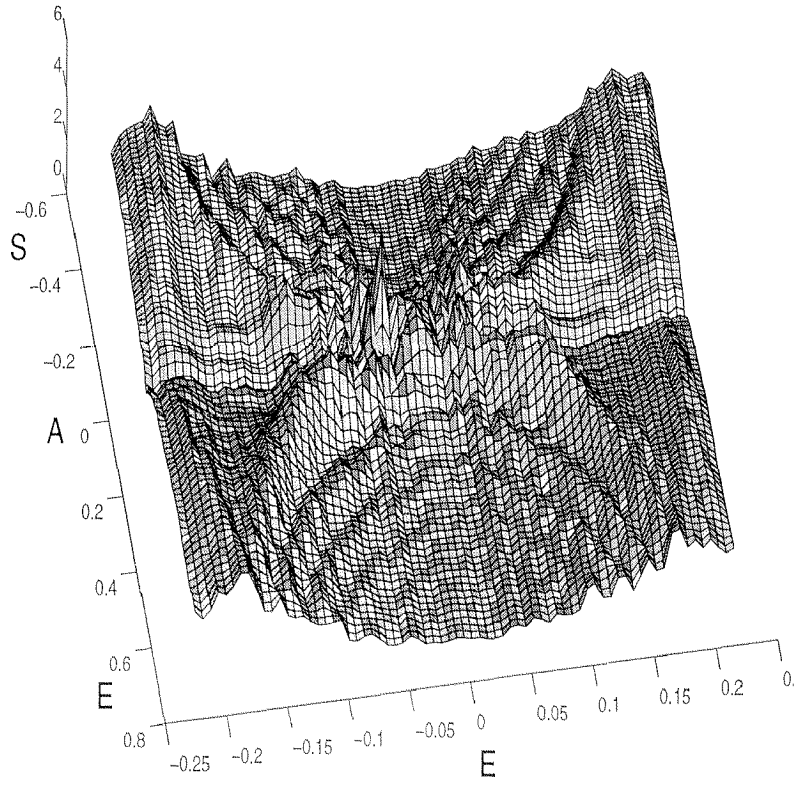

Figure 5.7: Local density of states for the d-wave system at the average field $\bar{B} = 0.2$. The path along which the LDOS is depicted in Fig. 5.1 (a).

band structure are sensitive to changes in the lattice constant of the order of $1/k_F$. It is an open question, whether such band structures can be observed experimentally. Finally, for the d-wave system the band structure is considerably more complicated than in the previous cases and has no flat bound state bands. The local density of states, however, shows a distinct feature of ridges of enhanced LDOS, merging into a small peak at zero bias. This finding is in accordance with former results[29].

In summary, this method to solve self-consistently the vortex lattice problem for different symmetries of the order parameter has proved to give qualitatively satisfying results. Clearly the method has to be refined considerably to obtain also quantitative results which go beyond the known features from other techniques. This is especially true for the vortex center region, where the method works not entirely satisfactory. However, since the method does not contain any quasiclassical approximations, it is a useful tool to investigate the physics of superconductors near the quantum limit.

Appendix A

Partial Wave Decomposition

A.1 Partial wave expansion in the limits $|\eta_s|, |\eta_{d'}| \ll |\eta_d|$

We consider the tetragonal FED Eq. (2.5) with the Ansatz

$$\begin{aligned} \eta_d &= d(r)e^{i\theta} \qquad\qquad d(r) \in \mathbb{R} \\ \boldsymbol{A} &= A(r)\hat{\boldsymbol{e}}_{\boldsymbol{\theta}}, \end{aligned} \tag{A.1}$$

and the partial wave expansion for η_s

$$\eta_s = \sum_{n=-\infty}^{+\infty} s_n(r)e^{in\theta}. \tag{A.2}$$

To establish the radial problem, we integrate the FED over the angle θ

$$\begin{aligned} \mathcal{F}(r) &= \frac{1}{2\pi}\int_0^{2\pi} d\theta f(r,\theta) \\ &= \mathcal{F}_d + \frac{1}{2}\mathcal{F}_{1,1} + \tilde{\mathcal{F}}_{3,-1} + \sum_{\substack{n>1 \\ n\neq 3}} \mathcal{F}_{n,-n+2} \\ &\quad + \mathcal{F}_{4^{\text{th}}} + 2\kappa^2\boldsymbol{B}^2. \end{aligned} \tag{A.3}$$

The positive definite term $\mathcal{F}_{4^{\text{th}}}$ contains all fourth order expressions in s_i, $\mathcal{F}_d$ is the usual pure d-wave FED and the other terms have the structure

$$\begin{aligned} &\mathcal{F}_{n,-n+2} = \\ &= \tilde{\alpha}(|s_n|^2 + |s_{-n+2}|^2) + \tilde{\mu}(|s_n'|^2 + |s_{-n+2}'|^2) \\ &\quad + \tilde{\mu}\Big(\frac{n}{r} - 2A\Big)^2|s_n|^2 + \tilde{\mu}\Big(\frac{-n+2}{r} - 2A\Big)^2|s_{-n+2}|^2 \end{aligned}$$

$$+\tilde{\gamma}_1 d^2(|s_n|^2+|s_{-n+2}|^2)+2\tilde{\gamma}_2 d^2(s_n s_{-n+2}+s_n^* s_{-n+2}^*)$$

$$\tilde{\mathcal{F}}_{3,-1} =$$

$$= \mathcal{F}_{3,-1}+\tilde{\delta}(s_3+s_3^*)\,\mathcal{K}_3(d,A)+\tilde{\delta}(s_{-1}+s_{-1}^*)\,\mathcal{K}_{-1}(d,A). \tag{A.4}$$

The functions $\mathcal{K}_i$ are defined in Eq. (2.16). One advantage of this partial wave decomposition is, that partial waves $s_n(r)$ couple only in distinct pairs, if we disregard the small fourth order coupling terms. With the assumption $|\eta_d|^2 \leq \frac{1}{2}$, the FED-parts $\mathcal{F}_{n,-n+2}$ are positive definite, if

$$2\tilde{\alpha} > (2|\tilde{\gamma}_2|-\tilde{\gamma}_1). \tag{A.5}$$

This condition is fulfilled because of the stability criterion (2.10) and our choice $\tilde{\alpha}>1$. The term $\mathcal{F}_{1,1}$ is positive definite as well. Since the $\mathcal{F}_{n,-n+2}$, $(n\neq -1,3)$ are zero for $|s_n|=|s_{-n+2}|=0$, the solution minimizing $\mathcal{F}$ has only the two non-zero partial waves, s_{-1} and s_3. The reality of s_{-1} and s_3 is shown in a similar way. The remaining problem is to minimize the free energy $\int r dr \mathcal{F}(r)$ with

$$\begin{aligned}
\mathcal{F}(r) \;=\; & \Big\{\tilde{\alpha}((s_{-1}^2+s_3^2)+(s_{-1}^4+4s_{-1}^2s_3^2+s_3^4)) \\
& +\tilde{\mu}\Big(s_{-1}'^2+s_3'^2+\Big(-\frac{1}{r}-2A\Big)^2 s_{-1}^2+\Big(\frac{3}{r}-2A\Big)^2 s_3^2\Big) \\
& +\tilde{\gamma}_1 d^2(s_{-1}^2+s_3^2)+4\tilde{\gamma}_2 d^2 s_{-1}s_3 \\
& +2\tilde{\delta}(s_3\mathcal{K}_3(d,A)+s_{-1}\mathcal{K}_{-1}(d,A)) \\
& -d^2+d^4+d'^2+\Big(\frac{1}{r}-2A\Big)^2 d^2 \\
& +2\kappa^2\Big(\frac{A^2}{r^2}+2\frac{AA'}{r}+A'^2\Big)\Big\}.
\end{aligned} \tag{A.6}$$

For orthorhombic symmetry, the final FED is obtained in a similar way and reads

$$\begin{aligned}
\mathcal{F}(r) \;=\; & \Big\{\tilde{\alpha}((s_{-1}^2+s_1^2+s_3^2) \\
& \quad +(s_{-1}^4+s_1^4+s_3^4+4s_{-1}^2s_1^2+4s_{-1}^2s_3^2+4s_1^2s_3^2+4s_1^2s_{-1}s_3)) \\
& +\tilde{\mu}\Big(s_{-1}'^2+s_1'^2+s_3'^2+\Big(-\frac{1}{r}-2A\Big)^2 s_{-1}^2+\Big(\frac{1}{r}-2A\Big)^2 s_1^2+\Big(\frac{3}{r}-2A\Big)^2 s_3^2\Big) \\
& +2\tilde{\gamma}_0 d s_1+2\tilde{\gamma}_4 d^3 s_1 \\
& +\tilde{\delta}_x(s_3\mathcal{K}_3(d,A)+2s_1\mathcal{K}_1(d,A)+s_{-1}\mathcal{K}_{-1}^x(d,A)) \\
& -\tilde{\delta}_y(s_3\mathcal{K}_3(d,A)-2s_1\mathcal{K}_1^y(d,A)+s_{-1}\mathcal{K}_{-1}(d,A)) \\
& -d^2+d^4+d'^2+\Big(\frac{1}{r}-2A\Big)^2 d^2 \\
& +2\tilde{\kappa}^2\Big(\frac{A^2}{r^2}+2\frac{AA'}{r}+A'^2\Big)\Big\}.
\end{aligned} \tag{A.7}$$

For tetragonal symmetry with non-vanishing $\eta_{d'}$ and η_d, we perform the partial wave expansion for $\eta_{d'}$:

$$\eta_{d'} = \sum_{n=-\infty}^{+\infty} t_n(r) e^{in\theta}. \tag{A.8}$$

The only non-vanishing partial wave is then the imaginary part of $t_1(r)$, which is denoted simply by $t(r)$. The FED then reads

$$\begin{aligned}\mathcal{F}(r) &= \Big\{\tilde{\alpha}(t^2+t^4)+\tilde{\mu}\Big(t'^2+\Big(\frac{1}{r}-2A\Big)^2 t^2\Big) \\ &\quad - d^2+d^4+d'^2+\Big(\frac{1}{r}-2A\Big)^2 d^2 \\ &\quad + \tilde{\gamma}_1 d^2t^2 - 2\tilde{\gamma}_2 d^2t^2 + 4\tilde{\delta}\Big(\frac{1}{r}A+A'\Big)dt + 2\kappa^2\Big(\frac{A^2}{r^2}+2\frac{AA'}{r}+A'^2\Big)\Big\}. \end{aligned}\tag{A.9}$$

A.2 Asymptotics

We calculate the asymptotic behavior of $d(r)$, $A(r)$, $s_{-1}(r)$, and $s_3(r)$ at small r and at large r in the case of tetragonal symmetry with $\eta_{d'}=0$. Other cases can be calculated in a similar way and are not performed here explicitly. First, we consider the asymptotics for $\kappa<\infty$. In the limit $r\to 0$, we expand the functions $A(r), s_{-1}(r), s_3(r)$, and $d(r)$ in powers of r. Up to n-th order, we find $4n$ equations and $4n+4$ unknown parameters. The missing four equations are given by the boundary conditions at infinity. To third order, we obtain the asymptotic Ansatz ($r\to 0$)

$$\begin{aligned} A &= a_1 r + a_3 r^3, \\ s_{-1} &= b_1 r + b_3 r^3, \\ s_3 &= c_3 r^3, \\ d &= d_1 r + d_3 r^3, \end{aligned}\tag{A.10}$$

where the coefficients satisfy

$$\begin{aligned} 2\tilde{\alpha}b_1 - 16\tilde{\mu}b_3 + 8\tilde{\mu}a_1b_1 - 8\tilde{\delta}d_3 + 8\tilde{\delta}a_1d_1 &= 0, \\ 2d_1 + 16d_3 + 8a_1d_1 + 8\tilde{\delta}a_1b_1 + 8\tilde{\delta}b_3 + 24\tilde{\delta}c_3 &= 0, \\ \tilde{\mu}b_1^2 - d_1^2 - 8\kappa^2 a_3 &= 0. \end{aligned}\tag{A.11}$$

Note, that in the case without induced s-waves ($\tilde{\delta}=0$) we have

$$\begin{aligned} d_1^2 &= -8\kappa^2 a_3, \\ d_3 &= \Big(-\frac{1}{8}-\frac{1}{2}a_1\Big)d_1. \end{aligned}\tag{A.12}$$

For $r \to \infty$ and small s-waves, we expect exponential decays of $d(r)$ and $s_{-1}(r), s_3(r)$ towards their bulk values $1/\sqrt{2}$ and 0, respectively, whereas for the A-field, the total enclosed flux requires a primary asymptotic behavior $1/2r$ in our units. With the Ansatz $d = 1/\sqrt{2} - \tilde{d}(r)$ and $A(r) = 1/2r + \tilde{A}(r)$ and the convenient definition $s^{\pm} = s_{-1} \pm s_3$, the asymptotic solution can be expressed as

$$\begin{aligned} \tilde{A}(r) &\sim A_\infty r^{-\frac{1}{2}} e^{-Kr}, \\ s^-(r) &\sim S^-_\infty r^{-\frac{1}{2}} e^{-Kr}, \\ s^+(r) &\sim S^+_\infty r^{-1} e^{-2Kr}, \\ \tilde{d}(r) &\sim D_\infty r^{-1} e^{-2Kr}. \end{aligned} \tag{A.13}$$

The exponent K is given for small $\tilde{\delta}$ by

$$K^2 = \frac{1}{\kappa^2}\Big(1 + \frac{\tilde{\delta}^2}{G^-\kappa^2 - 2\tilde{\mu}} + O(\tilde{\delta}^4)\Big), \tag{A.14}$$

and has the correct limit $K = 1/\kappa$ for $\tilde{\delta} \to 0$. We have introduced $G^{\pm} = 2\tilde{\alpha} + \tilde{\gamma}_1 \pm 2\tilde{\gamma}_2$, and the minus sign in front of the square root gives the solution valid for $G^- > \tilde{\mu}$. Thus, the s-wave components modify the exponential decay of the d-wave and the A-field. Since s^+ vanishes faster than s^-, we find for the partial waves the asymptotics

$$s_{-1} \sim -s_3 \sim \frac{S^-_\infty}{2} r^{-\frac{1}{2}} e^{-Kr}. \tag{A.15}$$

Finally, we consider the coefficients $A_\infty, S^{\pm}_\infty$, and D_∞. We have $A_\infty < 0$ since the included flux in a circle with radius r is smaller than the flux quantum Φ_0. For $\tilde{\delta} \to 0$, the other coefficients obey

$$\begin{aligned} D_\infty &= \frac{\sqrt{2} A^2_\infty}{1 - \frac{2}{\kappa^2}} + O(\tilde{\delta}^2), \\ S^-_\infty &= \tilde{\delta}\, \frac{2\sqrt{2}\,\kappa A_\infty}{G^-\kappa^2 - 2\tilde{\mu}} + O(\tilde{\delta}^3), \\ S^+_\infty &= \tilde{\delta}\, \frac{4\sqrt{2} A^2_\infty}{G^+ - \frac{8\tilde{\mu}}{\kappa^2}} \Big(\frac{\kappa^2 - 4}{\kappa^2 - 2}\Big) + O(\tilde{\delta}^3). \end{aligned} \tag{A.16}$$

A_∞ cannot be determined from the asymptotic equations. Especially important is the behavior of the coefficient S^+_∞, which shows a κ-dependent sign change at $\kappa = 2$. This will later be important for determining the possible number of vortices of the s-wave.

Let us now turn to the limiting case $\kappa = \infty$ ($e = 0$). The asymptotics at small r are obtained from Eq. (A.11) by dropping the last equation and putting all coefficients $a_i \equiv 0$. This corresponds to the fact that we have no vector potential $A(r)$ in the problem. The special case without induced s-waves ($\tilde{\delta} = 0$) leads to

$$d_3 = -\frac{1}{8} d_1. \tag{A.17}$$

For large r, the s-waves decay algebraically, as Berlinsky et al.[25] have shown:

$$\begin{aligned} s_{-1} &\sim B_2 \frac{1}{r^2}, \\ s_3 &\sim C_2 \frac{1}{r^2}, \\ d(r) &= \frac{1}{\sqrt{2}} - \frac{\sqrt{2}}{4r^2}. \end{aligned} \tag{A.18}$$

The coefficients B_2 and C_2 have the properties $|B_2/C_2| < 1$, implying $|s_{-1}| < |s_3|$, and $B_2/C_2 < 0$ (provided that $2\tilde{\alpha} + \tilde{\gamma}_1 > -6\tilde{\gamma}_2$), which determines the relative phase of s_{-1} and s_3 to be π.

Appendix B

Ginzburg-Landau Theory for Vortex Lattice

The minimization procedure proposed by Brandt[60] for s-waves consists basically of three steps. In a first step, the free energy density is written in gauge invariant quantities only, and a set of corresponding Ginzburg-Landau type equations is derived. Second, these gauge invariant quantities can be expanded conveniently in reciprocal space, making use of the known mean penetrating field $\bar{B}$ and the geometry of the unit cell. The GL equations then can be written in the form $(-\boldsymbol{\nabla}^2+2\kappa^2)\omega = g_i(\omega,\eta,\sigma,\boldsymbol{Q})$, where g_i is treated as an inhomogeneity of this London-type equation. Insertion of the reciprocal space decomposition and extraction of single components by averaging over $\cos \boldsymbol{kr}$ leads to a well defined iteration scheme for the reciprocal space components.

B.1 Formulation in gauge invariant quantities

To write the whole free energy density in gauge invariant quantities, we introduce

$$\begin{aligned} \omega &= |\eta_-|^2 \\ \eta_- &= |\eta_-| e^{i\phi(\boldsymbol{x})} \\ \eta_+ &= (\eta + i\sigma) e^{i\phi(\boldsymbol{x})} \\ \boldsymbol{Q} &= \boldsymbol{A} - \frac{\boldsymbol{\nabla}\phi}{\kappa} \end{aligned} \tag{B.1}$$

and obtain the gauge invariant form (see Eq. (3.29))

$$\begin{aligned} f &= -\omega + \frac{\omega^2}{2} + \frac{(\boldsymbol{\nabla}\omega)^2}{4\kappa^2\omega} + \omega\boldsymbol{Q}^2 + h^2 \\ &\quad -(\eta^2+\sigma^2) + \frac{1}{2}(\eta^2+\sigma^2)^2 + 2\omega(\eta^2+\sigma^2) + \nu\omega(\eta^2-\sigma^2) \end{aligned}$$

$$
\begin{aligned}
&+\left(\frac{\boldsymbol{\nabla}\sigma}{\kappa}-\boldsymbol{Q}\eta\right)^2+\left(\frac{\boldsymbol{\nabla}\eta}{\kappa}+\boldsymbol{Q}\sigma\right)^2\\
&+(1+\nu)\left(Q_x\omega^{\frac{1}{2}}\left(Q_x\eta-\frac{\partial_x\sigma}{\kappa}\right)+\frac{1}{2\kappa}\frac{\partial_x\omega}{\omega^{\frac{1}{2}}}\left(\frac{\partial_x\eta}{\kappa}+Q_x\sigma\right)\right)-(x\leftrightarrow y)\\
&+(1-\nu)\left(Q_y\omega^{\frac{1}{2}}\left(Q_x\sigma+\frac{\partial_x\eta}{\kappa}\right)-\frac{1}{2\kappa}\frac{\partial_y\omega}{\omega^{\frac{1}{2}}}\left(Q_x\eta-\frac{\partial_x\sigma}{\kappa}\right)\right)+(x\leftrightarrow y). \quad \text{(B.2)}
\end{aligned}
$$

We derive gauge invariant Ginzburg-Landau equations by derivation of f with respect to ω, η, σ, and $\boldsymbol{Q}$, respectively. Finally we take the curl of the $\boldsymbol{Q}$-equation to obtain an equation including B. The corresponding set of equations is (using $\boldsymbol{\nabla}\boldsymbol{Q}=0$)

$$
\begin{aligned}
(-\boldsymbol{\nabla}^2+2\kappa^2)\omega &= 2\kappa^2\Bigg[2\omega-\omega^2-\frac{(\boldsymbol{\nabla}\omega)^2}{4\kappa^2\omega}-\omega\boldsymbol{Q}^2-(2+\nu)\omega\eta^2-(2-\nu)\omega\sigma^2\\
&\quad-\frac{1+\nu}{2}\omega^{\frac{1}{2}}\left(Q_x^2\eta-2Q_x\frac{\partial_x\sigma}{\kappa}-\frac{\partial_xQ_x}{\kappa}\sigma-\frac{\partial_x^2\eta}{\kappa^2}\right)-(x\leftrightarrow y)\\
&\quad-\frac{1-\nu}{2}\omega^{\frac{1}{2}}\left(Q_xQ_y\sigma+Q_y\frac{\partial_x\eta}{\kappa}+Q_x\frac{\partial_y\eta}{\kappa}+\frac{\partial_yQ_x}{\kappa}\eta-\frac{\partial_x\partial_y\sigma}{\kappa^2}\right)\\
&\quad+(x\leftrightarrow y)\Bigg],\\
(-\boldsymbol{\nabla}^2+\bar{\omega})B &= -(\omega-\bar{\omega})B-(\partial_x\omega Q_y-\partial_y\omega Q_x)\\
&\quad+\frac{2}{\kappa}\left(\partial_x\eta\partial_y\sigma-\partial_y\eta\partial_x\sigma\right)-2\eta\left(\partial_x\eta Q_y-\partial_y\eta Q_x\right)\\
&\quad-2\sigma\left(\partial_x\sigma Q_y-\partial_y\sigma Q_x\right)-(\eta^2+\sigma^2)(\partial_xQ_y-\partial_yQ_x)\\
&\quad+\frac{1+\nu}{2}\Bigg[\frac{\sigma}{\kappa}\left(\frac{\partial_x\partial_y\omega}{\omega^{\frac{1}{2}}}-\frac{(\partial_x\omega)(\partial_y\omega)}{2\omega^{\frac{3}{2}}}\right)-\frac{2\omega^{\frac{1}{2}}}{\kappa}\partial_x\partial_y\sigma\\
&\quad+2\omega^{\frac{1}{2}}(\partial_x\eta Q_y+\partial_y\eta Q_x)\\
&\quad+\frac{\eta}{\omega^{\frac{1}{2}}}(\partial_x\omega Q_y+\partial_y\omega Q_x)+2\eta\omega^{\frac{1}{2}}(\partial_xQ_y+\partial_yQ_x)\Bigg]\\
&\quad+\frac{1-\nu}{2}\Bigg[\frac{\eta}{2\kappa}\left(\frac{(\partial_x^2-\partial_y^2)\omega}{\omega^{\frac{1}{2}}}-\frac{(\partial_x\omega)^2-(\partial_y\omega)^2}{2\omega^{\frac{3}{2}}}\right)-\frac{\omega^{\frac{1}{2}}}{\kappa}(\partial_x^2-\partial_y^2)\eta\\
&\quad-2\omega^{\frac{1}{2}}(\partial_x\sigma Q_x-\partial_y\sigma Q_y)-\frac{\sigma}{\omega^{\frac{1}{2}}}(\partial_x\omega Q_x-\partial_y\omega Q_y)\\
&\quad-2\sigma\omega^{\frac{1}{2}}(\partial_xQ_x-\partial_yQ_y)\Bigg],\\
(-\boldsymbol{\nabla}^2+2\kappa^2)\eta &= \kappa^2\Bigg[3\eta-\eta(\eta^2+\sigma^2)-(2+\nu)\omega\eta+\frac{2}{\kappa}(\boldsymbol{\nabla}\sigma)\boldsymbol{Q}-\boldsymbol{Q}^2\eta\\
&\quad-\frac{1+\nu}{2}\left(Q_x^2\omega^{\frac{1}{2}}-\frac{\partial_x^2\omega}{2\kappa^2\omega^{\frac{1}{2}}}+\frac{(\partial_x\omega)^2}{4\kappa^2\omega^{\frac{3}{2}}}\right)-(x\leftrightarrow y)\\
&\quad+\frac{1-\nu}{2}\left(\frac{Q_x\partial_y\omega}{2\kappa\omega^{\frac{1}{2}}}+\frac{Q_y\partial_x\omega}{2\kappa\omega^{\frac{1}{2}}}+\frac{(\partial_xQ_y)\omega^{\frac{1}{2}}}{\kappa}\right)+(x\leftrightarrow y)\Bigg],
\end{aligned}
$$

$$
\begin{aligned}
(-\boldsymbol{\nabla}^2+2\kappa^2)\sigma &= \kappa^2\Big[3\sigma-\sigma(\eta^2+\sigma^2)-(2-\nu)\omega\sigma-\frac{2}{\kappa}(\boldsymbol{\nabla}\eta)\boldsymbol{Q}-\boldsymbol{Q}^2\sigma \\
&\quad -\frac{1+\nu}{2}\left(\frac{Q_x\partial_x\omega}{\kappa\omega^{\frac{1}{2}}}+\frac{(\partial_x Q_x)\omega^{\frac{1}{2}}}{\kappa}\right)-(x\leftrightarrow y) \\
&\quad -\frac{1-\nu}{2}\left(Q_xQ_y\omega^{\frac{1}{2}}-\frac{\partial_x\partial_y\omega}{2\kappa^2\omega^{\frac{1}{2}}}+\frac{(\partial_x\omega)(\partial_y\omega)}{4\kappa^2\omega^{\frac{3}{2}}}\right)+(x\leftrightarrow y)\Big]. \qquad \text{(B.3)}
\end{aligned}
$$

In addition to the well known Ginzburg-Landau equations derived above, further equations are fulfilled in the minimal configuration. One equation particularly helpful in the s-wave case (see Ref.[60]) is the derivative with respect to the absolute value of the order parameters. Writing the free energy density as

$$f = f(\phi\omega, \zeta^{\frac{1}{2}}\eta, \zeta^{\frac{1}{2}}\sigma) \qquad \text{(B.4)}$$

and deriving with respect to ϕ and ζ, leads to the equations (after multiplication with ϕ and ζ, respectively)

$$
\begin{aligned}
\omega^2 &= \omega-\omega\boldsymbol{Q}^2-\frac{(\boldsymbol{\nabla}\omega)^2}{4\kappa^2\omega}-(2+\nu)\omega\eta^2-(2-\nu)\omega\sigma^2 \\
&\quad -\frac{1+\nu}{2}f_{1+\nu}-\frac{1-\nu}{2}f_{1-\nu}, \qquad \text{(B.5)}
\end{aligned}
$$

$$
\begin{aligned}
\eta^2+\sigma^2 &= (\eta^2+\sigma^2)^2+(2+\nu)\omega\eta^2+(2-\nu)\omega\sigma^2+\left(\frac{\boldsymbol{\nabla}\sigma}{\kappa}-\boldsymbol{Q}\eta\right)^2+\left(\frac{\boldsymbol{\nabla}\eta}{\kappa}+\boldsymbol{Q}\sigma\right)^2 \\
&\quad +\frac{1+\nu}{2}f_{1+\nu}+\frac{1-\nu}{2}f_{1-\nu}, \qquad \text{(B.6)}
\end{aligned}
$$

where the terms $f_{1\pm\nu}$ are the corresponding expressions of Eq. (3.29) with leading factors $(1\pm\nu)$. Subtraction of the two above equations Eqs. (B.5,B.6) from the expression for the free energy density Eq. (3.29) leads to an alternative expression for the free energy density in the minimal configuration

$$f = -\frac{\omega^2}{2}-\frac{1}{2}(\eta^2+\sigma^2)^2-(2+\nu)\omega\eta^2-(2-\nu)\omega\sigma^2+h^2 = -\langle f^4\rangle+B^2. \qquad \text{(B.7)}$$

B.2 Geometry and discretization

The geometry of the unit cell can be described by four parameters $\theta_1, \bar{B}, x_r, y_r$, which are connected to the basic quantities by the following relations

$$V_{uc} = x_1y_2 = \frac{\Phi_0}{\bar{B}} = \frac{2\pi}{\kappa\bar{B}}$$

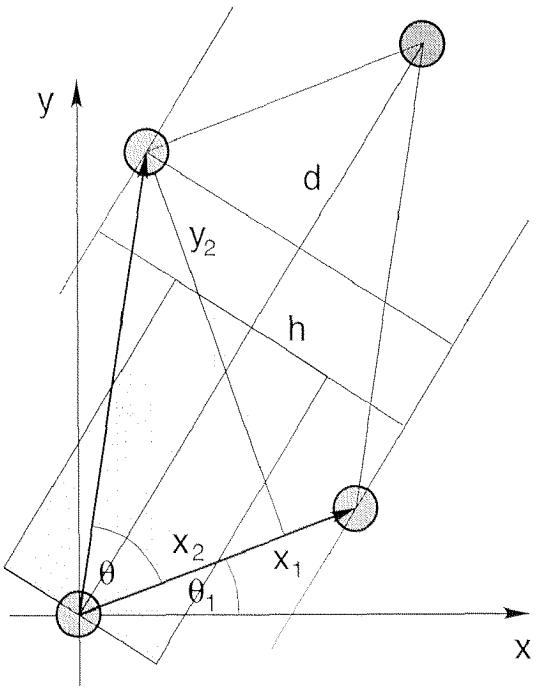

Figure B.1: Schematic illustration of the geometry parameters. The shaded area is the half unit cell (oriented along the unit cell diagonal), in which the FED is minimized.

$$\begin{aligned} x_1 &= \sqrt{\frac{V_{uc}}{y_r}} \\ x_r &= \frac{x_2}{x_1} \\ y_r &= \frac{y_2}{x_1} \\ d &= x_1\sqrt{(1+x_r)^2+y_r^2} \\ h &= \frac{V_{uc}}{d} = x_1\frac{y_r}{\sqrt{(1+x_r)^2+y_r^2}} \\ \theta &= \arctan\left(\frac{y_2}{x_2}\right) = \arctan\left(\frac{y_r}{x_r}\right). \end{aligned} \tag{B.8}$$

We then have the lattice vectors

$$\boldsymbol{R}_{m,n} = \Big((mx_1+nx_2)\cos\theta_1 - ny_2\sin\theta_1, (mx_1+nx_2)\sin\theta_1 + ny_2\cos\theta_1\Big), \tag{B.9}$$

and the reciprocal lattice vectors

$$\begin{aligned} \boldsymbol{k}_{m,n} &= \frac{2\pi}{V_{uc}}\Big((mx_2-nx_1)\sin\theta_1 + my_2\cos\theta_1, (nx_1-mx_2)\cos\theta_1 + my_2\sin\theta_1\Big) \\ \boldsymbol{k}^2_{m,n} &= \left(\frac{2\pi}{V_{uc}}\right)^2\Big((mx_2-nx_1)^2+(my_2)^2\Big) \end{aligned} \tag{B.10}$$

Choosing n_d points on the interval $(0, d/2)$, and correspondingly an (even) number of points n_h on $(-h/2, h/2)$

$$n_h = n_d \frac{2h}{d}, \tag{B.11}$$

we obtain the grid point vectors

$$\begin{aligned}
\boldsymbol{x}_{i,j} &= \left(d\ \frac{i-\frac{1}{2}}{2n_d}\right)\hat{\boldsymbol{d}} + \left(h\ \frac{j-\frac{n_h}{2}-\frac{1}{2}}{n_h}\right)\hat{\boldsymbol{h}} \\
&= \left(\left(\frac{i-\frac{1}{2}}{2n_d}\right)\Big((x_1+x_2)\cos\theta_1 - y_2\sin\theta_1\Big)\right. \\
&\quad + \left(\frac{j-\frac{n_h}{2}-\frac{1}{2}}{n_h}\right)\frac{h}{d}\Big((x_1+x_2)\sin\theta_1 + y_2\cos\theta_1\Big)\Big)\,\hat{\boldsymbol{x}} \\
&\quad + \left(\left(\frac{i-\frac{1}{2}}{2n_d}\right)\Big((x_1+x_2)\sin\theta_1 + y_2\cos\theta_1\Big)\right. \\
&\quad - \left.\left(\frac{j-\frac{n_h}{2}-\frac{1}{2}}{n_h}\right)\frac{h}{d}\Big((x_1+x_2)\cos\theta_1 - y_2\sin\theta_1\Big)\right)\hat{\boldsymbol{y}}.
\end{aligned} \tag{B.12}$$

As cutoff parameter in the reciprocal space we use (along Brandt[60])

$$|\boldsymbol{k}_{m,n}| \le k_{max} \approx \sqrt{c\frac{N}{V_{uc}}} \tag{B.13}$$

with $c = 10, 20$ and $N = n_h n_d$ the number of grid points. We expand the order parameters and the B-field in reciprocal lattice vectors

$$\begin{aligned}
\omega(\boldsymbol{r}) &= {\sum_{m,n}}' a_{m,n}(1-\cos\boldsymbol{k}_{m,n}\boldsymbol{r}) \\
B(\boldsymbol{r}) &= \bar{B} + {\sum_{m,n}}' b_{m,n}\cos\boldsymbol{k}_{m,n}\boldsymbol{r} \\
\boldsymbol{Q}(\boldsymbol{r}) &= \boldsymbol{Q}_A(\boldsymbol{r}) + {\sum_{m,n}}' b_{m,n}\frac{\hat{\boldsymbol{z}}\wedge\boldsymbol{k}_{m,n}}{\boldsymbol{k}_{m,n}^2}\sin\boldsymbol{k}_{m,n}\boldsymbol{r} \\
\eta(\boldsymbol{r}) &= {\sum_{m,n}}' c_{m,n}(1-\cos\boldsymbol{k}_{m,n}\boldsymbol{r}) \\
\sigma(\boldsymbol{r}) &= {\sum_{m,n}}' d_{m,n}(1-\cos\boldsymbol{k}_{m,n}\boldsymbol{r}),
\end{aligned} \tag{B.14}$$

where the primed sum stands for summation over all $(m,n) \neq (0,0)$. Further we find $\nabla\boldsymbol{Q} = \nabla\boldsymbol{Q}_A = 0$, and

$$\nabla\wedge\boldsymbol{Q}_A = \left(\bar{B} - \Phi_0\sum_{i,j}\delta^{2D}(\boldsymbol{r}-\boldsymbol{R}_{i,j})\right)\hat{\boldsymbol{z}}, \tag{B.15}$$

where the singular contribution coming from the vortex phase field leads to vanishing average curl of the gauge invariant velocity field $\boldsymbol{Q}$. As initial condition we use the

Abrikosov solution near B_{c2} for the main order parameter component and the B-field, and zero for the admixed component. The corresponding expression for the order parameter has the coefficients[63, 64]

$$a^A_{m,n} = -(-1)^{m+mn+n} \exp\left(-\boldsymbol{k}^2_{m,n} V_{uc} 8\pi\right), \tag{B.16}$$

and for the gauge invariant velocity we find

$$\boldsymbol{Q}_A = \frac{\boldsymbol{\nabla}\omega_A \wedge \hat{\boldsymbol{z}}}{2\kappa\omega_A} = \left(\frac{\partial_y \omega_A}{2\kappa\omega_A}, -\frac{\partial_x \omega_A}{2\kappa\omega_A}\right). \tag{B.17}$$

B.3 Minimization technique

Taking the average of Eqs. (3.30) multiplied by $\cos(\boldsymbol{k}_{m,n}\boldsymbol{r})$ over the half unit cell, we determine iteratively the Fourier components of order parameters and B-fields. The left hand side reads ($\boldsymbol{k}_{m,n} \neq 0$)

$$\begin{aligned}
&\Big\langle (-\boldsymbol{\nabla}^2 + 2\kappa^2)\omega \cos(\boldsymbol{k}_{m,n}\boldsymbol{r}) \Big\rangle\Big|_{\frac{1}{2}V_{uc}} \\
&= (\boldsymbol{k}^2_{m,n} + 2\kappa^2)\Big\langle \omega \cos(\boldsymbol{k}_{m,n}\boldsymbol{r}) \Big\rangle\Big|_{\frac{1}{2}V_{uc}} \\
&= -(\boldsymbol{k}^2_{m,n} + 2\kappa^2) \sum_{m',n'} a_{m',n'} \Big\langle \cos(\boldsymbol{k}_{m',n'}\boldsymbol{r}) \cos(\boldsymbol{k}_{m,n}\boldsymbol{r}) \Big\rangle\Big|_{\frac{1}{2}V_{uc}} \\
&= -(\boldsymbol{k}^2_{m,n} + 2\kappa^2) a_{m,n},
\end{aligned} \tag{B.18}$$

and thus we obtain the Brandt iteration equations

$$\begin{aligned}
a_{m,n} &= -\frac{\Big\langle (r.h.s.) \cos(\boldsymbol{k}_{m,n}\boldsymbol{r}) \Big\rangle\Big|_{\frac{1}{2}V_{uc}}}{\boldsymbol{k}^2_{m,n} + 2\kappa^2} \\
b_{m,n} &= \frac{\Big\langle (r.h.s.) \cos(\boldsymbol{k}_{m,n}\boldsymbol{r}) \Big\rangle\Big|_{\frac{1}{2}V_{uc}}}{\boldsymbol{k}^2_{m,n} + \bar{\omega}} \\
c_{m,n} &= -\frac{\Big\langle (r.h.s.) \cos(\boldsymbol{k}_{m,n}\boldsymbol{r}) \Big\rangle\Big|_{\frac{1}{2}V_{uc}}}{\boldsymbol{k}^2_{m,n} + 2\kappa^2} \\
d_{m,n} &= -\frac{\Big\langle (r.h.s.) \cos(\boldsymbol{k}_{m,n}\boldsymbol{r}) \Big\rangle\Big|_{\frac{1}{2}V_{uc}}}{\boldsymbol{k}^2_{m,n} + 2\kappa^2}.
\end{aligned} \tag{B.19}$$

Together with an equation coming from Eq. (B.5), which relaxes the absolute value of the dominant order parameter separately, this iterative procedure is very fast convergent for s-waves[60]. For p-waves, the first few iterations also converge very fast

towards the physical solution, however further iteration leads in the most cases to oscillations between several locally minimal solutions.

To minimize the Gibbs-Ginzburg-Landau functional to its global minimum, we simply formulate the free energy expression Eq. (3.29) in terms of the (rescaled) reciprocal space components $a_{m,n}, b_{m,n}/\bar{B}, c_{m,n}$ and $d_{m,n}$ and the average field $\bar{B}$ used in the Brandt steps, and use a standard relaxation method. Since the minima of typical Ginzburg-Landau free energy functionals are usually very shallow in terms of the reciprocal space vectors, it is important for an efficient solution to have a good initial guess, which in this context is given by the output of the Brandt method.

Appendix C

Implementation of Vortex Solutions

C.1 Bogoliubov-de Gennes formalism: Details

C.1.1 BdG-equations for s- and d-wave symmetry

As mentioned in Section 4.2, we derive here briefly the equations for the gap function for s- and d-wave symmetry in center-of-mass coordinates. In the case of s-waves, the result is immediately clear: since the interaction potential is basically a δ-function, we end up with the zero order derivative terms leading to the usual equation

$$\Delta_s(\boldsymbol{R}, k) = v_0 D(\boldsymbol{R}, \boldsymbol{R}), \tag{C.1}$$

and with the definition

$$\Delta_s(\boldsymbol{R}, k) \equiv \frac{1}{V}\eta_s(\boldsymbol{R}) \tag{C.2}$$

we obtain the self-consistent gap equation

$$\eta_s(\boldsymbol{R}) = V v_0 \sum_n v_n^*(\boldsymbol{R}) u_n(\boldsymbol{R}) \tanh\left(\frac{\beta E_n}{2}\right). \tag{C.3}$$

The off-diagonal integral is also easily performed, leading to

$$\int d^3\boldsymbol{r}' \Delta_s(\boldsymbol{r}, \boldsymbol{r}') v(\boldsymbol{r}') = \eta_s(\boldsymbol{r}) v(\boldsymbol{r}). \tag{C.4}$$

More involved is the situation for the d-wave symmetry. Using the model potential given in Eq. (4.9), we find

$$\Delta_d(\boldsymbol{R}, k) =$$

$$
\begin{aligned}
&= \frac{1}{V}\int d^3\boldsymbol{\rho}\,\Delta_d(\boldsymbol{r},\boldsymbol{r}')e^{-i\boldsymbol{\rho}\boldsymbol{k}} \\
&= \frac{v_0}{(2\pi)^3}\int d^3\boldsymbol{\rho}\,d^3\boldsymbol{k}'\,\frac{(k_x'^2-k_y'^2)^2}{4k_F^4}e^{i\boldsymbol{\rho}\boldsymbol{k}'}D(\boldsymbol{R}+\frac{1}{2}\boldsymbol{\rho},\boldsymbol{R}-\frac{1}{2}\boldsymbol{\rho})e^{-i\boldsymbol{\rho}\boldsymbol{k}} \\
&= \cdots \\
&= v_0\Bigg(\frac{(k_x^2-k_y^2)^2}{4k_F^4}+\frac{i}{2k_F^4}\begin{pmatrix}k_x\\-k_y\end{pmatrix}(k_x^2-k_y^2)(\boldsymbol{\nabla}_1-\boldsymbol{\nabla}_2) \\
&\quad -\frac{1}{4k_F^4}(k_x^2-k_y^2)\left[(\partial_{1x}^2-\partial_{1y}^2)+(\partial_{2x}^2-\partial_{2y}^2)-2(\partial_{1x}\partial_{2x}-\partial_{1y}\partial_{2y})\right] \\
&\quad +\frac{1}{4k_F^4}2k_xk_y\left[\partial_{1x}\partial_{1y}+\partial_{2x}\partial_{2y}-\partial_{1x}\partial_{2y}-\partial_{1y}\partial_{2x}\right] \\
&\quad -\frac{1}{8k_F^4}k^2\left[\boldsymbol{\nabla}_1^2+\boldsymbol{\nabla}_2^2-2\boldsymbol{\nabla}_1\cdot\boldsymbol{\nabla}_2\right]\Bigg)D(\boldsymbol{R},\boldsymbol{R}) \\
&= -\frac{v_0}{4k_F^4}(k_x^2-k_y^2)\left[(\partial_{1x}^2-\partial_{1y}^2)+(\partial_{2x}^2-\partial_{2y}^2)-2(\partial_{1x}\partial_{2x}-\partial_{1y}\partial_{2y})\right]D(\boldsymbol{R},\boldsymbol{R}). \qquad \text{(C.5)}
\end{aligned}
$$

While the odd terms in $\boldsymbol{k}$ vanish due to symmetry reasons, all even terms in $\boldsymbol{k}$ lead in principle to non-vanishing pairing. In the last line, we thus restricted to the desired interaction channel given here through the $k_x^2-k_y^2$-symmetry in the relative momentum. This is also why higher order gradients were not taken into account in the derivation above. Defining

$$
\Delta_d(\boldsymbol{R},\boldsymbol{k}) \equiv \frac{1}{Vk_F^2}\eta_d(\boldsymbol{R})(k_x^2-k_y^2), \qquad \text{(C.6)}
$$

we end up with the self-consistent gap equation

$$
\begin{aligned}
\eta_d(\boldsymbol{R}) \;=\; -\frac{V}{4k_F^2}v_0\sum_n\Big(&v_n^*(\boldsymbol{R})(\partial_x^2-\partial_y^2)u_n(\boldsymbol{R})+u_n(\boldsymbol{R})(\partial_x^2-\partial_y^2)v_n^*(\boldsymbol{R}) \\
&-2\Big(\partial_x v_n^*(\boldsymbol{R})\partial_x u_n(\boldsymbol{R})-\partial_y v_n^*(\boldsymbol{R})\partial_y u_n(\boldsymbol{R})\Big)\Big)\tanh\left(\frac{\beta E_n}{2}\right) \qquad \text{(C.7)}
\end{aligned}
$$

for d-waves. Finally, the off-diagonal integral is performed analogously as in the p-wave case, leading to

$$
\begin{aligned}
\int d^3\boldsymbol{r}'\Delta_d(\boldsymbol{r},\boldsymbol{r}')v(\boldsymbol{r}') \;=\; -\frac{1}{k_F^2}\Big(&\eta_d(\boldsymbol{r})(\partial_x^2-\partial_y^2)+\Big((\partial_x\eta_d(\boldsymbol{r}))\partial_x-(\partial_y\eta_d(\boldsymbol{r}))\partial_y\Big) \\
&+\frac{1}{4}\Big((\partial_x^2-\partial_y^2)\eta_d(\boldsymbol{r})\Big)\Big)v(\boldsymbol{r}). \qquad \text{(C.8)}
\end{aligned}
$$

C.1.2 Gauge invariance

In this section, we prove the gauge invariance of the gradient expansion used above. In detail, we show that this transformation commutes with the gauge invariance, which

means that first performing a gauge transformation in the full system and expanding the transformed system has the same effect as first doing the gradient expansion and then implementing the gauge transformation. A gauge transformation in the quasiparticle amplitudes has the effect

$$\begin{pmatrix} u \\ v \end{pmatrix} \to \begin{pmatrix} ue^{i\chi} \\ ve^{-i\chi} \end{pmatrix}, \tag{C.9}$$

where $\chi(\boldsymbol{r})$ corresponds to a local gauge transformation. It is clear that the gap function then transforms as

$$\Delta(\boldsymbol{r},\boldsymbol{r}') \to \Delta(\boldsymbol{r},\boldsymbol{r}')e^{i(\chi(\boldsymbol{r})+\chi(\boldsymbol{r}'))}. \tag{C.10}$$

Performing the gradient expansion on this transformed gap function, we obtain

$$\begin{aligned}
&\Delta_{\text{transf}}(\boldsymbol{R},\boldsymbol{k}) = \\
&= \frac{1}{V}\int d^3\boldsymbol{\rho}\ \Delta(\boldsymbol{r},\boldsymbol{r}')\ e^{i(\chi(\boldsymbol{r})+\chi(\boldsymbol{r}'))}e^{-i\boldsymbol{\rho}\boldsymbol{k}} \\
&= \frac{v_0}{(2\pi)^3}\int d^3\boldsymbol{\rho}\ d^3\boldsymbol{k}'\ \frac{\boldsymbol{k}'^2}{2k_F^2}e^{i\boldsymbol{\rho}\boldsymbol{k}'}D(\boldsymbol{R}+\frac{1}{2}\boldsymbol{\rho},\boldsymbol{R}-\frac{1}{2}\boldsymbol{\rho})\ e^{i\left(\chi(\boldsymbol{R}+\frac{1}{2}\boldsymbol{\rho})+\chi(\boldsymbol{R}-\frac{1}{2}\boldsymbol{\rho})\right)}e^{-i\boldsymbol{\rho}\boldsymbol{k}} \\
&= \frac{v_0}{(2\pi)^3}\int d^3\boldsymbol{\rho}\ d^3\boldsymbol{k}'\ \frac{\boldsymbol{k}'^2}{2k_F^2}e^{i\boldsymbol{\rho}\boldsymbol{k}'}\left(1+\frac{1}{2}\boldsymbol{\rho}\boldsymbol{\nabla}_1-\frac{1}{2}\boldsymbol{\rho}\boldsymbol{\nabla}_2+O(\rho^2\partial_i\partial_j)\right)D(\boldsymbol{R},\boldsymbol{R})e^{2i\chi(\boldsymbol{R})} \\
&\qquad\qquad \times\left(1+\frac{1}{2}\boldsymbol{\rho}(i\boldsymbol{\nabla}\chi-i\boldsymbol{\nabla}\chi)+O\Big(\rho^2 g(\boldsymbol{R})\Big)\right)e^{-i\boldsymbol{\rho}\boldsymbol{k}} \\
&= \frac{v_0}{(2\pi)^3}e^{2i\chi(\boldsymbol{R})}\int d^3\boldsymbol{\rho}\ d^3\boldsymbol{k}'\Big(1+(\boldsymbol{\nabla}_1-\boldsymbol{\nabla}_2)\frac{i\boldsymbol{\nabla}_{\boldsymbol{k}}}{2}+O\Big(i^2\partial_{k_i}\partial_{k_j}\partial_i\partial_j\Big) \\
&\qquad\qquad +O\Big(\rho^2 g(\boldsymbol{R})\Big)\Big)D(\boldsymbol{R},\boldsymbol{R})\frac{\boldsymbol{k}'^2}{2k_F^2}e^{i\boldsymbol{\rho}(\boldsymbol{k}'-\boldsymbol{k})} \\
&= \Delta(\boldsymbol{R},\boldsymbol{k})e^{2i\chi(\boldsymbol{R})},
\end{aligned} \tag{C.11}$$

where we used (Eq.) and $D(\boldsymbol{R},\boldsymbol{R})=0$. Consequently, we find

$$\eta_\pm(\boldsymbol{R}) \to \eta_\pm(\boldsymbol{R})e^{2i\chi(\boldsymbol{R})}. \tag{C.12}$$

On the other hand we can use the center-of-mass form of the self-consistency relation and perform the gauge transformation again on the level of quasiparticles and find (arguments $\boldsymbol{R}$ suppressed)

$$\begin{aligned}
&\eta_{\pm,\text{transf}} = \\
&= -\frac{iV}{2\sqrt{2}k_F}v_0\sum_n\left(v_n^*e^{i\chi}\Box_\pm u_n e^{i\chi}-u_n e^{i\chi}\Box_\pm v_n^* e^{i\chi}\right)\tanh\left(\frac{\beta E_n}{2}\right) \\
&= -\frac{iV}{2\sqrt{2}k_F}v_0e^{2i\chi}\sum_n\left(v_n^*(\Box_\pm+i\Box_\pm\chi)u_n-u_n(\Box_\pm+i\Box_\pm\chi)v_n^*\right)\tanh\left(\frac{\beta E_n}{2}\right) \\
&= \eta_\pm e^{2i\chi},
\end{aligned} \tag{C.13}$$

which is obviously compatible with the former result.

The same procedure can be done with the off-diagonal elements. The first approach leads to

$$\begin{aligned}
&\left[\int d^3\boldsymbol{r}'\Delta(\boldsymbol{r},\boldsymbol{r}')v(\boldsymbol{r}')\right]_{\text{transf}} = \\
&= \frac{1}{(2\pi)^3}\iint d^3\boldsymbol{r}'d^3\boldsymbol{k}e^{ik\rho}\frac{\boldsymbol{k}}{k_F}\boldsymbol{\eta}(\boldsymbol{R})e^{2i\chi(\boldsymbol{R})}v(\boldsymbol{r}')e^{-i\chi(\boldsymbol{r}')} \\
&= -\frac{i}{(2\pi)^3 k_F}\iint d^3\boldsymbol{r}'d^3\boldsymbol{k}e^{ik\rho}\boldsymbol{\nabla}_{r'}\left(\boldsymbol{\eta}(\boldsymbol{R})e^{2i\chi(\boldsymbol{R})}v(\boldsymbol{r}')e^{-i\chi(\boldsymbol{r}')}\right) \\
&= -\frac{i}{k_F}\left(v\frac{1}{2}(\boldsymbol{\nabla}\boldsymbol{\eta})e^{i\chi}+v\boldsymbol{\eta}e^{i\chi}i\boldsymbol{\nabla}\chi+(\boldsymbol{\nabla}v)\boldsymbol{\eta}e^{i\chi}+v\boldsymbol{\eta}e^{i\chi}(-i)\boldsymbol{\nabla}\chi\right)\Big|_r \\
&= -\frac{i}{k_F}e^{i\chi(\boldsymbol{r})}\left(\boldsymbol{\eta}(\boldsymbol{r})\boldsymbol{\nabla}+\frac{1}{2}(\boldsymbol{\nabla}\boldsymbol{\eta}(\boldsymbol{r}))\right)v(\boldsymbol{r}) \\
&= -\frac{i}{\sqrt{2}k_F}e^{i\chi(\boldsymbol{r})}\sum_{\pm}\left(\eta_{\pm}(\boldsymbol{r})\Box_{\mp}+\frac{1}{2}(\Box_{\mp}\eta_{\pm}(\boldsymbol{r}))\right)v(\boldsymbol{r}) \\
&= e^{i\chi(\boldsymbol{r})}\int d^3\boldsymbol{r}'\Delta(\boldsymbol{r},\boldsymbol{r}')v(\boldsymbol{r}'),
\end{aligned} \tag{C.14}$$

which is compatible with (arguments $\boldsymbol{r}$ suppressed)

$$\begin{aligned}
&\left[-\frac{i}{\sqrt{2}k_F}\sum_{\pm}\left(\eta_{\pm}\Box_{\mp}+\frac{1}{2}(\Box_{\mp}\eta_{\pm})\right)v\right]_{\text{transf}} = \\
&= -\frac{i}{\sqrt{2}k_F}\sum_{\pm}\left(e^{2i\chi}\eta_{\pm}\Box_{\mp}+\frac{1}{2}\Big(\Box_{\mp}(e^{2i\chi}\eta_{\pm})\Big)\right)ve^{-i\chi} \\
&= -\frac{i}{\sqrt{2}k_F}e^{i\chi}\sum_{\pm}\left(\eta_{\pm}(\Box_{\mp}-i\Box_{\mp}\chi)+\frac{1}{2}\Big(2i(\Box_{\mp}\chi)\eta_{\pm}+\Box_{\mp}\eta_{\pm}\Big)\right)v \\
&= -\frac{i}{\sqrt{2}k_F}e^{i\chi}\sum_{\pm}\left(\eta_{\pm}\Box_{\mp}+\frac{1}{2}(\Box_{\mp}\eta_{\pm})\right)v.
\end{aligned} \tag{C.15}$$

C.2 Bulk solution

As in the p-wave case we assume $\eta=\eta_\infty$ and use plane wave solutions to express the hamiltonian in the following form

$$\begin{pmatrix}\xi_{\boldsymbol{k}} & \eta\\ \eta^* & -\xi_{\boldsymbol{k}}\end{pmatrix}\begin{pmatrix}u_{\boldsymbol{k}}\\ v_{\boldsymbol{k}}\end{pmatrix}=E_{\boldsymbol{k}}\begin{pmatrix}u_{\boldsymbol{k}}\\ v_{\boldsymbol{k}}\end{pmatrix}. \tag{C.16}$$

Diagonalization of the eigenvalue problem leads to

$$E_{\boldsymbol{k}} = \pm\sqrt{\xi_{\boldsymbol{k}}^2+|\eta|^2}$$

$$
\begin{aligned}
u_{\boldsymbol{k}} &= \sqrt{\frac{1}{2}\left(1 \pm \frac{\xi_{\boldsymbol{k}}}{E_{\boldsymbol{k}}}\right)} \\
v_{\boldsymbol{k}} &= \pm e^{i\alpha}\sqrt{\frac{1}{2}\left(1 \mp \frac{\xi_{\boldsymbol{k}}}{E_{\boldsymbol{k}}}\right)},
\end{aligned}
\tag{C.17}
$$

where the phase is determined through

$$
e^{i\alpha} = \frac{\eta^*}{|\eta|}. \tag{C.18}
$$

Inserting this result into the gap-equation, we obtain

$$
\begin{aligned}
\eta &= v\sum_{E_{\boldsymbol{k}}} u_{\boldsymbol{k}} v_{\boldsymbol{k}}^* \tanh\left(\frac{\beta E_{\boldsymbol{k}}}{2}\right) \\
&= v\sum_{E_{\boldsymbol{k}}} \frac{\eta}{2E_{\boldsymbol{k}}} \tanh\left(\frac{\beta E_{\boldsymbol{k}}}{2}\right),
\end{aligned}
\tag{C.19}
$$

and thus the self-consistency equation ($T = 0$)

$$
\begin{aligned}
1 &= v\sum_{E_{\boldsymbol{k}}} \frac{1}{2|E_{\boldsymbol{k}}|} = v\sum_{E_{\boldsymbol{k}}\geq 0} \frac{1}{E_{\boldsymbol{k}}} \\
&= v\frac{N^{2D}(0)}{2}\int_{-E_c}^{E_c} d\xi_{\boldsymbol{k}} \frac{1}{\sqrt{\xi_{\boldsymbol{k}}^2 + |\eta|^2}} \\
&\sim v N^{2D}(0) \ln\frac{2E_c}{|\eta|} \\
&= \frac{v N^{2D} k_F}{2\pi|\Delta|_\infty}\left(\log\left|\frac{E_c + W}{-E_c + W}\right|\right),
\end{aligned}
\tag{C.20}
$$

where

$$
W = \sqrt{E_c^2 + |\Delta|_\infty^2}. \tag{C.21}
$$

In rescaled units, we have simply to put $|\Delta|_\infty = 1$.

C.3 Vortex solutions

As outlined in Section 4.4, we write the quasiparticles in the Bessel-function basis set given in Eq. (4.47). Below we calculate the hamiltonian in the subspaces to constant l in terms of these basis functions as well as all self-consistency relations in radial coordinates. Together with the Maxwell equations, we have complete sets of equations.

C.3.1 *s*-wave

The hamiltonian for angular momentum number l reads

$$\begin{pmatrix} h_l & \frac{V_{2D}v}{2\pi}\hat{\eta} \\ \frac{V_{2D}v}{2\pi}\hat{\eta}^* & -h_{-(l+1)} \end{pmatrix} \tag{C.22}$$

with

$$h_l(r) = -\frac{E_F^0}{k_F^2}\left(\partial_r^2 + \frac{1}{r}\partial_r - \frac{l^2}{r^2} - \frac{2l\gamma_A A(r)}{r} - \gamma_A^2 A^2(r)\right) - E_F - \gamma_\Phi \Phi(r). \tag{C.23}$$

The self-consistency relation for the gap function reads

$$\eta(r,\varphi) = \frac{V_{2D}v}{2\pi}\hat{\eta}(r)e^{-i\varphi} \tag{C.24}$$

with

$$\hat{\eta}(r) = 2\sum_{n,l\geq 0} v_{n,l+1}u_{n,l}\tanh\left(\frac{\beta E_{n,l}}{2}\right), \tag{C.25}$$

and the two remaining self-consistency relations for current and charge are

$$\begin{aligned} j(r) &= -\frac{1}{\pi}\sum_{n,l\geq 0}\left(u_{n,l}^2\left(\frac{l}{r}+\gamma_A A\right)f(E_{n,l}) - v_{n,l+1}^2\left(\frac{l+1}{r}-\gamma_A A\right)\Big(1-f(E_{n,l})\Big)\right) \\ \rho_e(r) &= -\frac{1}{\pi}\sum_{n,l\geq 0} u_{n,l}^2 f(E_{n,l}) + v_{n,l+1}^2\Big(1-f(E_{n,l})\Big). \end{aligned} \tag{C.26}$$

Finally, the local density of states reads

$$N^\delta(r,E) = \frac{2}{\pi}\left(\sum_{n,l\geq 0} u_{n,l}^2\frac{\delta}{(E-E_{n,l})^2+\delta^2} + v_{n,l+1}^2\frac{\delta}{(E+E_{n,l})^2+\delta^2}\right). \tag{C.27}$$

Matrix elements

With the basis functions

$$\begin{aligned} u_{n,l}(r) &= \sum_j u_{l,j}^n f_{l,j}(r) = \sum_j u_{l,j}^n N_{l,j} J_{|l|}\left(\frac{Z_{l,j}}{R}r\right) \\ v_{n,l+1}(r) &= \sum_j v_{l+1,j}^n f_{l+1,j}(r), \end{aligned} \tag{C.28}$$

we obtain for the diagonal blocks

$$\begin{aligned} \mathcal{H}_{l,i,j} &= \int_0^R f_{l,i}(r) h_l f_{l,j}(r) r dr \\ &= \left(\frac{E_F^0}{k_F^2}\left(\frac{Z_{l,j}}{R}\right)^2 - E_F\right)\delta_{i,j} \pm \frac{E_F^0}{k_F^2}\int_0^R 2l\gamma_A A(r) f_{l,i}(r) f_{l,j}(r) dr \\ &\quad + \int_0^R \left(\frac{E_F^0}{k_F^2}\gamma_A^2 A^2(r) - \gamma_\Phi \Phi(r)\right) f_{l,i}(r) f_{l,j}(r) r dr, \end{aligned} \tag{C.29}$$

where the lower right diagonal block is $-\mathcal{H}_{l+1,i,j}$ with the lower sign. The upper right off-diagonal block then is

$$\mathcal{H}^{\eta}_{l,i,j} = \frac{V_{2D}\upsilon}{2\pi}\int_0^R f_{l,i}(r)\hat{\eta}(r)f_{l+1,j}(r)rdr, \tag{C.30}$$

and the self-consistency relation

$$\hat{\eta}(r) = 2\sum_{n,l\geq 0} u_{n,l}(r)v_{n,l+1}(r)\tanh\left(\frac{\beta E_{n,l}}{2}\right). \tag{C.31}$$

C.3.2 p-wave (S)

The hamiltonian for angular momentum number l reads

$$\begin{pmatrix} h_l & \frac{V_{2D}\upsilon}{8\pi k_F^2}\sum_{\pm}\left(\hat{\eta}_{\pm}\left(\partial_r \pm \frac{l}{r}\right) + \frac{1}{2}\left(\left(\partial_r + \frac{1}{r}\right)\hat{\eta}_{\pm}\right)\right) \\ -\frac{V_{2D}\upsilon}{8\pi k_F^2}\sum_{\pm}\left(\hat{\eta}_{\pm}\left(\partial_r \mp \frac{l}{r}\right) + \frac{1}{2}\left(\left(\partial_r + \frac{1}{r}\right)\hat{\eta}_{\pm}\right)\right) & -h_{-l} \end{pmatrix} \tag{C.32}$$

with

$$h_l(r) = -\frac{E_F^0}{k_F^2}\left(\partial_r^2 + \frac{1}{r}\partial_r - \frac{l^2}{r^2} - \frac{2l\gamma_A A(r)}{r} - \gamma_A^2 A^2(r)\right) - E_F - \gamma_\Phi\Phi(r). \tag{C.33}$$

The self-consistency relation for the gap function reads

$$\eta_{\pm}(r,\varphi) = \frac{V_{2D}\upsilon}{4\sqrt{2}\pi k_F}\hat{\eta}_{\pm}(r)e^{\pm i\varphi} \tag{C.34}$$

with

$$\hat{\eta}_{\pm}(r) = -\sum_{n,l\geq 0}(2-\delta_{l,0})\left(\mp\frac{2l}{r}v_{n,l}u_{n,l} + v_{n,l}\partial_r u_{n,l} - u_{n,l}\partial_r v_{n,l}\right)\tanh\left(\frac{\beta E_{n,l}}{2}\right), \tag{C.35}$$

and the two remaining self-consistency relations for current and charge are

$$\begin{aligned} j(r) &= -\frac{1}{2\pi}\sum_{n,l\geq 0}(2-\delta_{l,0})\left(u_{n,l}^2\left(\frac{l}{r}+\gamma_A A\right)f(E_{n,l}) - v_{n,l}^2\left(\frac{l}{r}-\gamma_A A\right)\left(1-f(E_{n,l})\right)\right) \\ \rho_e(r) &= -\frac{1}{2\pi}\sum_{n,l\geq 0}(2-\delta_{l,0})\left(u_{n,l}^2 f(E_{n,l}) + v_{n,l}^2\left(1-f(E_{n,l})\right)\right). \end{aligned} \tag{C.36}$$

Finally, the local density of states reads

$$N^{\delta}(r,E) = \frac{1}{\pi}\left(\sum_{n,l\geq 0}(2-\delta_{l,0})u_{n,l}^2\frac{\delta}{(E-E_{n,l})^2+\delta^2} + v_{n,l}^2\frac{\delta}{(E+E_{n,l})^2+\delta^2}\right). \tag{C.37}$$

Matrix elements

With the basis functions

$$\begin{aligned} u_{n,l}(r) &= \sum_j u^n_{l,j} f_{l,j}(r) = \sum_j u^n_{l,j} N_{l,j} J_{|l|}\left(\frac{Z_{l,j}}{R} r\right) \\ v_{n,l}(r) &= \sum_j v^n_{l,j} f_{l,j}(r), \end{aligned} \tag{C.38}$$

we obtain for the diagonal blocks

$$\begin{aligned} \mathcal{H}_{l,i,j} &= \int_0^R f_{l,i}(r) h_l f_{l,j}(r) r dr \\ &= \left(\frac{E_F^0}{k_F^2}\left(\frac{Z_{l,j}}{R}\right)^2 - E_F\right)\delta_{i,j} \pm \frac{E_F^0}{k_F^2}\int_0^R 2l\gamma_A A(r) f_{l,i}(r) f_{l,j}(r) dr \\ &\quad + \int_0^R \left(\frac{E_F^0}{k_F^2}\gamma_A^2 A^2(r) - \gamma_\Phi \Phi(r)\right) f_{l,i}(r) f_{l,j}(r) r dr, \end{aligned} \tag{C.39}$$

where the lower right diagonal block is $-\mathcal{H}_{l,i,j}$ with the lower sign. The upper right off-diagonal block then is

$$\begin{aligned} \mathcal{H}^\eta_{l,i,j} &= \frac{V_{2D}\upsilon}{8\pi k_F^2}\int_0^R r f_{l,i}(r) \sum_\pm \left(\hat\eta_\pm(r)\left(\partial_r \pm \frac{l}{r} + \frac{1}{2r}\right)\right) f_{l,j}(r) dr \\ &\quad + \frac{V_{2D}\upsilon}{8\pi k_F^2}\int_0^R f_{l,i}(r) f_{l,j}(r) \sum_\pm \frac{1}{2}\Big(\partial_r \hat\eta_\pm(r)\Big) r dr \\ &= \frac{V_{2D}\upsilon}{8\pi k_F^2}\int_0^R \Big(\hat\eta_+(r) + \hat\eta_-(r)\Big)\frac{1}{2}\left(\frac{Z_{l,i}}{R} N_{l,i} J_{|l|+1}\left(\frac{Z_{l,i}}{R} r\right) f_{l,j}(r) - \{i \rightleftharpoons j\}\right) r dr \\ &\quad + \frac{V_{2D}\upsilon}{8\pi k_F^2}\int_0^R \Big(\hat\eta_+(r) - \hat\eta_-(r)\Big)\, l\, f_{l,i}(r) f_{l,j}(r) dr, \end{aligned} \tag{C.40}$$

and the self-consistency relation

$$\begin{aligned} \hat\eta_+(r) + \hat\eta_-(r) &= 2\sum_{n,l\geq 0}(2-\delta_{l,0})\left(v_{n,l}(r)\sum_j u^n_{l,j}\frac{Z_{l,j}}{R} N_{l,j} J_{|l|+1}\left(\frac{Z_{l,j}}{R} r\right)\right. \\ &\qquad \left. - u_{n,l}(r)\sum_j v^n_{l,j}\frac{Z_{l,j}}{R} N_{l,j} J_{|l|+1}\left(\frac{Z_{l,j}}{R} r\right)\right)\tanh\left(\frac{\beta E_{n,l}}{2}\right) \\ \hat\eta_+(r) - \hat\eta_-(r) &= 8\sum_{n,l>0}\frac{l}{r} u_{n,l}(r) v_{n,l}(r)\tanh\left(\frac{\beta E_{n,l}}{2}\right). \end{aligned} \tag{C.41}$$

C.3.3 p-wave (U)

The hamiltonian for angular momentum number l reads

$$\begin{pmatrix} h_{l-1} & \frac{V_{2D}v}{8\pi k_F^2}\sum_{\pm}\left(\hat{\eta}_{\pm}\left(\partial_r \pm \frac{l+1}{r}\right)+\frac{1}{2}\left(\left(\partial_r+\frac{1\mp 2}{r}\right)\hat{\eta}_{\pm}\right)\right) \\ -\frac{V_{2D}v}{8\pi k_F^2}\sum_{\pm}\left(\hat{\eta}_{\pm}\left(\partial_r \mp \frac{l-1}{r}\right)+\frac{1}{2}\left(\left(\partial_r+\frac{1\mp 2}{r}\right)\hat{\eta}_{\pm}\right)\right) & -h_{-(l+1)} \end{pmatrix} \tag{C.42}$$

with

$$h_l(r) = -\frac{E_F^0}{k_F^2}\left(\partial_r^2+\frac{1}{r}\partial_r-\frac{l^2}{r^2}-\frac{2l\gamma_A A(r)}{r}-\gamma_A^2 A^2(r)\right)-E_F-\gamma_\Phi\Phi(r). \tag{C.43}$$

The self-consistency relation for the gap function reads

$$\eta_{\pm}(r,\varphi) = \frac{V_{2D}v}{4\sqrt{2}\pi k_F}\hat{\eta}_{\pm}(r)e^{\pm i\varphi-2i\varphi} \tag{C.44}$$

with

$$\begin{aligned}\hat{\eta}_{\pm}(r) &= -\sum_{n,l\geq 0}(2-\delta_{l,0})\left(\mp\frac{2l}{r}v_{n,l+1}u_{n,l-1}+v_{n,l+1}\partial_r u_{n,l-1}\right.\\ &\qquad\left.-u_{n,l-1}\partial_r v_{n,l+1}\right)\tanh\left(\frac{\beta E_{n,l}}{2}\right),\end{aligned} \tag{C.45}$$

and the two remaining self-consistency relations for current and charge are

$$\begin{aligned} j(r) &= -\frac{1}{2\pi}\sum_{n,l\geq 0}(2-\delta_{l,0})\left(u_{n,l-1}^2\left(\frac{l-1}{r}+\gamma_A A\right)f(E_{n,l})\right.\\ &\qquad\left.-v_{n,l+1}^2\left(\frac{l+1}{r}-\gamma_A A\right)\Big(1-f(E_{n,l})\Big)\right)\\ \rho_e(r) &= -\frac{1}{2\pi}\sum_{n,l\geq 0}(2-\delta_{l,0})\left(u_{n,l-1}^2 f(E_{n,l})+v_{n,l+1}^2\Big(1-f(E_{n,l})\Big)\right). \end{aligned} \tag{C.46}$$

Finally, the local density of states reads

$$N^{\delta}(r,E) = \frac{1}{\pi}\left(\sum_{n,l\geq 0}(2-\delta_{l,0})u_{n,l-1}^2\frac{\delta}{(E-E_{n,l})^2+\delta^2}+v_{n,l+1}^2\frac{\delta}{(E+E_{n,l})^2+\delta^2}\right). \tag{C.47}$$

Matrix elements

With the basis functions

$$\begin{aligned} u_{n,l-1}(r) &= \sum_j u_{l-1,j}^n f_{l-1,j}(r) = \sum_j u_{l-1,j}^n N_{l-1,j}J_{|l-1|}\left(\frac{Z_{l-1,j}}{R}r\right)\\ v_{n,l+1}(r) &= \sum_j v_{l+1,j}^n f_{l+1,j}(r), \end{aligned} \tag{C.48}$$

we obtain for the diagonal blocks

$$\begin{aligned}\mathcal{H}_{l,i,j} &= \int_0^R f_{l-1,i}(r) h_{l-1} f_{l-1,j}(r) r dr \\ &= \left(\frac{E_F^0}{k_F^2} \left(\frac{Z_{l-1,j}}{R} \right)^2 - E_F \right) \delta_{i,j} \pm \frac{E_F^0}{k_F^2} \int_0^R 2(l-1)\gamma_A A(r) f_{l-1,i}(r) f_{l-1,j}(r) dr \\ &\quad + \int_0^R \left(\frac{E_F^0}{k_F^2} \gamma_A^2 A^2(r) - \gamma_\Phi \Phi(r) \right) f_{l-1,i}(r) f_{l-1,j}(r) r dr, \end{aligned} \tag{C.49}$$

where the lower right diagonal block is $-\mathcal{H}_{l+1,i,j}$ with the lower sign. The upper right off-diagonal block then is

$$\begin{aligned}\mathcal{H}^\eta_{l,i,j} &= \frac{V_{2D}\upsilon}{8\pi k_F^2} \int_0^R f_{l-1,i}(r) \sum_\pm \left(\hat{\eta}_\pm(r) \left(\partial_r \pm \frac{l+1}{r} + \frac{1 \mp 2}{2r} \right) \right) f_{l+1,j}(r) r dr \\ &\quad + \frac{V_{2D}\upsilon}{8\pi k_F^2} \int_0^R f_{l-1,i}(r) f_{l+1,j}(r) \sum_\pm \frac{1}{2} \Big(\partial_r \hat{\eta}_\pm(r) \Big) r dr \\ &= \frac{V_{2D}\upsilon}{8\pi k_F^2} \int_0^R \Big(\hat{\eta}_+(r) + \hat{\eta}_-(r) \Big) \frac{1}{2} \left(\frac{Z_{l-1,i}}{R} N_{l-1,i} J_{|l-1|+1} \left(\frac{Z_{l-1,i}}{R} r \right) f_{l+1,j}(r) \right. \\ &\qquad \left. - \left\{ \begin{matrix} i \\ l-1 \end{matrix} \rightleftharpoons \begin{matrix} j \\ l+1 \end{matrix} \right\} \right) r dr \\ &\quad + \frac{V_{2D}\upsilon}{8\pi k_F^2} \int_0^R \Big(\hat{\eta}_+(r) + \hat{\eta}_-(r) \Big) \frac{1}{2} f_{l-1,i}(r) f_{l+1,j}(r) (1 - \delta_{l,0}) dr \\ &\quad + \frac{V_{2D}\upsilon}{8\pi k_F^2} \int_0^R \Big(\hat{\eta}_+(r) - \hat{\eta}_-(r) \Big) l \; f_{l-1,i}(r) f_{l+1,j}(r) dr, \end{aligned} \tag{C.50}$$

and the self-consistency relation

$$\begin{aligned}\hat{\eta}_+(r) + \hat{\eta}_-(r) &= 2 \sum_{n,l \geq 0} (2 - \delta_{l,0}) \left(\frac{2}{r} u_{n,l-1}(r) v_{n,l+1}(r) \right. \\ &\quad + v_{n,l+1}(r) \sum_j u^n_{l-1,j} \frac{Z_{l-1,j}}{R} N_{l-1,j} J_{|l-1|+1} \left(\frac{Z_{l-1,j}}{R} r \right) \\ &\quad \left. - u_{n,l-1}(r) \sum_j v^n_{l+1,j} \frac{Z_{l+1,j}}{R} N_{l+1,j} J_{|l+1|+1} \left(\frac{Z_{l+1,j}}{R} r \right) \right) \tanh \left(\frac{\beta E_{n,l}}{2} \right) \\ \hat{\eta}_+(r) - \hat{\eta}_-(r) &= 8 \sum_{n,l>0} \frac{l}{r} u_{n,l-1}(r) v_{n,l+1}(r) \tanh \left(\frac{\beta E_{n,l}}{2} \right). \end{aligned} \tag{C.51}$$

C.4 Varia

C.4.1 Density of states

All following quantities are defined including the degeneracy in the spin variable.

Number of states in a volume with energy smaller than E_c

$$\begin{aligned} N^{3D} &= 2\left(\frac{2mE_c}{\hbar^2}\right)^{\frac{3}{2}}\frac{4\pi}{3}\left(\frac{L}{2\pi}\right)^3 = \left(\frac{2mE_c}{\hbar^2}\right)^{\frac{3}{2}}\frac{V^{3D}}{3\pi^2} \\ N^{2D} &= 2\left(\frac{2mE_c}{\hbar^2}\right)\pi\left(\frac{L}{2\pi}\right)^2 = \left(\frac{2mE_c}{\hbar^2}\right)\frac{V^{2D}}{2\pi}. \end{aligned} \tag{C.52}$$

Density of electrons at E_F

$$\begin{aligned} n^{3D} &= \frac{N^{3D}(E_F)}{V^{3D}} = \frac{k_F^3}{3\pi^2} \\ n^{2D} &\equiv n_s = \frac{k_F^2}{2\pi}. \end{aligned} \tag{C.53}$$

Density of states at E_F

$$\begin{aligned} N^{3D}(0) &= \frac{\partial N^{3D}(E)}{\partial E}\Big|_{E_F} = \frac{V^{3D}k_F^3}{2\pi^2 E_F} \\ N^{2D}(0) &= \frac{V^{2D}k_F^2}{2\pi E_F}. \end{aligned} \tag{C.54}$$

Density of states at E_F per volume

$$\begin{aligned} n^{3D}(0) &= \frac{\partial n^{3D}(E)}{\partial E}\Big|_{E_F} = \frac{k_F^3}{2\pi^2 E_F} \\ n^{2D}(0) &= \frac{k_F^2}{2\pi E_F} = \frac{n_s}{E_F}. \end{aligned} \tag{C.55}$$

Be aware that the definition of the density of states corresponds to the way it is used in the text (the sum is restricted to the Hilbert space with $|\xi_{\boldsymbol{k}}| \leq E_c$)

$$\begin{aligned} \sum_{E_{\boldsymbol{k}}\geq 0} &= \left(\frac{L}{2\pi}\right)^2\int d^2\boldsymbol{k} = \frac{V^{2D}}{2\pi}\int kdk \\ &= \frac{V^{2D}}{2\pi}\frac{m}{\hbar^2}\int_{-E_c}^{E_c} d\xi_{\boldsymbol{k}} = \frac{V^{2D}}{2\pi}\frac{k_F^2}{2E_F}\int_{-E_c}^{E_c} d\xi_{\boldsymbol{k}} \equiv \frac{N^{2D}(0)}{2}\int_{-E_c}^{E_c} d\xi_{\boldsymbol{k}}. \end{aligned} \tag{C.56}$$

C.4.2 Screenings

From London approach we have

$$\boldsymbol{A} = -\frac{mc}{n^{3D}e^2}\dot{\boldsymbol{j}} = \frac{mc}{\mu_p n^{3D}e^2}\boldsymbol{\nabla}^2\boldsymbol{A} \equiv \lambda_L^2\boldsymbol{\nabla}^2\boldsymbol{A}, \tag{C.57}$$

and thus the London penetration depth (in physical units)

$$\lambda_L = \sqrt{\frac{mc}{\mu_p e^2 n_z n_s}}, \tag{C.58}$$

and the permeability μ in dimensionless form (using the Maxwell equations)

$$\mu = \mu_p \frac{j_{sc}\xi^2}{A_{sc}} = 1. \tag{C.59}$$

For the Thomas-Fermi screening we find

$$\Phi = -\frac{E_F}{n^{3D}e^2}\rho = \frac{\epsilon_p E_F}{n^{3D}e^2}\boldsymbol{\nabla}^2\Phi \equiv \lambda_{TF}^2\boldsymbol{\nabla}^2\Phi, \tag{C.60}$$

and thus the Thomas-Fermi penetration depth (in physical units)

$$\lambda_{TF} = \sqrt{\frac{\epsilon_p E_F}{e^2 n_z n_s}}, \tag{C.61}$$

and the dielectricity ϵ in dimensionless form (using the Maxwell equations)

$$\epsilon = \epsilon_p \frac{\Phi_{sc}}{\rho_{sc}\xi^2} = 1. \tag{C.62}$$

C.4.3 Temperature dependent local density of states

Instead of the expression for the local density of states used above (here for s-waves, generalization to other types correspondingly)

$$N^\delta(r,E) = \frac{2}{\pi}\left(\sum_{n,l\geq 0} u_{n,l}^2 \frac{\delta}{(E-E_{n,l})^2+\delta^2} + v_{n,l+1}^2 \frac{\delta}{(E+E_{n,l})^2+\delta^2}\right) \tag{C.63}$$

with the artificial smearing parameter δ, there is a more natural expression using thermal smearing

$$N(r,E) = \beta\left(\sum_{n,l\geq 0} u_{n,l}^2 \frac{e^{\beta(E_{n,l}-E)}}{(1+e^{\beta(E_{n,l}-E)})^2} + v_{n,l+1}^2 \frac{e^{\beta(E_{n,l}+E)}}{(1+e^{\beta(E_{n,l}+E)})^2}\right). \tag{C.64}$$

Appendix D

Implementation of Lattice Solutions

D.1 Expansion in Bloch basis

In the following, we present the detailed form of the matrix elements of the hamiltonian with respect to the basis functions given in Eq. (5.35). The calculations are easy and make repeated use of the vanishing divergence of the vector potential in singular gauge, $((\boldsymbol{k}-\boldsymbol{k}')\boldsymbol{Q}_{k-k'}=0)$ and the symmetry properties of the occurring quantities as outlined below. The quasiparticle wavefunctions are decomposed as ($V_{2D}=V$)

$$\begin{aligned} u_{n,\boldsymbol{K}}(\boldsymbol{r}) &= \sum_{k} u_{n,\boldsymbol{K},k}\phi_{\boldsymbol{K},k}(\boldsymbol{r}) = \sum_{k} u_{n,\boldsymbol{K},k}\frac{1}{\sqrt{V}}e^{i(\boldsymbol{K}+k)\boldsymbol{r}} \\ v_{n,\boldsymbol{K}}(\boldsymbol{r}) &= \sum_{k} v_{n,\boldsymbol{K},k}\phi_{\boldsymbol{K},k}(\boldsymbol{r}). \end{aligned} \tag{D.1}$$

D.1.1 s-wave

For the upper left diagonal block we obtain

$$\begin{aligned} \mathcal{H}_{\boldsymbol{K},k,k'} &= \int_V \phi^*_{\boldsymbol{K},k}\left(\frac{1}{k_F^2}\left(\frac{1}{i}\boldsymbol{\nabla}-\boldsymbol{Q}_A(\boldsymbol{r})\right)^2-1\right)\phi_{\boldsymbol{K},k'}d^2\boldsymbol{r} \\ &= \left(\frac{(\boldsymbol{K}+\boldsymbol{k}')^2}{k_F^2}-1\right)\delta_{k,k'}-\frac{1}{k_F^2}(2\boldsymbol{K}+\boldsymbol{k}+\boldsymbol{k}')\boldsymbol{Q}_{A,k-k'} \\ &\quad +\frac{1}{k_F^2}\sum_q \boldsymbol{Q}_{A,q}\boldsymbol{Q}_{A,k-k'-q}, \end{aligned} \tag{D.2}$$

and correspondingly for the lower right block

$$\begin{aligned}\mathcal{H}_{\boldsymbol{K},k,k'} &= -\left(\frac{(\boldsymbol{K}+\boldsymbol{k}')^2}{k_F^2}-1\right)\delta_{k,k'}-\frac{1}{k_F^2}(2\boldsymbol{K}+\boldsymbol{k}+\boldsymbol{k}')\boldsymbol{Q}_{B,k-k'} \\ &\quad -\frac{1}{k_F^2}\sum_q \boldsymbol{Q}_{B,q}\boldsymbol{Q}_{B,k-k'-q}. \end{aligned} \tag{D.3}$$

The upper right off-diagonal block reads

$$\begin{aligned}\mathcal{H}^{\eta}_{\boldsymbol{K},k,k'} &= \int_V \phi^*_{\boldsymbol{K},k}\eta_s\phi_{\boldsymbol{K},k'}d^2\boldsymbol{r} \\ &= \eta_{s\boldsymbol{k}-\boldsymbol{k}'}, \end{aligned} \tag{D.4}$$

and the lower left block

$$\mathcal{H}^{\eta^*}_{\boldsymbol{K},k,k'} = \eta^*_{s\boldsymbol{k}'-\boldsymbol{k}}, \tag{D.5}$$

where we used the convention

$$\eta^*_{\boldsymbol{k}} \equiv (\eta_{\boldsymbol{k}})^*. \tag{D.6}$$

Finally, the self-consistency equation for the order parameter can be written as

$$\begin{aligned}\eta_s &= V\upsilon\sum_n v^*_n u_n \tanh\frac{\beta E_n}{2} \\ &= \upsilon\sum_{n,\boldsymbol{K},k,k'} v^*_{n,\boldsymbol{K},k}u_{n,\boldsymbol{K},k'}e^{i(\boldsymbol{k}'-\boldsymbol{k})\boldsymbol{r}}\tanh\frac{\beta E_n}{2}, \end{aligned} \tag{D.7}$$

and thus the Fourier components obey the self-consistency equation

$$\begin{aligned}\eta_{s\boldsymbol{q}} &= \frac{1}{2V_{uc}}\int_{2V_{uc}} e^{-i\boldsymbol{q}\boldsymbol{r}}\eta_s(\boldsymbol{r})d^2\boldsymbol{r} \\ &= \upsilon\sum_{n,\boldsymbol{K}}\left(\sum_k v^*_{n,\boldsymbol{K},k}u_{n,\boldsymbol{K},k+q}\right)\tanh\frac{\beta E_n}{2}. \end{aligned} \tag{D.8}$$

D.1.2 p-wave

The implementation for the p-wave is similar as above. The difference occurs in the off-diagonal blocks and the order parameter, which are both considerably more complicated. For the upper right block of the hamiltonian we find

$$\begin{aligned}\mathcal{H}^{\eta}_{\boldsymbol{K},k,k'} &= \int_V \phi^*_{\boldsymbol{K},k}\left(-\frac{i}{k_F}\left(\boldsymbol{\eta}\boldsymbol{\nabla}+\frac{1}{2}(\boldsymbol{\nabla}\boldsymbol{\eta})+\frac{i}{2}\boldsymbol{\eta}\left(\boldsymbol{Q}_B-\boldsymbol{Q}_A\right)\right)\right)\phi_{\boldsymbol{K},k'}d^2\boldsymbol{r} \\ &= \frac{1}{2k_F}\boldsymbol{\eta}_{\boldsymbol{k}-\boldsymbol{k}'}(2\boldsymbol{K}+\boldsymbol{k}+\boldsymbol{k}')+\frac{1}{2k_F}\sum_q \boldsymbol{\eta}_{\boldsymbol{k}-\boldsymbol{k}'-\boldsymbol{q}}(\boldsymbol{Q}_{B,q}-\boldsymbol{Q}_{A,q}), \end{aligned} \tag{D.9}$$

and consequently for the lower left block

$$\mathcal{H}^{\eta^*}_{\boldsymbol{K},\boldsymbol{k},\boldsymbol{k}'} = \frac{1}{2k_F}\boldsymbol{\eta}^*_{\boldsymbol{k}'-\boldsymbol{k}}(2\boldsymbol{K}+\boldsymbol{k}+\boldsymbol{k}') + \frac{1}{2k_F}\sum_{\boldsymbol{q}}\boldsymbol{\eta}^*_{\boldsymbol{k}'-\boldsymbol{k}+\boldsymbol{q}}(\boldsymbol{Q}_{B,\boldsymbol{q}}-\boldsymbol{Q}_{A,\boldsymbol{q}}). \tag{D.10}$$

The self-consistency equation for the order parameter can be written as

$$\begin{aligned}\boldsymbol{\eta} &= -\frac{iV}{2k_F}\upsilon\sum_n (v^*_n\boldsymbol{\nabla}u_n - u_n\boldsymbol{\nabla}v^*_n + i(\boldsymbol{Q}_B-\boldsymbol{Q}_A)v^*_n u_n)\tanh\frac{\beta E_n}{2}\\ &= \frac{\upsilon}{2k_F}\sum_{n,\boldsymbol{K},\boldsymbol{k},\boldsymbol{k}'} v^*_{n,\boldsymbol{K},\boldsymbol{k}}u_{n,\boldsymbol{K},\boldsymbol{k}'}e^{i(k'-k)r}\,(2\boldsymbol{K}+\boldsymbol{k}+\boldsymbol{k}'+\boldsymbol{Q}_B-\boldsymbol{Q}_A)\tanh\frac{\beta E_n}{2},\end{aligned} \tag{D.11}$$

and the Fourier components obey the self-consistency equation

$$\begin{aligned}\boldsymbol{\eta}_{\boldsymbol{q}} &= \frac{1}{2V_{uc}}\int_{2V_{uc}} e^{-i\boldsymbol{q}\boldsymbol{r}}\boldsymbol{\eta}(\boldsymbol{r})d^2\boldsymbol{r}\\ &= \frac{\upsilon}{2k_F}\sum_{n,\boldsymbol{K}}\Bigg(\sum_{\boldsymbol{k}} v^*_{n,\boldsymbol{K},\boldsymbol{k}}u_{n,\boldsymbol{K},\boldsymbol{k}+\boldsymbol{q}}\,(2\boldsymbol{K}+\boldsymbol{k}+\boldsymbol{k}')\\ &\qquad + \sum_{\boldsymbol{k},\boldsymbol{k}'} v^*_{n,\boldsymbol{K},\boldsymbol{k}}u_{n,\boldsymbol{K},\boldsymbol{k}'}\,(\boldsymbol{Q}_B-\boldsymbol{Q}_A)_{\boldsymbol{q}-\boldsymbol{k}'+\boldsymbol{k}}\Bigg)\tanh\frac{\beta E_n}{2}.\end{aligned} \tag{D.12}$$

D.1.3 d-wave

Here, the upper right off-diagonal block is calculated to be

$$\begin{aligned}\mathcal{H}^{\eta}_{\boldsymbol{K},\boldsymbol{k},\boldsymbol{k}'} &= \frac{1}{k_F^2}\Big(K_x+\frac{1}{2}(k_x+k'_x)\Big)^2\eta_{d\boldsymbol{k}-\boldsymbol{k}'} - \{x\leftrightharpoons y\}\\ &\quad -\frac{1}{k_F^2}\Big(K_x+\frac{1}{2}(k_x+k'_x)\Big)\sum_{\boldsymbol{q}}\eta_{d\boldsymbol{k}-\boldsymbol{k}'-\boldsymbol{q}} - \{x\leftrightharpoons y\}\\ &\quad +\frac{1}{4k_F^2}\sum_{\boldsymbol{q}}\eta_{d\boldsymbol{k}-\boldsymbol{k}'-\boldsymbol{q}}\Big[(Q^x_A-Q^x_B)^2\Big]_{\boldsymbol{q}} - \{x\leftrightharpoons y\}\\ &\quad +\frac{i}{4k_F^2}\sum_{\boldsymbol{q}}\eta_{d\boldsymbol{k}-\boldsymbol{k}'-\boldsymbol{q}}\Big[(\partial_x^2-\partial_y^2)(\phi_A+\phi_B)\Big]_{\boldsymbol{q}}.\end{aligned} \tag{D.13}$$

The expression for the lower left block is the same, but with $\eta_{d\boldsymbol{k}-\boldsymbol{k}'-\boldsymbol{q}}$ replaced by $\eta^*_{d\boldsymbol{k}'-\boldsymbol{k}+\boldsymbol{q}}$ and with the last sign reversed in front of the term proportional to $(\phi_A+\phi_B)$. The Fourier components of the self-consistent order parameter then obey the equation

$$\begin{aligned}\eta_{d\boldsymbol{q}} &= \frac{\upsilon_0}{4k_F^2}\sum_{n,\boldsymbol{K}}\Bigg(\sum_{\boldsymbol{k}} v^*_{n,\boldsymbol{K},\boldsymbol{k}}u_{n,\boldsymbol{K},\boldsymbol{k}+\boldsymbol{q}}\Big((2K_x+k_x+k'_x)^2+(2K_y+k_y+k'_y)^2\Big)\\ &\quad +\sum_{\boldsymbol{k},\boldsymbol{k}'} v^*_{n,\boldsymbol{K},\boldsymbol{k}}u_{n,\boldsymbol{K},\boldsymbol{k}'}\Big([(Q^x_A-Q^x_B)^2-(Q^y_A-Q^y_B)^2]_{\boldsymbol{q}-\boldsymbol{k}'+\boldsymbol{k}}\end{aligned}$$

$$-i[(\partial_x^2-\partial_y^2)(\phi_A+\phi_B)]_{\boldsymbol{q}-\boldsymbol{k}'+\boldsymbol{k}}$$
$$-2[(Q_A^x-Q_B^x)_{\boldsymbol{q}-\boldsymbol{k}'+\boldsymbol{k}}(2K_x+k_x+k_x')-\{x\leftrightharpoons y\}]\Big)\Big)\tanh\frac{\beta E_n}{2}. \quad \text{(D.14)}$$

D.1.4 Details of implementation

Initial guess for the dominant order parameter

In real space, our initial guess for the order parameter is

$$\eta=\eta_\infty\left(1-\sum_i\left(1-\tanh\frac{|\boldsymbol{r}-\boldsymbol{r}_i|}{\xi}\right)\right), \quad \text{(D.15)}$$

which leads to the Fourier components

$$\begin{aligned}\eta_{\boldsymbol{k}} &= \frac{1}{2V_{uc}}\int_{2V_{uc}}\eta(\boldsymbol{r})e^{-i\boldsymbol{k}_{m,n}\boldsymbol{r}}d^2\boldsymbol{r}\\ &= \eta_\infty\delta_{m,n;0,0}-\frac{\eta_\infty}{2V_{uc}}\sum_{i\in A,B}\int_{2V_{uc}}\left(1-\tanh\frac{|\boldsymbol{r}-\boldsymbol{r}_i|}{\xi}\right)e^{-i\boldsymbol{k}_{m,n}\boldsymbol{r}}d^2\boldsymbol{r}\\ &= \eta_\infty\delta_{m,n;0,0}-\frac{\eta_\infty}{2V_{uc}}\left(1+e^{-i\pi(m+n)}\right)\int\left(1-\tanh\frac{r}{\xi}\right)e^{-i\boldsymbol{k}_{m,n}\boldsymbol{r}}d^2\boldsymbol{r}\\ &= \eta_\infty\delta_{m,n;0,0}-\frac{2\pi\eta_\infty}{2V_{uc}}\left(1+e^{-i\pi(m+n)}\right)\int_0^\infty drr\left(1-\tanh\frac{r}{\xi}\right)J_0(kr). \quad \text{(D.16)}\end{aligned}$$

Bibliography

[1] J. G. Bednorz and K. A. Müller, Z. Phys. B **64**, 189 (1986).

[2] H. R. Ott et al., Phys. Rev. Lett. **52**, 1915 (1984).

[3] R. A. Fisher et al., Phys. Rev. Lett. **62**, 1411 (1989).

[4] M. Sigrist and K. Ueda, Rev. Mod. Phys. **63**, 239 (1991).

[5] S. Yip and A. Garg, Phys. Rev. B **48**, 3304 (1993).

[6] W. N. Hardy, D. A. Bonn, D. C. Morgan, R. Liang, and K. Zhang, Phys. Rev. Lett. **70**, 3999 (1993).

[7] K. Zhang et al., Phys. Rev. Lett. **73**, 2484 (1994).

[8] J. A. Martindale et al., Phys. Rev. B **47**, 9155 (1993).

[9] I. Maggio-Aprile, C. Renner, A. Erb, E. Walker, and O. Fischer, Phys. Rev. Lett. **75**, 2754 (1995).

[10] C. Renner and Ø. Fischer, Phys. Rev. B **51**, 9208 (1995).

[11] C. Renner, B. Revaz, J.-Y. Genoud, K. Kadowaki, and Ø. Fischer, Phys. Rev. Lett. **80**, 149 (1998).

[12] C. Renner, B. Revaz, K. Kadowaki, I. Maggio-Aprile, and Ø. Fischer, Phys. Rev. Lett. **80**, 3606 (1998).

[13] Z. X. Shen et al., Phys. Rev. Lett. **70**, 1553 (1993).

[14] H. Ding et al., Phys. Rev. Lett. **74**, 2784 (1995).

[15] D. A. Wollman, D. J. van Harlingen, W. C. Lee, D. M. Ginsberg, and A. J. Leggett, Phys. Rev. Lett. **71**, 2134 (1993).

[16] D. A. Brawner and H. R. Ott, Phys. Rev. B **50**, 6530 (1994).

[17] C. C. Tsuei et al., Phys. Rev. Lett. **73**, 593 (1994).

[18] D. A. Wollman, D. J. van Harlingen, W. C. Lee, D. M. Ginsberg, and A. J. Leggett, Phys. Rev. Lett. **74**, 797 (1995).

[19] D. J. V. Harlingen, Rev. Mod. Phys. **67**, 515 (1995).

[20] C. C. Tsuei et al., Science **271**, 329 (1996).

[21] Y. Maeno et al., Nature **372**, 532 (1994).

[22] R. Heeb, A. van Otterlo, M. Sigrist, and G. Blatter, Phys. Rev. B **54**, 9385 (1996).

[23] A. A. Abrikosov, Sov. Phys. JETP **5**, 1174 (1957).

[24] P. I. Soininen, C. Kallin, and A. J. Berlinsky, Phys. Rev. B **50**, 13883 (1994).

[25] A. J. Berlinsky, A. L. Fetter, M. Franz, C. Kallin, and P. I. Soininen, Phys. Rev. Lett. **75**, 2200 (1995).

[26] M. Franz, C. Kallin, P. I. Soininen, A. J. Berlinsky, and A. L. Fetter, Phys. Rev. B **53**, 5795 (1996).

[27] Y. Ren, J. Xu, and C. S. Ting, Phys. Rev. Lett. **74**, 3680 (1995).

[28] J. Xu, Y. Ren, and C. S. Ting, Phys. Rev. B **53**, R2991 (1996).

[29] M. Ichioka, N. Hayashi, N. Enomoto, and K. Machida, Phys. Rev. B **53**, 2233 (1996).

[30] B. Keimer et al., Phys. Rev. Lett. **73**, 3459 (1994).

[31] H. Won and K. Maki, Phys. Rev. B **53**, 5927 (1996).

[32] A. G. Sun, D. A. Gajewski, M. B. Maple, and R. C. Dynes, Phys. Rev. Lett. **72**, 2267 (1994).

[33] M. Sigrist, K. Kuboki, P. A. Lee, A. J. Millis, and T. M. Rice, Phys. Rev. B **53**, 2835 (1996).

[34] R. Joynt, Phys. Rev. B **41**, 4271 (1990).

[35] D. L. Feder and C. Kallin, Phys. Rev. B **55**, 559 (1997).

[36] N. Enomoto, M. Ichioka, and K. Machida, J. Phys. Soc. Jpn. **66**, 204 (1997).

[37] C. R. Hu, Phys. Rev. B **6**, 1756 (1972).

[38] R. Heeb and D. F. Agterberg, Phys. Rev. B **59**, 7076 (1999).

[39] T. M. Riseman et al., Nature **396**, 242 (1998).

[40] E. M. Forgan and D. M. Paul, submitted to Nature (1999).

[41] P. G. Kealey et al., submitted to Phys. Rev. Lett. (2000).

[42] R. Balian and N. R. Werthamer, Phys. Rev. **131**, 1553 (1963).

[43] T. M. Rice and M. Sigrist, J. Phys. Condens. Matter **7**, L643 (1995).

[44] G. M. Luke et al., Nature **394**, 558 (1998).

[45] D. F. Agterberg, Phys. Rev. Lett. **80**, 5184 (1998).

[46] A. P. Mackenzie et al., Phys. Rev. Lett. **76**, 3786 (1996).

[47] T. Oguchi, Phys. Rev. B **51**, 1385 (1995).

[48] D. J. Singh, Phys. Rev. B **52**, 1358 (1995).

[49] T. Imai, A. W. Hunt, K. R. Thurber, and F. C. Chou, Phys. Rev. Lett. **81**, 3006 (1998).

[50] D. F. Agterberg, T. M. Rice, and M. Sigrist, Phys. Rev. Lett. **78**, 3374 (1997).

[51] I. I. Mazin, D. A. Papaconstantopoulos, and D. J. Singh, preprint: cond-mat/9907442 (1999).

[52] T. Oguchi, private communication (2000).

[53] V. G. Kogan et al., Phys. Rev. B **54**, 12386 (1996).

[54] K. Park and D. A. Huse, Phys. Rev. B **58**, 9427 (1998).

[55] I. Affleck, M. Franz, and M. H. S. Amin, Phys. Rev. B **55**, R704 (1997).

[56] Y. D. Wilde et al., Phys. Rev. Lett. **78**, 4273 (1997).

[57] A. P. Mackenzie et al., Phys. Rev. Lett. **80**, 161 (1998).

[58] D. F. Agterberg, Phys. Rev. B **58**, 14484 (1998).

[59] E. H. Brandt, J. Low Temp. Phys. **26**, 709, 735 (1977).

[60] E. H. Brandt, Phys. Rev. Lett. **78**, 2208, 2211 (1997).

[61] M. M. Doria, J. E. Gubernatis, and D. Rainer, Phys. Rev. B **39**, 9573 (1989).

[62] M. M. Doria, J. E. Gubernatis, and D. Rainer, Phys. Rev. B **41**, 6335 (1990).

[63] E. H. Brandt, Phys. Stat. Sol. **36**, 381, 393 (1969).

[64] J. M. Delrieu, J. Low Temp. Phys. **6**, 197 (1972).

[65] E. Dumont, private communication (2000).

[66] K. Yoshida, private communication (1996).

[67] K. Yoshida, Y. Maeno, S. Nishizaki, and T. Fujita, Physica C **263**, 519 (1996).

[68] G. Eilenberger, Z. Phys. **214**, 195 (1968).

[69] L. Kramer and W. Pesch, Z. Phys. **269**, 59 (1974).

[70] C. Caroli, P. G. de Gennes, and J. Matricon, Phys. Lett. **9**, 307 (1964).

[71] C. Caroli and J. Matricon, Phys. Kondens. Mater. **3**, 380 (1965).

[72] H. F. Hess, R. B. Robinson, R. C. Dynes, J. M. Valles, Jr., and J. V. Waszczak, Phys. Rev. Lett. **62**, 214 (1989).

[73] H. F. Hess, R. B. Robinson, and J. V. Waszczak, Phys. Rev. Lett. **64**, 2711 (1990).

[74] H. F. Hess, R. B. Robinson, and J. V. Waszczak, Physica B **169**, 422 (1991).

[75] J. D. Shore, M. Huang, A. T. Dorsey, and J. P. Sethna, Phys. Rev. Lett. **62**, 3089 (1989).

[76] F. Gygi and M. Schlüter, Phys. Rev. B **41**, 822 (1990).

[77] F. Gygi and M. Schlüter, Phys. Rev. B **43**, 7609 (1991).

[78] F. Gygi and M. Schlüter, Phys. Rev. Lett. **65**, 1820 (1990).

[79] N. Hayashi, M. Ichioka, and K. Machida, Phys. Rev. Lett. **77**, 4074 (1996).

[80] N. Hayashi, M. Ichioka, and K. Machida, Phys. Rev. B **56**, 9052 (1997).

[81] M. Ichioka, N. Hayashi, and K. Machida, Phys. Rev. B **55**, 6565 (1997).

[82] N. Hayashi, T. Isoshima, M. Ichioka, and K. Machida, Phys. Rev. Lett. **80**, 2921 (1998).

[83] M. Kato and K. Maki, preprint: condmat/9810187 (1998).

[84] D. I. Khomskii and A. Freimuth, Phys. Rev. Lett. **75**, 1384 (1995).

[85] M. V. Feigel'man, V. D. Geshkenbein, A. I. Larkin, and V. M. Vinokur, Pis'ma Zh. Eksp. Teor. Fiz. **62**, 811 (1995), [JETP Lett. **62**, 834 (1995)].

[86] G. Blatter, M. V. Feigel'man, V. B. Geshkenbein, A. I. Larkin, and A. van Otterlo, Phys. Rev. Lett. **77**, 566 (1996).

[87] N. Hayashi, M. Ichioka, and K. Machida, J. Phys. Soc. Jpn. **67**, 3368 (1998).

[88] N. B. Kopnin and M. M. Salomaa, Phys. Rev. B **44**, 9667 (1991).

[89] M. Matsumoto and M. Sigrist, J. Phys. Soc. Jpn. **68**, 724 (1999).

[90] J. Goryo and K. Ishikawa, J. Phys. Soc. Jpn. **67**, 3006 (1998).

[91] J. Goryo and K. Ishikawa, Phys. Rev. A **260**, 294 (1999).

[92] J. Goryo, preprint: condmat/9908113 (1999).

[93] M. Matsumoto, A. Furusaki, and M. Sigrist, private communication (2000).

[94] G. E. Volovik, preprint: condmat/9909426 v2 (1999).

[95] P. G. de Gennes, *Superconductivity of Metals and Alloys*, Addison-Wesley, 1989.

[96] M. Matsumoto and M. Sigrist, J. Phys. Soc. Jpn. **68**, 994 (1999).

[97] G. E. Volovik, Sov. Phys. JETP Lett. **58**, 469 (1993).

[98] K. A. Moler et al., Phys. Rev. Lett. **73**, 2744 (1994).

[99] Y. Wang and A. H. MacDonald, Phys. Rev. B **52**, R3876 (1995).

[100] N. Schopohl and K. Maki, Phys. Rev. B **52**, 490 (1995).

[101] K. Maki, N. Schopohl, and H. Won, Physica B **204**, 214 (1995).

[102] Y. Morita, M. Kohmoto, and K. Maki, Phys. Rev. Lett. **78**, 4841 (1997).

[103] M. Franz and M. Ichioka, Phys. Rev. Lett. **79**, 4513 (1997).

[104] Y. Morita, M. Kohmoto, and K. Maki, Phys. Rev. Lett. **79**, 4514 (1997).

[105] M. Franz and Z. Tešanović, Phys. Rev. Lett. **80**, 4763 (1997).

[106] A. S. Melnikov, J. Phys. Condens. Matter **21**, 4219 (1999).

[107] E. Brown, Phys. Rev. **133**, A1038 (1964).

[108] T. Kita, J. Phys. Soc. Jpn. **67**, 2067 (1998).

[109] T. Kita, J. Phys. Soc. Jpn. **67**, 2075 (1998).

[110] K. Yasui and T. Kita, Phys. Rev. Lett. **83**, 4168 (1999).

[111] M. Franz and Z. Tešanović, Phys. Rev. Lett. **84**, 554 (2000).

[112] M. Nielsen and P. Hedegård, Phys. Rev. B **51**, 7679 (1995).

[113] P. Hedegård and A. Hoff, Physica B **194-196**, 1075 (1995).

[114] P. A. M. Dirac, Proc. Roy. Soc. (London), Ser. A **133**, 60 (1931).

[115] P. A. M. Dirac, Phys. Rev. **74**, 817 (1948).

Acknowledgments

It is a great pleasure to express my gratitude to my supervisor Gianni Blatter. After the studies here at the ETH, he motivated me to write a diploma thesis in his group and showed me thereby my way into solid state physics. Although I was during the four years at the institute certainly not the most regular guest in his office, he always was interested in my progress and guided me with his knowledge and criticism. I profited a lot from his intuitive physical understanding which often enough saved me from burying myself in numerical details. Further, I learned a lot about the art of presentation and "public relations" in his formidable seminar talks and undergraduate lectures. I am grateful to have had the possibility to train these skills by presenting my work at numerous conferences. Last but not least, I especially enjoyed the excellent atmosphere in his solid state group, be it in everyday life at the institute, be it at the many midsummer parties under the care of Ilona in Otelfingen.

This thesis could hardly have been written without the continuous help of many mentors and collaborators. During my diploma thesis, I made my first steps in the theory of superconductivity under the guidance of Anne van Otterlo. His ability to reduce complicated facts to a simple idea helped me a lot in these early days. During the first months of my thesis, I got into contact with Manfred Sigrist, who should turn out as one of my most important mentors. It was a lucky decision for me, when he decided to come back to the ETH for some years. I owe a depth of gratitude to him for his continuous support during all the last four years. I benefit-ted a lot of his deep understanding of the physics of unconventional superconductors, and he supplied me with many stimulating ideas how to overcome my problems. Moreover I wish to thank him for giving me the possibility to stay several weeks at the Yukawa Institute for Theoretical Physics in Kyoto, and for his hospitality in his flat. It was a very fruitful stay, and a lasting experience for me. In this context I thank his whole group for receiving me in their institute, especially Okuno-san for introducing me into the high art of Origami.

I am particularly thankful also to Daniel Agterberg. During his stay at ETH, he initiated our common work about Sr_2RuO_4 and introduced me in this way to a very interesting growing field. Having done pioneering work about this material, he let me

profit a lot from his skills. I especially appreciated his uncomplicated style and his patience. I very much enjoyed also the short stay with his family in Tallahassee.

During my stay in Kyoto, I got to know Masashige Matsumoto. After realizing that we were working on the same problem, we decided later to follow the project in common. It is a pleasure to work with him, regardless of the problems due to the big distance.

I would very much like to thank Maurice Rice for co-refereeing my thesis. His spontaneous agreement was a great pleasure for me.

A special thank goes to all my office mates at E8. When I moved my first few books into my new office, I did not expect this kind of extraordinary atmosphere. The constant support of Orlando Wagner, Bruce Normand, Helmut Katzgraber, Malek Bou-Diab and Hanspeter Büchler in physical as well as other questions was often enough the basis for a following success. I often wondered whether every office team invests so much of its creativity to invent new distractions.... Special thanks to Malek for his constant support in computer questions. I especially profited also from his deep understanding of the biography of General Patton. A special thank goes to Pickwick, who gave me the few moments of distraction during the end of my thesis.

At this point I want to express my thanks to my friends and colleagues Beat Ammon, Walter Aschbacher, Matthew Dodgson, Hans Peter Dreyer, Elisabeth Dumont, Alban Fauchère, Ted Forgan, Beat Frischmuth, Dima Geshkenbein, Denis Gorokhov, Stefan Haas, Elmar Heeb, Andreas Honecker, Carsten Honerkamp, Michael Hunziker, Markus Hütter, Dima Ivanov, Markus Kasper, Paul Kealey, Matthias Körner, Daniel Kuhn, Andreas Läuchli, Henrik Nordborg, Felix Schlenk, Andreas Schönenberger, Thomas Siller, Ivo Stalder, Matthew Steiner, Matthias Troyer, and Mischa Zhitomirskii. Although I missed virtually every Thursday-evening seminar, I enjoyed the good atmosphere in the theory building.

This thesis would never have been written without the continuous support of my family. Especially my parents motivated me always with their moral and financial support. They gave me the possibility to learn how beautiful the nature is organized, and I hope I will be able to pass on this enthusiasm to many other people in the future. In the last few years, my greatest moral support came from Ursula. Laughing with her and planning our common future healed many sorrows in these last months. She always found the right words to motivate me for some more efforts.

Last but not least, I gratefully acknowledge the financial assistance of the Swiss National Foundation.

Curriculum Vitae

Personal Dates

Name:	Rolf Heeb
Born:	March 14, 1970 in Rapperswil, SG
Nationality:	Switzerland

Education

4/1977–4/1983	Primary school in Rapperswil
4/1983–4/1985	Secondary school in Rapperswil
4/1985–1/1990	High school in Wattwil
1/1990	Final degree: Matura
9/1990–4/1995	Undergraduate studies in physics at the Swiss Federal Institute of Technology Zürich (ETH-Zürich)
11/1995	Diploma thesis on "Vortices in d-wave superconductors" at the Institute of Theoretical Physics, ETH-Zürich under the supervision of Prof. G. Blatter
11/1995–3/2000	Graduate studies at the Institute of Theoretical Physics at the ETH-Zürich under the supervision of Prof. G. Blatter